Poly(3,4-ethylenedioxythiophene) and Viologen Based Materials for Electrochromic Devices

Rambabu Sydam

A Dissertation Submitted to the
Indian Institute of Technology Hyderabad
In Partial Fulfillment of the Requirements for
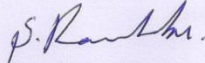Doctor of Philosophy

भारतीय प्रौद्योगिकी संस्थान हैदराबाद
Indian Institute of Technology Hyderabad

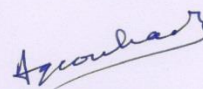Department of Chemistry

March, 2015

Declaration

I declare that this written submission represents my ideas in my own words, and where others' ideas or words have been included, I have adequately cited and referenced the original sources. I also declare that I have adhered to all principles of academic honesty and integrity and have not misrepresented or fabricated or falsified any idea/data/fact/source in my submission. I understand that any violation of the above will be a cause for disciplinary action by the Institute and can also evoke penal action from the sources that have thus not been properly cited, or from whom proper permission has not been taken when needed.
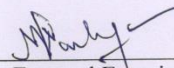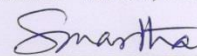
(Rambabu Sydam)

(CY11P018)

Approval Sheet

This thesis entitled **"Poly(3,4-ethylenedioxythiophene) and Viologen Based Materials for Electrochromic Devices"** by Rambabu Sydam is approved for the degree of Doctor of Philosophy from the Indian Institute of Technology Hyderabad.

External Examiner
Prof. A.Q. Contractor
Department of Chemistry
Indian Institute of Technology Bombay
Mumbai - 400076, India
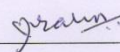
External Examiner
Prof. M. V. Sangaranaryanan
Department of Chemistry
Indian Institute of Technology Madras
Chennai- 600036, India

Internal Examiner
Dr. Surendra K. Martha
Department of Chemistry
Indian Institute of Technology Hyderabad
Yeddumailaram - 502205, India

Adviser
Dr. M. Deepa
Associate Professor
Department of Chemistry
Indian Institute of Technology Hyderabad
Yeddumailaram - 502205, India

Chairman
Dr. Praveen Meduri
Department of Chemical Engineering
Indian Institute of Technology Hyderabad
Yeddumailaram - 502205, India

Acknowledgements

Nomenclature

EC: Electrochromism

ECD: Electrochromic device

CE: Coloration efficiency

WE: Write-erasure efficiency

IL: Ionic liquid

CV: Cyclic voltammetry

CA: Chronoamperometry

LSV: Linear sweep voltammetry

EIS: Electrochemical impedance spectroscopy

AFM: Atomic force microscopy

KPFM: Kelvin probe force microscopy

FTIR: Fourier transform infrared spectroscopy

TGA: Thermogravimetric analysis

FE SEM: Field emission scanning electron microscopy

XPS: X-ray photoelectron spectroscopy

XRD: X-ray diffraction

ITO: Indium tin oxide (In_2O_3:Sn)

FTO: Fluorine doped tin oxide (SnO_2:F)

CP: Conjugated polymer

PB: Prussian blue

HV: Heptyl viologen

ECRA mirror: Antiglare electrochromic rearview mirror

PET: Poly(ethyleneterephthalate)

PEDOT: Poly(3,4-ethylenedioxythiophene)

Contents

Abstract

Electroactive materials which undergo reversible optical changes through electrochemical redox reactions by the application of an electric field are called electrochromic (EC) materials. Among various electrochromes, organic electrochromes such as poly(3,4-ethylenedioxythiophene) (PEDOT) and viologens can modulate visible light and offer high contrast ratios and fast switching times. In the present thesis, PEDOT/fulleropyrrolidine films were prepared for the first time and the optical response of the film is completely altered by the presence of the fullerene derivative; a coloration efficiency of 386 cm^2 C^{-1} was acheived. Electrohromic devicves (ECDs) with a PEDOT film as cathode and a Prussian blue (PB) film as anode were constructured and the superior EC performance of the an *in-situ* polymerized ionic liquid based gel electrolyte compared to a conventional gel electrolyte was demonstrated. The optimized *in-situ* polymerized gel was then used in a heptyl viologen based ECD and the switching of a large area device (8 cm × 6 cm) for antiglare electrochromic rearview (ECRA) mirrors was demonstrated. PEDOT films were then transposed over plastic substrates and their ability to serve as a transparent conductor and an electrochromic electrode was shown. Similarly viologens offer different colors depending on the N-substituent. Although a variety of viologens were synthesized in the past, a reversible and high write-erase efficiency continues to pose a formidable challenge. To address this concern, new derivatives of viologens were synthesized by the use of substituents like butylbenzimidazole and ethylindole, their ECDs were constructed and characterized. Further, a hybrid viologen was also prepared by using a phosphonitrillic trimer ($P_3N_3Cl_6$) as a central core and the potential of this viologen for durable, high contrast ECDs was shown. These viologen based ECDs showed very high contrast ratios, high coloration efficiencies, short response times and the devices can endure more than 2000 cycles without undergoing degradation. These devices and materials are very much useful for applications such as flexible displays, energy saving switchable windows in buildings and automobiles and ECRA mirrors.

1

Chapter 1

Electrochromic materials, films, devices and applications

1.1 Introduction to electrochromism

Chromism is a process by which the color of a material changes reversibly through an external stimulus. Depending upon the nature of the external input, the ensuing change is called photochromism (photon) [1] or thermochromism (heat) [2], or solvatochromism (solvent) [3], or electrochromism (electron) [4] or piezochromism (pressure) [5]. Of particular interest, is electrochromism (EC). Electrochromism is defined as a reversible optical change brought about in a material through redox reactions, by an application of an electric voltage or current. The first color change following electrochemical reduction of a solid, tungsten trioxide, was that of Kobosew and Nekrassow in 1930. But later, Deb's demonstration of reversible, electrically induced coloration in thin films of transition metal oxides [6] in the late 1960s and 1970s provoked significant efforts to study EC materials and EC devices (ECDs) for applications like displays and ECRA mirrors [7,8] . Motivated by the potential for significant energy savings from reduced cooling and heating loads, research in this area has shifted towards developing EC windows that dynamically control sun light entering a building [9-11]. An optimized EC window would provide separate, dynamic control over the transmission of visible and NIR solar radiation using materials with high optical contrast, fast switching times, long cycle life, and low manufacturing cost. Many inorganic and organic materials including metal coordination complexes, both in solution and as polymer films, inorganic charge-transfer complexes, transition metal oxides (especially tungsten trioxide, WO_3), viologens (4,4′-bipyridylium salts) and conjugated conducting polymers such as polypyrroles and polythiophenes exhibit redox states with distinct electronic visible absorption bands [12-16]. When the switching of redox states generates new or different visible region bands, the material is said to be electrochromic (EC). EC materials are currently attracting much interest in academia and industry for their fascinating spectroelectrochemical properties and their commercial applications. Since EC materials can be easily assembled into solid-state ECDs, they find applications in controllable light-reflective or light-transmissive ECDs for optical information and storage, high contrast displays, fast switching ECRA mirrors, sunglasses, protective eyewear for military, controllable aircraft canopies, glare-reduction systems for offices and smart windows for use in cars and in buildings [17-23]. Of these, ECRA mirrors for cars have already achieved

considerable commercial success. These safety ECDs prevent mirror-reflected glare which causes an 'after image' to stay on the eye's retina.

Among the various available solar control windows such as tinted, reflective, photochromic, thermochromic, suspended particle- and liquid crystal- devices, EC windows offer the best compromise between electric lighting energy and electric cooling energy (Figure 1.1) [24]. However, EC windows are expensive. The energy saving attribute nonetheless provides the impetus to develop novel EC materials and ECDs.
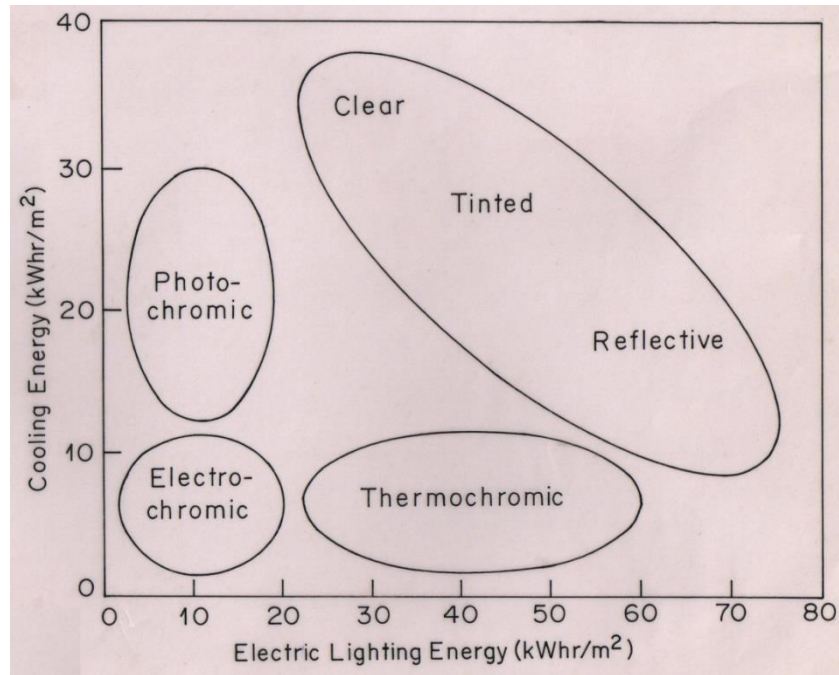
Figure 1.1 Plot of cooling energy *versus* electric lighting energy for various solar control windows such as photochromic, EC, thermochromic etc. Adapted from internet: http://www.mge.com/saving-energy/business/bea/article_detail.htm?nid=1831. All content copyright 1986-2015 E Source Companies LLC [24].

Although a vast number of chemical species exhibit EC properties, only those with favorable EC performance parameters and long operational life are potentially useful for commercial applications. Electrochromic polymers that can change between a transparent colorless form and an opaque black form offer potential uses in non-emissive displays or signage and prototype of smart sunglasses are shown in Figure 1.2. Thus, most EC applications require EC materials with a high contrast ratio, large coloration efficiency (wavelength dependent absorbance change/charge injected per unit area), prolonged cycle life, and write-erase efficiency (% of originally produced color that may be subsequently electro-bleached).

While displays need fast response times, by contrast, for smart windows, response times of up to several minutes, is acceptable.
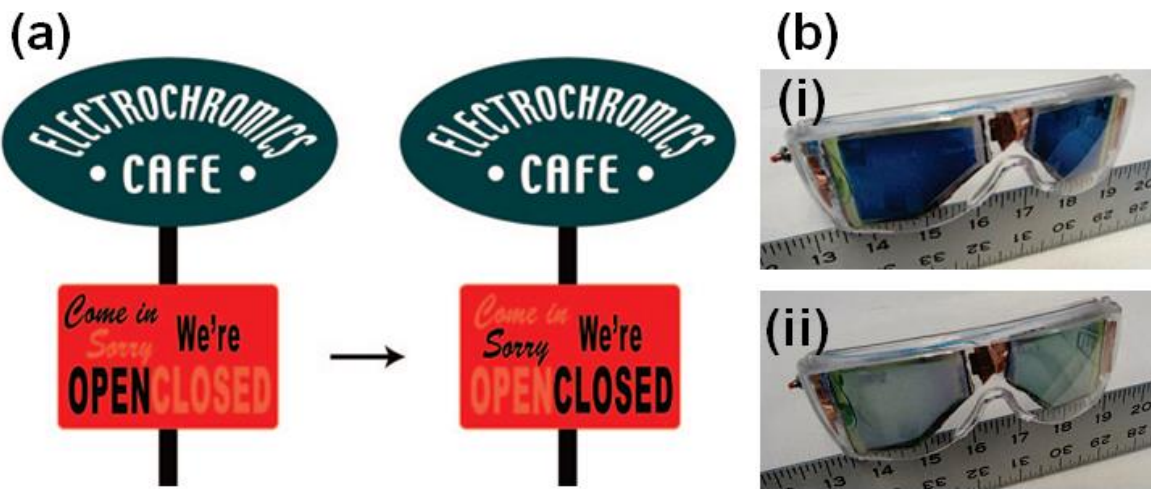
Figure 1.2 (a) Electrochromic polymers that can change between a transparent colorless form and an opaque black form offer potential uses in non-emissive displays or signage. Reprinted with permission from Nat. Mater. 7 (2008) 766. Copyright (2008) Nature Publishing Group [25]. (b) Prototype of smart sunglasses as constructed by Xu et al. A battery powers the switching process from (i) a deeply colored state to (ii) a fully transparent state of a prototype of smart sunglasses. Reprinted with permission from Polym. Eng. Sci. 48 (2008) 2224. Copyright (2008) Wiley-VCH Verlag GmbH & Co. KGaA, Weinheim, Germany [26].

1.2 ECD operation

An ECD is an electrochemical cell wherein optical changes are produced by electrochemical reactions of two or more redox-active materials separated by an ion-conducting layer. EC switching of these ECDs is limited by the diffusion of ions from one layer to another. ECDs are designed to operate in either absorptive/transmissive or reflective mode. An absorption/transmission-type ECD operates by the reversible switching of an EC material between a colored (absorptive) and a transmissive (bleached) state on a transparent conducting substrate. To achieve high contrast values in such a ECD, two complementary materials are used, namely, a cathodically coloring material and an anodically coloring material, deposited onto transparent electrodes (e.g., In_2O_3:Sn/glass (ITO/glass), ITO coated poly(ethylene terephthalate) (ITO/PET) or poly(3,4-ethylenedioxythiophene)-poly(styrene sulfonate) coated PET (PEDOT-PSS/PET), and separated by an electrolyte (a liquid or a viscous gel or a solid) to allow ion transport as shown in Figure 1.3. Therefore, when both these EC materials are assembled in a sandwich configuration and an external voltage is applied, the ECD switches between a colored state and a transmissive state.
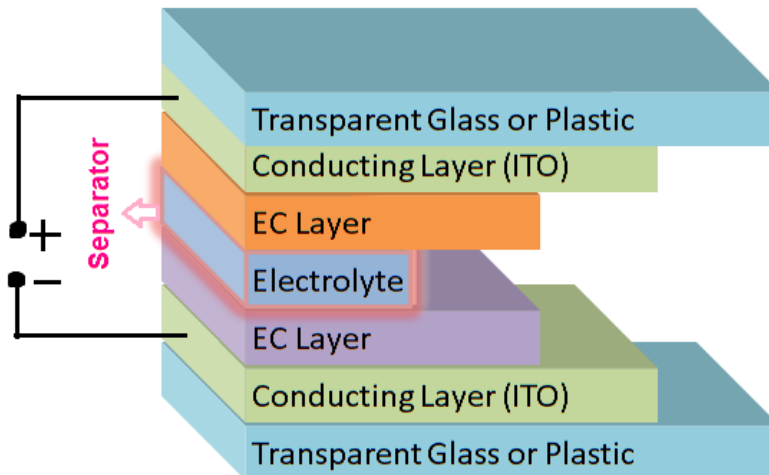
Figure 1.3 Schematic of an ECD.

1.2.1 Classification of EC materials

   Using a simple classification system developed by Chang et al., [27], EC materials can be classified into three simple types on the basis of the solubility of each redox state.

(i) Type-I: In a given electrolyte solution, type I EC materials are soluble in both the reduced and the oxidized states. Examples are the viologen: N,N′-dimethyl-4,4′-bipyridylium [methyl viologen (MV)] and numerous metal complexes and organic redox indicators.

 (ii) Type-II: These EC materials are soluble in one redox state but form a solid film on the surface of an electrode following electron transfer. Examples are N,N′-bis(n-heptyl)-4,4′-bipyridylium (HV) in water and the reversible electrodeposition of metals.

(iii) Type-III : In type-III EC materials, such as tungsten oxide (WO_3), polymeric viologens, conjugated conducting polymers, metallopolymers, and the metal hexacyanometallate like PB, both or all redox states are solid, and these systems are studied as thin films on electrode surfaces.

1.2.2 Electrolytes in ECDs

   As ECDs require electrolyte for their operation, with regard to durability, chemical compatibility between the electrolyte and the electrochromic films without the loss of optical transparency is very much important for display applications. In this regard, electrolytes used for the fabrication of ECDs are ionic liquids (ILs) or inorganic salts dissolved in organic solvents and ionogels. Ionogels are used so that leakage free devices can be realized.

1.2.2(a) ILs

   A salt melting below the normal boiling point of water is known as an IL, thus forming liquids that are comprised entirely of cations and anions at room temperature. In contrast to conventional organic liquids/solvents, important physical properties of ILs such as viscosity, density, melting point and

5

conductivity can be tuned to suit a particular need by the appropriate choice of the cation/anion combination. ILs typically contain a large bulky asymmetric cation together with a smaller π-delocalized anion which overwhelmingly exhibit electrostatic interactions; thereby preventing the formation of a structured lattice [28]. ILs exhibit good thermal stability, are intrinsically conductive and have been shown to have electrochemical stability windows as wide as 5.0 V in some cases [29 -31]. Thus ILs play a major role for device fabrication.

1.2.2(b) Ionogels

A polymer gel is defined as an interconnected polymer network formed within a liquid phase [32-34]. When the polymer network is generated in the presence of IL, the resultant gel has been termed as an ionogel within literature. Ionogels are therefore a new class of hybrid material that combine the physical properties of both the polymer gel and the physically entrapped IL within [35,36]. ECDs based on solid polymeric electrolytes (SPEs) are desirable for the development of energy efficient windows or "smart windows". In order to have an efficient and reproducible performance of an ECD, the ohmic drop across the device needs to be minimized. This can be achieved with an electrolyte having a conductivity greater than 10^{-4} S cm^{-1}at room temperature. Several approaches have been followed to prepare SPEs with such properties. A variety of PMMA based gels consisting of solutions of lithium salts in propylene carbonate-ethylene carbonate mixture reported by Scrosati et al. [37], have shown the very important role played by PMMA. Our group in particular have detailed the use of ionogels by synthesizing them using *in-situ* thermal polymerization techniques for electro-optical devices especially for the ECDs.

1.3 Viologens

Viologens are formed by the di-quaternization of 4,4′-bipyridine to form 1,1′-disubstituted-4,4′-bipyridinium salts. The common name of 'viologen' was coined by Michaelis, who noted that a violet color formed, when a 1,1′-dimethyl-4,4′-bipyridinium salt underwent a one-electron reduction to form a radical cation [18,38,39].

(1)
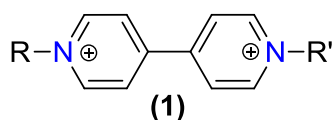
Symmetric viologen if R, R' are same
Asymmetric viologen if R, R' are different

Scheme 1.1: Generic structure of a viologen.

The three common redox forms of viologen are (i) bipyridinium dications (V^{2+}), (ii) bipyridinium radical cations ($V^{+\bullet}$) and (iii) di-reduced bipyridinium compounds (V^0). Of the three common viologen redox states (Scheme 1.2), the dication is colorless when pure unless optical charge transfer with the

6

counter anion occurs. One electron reduction forms the radical cation, the stability of which is attributable to the delocalization of the radical electron throughout the π framework of the bipyridyl nucleus; the N,N′ substituents commonly bear some of the charge.

$$R-N^{\oplus} \underset{}{} \bigcirc \bigcirc ^{\oplus}N-R \quad \underset{-e^-}{\overset{+e^-}{\rightleftharpoons}} \quad R-N^{\oplus} \bigcirc \overset{\bullet}{\bigcirc} N-R \quad \underset{-e^-}{\overset{+e^-}{\rightleftharpoons}} \quad R-N \bigcirc = \bigcirc N-R$$

$$V^{2+} \qquad\qquad\qquad\qquad V^{+\bullet} \qquad\qquad\qquad\qquad V^0$$
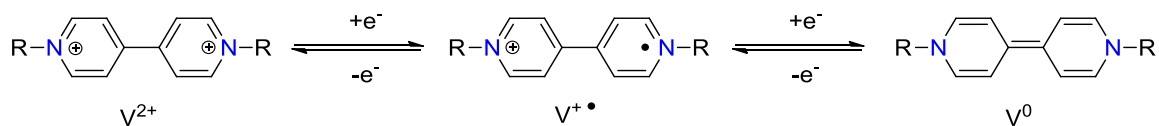
Scheme 1.2: Reversible redox reactions of a viologen, brought about by an electric field.

Viologen radical cations are intensely colored, with high molar absorption coefficients, owing to an optical charge transfer between the (formally) +1-valent and zero-valent nitrogens. Suitable choice of nitrogen substituents in viologens to attain the appropriate molecular orbital energy levels can, in principle, impart a color of choice for the radical cation. For example, alkyl groups lead to a blue-violet color, whereas the radical cation of N,N′-bis(4-cyanophenyl)-4,4′-bipyridylium (cyanophenyl paraquat) in acetonitrile has an intense green color. The intensity of the color exhibited by di-reduced viologens (Scheme 1.2) is low because no optical charge transfer or internal transition corresponding to visible wavelengths is accessible. The working of a viologen based ECD is shown in the Figure 1.4.
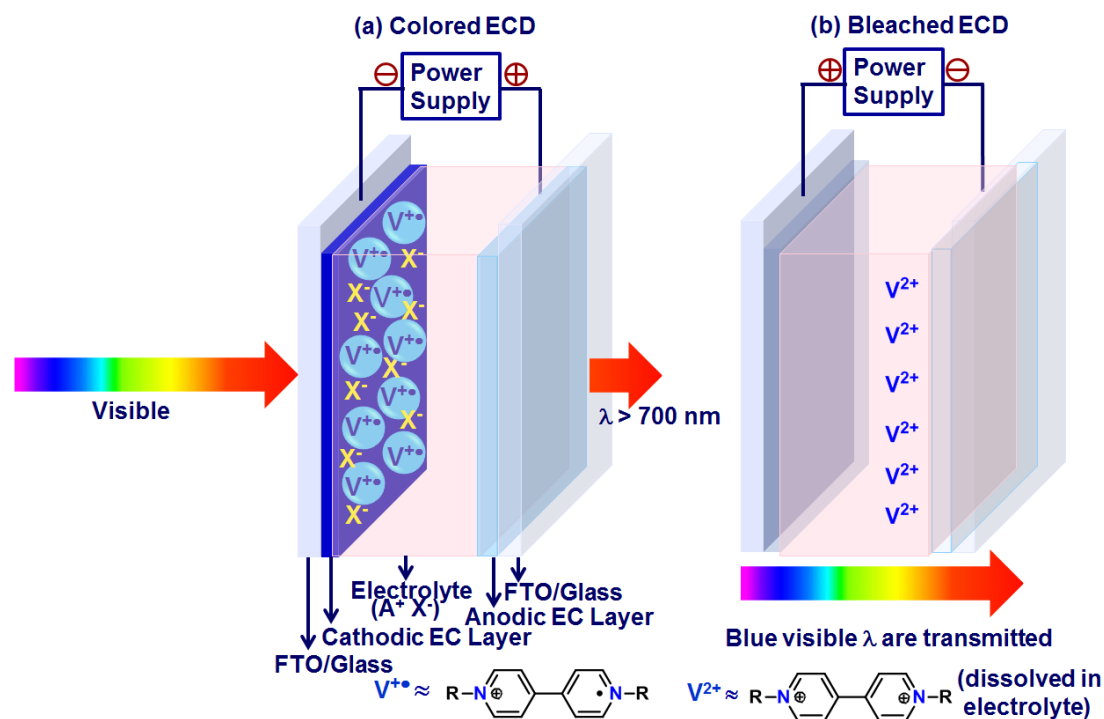
Figure 1.4 Schematic shows a viologen based ECD in its' colored and bleached states.

Upon reduction, the intense blue-colored $V^{+\bullet}$ radical cation film is formed, thus modulating visible radiation. Upon oxidation, V^{2+} salt is regenerated, and it dissolves in the electrolyte. This state is colorless and in this state, all visible wavelengths are transmitted by the ECD. The type of organic groups (alkyl,

benzyl, and phenyl) at the pyridyl nitrogen controls their reduction potential and the spectral response. This is also reflected in the plethora of synthetic efforts concerning new electrochromic viologens with different functional groups [40,41].

1.3.1 Milestones and recent developments in viologens for electrochromics

The viologens have spurred considerable research interest, due to their significant commercial success. Gentex, NREL and Sage Electrochromics have successfully commercialized viologen based ECRA mirrors for vehicles. So the quest for high performance viologens stems from their huge potential in the commercial sector. ECRA mirror is a mirror in automobiles and other vehicles, designed to allow the driver to see rearward through the vehicle's backlight (rear windshield or windscreen). Current systems usually use photosensors mounted in the actual rear-view mirror to detect light and dim the mirror by means of electrochromism. This electrochromic feature has been also incorporated into side-view mirrors allowing them to dim and reduce glare as well. ECRA mirrors are currently being used for the safety driving in the night time. Current systems usually use photosensors mounted in the actual rear-view mirror to detect light and dim the mirror by means of electrochromism. This electrochromic feature has been also incorporated into side-view mirrors allowing them to dim and reduce glare as well. Some milestones and exciting developments in viologen electrochromics are discussed here. Recently, in a pioneering attempt, an EC ionic liquid (IL) containing a phosphonium core tethered to a viologen was adapted to a solid-state electrochromic platform, wherein the viologen modified IL served as both the electrolyte and the electrochrome and improved switching kinetics were achieved (Figure 1.5) [42]. One major advantage of the EC platform is the fact that the viologen is inherently a part of the IL and therefore no leaching occurs. The platform exhibited approximately 2 orders of magnitude faster switching kinetics (221 s to reach 95% absorbance) when compared to previously reported electrochromic ILs (18000 s) [42].
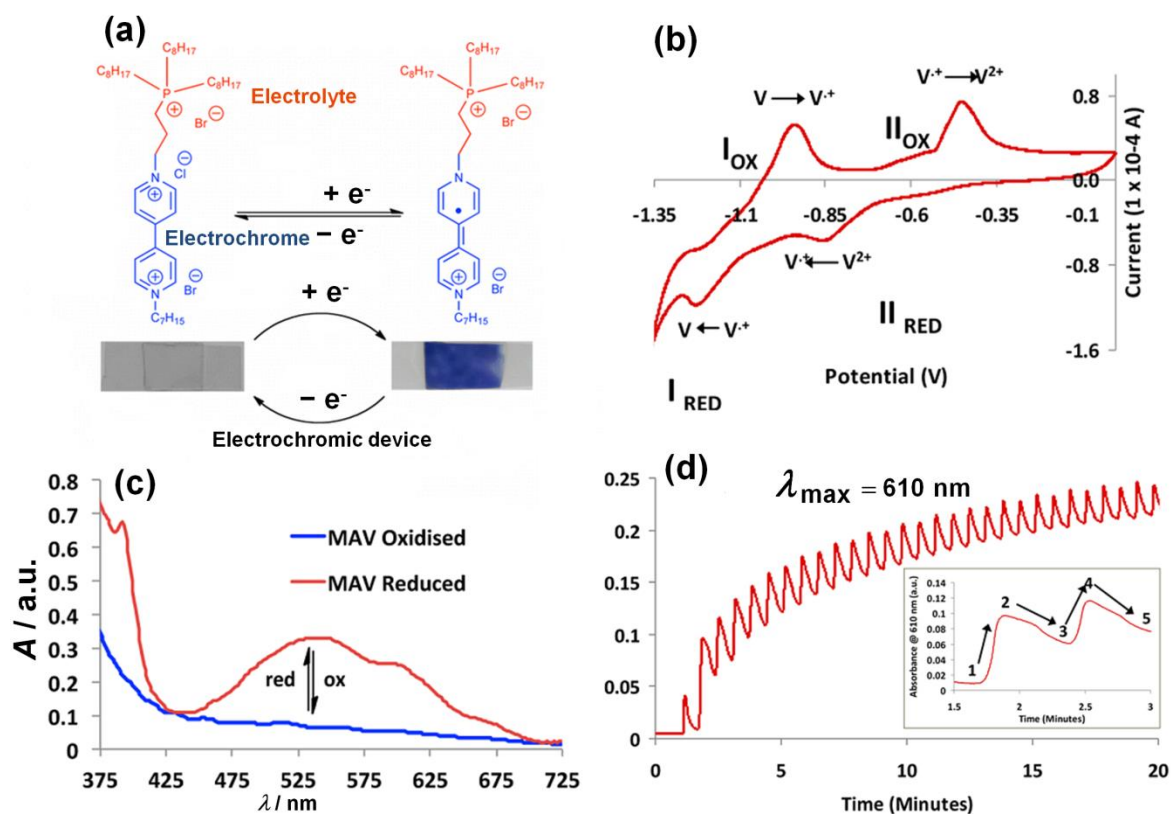
Figure 1.5 (a) An ECD with a viologen chromophore bound to the phosphonium cation of the IL [PV] and encapsulated in the sol−gel. (b) Cyclic voltammogram (scan rate, 100 mV s^{-1}) obtained for [PV], (c) UV−vis absorbance spectra obtained for both oxidized and reduced states of [PV]. (d) Changes in absorbance at 610 nm for ECD as a function of potential window $\pm$ 2 V and the incident scan rate was 100 mV/s. Reprinted with permission from ACS Appl. Mater. Interfaces 5 (2013) 55. Copyright (2013) American Chemical Society [42].

In another study, a new star-shaped 4,4′-bipyridine derivative (1,3,5-tri(1-methyl-4,4-bipyridinium bromide)-2,4,6-trimethyl benzene) TBTB, was synthesized and solid state ECDs based on TBTB were constructed successfully. The ECD presented a stable as well as multicolor electrochromic change from blue to violet–blue and then to violet–red between 0 V and +3.0 V (Figure 1.6). The ECD exhibited a fast switching time (~0.3 s for coloration and 0.5 s for bleaching) between the violet-blue (+2.0 V) reduced state and the transparent light blue oxidized state (−2.0 V), with a contrast ranging from 25% to 40% at 530 nm and a coloration efficiency of 279 cm^2 C^{-1} at 610 nm [43].
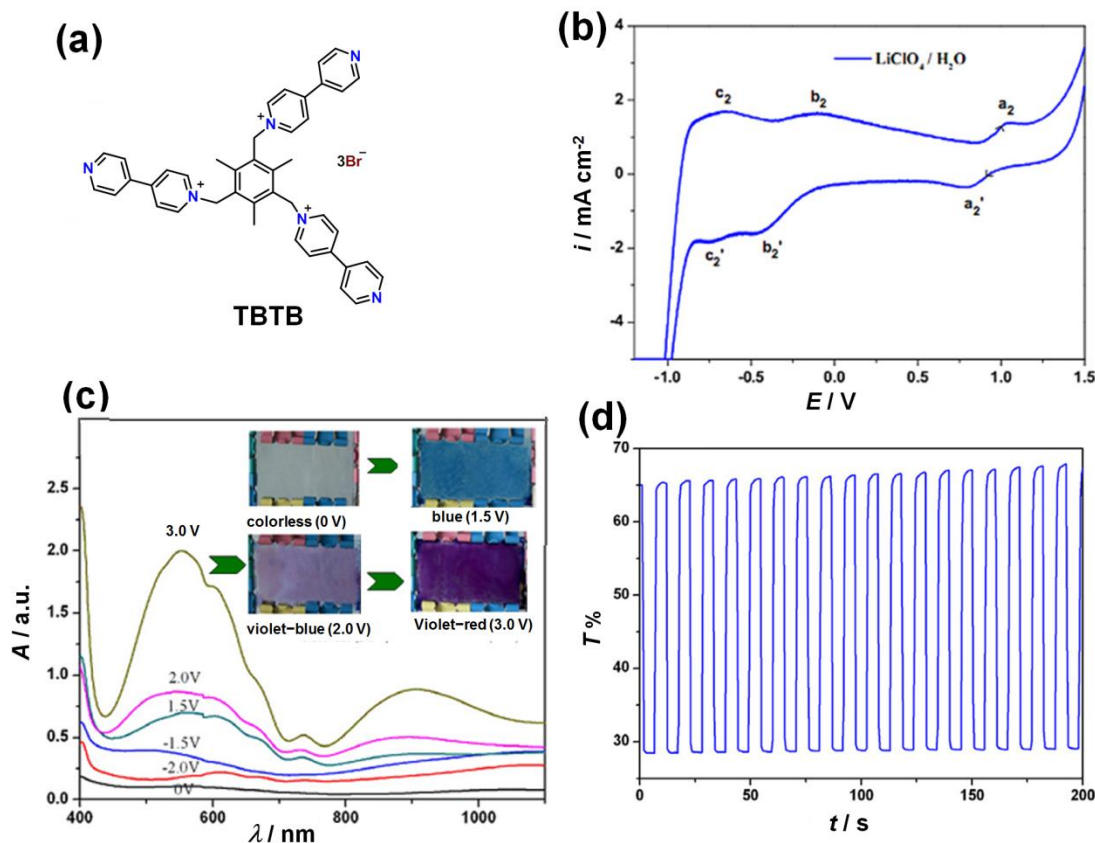
Figure 1.6 (a) The structure of 1,3,5-tri(1-methyl-4,4′-bipyridinium bromide)-2,4,6-trimethyl benzene (TBTB), (b) redox behavior of TBTB in an aqueous electrolyte of 0.1 M LiClO$_4$, (c) UV absorption spectra from −2.0 V to +3.0 V of an ECD based on TBTB; inset shows multichromic behavior of ECD at 0 V (colorless), +1.5 V (blue), +2.0 V (violet–blue), and +3.0 V (violet–red) and (d) Optical transmittance changes for the ECD based on TBTB, monitored at 530 nm, switched between −2.0 V and +2.0 V with a switch time of 5 s. Reprinted with permission from Org. Electron. 12 (2011) 1216. Copyright (2011) Elsevier B.V. [43].

In another report, a novel color-reinforcing ECD with methyl viologen (MV) and ruthenium purple (RP) was developed [44]. The anode and cathode reactions simultaneously exhibited comparable color responses. On coloration, the iron(II) hexacyanoruthenate(II) chromophore is oxidized to the purple iron(III) hexacyanoruthenate(II) chromophore of RP, and the MV^{2+} dication is reduced to the MV cation radical/dimer which as a mixture also appears purple (Figure 1.7).
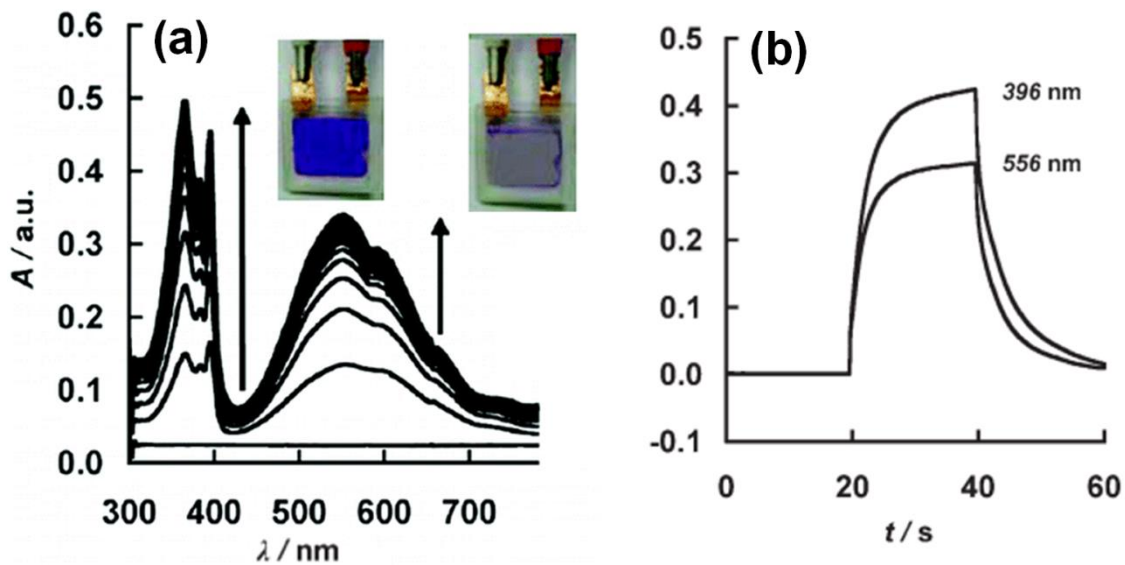
Figure 1.7 (a) UV-visible absorbance responses of an ECD comprising of RP/MV (at 5 mmol dm^{-3}) subjected to potential steps from −0.5 V (for 20 s) to +1.5 V (for 20 s) to −0.5 V (for 40 s) with KCl (0.5 mol dm^{-3}) as the electrolyte, (b) kinetic plot shows the absorbance changes at the two λ_{max} values in the UV and visible regions for the device. Reprinted with permission from Chem. Mater. 23 (2011) 4077. Copyright (2011) American Chemical Society [44].

In another report, Hammond et al., prepared a very high-contrast EC composite developed from the layer-by-layer (LbL) assembly of two readily available cathodically coloring electrochromic polymers: poly(hexyl viologen) (PXV) and the poly(3,4-ethylenedioxythiophene):poly(styrene sulfonate) (PEDOT:SPS) colloid, which showed a transmittance modulation of 82% at 525 nm [45]. The performance of PXV/PEDOT:SPS as a material for electrochromic applications was extremely competitive, with color-change response times ranging from 1 to 4 s and a high contrast between a transmissive oxidized state and a deep purple/blue reduced state. One unusual effect that was seen with this dual EC polymer was the exponential increase in the thickness with increasing layer-pair number (Figure 1.8). The authors showed that high contrast fast-switching multi-chromic displays are possible with the LbL technique along with the ease of fabrication of complex nano-composites in a simple processing platform.
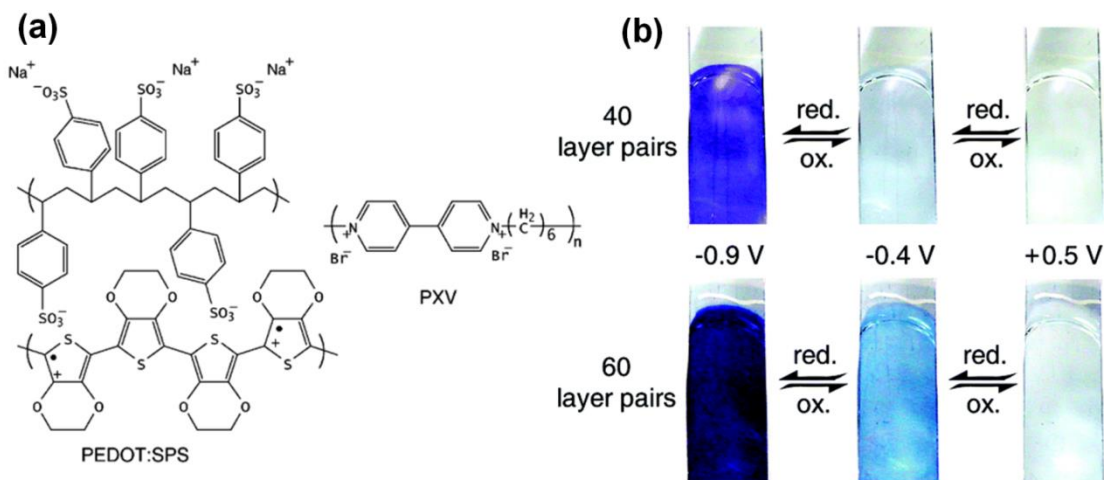
Figure 1.8 (a) Dual electrochrome composite of polycation species, poly(hexyl viologen) (PXV) and polyanion species, the PEDOT:SPS colloidal dispersion, (b) digital photographs of the coloration and bleaching of a $(PXV/PEDOT:SPS)_{40}$ and $(PXV/PEDOT:SPS)_{60}$, the films as shown are immersed in 0.1 M NH_4Cl in an electrochemical cell. Reprinted with permission from Chem. Mater. 15 (2003) 1575. Copyright (2003) American Chemical Society [45].

1.3.2 Organo-inorganic hybrid EC materials

Apart from viologens, an increasing scientific interest in the development of organo-inorganic hybrids for EC applications has been witnessed as well, due to the synergy of the two materials which leads to superior ECDs. In an earlier study, the formation of an inorganic-organic hybrid material from hexachlorocyclotriphosphazene, $(NPCl_2)_3$, and *para*-phenylenediamine precursors directly at the electrode surface was reported and the structure of the formed polymeric hybrid material is shown in the Figure 1.9a. In another study, Dallas et al., synthesized 2-D and 3-D covalent networks derived from triazine central cores and bridging aromatic diamines by nucleophilic substitutions of the reactive chlorine atoms of $(PNCl_2)_3$ [46]. The formation of a 3-D covalent network from the reaction of symmetric *para*-phenylenediamine with $(PNCl_2)_3$ was shown in Figure 1.9b. These materials utilizing the phosphazene core can be very much useful for designing novel organo-inorganic hybrid viologen materials for high contrast ECDs.
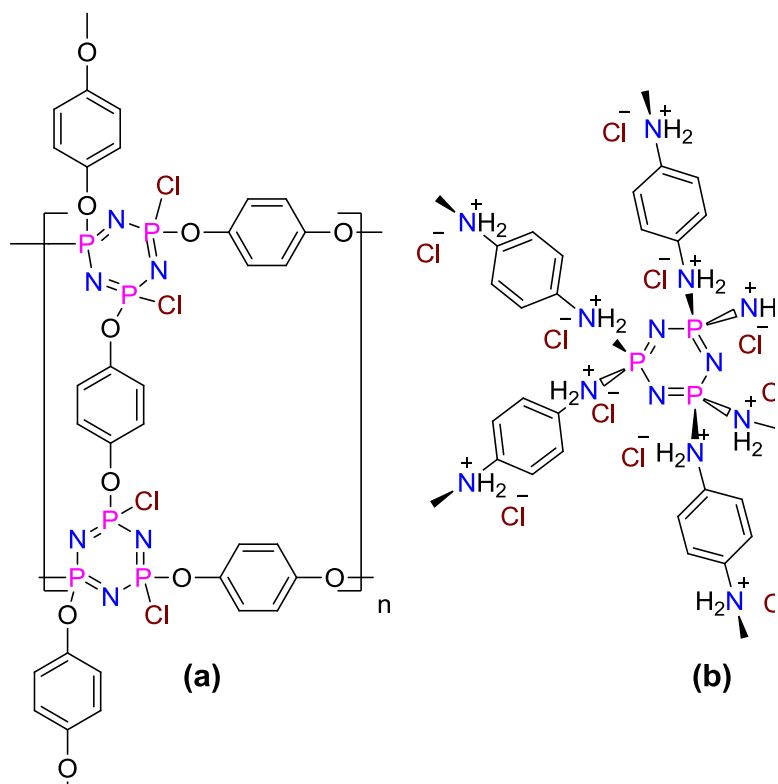
Figure 1.9 (a) The structure of polymeric hybrid material formed at the electrode surface from $(NPCl_2)_3$ and quinone precursors and (b) the proposed structure of the central unit in the 3-D covalent network of the hybrid material derived from 1,4-phenylenediamine and benzidine units.

1.4 Conjugated conducting polymers

Conducting polymers (CPs) are polymers composed of long chains of conjugated carbon (alternate single and double bonds), that are formed along with other kinds of atoms such as hydrogen, nitrogen, sulfur, oxygen, selenium etc. Before the famous discovery of Shirakawa et al., polymers were thought of and used as insulators. Alan Heeger, Alan MacDiarmid, and Hideki Shirakawa were awarded with The Nobel Prize in Chemistry for their discovery and elaboration of electronically conducting polymers in 2000 [47]. The three scientists found that polymer plastics can be made to conduct electricity if carbon atoms are linked via alternating single and double bonds, and electrons are either removed through oxidation or introduced through reduction. Chemical or electrochemical oxidation of resonance-stabilized aromatic molecules, such as thiophene, pyrrole, aniline, furan, carbazole, azulene, indole, and their derivatives, produces electroactive conjugated conducting polymers. Some examples of monomers for CPs are shown in Figure 1.10.
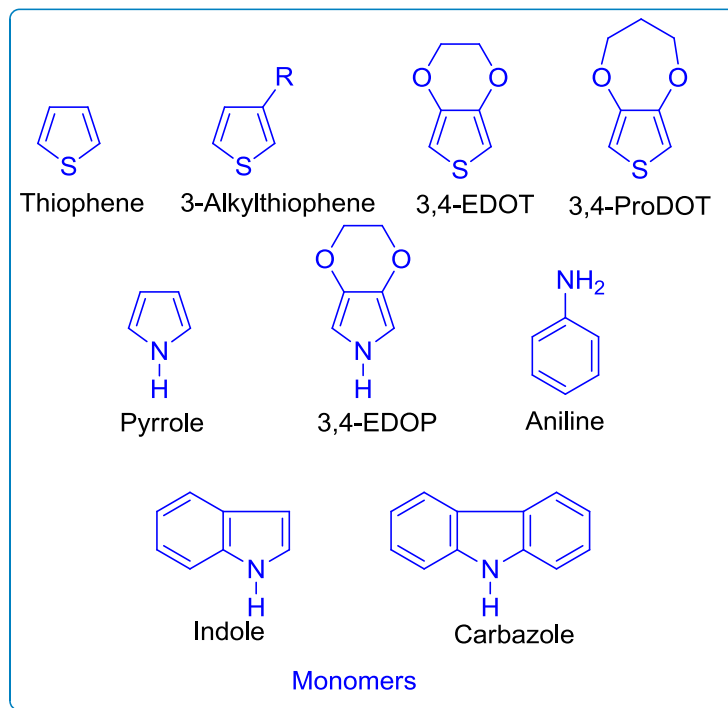
Figure 1.10 Some examples of monomers used for synthesizing CPs.

1.4.1 Origin of electrochromism in CPs

Electrochromism in CPs occurs through changes in the conjugated polymer's π-electronic character accompanied by reversible insertion and extraction of ions through the polymer film upon electrochemical oxidation and reduction. In their neutral (insulating) states, these polymers show semiconducting behavior with an energy gap (E_g) between the valence band (VB) or highest occupied molecular orbital (HOMO) and the conduction band (CB) or lowest unoccupied molecular orbital (LUMO). Upon electrochemical or chemical doping ("p-doping" for oxidation or "n-doped" by reduction), the band structure of the neutral polymer is modified, generating lower energy intraband transitions and creation of charged carriers (polarons and bipolarons), which are responsible for increased conductivity and optical modulation (Scheme 1.3). Garnier et al., in 1983 were the first to show the electrochemical polymerization and electrochromic switching of both substituted and unsubstituted poly(thiophenes) (PTs). Much attention was given towards adding the substituents at 3- and 4- positions of the thiophene ring to avoid hindrance at the sulfur atom, resulting in a whole new class of materials. Of these, PEDOT has been the most successful so far because of its' high stability in the oxidized state.

14
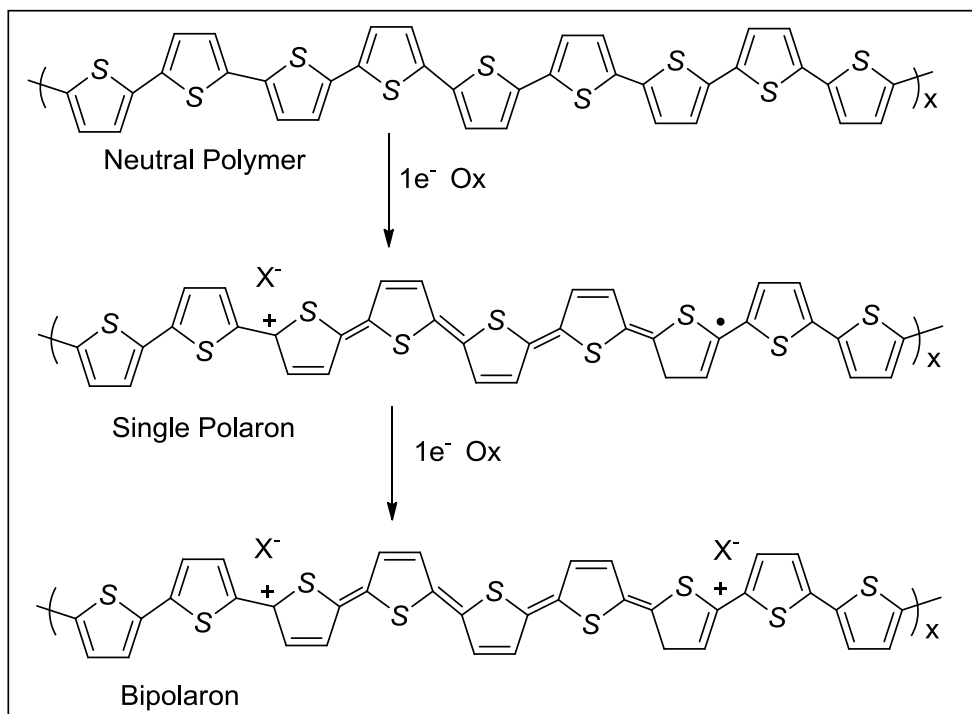
Scheme 1.3: Formation of polarons and bipolarons upon oxidative doping of poly(thiophene).

1.4.2 Multicolor electrochromism in CPs: Color control

The most significant advantage of conjugated polymers which comes to the forefront when used in ECDs, is the control to over EC modulation wavelengths via modification of the polymer structure. Through band gap control, one can vary the accessible color states in both the doped and neutral forms of the polymer. Numerous synthetic strategies exist for tuning the band gap of conjugated polymers [48]. In practice, this band gap control is achieved primarily through main chain and pendant group structural modification. In the simplest approach, substitution of the parent heterocycle is used to alter the band gap through induced steric or electronic effects.

1.4.3 Bandgap – color change effects

The color change or contrast between doped and undoped forms of a polymer depends on the magnitude of the band gap E_g. Thin films with $E_g > 3$ eV ($\sim$400 nm) are colorless and transparent in the undoped form, whereas in the doped form they generally absorb visible radiation. Those with $E_g \leq 1.7-1.9$ eV ($\sim$ 650−730 nm) are highly absorbing in the undoped form, but after doping, the free carrier absorption is relatively weak in the visible region because it is transferred to the near infrared. Polymers with intermediate bandgaps have distinct optical changes throughout the visible region and can exhibit several colors.

1.5 Poly(thiophene)s

Poly(thiophene)s are of particular interest as electrochromic materials due to their relative ease of chemical and electrochemical synthesis, environmental stability, and processability. Thin polymeric films of the parent poly(thiophene) are blue (λ_{max} = 730 nm) in the doped (oxidized) state and red (λ_{max} = 470 nm) in the undoped form. A vast number of substituted thiophenes have been synthesized, and this has led to the study of numerous novel poly(thiophene)s, with particular emphasis on poly(3-substituted thiophene)s and poly(3,4-disubstituted thiophene)s (Table 1.1).

Table 1.1. Poly(thiophene)s and their redox forms with different absorption maxima.

Monomer	Polymer λ_{max}/nm and color	
	Oxidized	Reduced
Thiophene	730 (blue)	470 (red)
3,4-Dimethylthiophene	750 (deep blue)	620 (pale brown)
2,2′-Bithiophene	680 (blue-gray)	460 (red-orange)

1.5.1 PEDOT

Among conjugated polymers such as poly(aniline), poly(thiophene), poly(pyrrole) etc, the derivative of poly(thiophene), PEDOT, is one of the most successful CPs, because of it's low band gap, excellent environmental stability, high electrical conductivity and good transparency, in the oxidized or doped state [49]. Optically transparent conducting electrodes are at the forefront of research in electronic devices, due to their application in flat panel displays and organic light emitting diodes (OLEDs). Poly(3,4-ethylenedioxythiophene):poly(styrenesulfonate), known as PEDOT:PSS, a water-soluble form of the polymer, is commercially available in form of aqueous suspensions and can be sourced from H. C. Starck. PEDOT:PSS, is today, arguably, the most successful conductive polymer in commercial applications. It is typically used for (a) developing antistatic coatings and (b) making the hole transport layer in organic solar cells, owing to a suitable work function, a strong propensity to scavenge holes and reasonably high optical transparency [49]. In particular, in solar cells and OLEDs, PEDOT offers the possibility of cost-effective manufacturing, flexibility, and exciting prospect of roll-to-roll large-scale production. PEDOT was first synthesized by Jonas et al. [50] via 3,4-ethylenedioxythiophene (EDOT) in the late 1980s. On the one hand, the ether oxygen linked to thiophene decreases the oxidation potential, but on the other, the ethyl bridge that connects the two oxygens minimizes the steric hindrance. It exhibits a very high conductivity of 300 S cm^{-1} and was found to be almost transparent in the thin film form. Even though it showed several advantageous properties, it was not suitable to be used in areas because of its insolubility. This issue was later resolved by using a water-soluble polyelectrolyte, PSS as a charge-balancing dopant during polymerization to yield PEDOT:PSS. The resulting product has all the exceptional qualities of PEDOT or even better at the expense of slight decrease in conductivity (10 S cm^{-}

[1]). With a highly conducting, almost transparent, stable doped state, a narrow optical band-gap of ~1.6 eV and a particularly low oxidation potential when compared to its unsubstituted poly(thiophene) parent, neutral deep blue PEDOT shows a relatively stable and highly transmissive sky blue oxidized state as demonstrated in the pioneering work of Inganas et al., who described the first electrochemically prepared PEDOT-based ECDs [51]. Considering the onset of the optical absorption of neutral PEDOT lying in the near-IR region of the electromagnetic spectrum, along with the minimal tailing in the visible of its charged carrier transitions produced on electrochemical oxidation (Figure 1.11), the excellent transmissivity of PEDOT aroused considerable interet as illustrated by the reports of Jonas, Heinze and Inganas and co-workers and has been the focus of a significant number of publications since then [52].
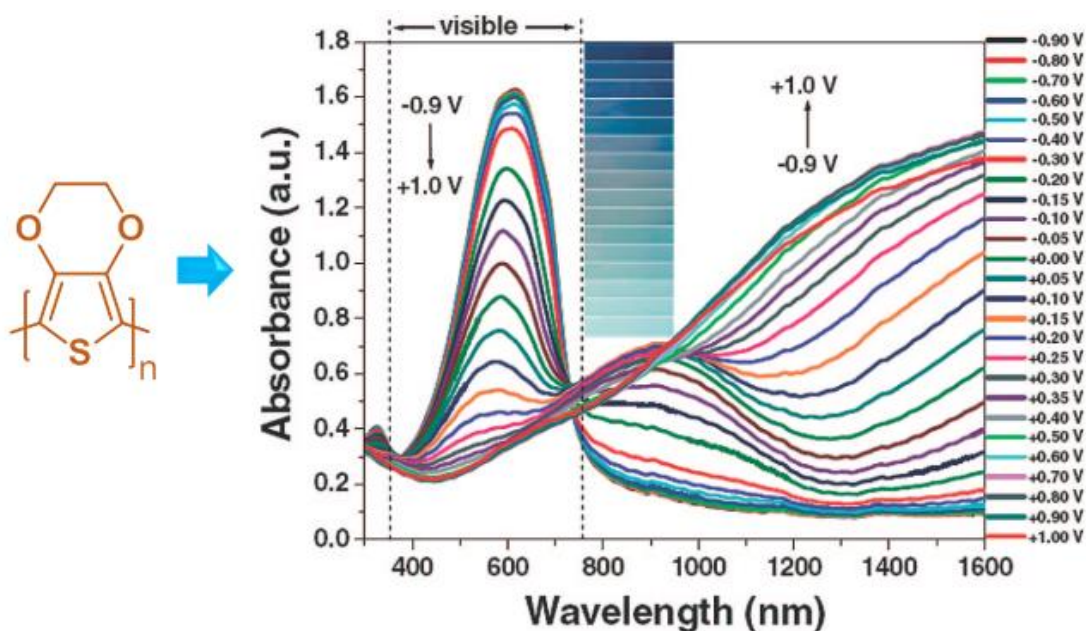
Figure 1.11 Spectroelectrochemistry of a thin film of PEDOT, the inset shows the variety of hues produced on application of various biases. Reprinted with permission from Adv. Mater. 16 (2004) 1905. Copyright (2004) Wiley-VCH Verlag GmbH & Co. KGaA, Weinheim, Germany [52].

1.5.2 PEDOT in reflective devices

Some important results achieved in PEDOT are summarized here. Reflective ECDs with CPs deposited onto metalized porous membranes were constructed. A 2×2 pixel type array device consisting of two conjugated polymers which displayed unique visible absorptions (blue and red) in the neutral state while maintaining the ability to switch to a very transmissive oxidized state was fabricated. PEDOT and poly(bis-EDOTdialkoxybenzene), (PBEDOT-B(OR)$_2$) were electrodeposited onto the porous membrane and then switched with a bias voltage of 1 V. As shown in Figure 1.12, at a bias of 1 V, PEDOT is blue

while PBEDOT-B(OR)$_2$ is red. When the bias is reversed and both polymers are fully oxidized, both polymers switch to a highly transmissive state, exposing the reflective gold surface [53].
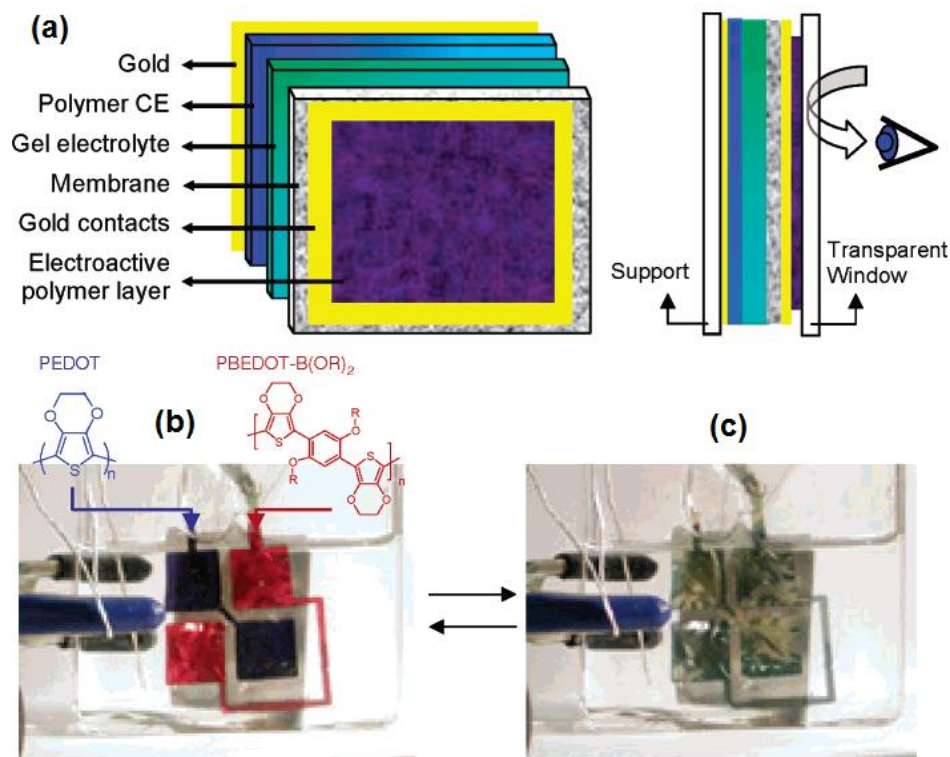
Figure 1.12 (a) A reflective device scheme using porous electrodes. Photographs of EC switching of PEDOT and PBEDOT-B(OR)$_2$ on a 2×2 pixel gold/membrane electrode: (b) both polymers in their neutral (colored) states and (c) polymers in their oxidized (bleached) states. Reprinted with permission from Chem. Mater. 16 (2004) 4401. Copyright (2004) American Chemical Society [53].

1.6 PEDOT in flexible applications

Due to the developments in the area of flexible electronic systems, novel daily life applications are expected to emerge, for instance, sensors or timers printed on goods, electronic newspapers, and wearable electronic devices and displays. Many of those forthcoming applications require low-cost production and flexible electrodes. Promising candidates for electrodes are conducting polymers, such as PEDOT. PEDOT was found to be almost transparent and highly stable in the form of thin oxidized films. The development of printed and flexible optoelectronics requires specific materials to be used as electrodes. These materials must satisfy a combination of properties. They must be electrically conducting, transparent, printable, and flexible. These pre-requisites are fulfilled by PEDOT:PSS. Polymer light emitting diodes have been successfully fabricated using the transparent plastic PEDOT-PSS electrodes instead of the traditionally used expensive ITO based system [54].

18

1.6.1 Deposition techniques for PEDOT films on flexible substrates

PEDOT thin films were obtained through oxidative chemical vapor deposition (oCVD) by using bromine as oxidant by Gleason et al., and authors obtained conductivities as high as 380 S cm^{-1} for PEDOT films deposited at 80 °C, which is significantly higher than that obtained for PEDOT films deposited using iron chloride as the oxidant at the same temperature [55]. PEDOT films were also deposited via a solventless oxidative chemical vapor deposition (oCVD) technique by Hammond et al., and these oCVD PEDOT films, about 100 nm thick on ITO/glass showed optical switching speeds of 13 and 8.5 s, for light-to-dark and dark-to-light transitions, respectively. The color contrast was 45% at 566 nm and the film was 85% stable over 150 redox cycles. An ECD using oCVD PEDOT that incorporates patterning capabilities is shown in Figure 1.13. This solid-state device consisted of oCVD PEDOT shadow-masked on ITO, electrolyte in a porous separator, and ITO as the counter electrode. The device was cycled between ±5 V [56].
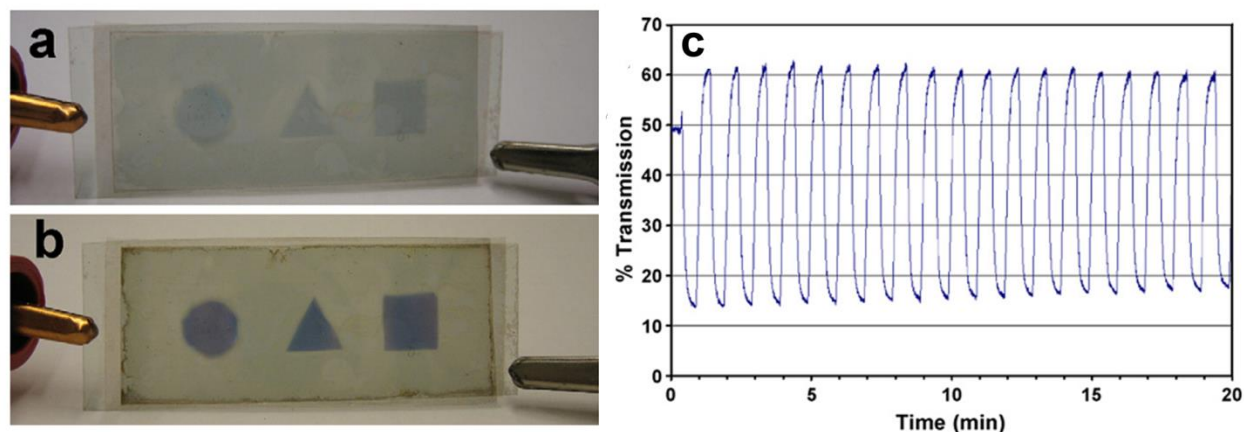
Figure 1.13 An ECD using oCVD PEDOT patterned with a shadow mask is demonstrated. The dark to light transition happens in less than 10 s while the light to dark transition takes about 1 min, (a) light state, (b) dark state and (c) average switching speeds for the first five cycles (based on 80% of full response) were 13 s for light-to-dark and 8.5 s for dark-to-light transitions. Reprinted with permission from Synth. Met. 157 (2007) 894. Copyright (2007) Elsevier [56].

1.7 Prussian Blue (PB)

In the last two decades, the only inorganic non-oxide materials that have attracted significant attention for use in low power electrochromic displays are largely those belonging to the metal hexacyanoferrate (HCNF) family [57,58]. PB belongs to an important family of mixed insoluble transition metal hexacyanoferrates which were extensively used as pigments in the formulation of paints, lacquers and printing inks. The chemical formulae for insoluble and soluble PB are $Fe_4[Fe(CN)_6]_3$ and $KFe[Fe(CN)_6]_3$ respectively, and both of these forms possess a brilliant blue color: "cyan". A valence change of the

component metal centers in the crystal causes a change in the energy of the charge transfer oscillation and induces electrochromism. The intense blue color of the iron(III) hexacyanoferrate(II) chromophore arises from the inter valence charge transfer (IVCT) between the mixed-valence iron oxidation states [59] and can be removed by oxidation or reduction. The important forms of the PB during redox process are shown in Table 1.2.

Table 1.2: Some of the important PB redox states

State	Name	Acronym
$Fe(III)[Fe(III)(CN)_6]$	Prussian Brown	PX
$Fe(III)[Fe(III(CN)_6]KFe(II)[Fe(III)(CN)_6]$ – intermediate	Berlin Green	BG
$KFe(II)[Fe(III)(CN)_6]$	Prussian Blue	PB
$K_2Fe(II)[Fe(II)(CN)_6]$	Prussian White	PW

1.8 Objectives of the present work

From the above survey, it is evident that in solution phase electrochromic compounds, the viologens, and in EC conducting polymers, PEDOT are the two most promising candidates for both reflective and transmissive solar/light control applications. In this thesis, new viologens were developed and their electrochemistry was studied. Some new insights into the electrochromism of PEDOT on rigid and flexible substrates are given.

The objectives of the work described in present thesis are summarized here.

   i.   To synthesize PEDOT using poly(diallyldimethylammonium chloride) (PDDA)solution as a dopant source and its' composites using the fullerene derivative: N-methyl fulleropyrrolidine (N-FP) and to analyze the nanoscale conduction behavior of these materials and to study their electrochromic characteristics.

   ii. To synthesize PEDOT films by electropolymerization and to study the effect of an *in-situ* polymerized IL based gel electrolyte on the PEDOT based ECD and electrochemical properties.

   iii. Development of HV based large area ECDs by using an electrolyte injection technique for ECRA mirrors and its' demonstration.

   iv. To prepare conducting PET flexible electrodes using PEDOT by a chemical bath polymerization technique and to study its' device electrochromic characteristics.

   v.   To synthesize new derivatives of viologen containing moieties such as Indole, Imidazole and a hexacyclic phoshonitrillic core and study their ECDs.

To meet the above-described aims, PEDOT based films were prepared by using a variety of solutions containing appropriate components on conducting glass substrates via electropolymerization route and PEDOT was also deposited on plastic PET films via electroless deposition from a chemical bath solution.

New viologen derivatives were synthesized and characterized and their ECDs were also studied using PB as a counter electrode.

Chapter 3 is on **"Influence of incorporation of N−methyl fulleropyrrolidine on the electrochromic performance of PEDOT",** wherein PEDOT films have been synthesized by a facile electropolymerization route by using poly(diallyldimethylammonium) chloride (PDDA) as the counter-ion source. To enhance their efficacy, the fullerene derivative N−methyl fulleropyrrolidine (N-FP) was embedded in the PEDOT/PDDA films for the electron-conducting ability of the N-FP can enhance the conductivity, optical contrast, and ion-storage capacity in PEDOT/PDDA/N-FP film compared to that of PEDOT/PDDA film. Both the PEDOT/PDDA and PEDOT/PDDA/N-FP films showed an unprecedented dramatic digression from the expected optical response of conventional PEDOT, exhibiting distinct $\pi-\pi^*$ absorptions in the visible region in air, corresponding to a bandgap of 1.1−1.3 eV, which is outside the established range (1.6–1.7 eV). The neutral state of these films showed split components, which was simultaneously accompanied by a reversible color change from bright blue (in oxidized form) to deep brown (in reduced form). This was a most unusual color transition for PEDOT, as it opposes the well-established colors that switch between dark blue (reduced) and sky blue (oxidized) tones. Atomic force microscopy and Kelvin probe force microscopy provided evidence for the higher nanoscale current-carrying capacity and lower localized work function for PEDOT/PDDA/N-FP than for PEDOT/PDDA; both the energetics and conductivity are conducive for fast redox switching. The obtained results for PEDOT/PDDA and PEDOT/PDDA/N-FP pave the way for the utilization of this material for electronic, electrochemical, and optical functions.

Chapter 4 is divided into two sub chapters as **4A and 4B.** In **chapter 4A,** PEDOT and PB films were deposited via electrodeposition route and the ECDs were fabricated by two approaches. In one approach, an *in-situ* polymerized IL based gel electrolyte using methylmethacrylate (MMA) monomer was used for PEDOT-PB (MMA) ECDs. In another approach, a gel with PMMA dispersed in IL was used. The *in-situ* polymerized device showed superior spectroelectrochemical properties compared to the PMMA based ECDs and these were discussed. In **Chapter 4B**, we extended the applicability of *in-situ* polymerized gel electrolyte approach and studied a HV based large area ECD for ECRA application. A HV based prototype ECRA mirror or device with PB as counter electrode, with an active area of about 8 cm × 6 cm was fabricated using an *in-situ* thermal polymerization technique with MMA monomer in the IL: 1-butyl-1-methyl pyrrolidinium bis(trifluoromethylsulfonyl)imide. Reflectance (specular) modulation for the ECRA device was observed to be 64% at 614 nm at a reduction potential of −3.0 V and an oxidation potential of +1.5 V. Switching times of the order of ~5 s were observed, to induce a 50% change of the total contrast. The ECRA device was also found to have a cycling life of at least a 1000 cycles of clear to

dark and dark to clear and a shelf life time of one year without undergoing degradation. Thus, the HV−PB (MMA) device is suitable for the application of fast switching ECRA mirrors in automobiles for safe driving in the night time.

   Chapter 5 is on the **"Preparation of conducting PET flexible electrodes using PEDOT and a study of a flexible ECD"** wherein PEDOT films were deposited by a chemical bath method using EDOT monomer on flexible plastic PET substrates. Uniform coverage of PEDOT over PET dimensions of ~20 cm × 6 cm was achieved. The sheet resistance of PEDOT/PET films was found to be 600 $\Omega/\square$ for a film with an optimized thickness of ~400 nm. The visible light transmittance offered by the film is 93% for an 80 nm thick film and it reduced nominally to 61% for a 400 nm thick film. Conducting atomic force microscopy studies showed the nanoscale conductivity of the PEDOT/PET film to be 0.103 S cm^{-1} and the film was found to be composed of high current carrying domains spread over micron length scales. The ability of the PEDOT/PET film to function as an optically transparent conducting electrode, was demonstrated by electrodeposition of PB on the same, followed by the construction of an electrochromic PEDOT-PB device. The device underwent a color change from pale blue to deep violet-blue, under applied bias, and exhibited coloration efficiencies of 92 cm^2 C^{-1} at λ_{max} of 585 nm and 750 cm^2 C^{-1} at 1190 nm. Repetitive cyclic voltammetry and kinetic data for the device revealed the device to be stable for 1000 cycles as it retained ~83% of its' original optical change, thus demonstrating its' use as an economically viable solar modulating smart window. The high homogeneity of the PEDOT deposit over PET, the optimal balance between conductivity and optical transparency, and the demonstration of an electro-optical device open up opportunities to employ this electrode in a variety of low cost optoelectronic devices.

   Chapter 6 is divided into two sub chapters as 6A and 6B**. Chapter 6A** deals with the **"Influence of a butyl imidazole in a viologen on its' electrochromic characteristics"** wherein a new electrochromic viologen, 1,1′-bis-[4-(5,6-dimethyl-1H-benzimidazole-1-yl)-butyl]-4,4′-bipyridinium dibromide (IBV) was synthesized by di-quaternization of 4,4′-bipyridyl using 1-(4-bromobutyl)-5,6-dimethyl-1H-benzimidazole. An ECD encompassing a dicyanamide IL based gel polymeric electrolyte with high ionic conductivity, a thermal decomposition temperature above 200 °C, and a stable voltage window of ~4 V with the IBV viologen dissolved therein, was constructed. The IBV−PB device underwent reversible transitions between transparent and deep blue hues; the color change was accompanied by high optical contrast (30.5% at 605 nm), a remarkably high coloration efficiency of 725 cm^2 C^{-1} at 605 nm and switching times of 2–3 s. The device was subjected to repetitive switching between the colored and bleached states and was found to incur almost no loss in redox activity, up to 1000 cycles, thus ratifying its' suitability for electrochromic window/display applications.

Chapter 6B deals with the **"Effect of ethyl indole in a viologen on its' electrochromic response".** A new electrochromic viologen, 1,1'-bis(2-(1H-indol-3-yl)ethyl)-4,4'-bipyridinium diperchlorate (IEV), comprising of a 4,4′-bipyridyl core, sandwiched between two indole moieties, was synthesized using 3-(2-bromoethyl)-indole. An ECD with PB and imidazolium imide IL based electrolyte with a high ionic conductivity, a thermal decomposition temperature above 150 °C, and a stable voltage window of ~3.6 V with the IEV viologen dissolved therein, was constructed. In this viologen, indole moieties of the IEV^{2+} salt are spatially close to the bipyridyl core, and the C_2–C_3 part of the indole is rich in electron density and thus these will function as donors to the electron deficient bipyridinium cations. This inherent feature of indole moieties can act like bleaching agents and bleach the viologen faster (IEV$^{+\bullet}\rightarrow$ IEV^{2+}) and this hypothesis was used for explaining the improved write–erase efficiency of the device. The device underwent reversible transitions between transparent and deep violet-blue hues under applied potentials of $\pm$ 1.5 V. The device color change was accompanied by a high optical contrast (52% at 605 nm), a large CE of 533 cm^2 C^{-1} at 605 nm and switching times of ~2 s and good stability during 2000 cycles.

Chapter 7 deals with the **"Effect of inclusion of a hexacyclic phoshonitrillic core in a viologen on its' electrochromic behavior"** wherein, a new organo-inorganic hybrid electrochromic material poly(cyclotriphosphazene–4,4′-bipyridinium) chloride salt was synthesized wherein each phosphorous in the triphosphazene core is linked by diquaternized 4,4′-bipyridyls (PPBP). ECDs were constructed with the PPBP hybrid dissolved in a highly conductive, thermally stable and electrochemically inert IL based gel electrolyte and a PB layer as the anode. The transparent PPBP material undergoes three reversible one electron-transfer reactions to yield a radical cation insoluble film which first acquires a purple hue and then turns deep blue. The PPBP-PB device showed an extremely large CE of 504 cm^2 C^{-1}, an exceptionally high transmission modulation of 70.5% at 590 nm, one among highest reported contrasts in organic electrochromics, a large reflectance contrast of 59.2% at 545 nm and fast switching kinetics.

Different instrumentation techniques used to characterize viologens PEDOT films and devices such as atomic force microscopy (AFM) with C-AFM, KPFM modes, UV-visible spectroscopy, electrochemical techniques such as cyclic voltammetry (CV), linear sweep voltammetry (LSV), chronoamperometry and electrochemical impedance spectroscopy (EIS), scanning electron microscopy (SEM), X-ray photoelectron spectroscopy (XPS) and Fourier transform infrared (FTIR) and Raman spectroscopies, X-ray diffraction (XRD) and thermogravimetric analysis (TGA) and active electrode materials / films and device preparation methods are described in the following **Chapter 2**.

References

[1] M. Irie, T. Seki, Y. Yokoyama, New Frontiers in Photochromism, Springer, Tokyo, Japan, 2013.

[2] J.C. Crano, R.J. Guglielmetti, Organic photochromic and thermochromic compounds, Kluwer Academic/Plenum Publishers, New York, 1999.

[3] E. Buncel, S. Rajagopal, Acc. Chem. Res. 23 (1990) 226.

[4] P.M.S. Monk, R.J. Mortimer, D.R. Rosseinsky, Electrochromism and Electrochromic Devices, Chambridge University Press, Cambridge, 2007.

[5] Y. Muramastu, T. Yamamoto, M. Hasegawa, T. Yagi, H. Koinuma, Polymer 42 (2001) 6673.

[6] S.K. Deb, Appl. Opt. Suppl. 3 (1969) 192.

[7] R.J. Mortimer, A.L. Dyer, J.R. Reynolds, Displays 27 (2006) 2.

[8] C.E. Tracy, J.-G. Zhang, D.K. Benson, A.W. Czanderna, S.K. Deb, Electrochim. Acta 44 (1999) 3195.

[9] C.M. Lampert, Sol. Energy Mat. 11 (1984) 1.

[10] P. van Konynenburg, S. Marsland, S. McCoy, Sol. Energy Mat. 19 (1989) 27.

[11] T. Kamimori, J. Nagai, M. Mizuhashi, Proc. SPIE 653 (1986) 2.

[12] R.D. Rauh, Electrochim. Acta 44 (1999) 3165.

[13] D.R. Rosseinsky, R.J. Mortimer, Adv. Mater. 13 (2001) 783.

[14] T. Kubo, H. Watanabe, Solid State Ionics 165 (2003) 209.

[15] R.J. Mortimer, A.L. Dyer, J.R. Reynolds, Displays 2 (2006) 27.

[16] X. Tu, X. Fu, Q. Jiang, Z. Liu, G. Chen, Dyes Pigm. 88 (2011) 39.

[17] H.J. Kim, J.K. Seo, Y.J. Kim, H.K. Jeong, G.I. Lim, Y.S. Choi, W.I. Lee, Sol. Energy Mater. Sol. Cells 93 (2009) 2108.

[18] P.M.S. Monk, The Viologens: Physicochemical Properties, Synthesis and Applications of the Salts of 4,4′-Bipyridine, Wiley, Chichester, 1998.

[19] P.R. Somani, S. Radhakrishnan, Mater. Chem. Phys. 77 (2002) 117.

[20] G. Bar, N. Larina, L. Grinis, V. Lokshin, R. Gvishi,I. Kiryuschev, A. Zaban, V. Khodorkovsky, Sol. Energy Mater. Sol. Cells 99 (2012) 123.

[21] A. Azens, C.G. Granqvist, J. Solid State Electrochem. 7 (2003) 64.

[22] F.A.R. Silva, M.J.A. Sales, R.S. Angélica, E.R. Maia, A.M. Ceschin, Appl. Surf. Sci. 257 (2011) 8594.

[23] K. Gurunathan, A.V. Murugan, R. Marimuthu, U.P. Mulik, D.P. Amalnerkar, Mater. Chem. Phys. 61 (1999) 173.

[24] Internet: http://www.mge.com/saving-energy/business/bea/article_detail.htm?nid=1831. All content copyright 1986-2015 E Source Companies LLC.

[25] F.C. Krebs, Nat. Mater. 7 (2008) 766.

[26] C. Ma, M. Taya, C. Xu, Polym. Eng. Sci. 48 (2008) 2224.

[27] I.F. Chang, B.L Gilbert, T.I. Sun, J. Electrochem. Soc. 122 (1975) 955.

[28] C. Zhao, G. Burrell, A.A.J. Torriero, F. Separovic, N.F. Dunlop, D.R. MacFarlane, A.M. Bond, J. Phys. Chem. B 112 (2008) 6923.

[29] J.R. Nair, C. Gerbaldi, M. Destro, R. Bongiovanni, N. Penazzi, React. Funct. Polym. 71 (2011) 409.

[30] S. Desai, R.L. Shepherd, C. Innis, P. Murphy, C. Hall, R. Fabretto, G.G. Wallace, Electrochim. Acta 56 (2011) 4408.

[31] E. Zelazowska, E.J. Rysiakiewicz-Pasek, J. Non-Cryst. Solids 354 (2008) 4500.

[32] M. Lombardi, P. Fino, G. Malucelli, L. Montanaro, Compos. Struct. 94 (2012) 1067.

[33] P. Fino, M. Lombardi, A. Antonini, G. Malucelli, L. Montanaro, Composite Structures 94 (2012) 1060.

[34] H.-J. Ha, Y.H. Kwon, J.Y. Kim, S.-Y. Lee, Electrochim. Acta 57 (2011) 40.

[35] C. Pozo-Gonzalo, D. Mecerreyes, J.A. Pomposo, M. Salsamendi, R.Marcilla, H. Grande, R. Vergas, D. Barrios, J.M. Sanchez-Pena, Sol. Energy Mater. Sol. Cells 92 (2008) 101.

[36] H.-J. Ha, E.-H. Kil, Y.H. Kwon, J.Y. Kim, C.K. Lee, S.-Y. Lee, Energy Environ. Sci. 5 (2012) 6491.

[37] G.B. Appetcchi, F. Croce, B. Scrosati, Electrochim. Acta 40 (1995) 991.

24

[38] J. Bruinink, A.R. Kmetz, F.K. VonWilli, Non-emissive Electro-optic Displays, Plenum Press, New York, 1976.

[39] T.-H Kuo, C.-Y Hsu, K.-M Lee, K.-C. Ho, Sol. Energy Mater. Sol. Cells 93 (2009) 1755.

[40] P.R. Somani, S. Radhakrishnan, Mater. Chem. Phys. 77 (2002) 117.

[41] G. Bar, N. Larina, L. Grinis, V. Lokshin, R. Gvishi, I. Kiryuschev, A. Zaban, V. Khodorkovsky, Sol. Energy Mater. Sol. Cells 99 (2012) 123.

[42] A. Kavanagh, K.J. Fraser, R. Byrne, D. Diamond, ACS Appl. Mater. Interfaces 5 (2013) 55.

[43] G. Wang, X. Fu, J. Huang, C. Wu, L. Wu, Q. Du, Org. Electron. 12 (2011) 1216.

[44] R.J. Mortimer, T.S. Varley, Chem. Mater. 23 (2011) 4077.

[45] D.M. DeLongchamp, M. Kastantin, P.T. Hammond, Chem. Mater. 15 (2003) 1575.

[46] P. Dallas, A.B. Bourlinos, D. Petridis, N. Boukos, K. Papadokostaki, D. Niarchos, N. Guskos, Polymer 49 (2008) 1137.

[47] C.K. Chiang, C.R. Fincher, Y.W. Park, A.J. Heeger, H. Shirakawa, E.J. Louis, S.C. Gau A.G. MacDiarmid, Phys. Rev. Lett. 39 (1977) 1098.

[48] L. Groenendaal, F. Jonas, D. Freitag, H. Pielartzik, J.R. Reynolds, Adv. Mater. 12 (2000) 481.

[49] S. Kirchmeyer, K. Reuter, J. Mater. Chem. 15 (2005) 2077.

[50] F. Jonas, W. Kraft, B. Muys, Macromol. Symp. 100 (1995) 169.

[51] O. Inganas, I. Lundstrom, J. Electrochem. Soc. 131 (1984) 1129.

[52] G. Sonmez, H.B. Sonmez, C.K.F. Shen, F. Wudl, Adv. Mater. 16 (2004) 1905.

[53] A.A. Argun, P.H. Aubert, B.C. Thompson, I. Schwendeman, C.L. Gaupp, J. Hwang, N.J. Pinto, D.B. Tanner, A.G. MacDiarmid, J.R. Reynolds, Chem. Mater. 16 (2004) 4401.

[54] X. Crispin, F.L.E. Jakobsson, A. Crispin, P.C.M. Grim, P. Andersson, A. Volodin, C.V. Haesendonck, M.V.D. Auweraer, W.R. Salaneck, M. Berggren, Chem. Mater. 18 (2006) 4354.

[55] H. Chelawat, S. Vaddiraju, K.K. Gleason, Chem. Mater. 22 (2010) 2864.

[56] J.P. Lock, J.L. Lutkenhaus, N.S. Zacharia, S.G. Im, P.T. Hammond, K.K. Gleason, Synth. Met. 157 (2007) 894.

[57] K.K. Kasem, Mater. Sci. Eng. B 83 (2001) 97.

[58] C.-F. Lin, C.-Y. Hsu, H.-C. Lo, C.-L. Lin, L.-C. Chen, K.-C. Ho, Sol. Energy Mater. Sol. Cells 95 (2011) 3074.

[59] H.J. Buser, D. Schwarzenbach, W. Petter, A. Ludi, Inorg. Chem. 16 (1977) 2705.

Chapter 2

Materials, methods and characterization techniques

This chapter provides details about various materials, experimental procedures and techniques that were utilized during the synthesis and characterization of PEDOT films, viologen derivatives and ECDs.

2.1 Chemicals

Different chemicals which were used in the experiments performed in this thesis with their details are provided here. 3-(2-bromoethyl)-indole, methyl methacrylate or MMA, 2-hydroxyethyl methacrylate or HEMA, 4,4′-bipyridyl, 5,6-dimethyl-1H-benzimidazole, hexachlorotriphosphazene ($(PNCl_2)_3$), 3,4-ethylenedioxythiophene or EDOT, sodium bis(2-ethylhexyl) sulfosuccinate or AOT (M.W. ~288.38 g/mol), 1-ethyl-3-methyl imidazolium bis(trifluoromethylsylfonyl)imide,1-Ethyl-3-methylimidazolium dicyanamide ($EtMeIm^+$ $N(CN)_2^-$), 1-butyl-1-methylpyrrolidinium bis(trifluoromethylsulfonyl)imide ($[BuMePy][N(CF_3SO_2)_2]$), 1-butyl-1-methylpyrrolidinium trifluoromethanesulfonate ($BuMePy^+($ $CF_3SO_3)^-$), 1-ethyl-3-methylimidazolium tetracyanoborate ($EMIB(CN)_4$), lithium perchlorate, lithium trifluoromethanesulfonate, dimethyl sulfoxide (DMSO), methanol, propylene carbonate, ethanol, acetone, N,N-dimethylformamide (DMF), toluene, isopropanol (IPA), acetonitrile (ACN), ethyl acetate, dichloromethane (DCM), diethyl ether, n-hexane, camphorsulfonic acid or CSA, fullerene (C_{60}), paraformaldehyde, potassium hexacyanoferrate(III), benzoyl peroxide (with 25% H_2O), poly(diallyldimethylammonium chloride) solution (PDDA, average M.W.<100000, 35 wt % in water), N-methyl glycine or Sarcosine, ferric chloride, potassium carbonate, dimethylsulfoxide-d_6, methanol-d_4, chloroform-d, hydrochloric acid 35%, poly(ethyleneterephthalate) (PET, 100 μm thickness), ammonia, sodiumhydrosulfite, ammoniumperoxydisulphate, poly(methylmethacrylate) (PMMA, M.W. ~99600), 1-bromoheptane, 1,4-dibromobutan and sodium chloride.

Ultrapure water (resistivity ~18.2 M Ω cm) was obtained through Millipore Direct-Q3 UV system. SnO_2:F (FTO) coated glass substrates with a sheet resistance of about 14 Ω sq^{-1} were procured from Pilkington, washed with soap solution, flushed with copious amounts of distilled water and cleaned with acetone prior to use. Poly(ethylene terephthalate) (PET) plastic sheets of 100 μm thickness were used as flexible substrates. A 3M acrylic tape of 600 μm thickness was employed as the spacer, which was also used for holding the electrolyte, thus enabling the construction of ECDs.

2.2 Experimental

2.2.1 EC parameters for EC films or ECDs

(a) Optical contrast

Commonly reported as a percent transmittance change (ΔT, %) at a given wavelength, the electrochromic contrast is a primary tool in the overall characterization process of an electrochrome. While the control wavelength chosen is often the one at which the electrochrome exhibits its highest optical contrast, this EC contrast can practically be monitored and reported at any local absorption maximum, when desired. Transmittance values are generally recorded upon application of square-wave potential steps to the electroactive film placed in the beam of a spectrophotometer.

$$\Delta T(\lambda) = T_b(\lambda) - T_c(\lambda) \tag{2.1}$$

where $T_b(\lambda)$ is bleached state transmittance and $T_c(\lambda)$ is colored state transmittance of device under application of bias to ECD or film and $\Delta T(\lambda)$ is the transmittance change at a monochromatic wavelength.

(b) Coloration efficiency (CE)

The proportionality factor that relates the optical absorbance change of an electrochrome at a given wavelength (ΔOD) to the density of injected/ejected electrochemical charge necessary to induce a full switch (Q) is called coloration efficiency (CE). CE values are inherent to the electrochromic material under characterization, some being intensely colored by nature in at least one redox state while others display fainter tones over their doping/dedoping cycles, regardless of the deposited film thickness. CE is defined as the optical density change (ΔOD) induced as a function of the injected charge per unit area to produce the optical change.

$$CE \text{ or } \eta\,(\lambda) = \Delta OD\,(\lambda)\,/\,Q \tag{2.2}$$

$$(or)$$

$$\eta\,(\lambda) = \log(T_b(\lambda))/\log\,(T_c(\lambda))\,/\,Q \tag{2.3}$$

where η ($cm^2\,C^{-1}$) is the coloration efficiency at a given wavelength, T_b and T_c are the % transmission in bleached and colored states at a given wavelength.

(c) Switching kinetics

In the context of electrochromism, the switching rate can be defined as the time needed for an electrochrome to switch from one redox state to the other. It depends on several parameters such as the ability of the electrolyte to conduct ions as well as the ease of diffusion of these counter balancing ionic species across the EC active layer, the architecture of the device or the configuration of the cell and the magnitude of the external bias applied. The times taken by an ECD to undergo a 90% absorption increase or a 90% absorption drop (with respect to the absolute absorption modulation) in a half cycle are defined as the coloration and bleaching times respectively. Also it can be defined as the time required for %T

27

change to increase from 10% to 90% of its' full switch in a half cycle (bleaching time) and for %T to decrease from 90% to 10% of its' total magnitude (coloration time).

(d) Write-erase (WE) efficiency

The fraction (percentage) of the originally formed colored state that can subsequently be electrochemically bleached is called WE efficiency. For a successful display, the efficiency must approach 100%.

2.2.2 Deposition of anodically coloring PB films on FTO substrates

For the deposition of PB films, an aqueous solution containing $K_3[Fe(CN)_6]$ (10 mM) and $FeCl_3$ (10 mM) was prepared in 0.01 N HCl. An Ag/AgCl/KCl half-cell was used as the reference electrode, and two FTO coated glass plates were used as working and counter electrodes. A cyan blue colored deposit was obtained on the cathodic plate, upon application of a constant potential of -1.5 V (300 s). The films were rinsed in an aqueous solution comprising 0.01 N HCl: ultrapure water mixed in a 2:3 v/v ratio and preserved in petridishes.

2.2.3 PEDOT films by electrochemical polymerization

A generic method for synthesizing PEDOT films involves the preparation of a clear solution of the monomer 3,4-EDOT and a salt like $LiClO_4$ or an ionic surfactant like camphorsulfonic acid (or any ionic species) in an organic medium like acetonitrile and its' subsequent electropolymerization. A three electrode electrochemical cell comprising of a working electrode (FTO coated glass), a counter electrode (Pt rod/sheet or FTO coated glass) and a reference electrode (Ag/AgCl/KCl) was used (Figure 2.1). The electrodes were immersed in the solution containing the monomer. PEDOT films were deposited onto the working electrode by oxidative electropolymerization at room temperature by chronoamperometry. A fixed potential (chosen from a range between +1.2 to +1.5 V) was applied to the working electrode for a fixed duration of time (typically between 2−6 min.). Light sky blue colored PEDOT films were obtained which were washed in deionized water or an organic solvent, dried in air and stored in air. Equation (1) in Figure 2.1 represents the formation of polymer.
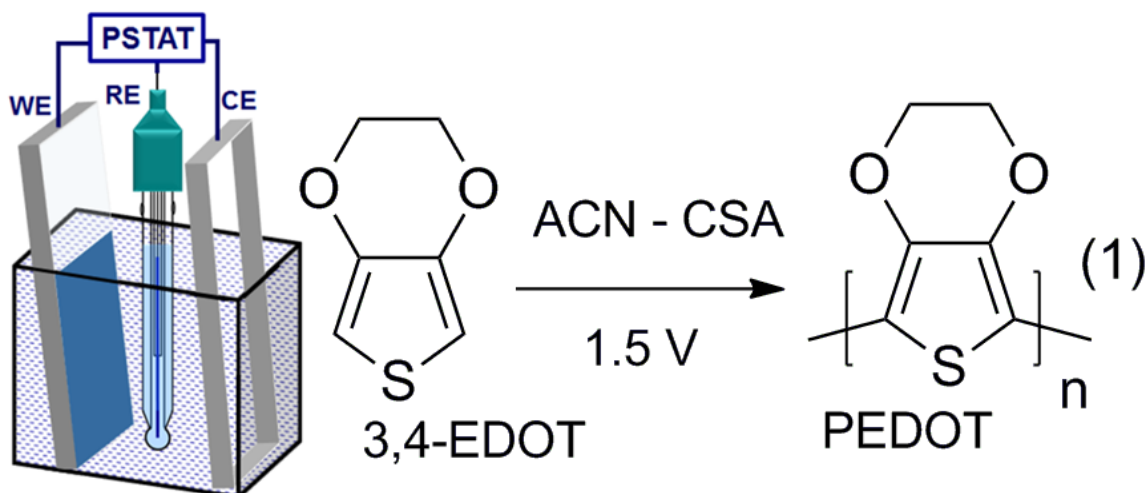
Figure 2.1: Schematic of the three electrode cell showing the formation of PEDOT; the bath contains 3,4-EDOT, camphorsulfonic acid (CSA) and ACN.

2.3 Instruments and characterization techniques

General: IR spectra were recorded on a Bruker Tensor 37 (FTIR) spectrophotometer. ^{1}H NMR spectra were recorded on a BrukerAvance 400 (400 MHz) spectrometer at 295 K in $CDCl_3$ or CD_3OD; chemical shifts (δ ppm) are reported in standard manner with reference to either an internal standard such as tetramethylsilane (TMS) ($\delta_H = 0.00$ ppm) or $CHCl_3$ ($\delta_H = 7.25$ ppm). ^{13}C NMR spectra were recorded on a BrukerAvance 400 (100 MHz) spectrometer at RT in $CDCl_3$ or CD_3OD; chemical shifts (δ ppm) are reported relative to $CHCl_3$ [$\delta_C = 77.00$ ppm (central line of triplet)]. In the ^{13}C NMR, the nature of carbons (C, CH, CH_2 and CH_3) was determined by recording the DEPT-135 spectra, and is given in parentheses and noted as s = singlet (for C), d = doublet (for CH), t = triplet (for CH_2) and q = quartet (for CH_3). In the ^{1}H-NMR, the following abbreviations were used throughout: s = singlet, d = doublet, t = triplet, q = quartet, qui = quintet, m = multiplet and brs. = broad singlet. The assignment of signals was confirmed by ^{1}H, ^{13}C CPD and DEPT spectra. High-resolution mass spectra (HR-MS) were recorded using an Agilent 6538 UHD Q-TOF using a multimode source, JEOL instrument (EI and FAB) or a Bruker Apex Qe instrument (ESI) and HRMS (FT-ICR): Bruker Daltonic APEX 2 with an electron spray ionization (ESI) and Shimadzu Biotech AXIMA Performance (MALDI/TOF). Reactions were monitored by TLC on silica gel using a combination of petroleum ether and ethyl acetate and dichloromethane as eluents. Solvents were distilled prior to use; petroleum ether with a boiling range of 60 to 80 °C was used. Hychem Sainor's silica gel (60 - 120 mesh) was used for column chromatography (approximately 20 g per one gram of crude material). Microwave synthesis was carried out in a CEM Discover system. All electrochemical measurements and electropolymerization were performed on an Autolab PGSTAT 302N coupled with a NOVA 1.9 software. Electropolymerizations were also performed on a Tarsom MC-01

electrophoresis supply. Charges intercalated / deintercalated during redox switching of the devices were determined by chronoamperometry. Electrochromic switching response of the devices was determined under square wave potentials, at a fixed monochromatic wavelength, at a fixed frequency, using a spectrophotometer, in kinetic mode. Electrochemical impedance spectroscopy (EIS) was also performed for the devices performed on an Autolab PGSTAT 302N with a frequency analyzer (FRA); an ac voltage of 10 mV was superimposed over different dc potentials. Z'' *versus* Z' plots were obtained over a frequency range of 10^6 Hz to 0.01 Hz. Surface morphology analysis was examined using a field emission scanning electron microscope (Carl Zeiss Supra 40 FE SEM). X-ray diffraction (XRD) patterns were recorded on a XRD, PANalytical, X'PertPRO instrument with Cu K_α (λ=1.5406 Å) radiation. Some characterization techniques which were extensively used in this work, are discussed here.

2.3.1 Chronoamperometry (CA)

In a controlled potential experiment, the potential is set at a constant value sufficient enough to bring about the rapid oxidation or reduction of the species and it is maintained at this value until only the oxidized or reduced species is present [1]. In this method, the potential of the working electrode is switched instantaneously between two potentials, either as a single step or repeated steps. The experiment is performed in a three electrode electrochemical cell comprising of a working (e.g. FTO coated glass), a counter (e.g. Pt) and reference (Ag/AgCl/KCl) electrode. In chronoamperometry, a fixed potential is applied to the working electrode and the current produced in the cell is monitored as a function of time (Figure 2.2).
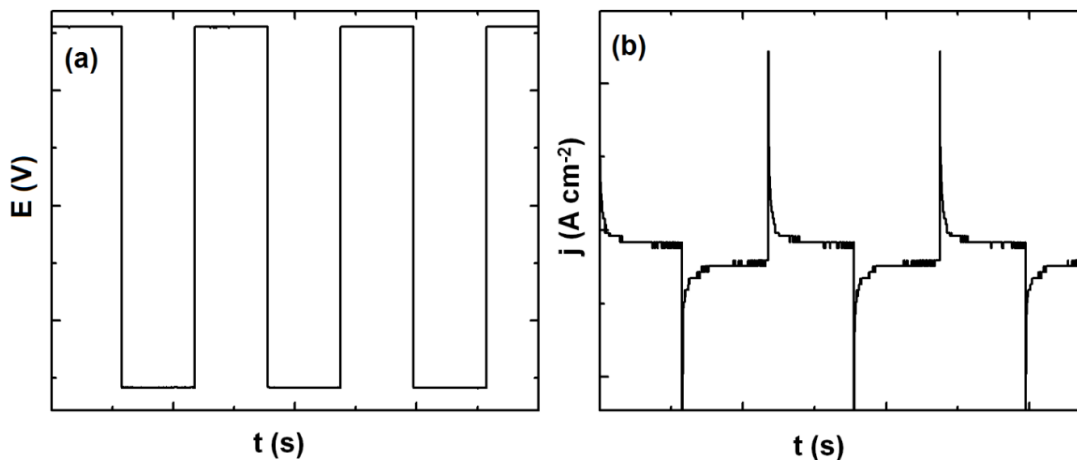
Figure 2.2: (a) Input square wave potential and (b) output current signal; both are functions of time.

The resultant graph is a plot of current *versus* time. In this thesis, CA has been used for (a) synthesis of films of CPs and (b) determination of charge density during coloration and bleaching of an electrochromic film with an Autolab PGSTAT 302N Potentiostat/Galvanostat. The integration of the I-t

curve obtained under a constant potential applied for a fixed period of time, i.e., $Q = \int I \, dt$ yields the charge intercalated/deintercalated during coloration/bleaching. These charge density values were used for the calculation of CEs of electroactive films.

2.3.2 Cyclic voltammetry (CV)

CV is a versatile tool which provides the complete electrochemical spectrum of an electroactive species. It provides both qualitative and quantitative information and is a fast and reliable characterization method. Cyclic voltammetry is also performed in a three electrode electrochemical cell, similar to the one used in chronoamperometry. In CV, the potential applied to the working electrode is continuously swept back and forth at a fixed scan rate between two set points such as E_1 and E_2, which maybe the same as start and end potentials. The potential applied to the working electrode is a triangular wave form as a function of time. The current produced at the working electrode is monitored as a function of the swept potential, over a specified voltage range. The resultant plot is a graph of current *versus* swept potential and is referred to as a cyclic voltammogram (Figure 2.3). The dynamic parameter, scan or sweep rate (ν) is variable and is expressed in mV s^{-1} units. The faradic current increases with scan rate due to the increased flux of electroactive material to the electrode at higher scan rates. The amount of increase in the faradic current is found to scale with the square root of the scan rate. The voltammogram furnishes information about the potentials at which the oxidation and reduction occur, how fast are these phenomena, the electrochemical potential stability window and the extent of reversibility of the electrode reactions under consideration. The scan rate, switching potentials, and the magnitudes of the anodic peak current (I_{pa}), cathodic peak current (I_{pc}), anodic peak potential (E_{pa}) and cathodic peak potential (E_{pc}) are the main parameters of cyclic voltammetry. CV when performed over several repetitive cycles, can provide information about the electrochemical stability of the electroactive material under study in terms of cycling lifetime. The electroactive species can be either dissolved in the electrolyte or it can be prepared in the form of a thin film on a conducting electrode (such as FTO coated glass) CV measures current (A) or current density (A cm^{-2}) as a function of applied voltage, which is swept at a constant rate, $\nu = dV/dt$.

In this dissertation, CV has been utilized in three electrode or two electrode configurations: (a) to discern the redox processes of PEDOT, PEDOT composites and viologens, (b) to characterize electrochromic devices, and (c) to determine the cycling stability of films or devices; all with an Autolab PGSTAT 302N Potentiostat/Galvanostat.
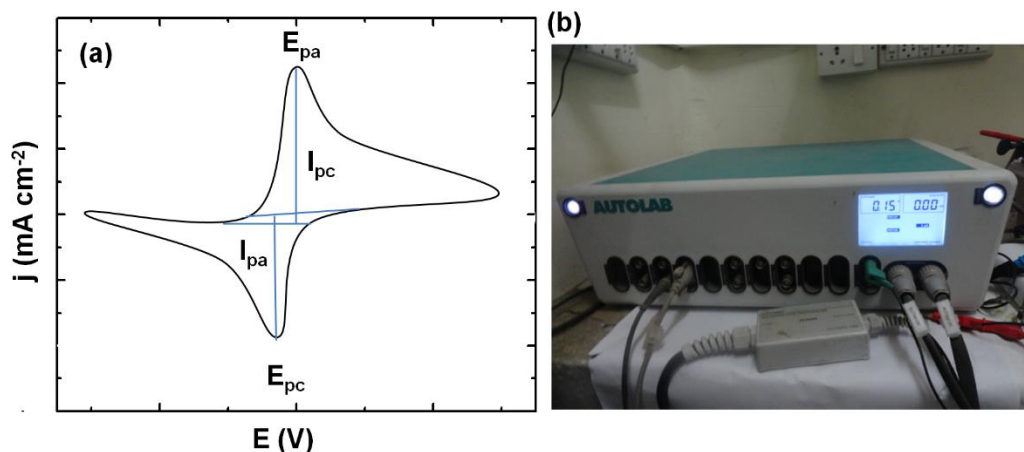
Figure 2.3: (a) A typical CV plot and (b) a photograph of Autolab PGSTAT 302N system used herein.

2.3.3 Linear sweep voltammetry (LSV)

In LSV, the potential applied to the working electrode is swept in one direction and only once, from a start potential E_1 to an end potential E_2 at a fixed scan rate and the current generated at electrode is plotted as a function of swept potential, to yield a I-V or a J (current density)-V curve. In this thesis, the LSV technique has been employed (a) to study the I-V or J-V characteristics of polymer electrolytes, (b) to determine the electrochemical potential stability window of polymer electrolytes and (c) conductivity of CPs / composites with an Autolab PGSTAT 302N Potentiostat/Galvanostat. From the straight-line fits, within the voltage windows in which the I-V response was almost linear, ambient temperature conductivities were determined by using equation (1), wherein d is the thickness of the sample and a is the area of the sample.

$$\sigma_{RT} = (I/V) \times (d/a) \tag{2.4}$$

2.3.4 Electrochemical impedance spectroscopy (EIS)

In an ac experiment, a sinusoidal voltage is applied to a cell and the resulting current passing through the cell as a result of this perturbation is determined. The two parameters that relate the current flowing to the applied potential are: (i) the ratio of the current and voltage maxima, V_{max} / I_{max} (analogous to resistance in dc measurements) and (ii) the phase difference 'θ' between the voltage and the current. The combination of these two parameters represents the impedance 'Z' of the cell. Both the magnitude of impedance ($|Z| = V_{max}$ / I_{max}) and the phase angle 'θ' are functions of applied frequency (f). The impedance of a cell is measured as a function of applied frequency, over a wide range, typically, 1 mHz - 1 MHz [2].

The impedance of a cell is a vector quantity and this vector may be represented by components: $|Z|$ Cosθ and $|Z|$ Sinθ. Z^* represents complex impedance. Z' and Z" are the real and imaginary components of the complex impedance Z^*.

$$Z^* = Z' - j\,Z'', \quad j = (-1)^{1/2} \tag{2.5}$$

The phase angle shift is given by: $\tan\phi = Z''/Z'$. The EIS data is expressed graphically in a Bode or a Nyquist plot (Figure 2.4). In a Bode plot, $\log|Z|$ and ϕ are both plotted against $\log\omega$ or f whereas, a Nyquist plot displays Z'' *versus* Z' for different values of ω or f. Unlike the Nyquist plot, the Bode plot illustrates frequency dependence of impedance. The phenomena that typically occur for an electroactive species in different frequency domains are: (a) at very high frequencies, the bulk resistance of the electrolyte and contact resistances dominate, (b) at intermediate frequencies, charge transfer impedance plays an important role and (c) at very low frequencies, the mass transport (diffusional resistance) controls impedance.
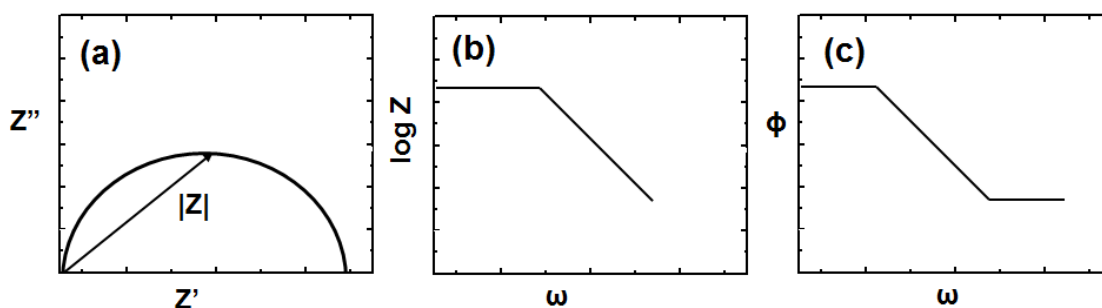
Figure 2.4: (a) Nyquist plot with impedance vector and Bode plots showing (b) log Z and (c) phase angle *versus* frequency.

In this thesis, EIS was employed to unravel the redox phenomena of devices and films by superimposing different dc potentials over ac potentials of a small magnitude between 5-20 mV. The measurements were performed on an Autolab PGSTAT 302N Potentiostat/Galvanostat/Frequency Response Analyzer coupled with a NOVA 1.9 software. EIS has also been used to measure conductivities of electrolytes (at room temperature and different temperatures) from the Z'' *versus* Z' plots, wherein the onset of the curve on the real axis corresponds to the resistance (R) of the electrolyte. Measurements were done between two Pt electrodes.

$$\sigma\,(T) = (1/R) \times (l/a) \tag{2.6}$$

where 'a' is the area of cross section of the two Pt electrodes and l is the distance between them.

2.3.5 Atomic force microscopy (AFM)

AFM (multimode) is a high-resolution imaging tool for the complete surface characterization of properties like topography, elasticity, friction, adhesion, and electrical/magnetic fields. AFM operates in contact, intermediate (tapping), and non-contact modes. In contact mode operation, the AFM tip touches the sample surface, and the tip-sample repulsive force deflects the tip-cantilever [3]. The cantilever deflection is monitored and used as a feedback signal. In intermediate and non-contact modes, the

cantilever is externally oscillated at, or close to, it's resonance frequency. The tip-sample interaction is altered as the tip-sample distance changes, leading to a change in oscillation amplitude (intermediate mode) and resonance frequency (non-contact mode). These amplitude and frequency changes, with respect to the reference amplitude and frequency, are used as feedback signals to obtain the topography of the sample surface. Therefore, intermediate mode and non-contact modes are referred as amplitude modulation (AM) and frequency modulation (FM) operation, respectively. In intermediate and non-contact mode AFM, the tip-sample interaction is perturbed by attractive and repulsive forces, causing amplitude or frequency changes in the oscillation of the AFM tip. In AM mode AFM, changes in the oscillation amplitude provide the feedback signal for imaging.

In this thesis, AFM was used for studying the topography of PEDOT and composite films and also to determine thickness of these films by constructing a sharp step of the film on FTO coated glass or flexible PET and allowing the tip (made of Pt/Ir) to run over the step, whilst simultaneously imaging the same. The height profile provided the film thickness. All AFM, C-AFM and KPFM data were recorded using a Veeco, Multimode 8 with ScanAsyst (Nanoscope 8.10 software).

2.3.6 Conductive atomic force microscopy (C-AFM)

C-AFM is a secondary imaging mode derived from contact AFM that measures conductivity variations across medium- to low- conducting and semiconducting materials. C-AFM employs a conductive probe tip. Typically, a dc bias is applied to the tip, and the sample is held at ground potential. While the z feedback signal is used to generate a normal contact AFM topography image, the current passing between the tip and sample is measured to generate the conductive AFM image. C-AFM images were recorded for CP films / composites. For C-AFM, cantilevers made of antimony doped silicon (n-doped; resistivity ~0.01 - 0.025 Ω cm) and coated with Pt/Ir or Co/Cr (20 nm) on the front and backside were obtained from Veeco. Spring constant of the tip was 0.2 N cm^{-2}. The current sensitivity was 1 nA V^{-1} and a load force of 49 nN was maintained between the tip and the sample. The sample deposited on FTO coated glass, (area ~10 mm^2) was attached to a stainless steel support with a conducting carbon tape. An even coat of silver paste was applied from the surface of the conducting polymer film, along the edge of the conducting glass substrate to the stainless steel plinth, and the topography, current images and point contact I-V profiles were recorded at room temperature. A crack free, pinhole free strip of silver paste was obtained upon drying, which was used for taking electrical contacts. The contact tip is scanned in contact with the sample surface. The z-feedback loop uses the dc cantilever defending a signal to maintain a constant force between the tip and the sample to generate topography images. Concurrently, a dc bias of 50 mV or in the same range was applied to the tip. The built-in pre-amplified scanner head measures the current passing through the tip and sample and images the current profiles.

2.3.7 Kelvin probe force microscopy (KPFM)

KPFM, also known as surface potential microscopy, is a non-contact variant of atomic force microscopy (AFM), and was invented in 1991 [4]. With KPFM, the work function of surfaces can be observed at atomic or molecular scales. The work function is the minimum energy (or work, usually measured in eV), needed to remove an electron from a solid, to a point immediately outside the solid surface (or energy needed to move an electron from the Fermi level into vacuum). When two different conductors are brought into electrical contact, for example, via an external wire contact, electrons will flow from the one with lower work function to the one with higher work function, equalizing the Fermi energies. If they are made into a parallel plate capacitor, equal and opposite charges will be induced on the surfaces. The potential established between these two surfaces is called the contact potential difference (V_{CPD}), contact potential, or surface potential, which equals the work function difference of the two materials. An external potential (also called the backing potential) is applied to the capacitor until the surface charges disappear. At this point, the external potential equals the V_{CPD}. KPFM can measure V_{CPD}, and therefore work functions, in the nanometer regime [5].

In the present work, surface potential maps of PEDOT and composite films were measured by employing cantilevers made of antimony doped silicon and with a metallized apex of Co/Cr or Pt/Ir on the front and the back side of the tip. The spring constant of tip was 1-5 N cm^{-2}. Cantilever properties were: resonant frequency of ~70 kHz, spring constant ~ 2 N/m, lever thickness 2.8 μm, lever length 240 μm, and a lever width of 30 μm. The tip height is 14 μm, and the tip radius is ~30 nm. The height data or topography was measured in tapping mode during the first pass, for every scan line. In the second pass, the tip lifts above the surface to an adjustable lift height, which was fixed at a value between 20-200 nm (for each sample), and scans the same line, while following the height profile recorded in the first pass. Potential maps are taken in interleave mode. We performed KPFM measurements by bringing the tip in proximity (at a fixed height above the sample) with respect to the top surface of the active film. No dc bias was applied to the sample during the measurement and a sinusoidal ac voltage of 5 V was applied to the tip during surface potential imaging.

2.3.8 Spectroelectrochemistry

A UV-Vis spectrum is plot of light absorbed or reflected or transmitted *versus w*avelength in the UV-visible range. Molecules containing π-electrons or non-bonding electrons (n-electrons) can absorb the energy in the form of ultraviolet or visible light to excite these electrons to higher anti-bonding molecular orbitals. Such a spectrum can often be produced directly by using a UV-Vis spectrophotometer.The method is most often used in a quantitative way to determine concentrations of an absorbing species in solution, using the Beer-Lambert law [6].

$$OD = A = \log (I_o/I) = \varepsilon\, c\, l \text{ (for solution)} \tag{2.7}$$

$$OD = A = \log (I_o/I) = \alpha\, d \text{ (for solid samples)} \tag{2.8}$$

A is the measured absorbance or OD (optical density) expressed in arbitrary units, I_o is the intensity of the incident light at a given wavelength, I is the transmitted intensity, l is the path length through the sample, and c, the concentration of the absorbing species. For each species and wavelength, ε is a constant known as the molar absorptivity or extinction coefficient. If the sample under study is a homogeneous solid, equation (2.8) can be applied, where α is the absorption coefficient at a given wavelength and d is the sample thickness.

In the present thesis, absorbance or transmittance spectra of conducting polymer films/devices/ solutions were recorded on a Shimadzu UV-Visible-NIR 3600 spectrophotometer either in an *in-situ* manner under dc potentials of different magnitudes (applied for a fixed duration of time, e.g. 60 s) or in the as-fabricated state without applying any bias. Absorption spectra of solutions were measured in quartz cuvettes of 1 cm path length using the same instrument. The optical density and/or transmittance of devices/films were measured under different potentials, each applied for a fixed time period. The charge Q/A or charge density values at each potential were determined by chronoamperometry, as discussed in an earlier section.

The time required for an electrochromic film (such as CP or composite films or viologens) or device to color from its bleached state or vice versa is termed as its response time. For most films/devices, response or switching time is of the order of a few seconds and is extremely useful for judging the suitability of a film for an electrochromic application. Electrochromic switching response of devices/films were measured under a square wave potential of fixed magnitude (e.g. $\pm$ 2 V) applied to the working electrode (CP film or viologens), at a fixed monochromatic wavelength such as λ_{max} of the CP or an appropriate wavelength at which high contrast is observed, using the same spectrophotometer, in kinetic mode. These measurements were done in a two electrode configuration either with a film as the working electrode and Pt as counter electrode in conjunction with a liquid electrolyte or in the device configuration with two complementary electrochromic films as working and counter electrodes. Step times or half-cycle times ranged between 1 to 5 s. The color-bleach kinetic plot is a graphical representation of absorbance or transmittance *versus* time (Figure 2.5), under a square wave bias from which switching times of CP or composite films/ devices were deduced. All *in-situ* spectrophotometry measurements of films colored/ bleached in electrolytes were implemented in a quartz cell. Devices based on CPs or viologens were directly inserted in the sample compartment during measurements. *In-situ* specular reflectance of the devices was measured on a T90+ (PG instruments) spectrometer, with a mirror at the rear of the device.

Switching of the PEDOT films was also measured on Avantes (Avaspec-2048) coupled with Autolab, in spectroelectrochemical mode in a quartz cell; the instrument is capable of scanning wavelengths from ~400 to 800 nm in 1 ms. The dynamic change in absorbance was measured during redox switching. The films were subjected to an oxidation potential of +1.0 V or reduction potentials of −1.0 V for durations of 3, 10, 15, 20, 25 and 30 s for these measurements.
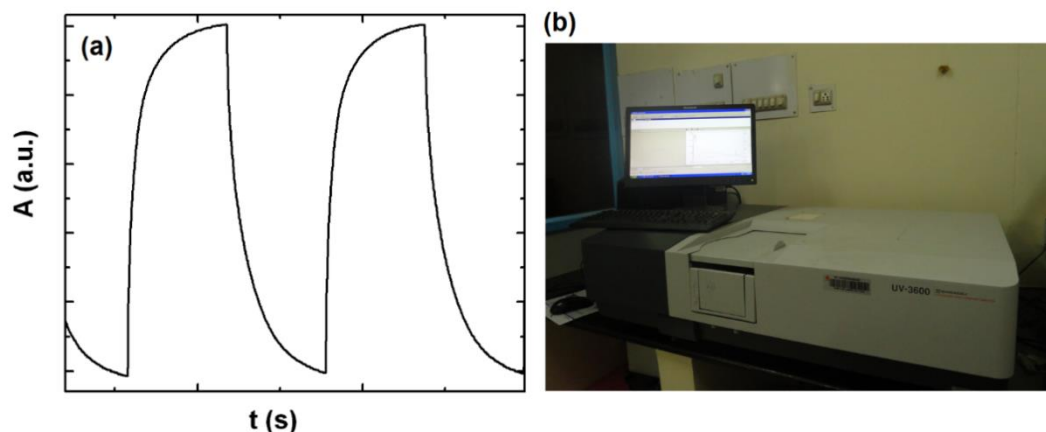
Figure 2.5: (a) A typical color-bleach kinetics plot and (b) a photograph of the UV-Vis spectrophotometer used herein.

2.3.9 Thermogravimetric analyzer (TGA)

In a TGA experiment, the variation in the weight of a substance is monitored as a function of temperature or time as the sample specimen is subjected to a controlled temperature program in a controlled atmosphere. TGA measures a sample's weight as it is heated or cooled in a furnace. A TGA consists of a sample pan that is supported by a precision balance. The pan resides in a furnace and is heated or cooled during the experiment. The mass of the sample is monitored during the experiment. A sample purge gas controls the sample environment. This gas is inert and flows over the sample and exits through an exhaust. Thermal stability of electrolytes was determined by TGA in this thesis. TGA data for the samples were collected on a Q600, TA instruments in nitrogen atmosphere.

References

[1] A.J. Bard, L.R. Faulkner, Electrochemical methods fundamentals and applications, 2nd ed. Wiley, New York, 2001.
[2] E. Barsoukov, J.R. Macdonald, Impedance spectroscopy: Theory, experiment, and applications, 2nd ed. Wiley-Blackwell, 2005.
[3] P. West, Introduction to atomic force microscopy: Theory, practice, applications, www. AFM University.org.
[4] M. Nonnenmacher, M.P. OBoyle, H.K. Wickramasinghe, Appl. Phys. Lett. 58 (1991) 2921.
[5] S. Kitamura, M. Iwatsuki, Appl. Phys. Lett.72 (1998) 3154.
[6] H.H. Parkampus, UV-Vis spectroscopy and applications, Spinger-Verlag, Berlin, New York, 1992.

Chapter 3

Influence of incorporation of N–methyl fulleropyrrolidine on the electrochromic performance of PEDOT

3.1 Introduction

Traditionally, the monomer EDOT when doped by insulating anions such as perchlorate [1], imide [2], surfactant based ions [3] or polyanions like poly(2-acrylamido-2-methyl-1-propanesulfonic acid) or PolyAMPS,[4] and poly(styrene sulfonate) or PSS, the latter revolutionized by Bayer Research Labs as the water soluble PEDOT:PSS formulation with far-reaching consequences in areas beyond electrochemistry [5,6], yields PEDOT, which has a sky blue hue in the as-fabricated or oxidized state and shows a broad absorption in the NIR region due to bi-polaronic transitions [7]. But there are hardly any reports on the use of polycation based solutions for electropolymerization of EDOT. Here we used poly(diallyldimethylammonium) chloride or PDDA as the counter ion source for electropolymerization of EDOT. The resulting PEDOT films had a bright bluish-purple shade instead of the pale blue hue; the latter being generally the color of PEDOT films grown by oxidative electropolymerization [1]. However, the most unusual feature of these as-fabricated PEDOT/PDDA films was that they showed an intense absorption at ~600 nm which typically arises due to π-π^* transitions. For conventional PEDOT films, the oxidized state is reflected in the bipolaronic peak at wavelengths above 800 nm and the reduced or neutral state manifests itself in the form of the π-π^* absorption in the visible region at ~590 nm [1,8]. Here, we obtained a film of PEDOT which not only showed a strong absorption in the visible region, but is also stable in air in this state, unlike the traditional neutral state PEDOT which has a zero tolerance to air [9-11]. Furthermore on electrochemically switching the PEDOT/PDDA film in an ionic liquid, the film showed reversible and reproducible transitions between deep blue and brown colors.

To amplify the optical and electronic response of the PEDOT/PDDA film, a fullerene derivative, namely, N-methyl fulleropyrrolidine (N-FP) was incorporated in the same and composite films were obtained. The use of fullerene and their derivatives had been till date quintessentially confined to organic photovoltaic cells, [12] but they have seldom been used to modify the optical and electronic functions of PEDOT. We preferred an electrophoretic method of synthesis, for it is well-established that fullerene

38

molecules easily form clusters with organic moieties in solution via supramolecular interactions and under an electrophoretic field, these clusters form organized structures on the electrode surface [13,14]. We used conducting atomic force microscopy (C-AFM) and kelvin probe force microscopy (KPFM) to assess how the nanoscale conduction behavior and localized work function of PEDOT/PDDA are influenced by the fullerene derivative. On the basis of detailed spectrophotometric, dynamic spectroelectrochemical and electrochemical measurements coupled with measurements at a nanometer scale spatial resolution, we have proposed a mechanism for the formation of partially reduced but air-stable PEDOT/PDDA films followed by a successful demonstration of a new brown color in PEDOT and then shown how a fullerene derivative augments the optical and electronic properties of PEDOT.

3.2 Experimental
3.2.1 Synthesis of N-FP and PEDOT films

A mixture of C_{60} (110 mg, 0.15 mmol), N-methyl glycine (27 mg, 0.30 mmol), and paraformaldehyde (23 mg, 0.75 mmol) was heated under reflux conditions at 110 °C in toluene (200 mL) under Ar for 2 h. The resulting brown solution was washed with water, dried over Na_2SO_4, and concentrated *in-vacuo*. Thin films of PEDOT/PDDA were synthesized on FTO conducting substrates in a two electrode cell configuration from water - isopropanol (1:1) solutions containing EDOT (0.1 M) and PDDA solution (1 mL, 35 wt % in water) per 10 mL of the precursor solution and PEDOT/PDDA/N-FP films were synthesized after dispersing N-FP (5-6 mg) to the above precursor solution using a Tarsons MC-01 electrophoresis power supply and by applying a fixed potential of 6 V for a duration of 1-2 minutes. The bluish-purple films were formed on the anodic electrode and were washed in deionized water and dried in air. The film thicknesses of the PEDTOT/PDDA and PEDOT/PDDA/N-FP films were measured by AFM technique by running an AFM tip over a step of a sample/blank FTO assembly and are found to be 0.64 and 0.71 μm respectively.

3.3 Results and discussion
3.3.1 Raman and XRD studies

Raman spectra of neat fullerene and N-methyl fulleropyrrolidine recorded at two different excitation wavelengths of 785 and 532 nm, are shown in Figure 3.1a and b. At $\lambda_{ex} = 785$ nm, neat fullerene shows sharp lines at 272, 428, 496, 770, 1423, 1467, 1572 cm^{-1}, attributable to $H_g(1)$, $H_g(2)$, $A_g(1)$, $Hg(4)$, $H_g(7)$, $A_g(2)$ and $H_g(8)$ modes [15,16]. When λ_{ex} was changed to green, i.e., 532 nm, among these Raman active lines, the most significant lines: the pentagonal pinch mode at 1461 cm^{-1} or $A_g(2)$, the radial vibration $H_g(1)$ mode at 269 cm^{-1} and the asymmetric $A_g(1)$ mode at 494 cm^{-1} are retained albeit slight downshifts to lower wavenumbers, which could be due to polymerization induced by the high energy green laser beam. Similar photo-assisted oligomerization of C_{60} molecules has been reported in the past [17].
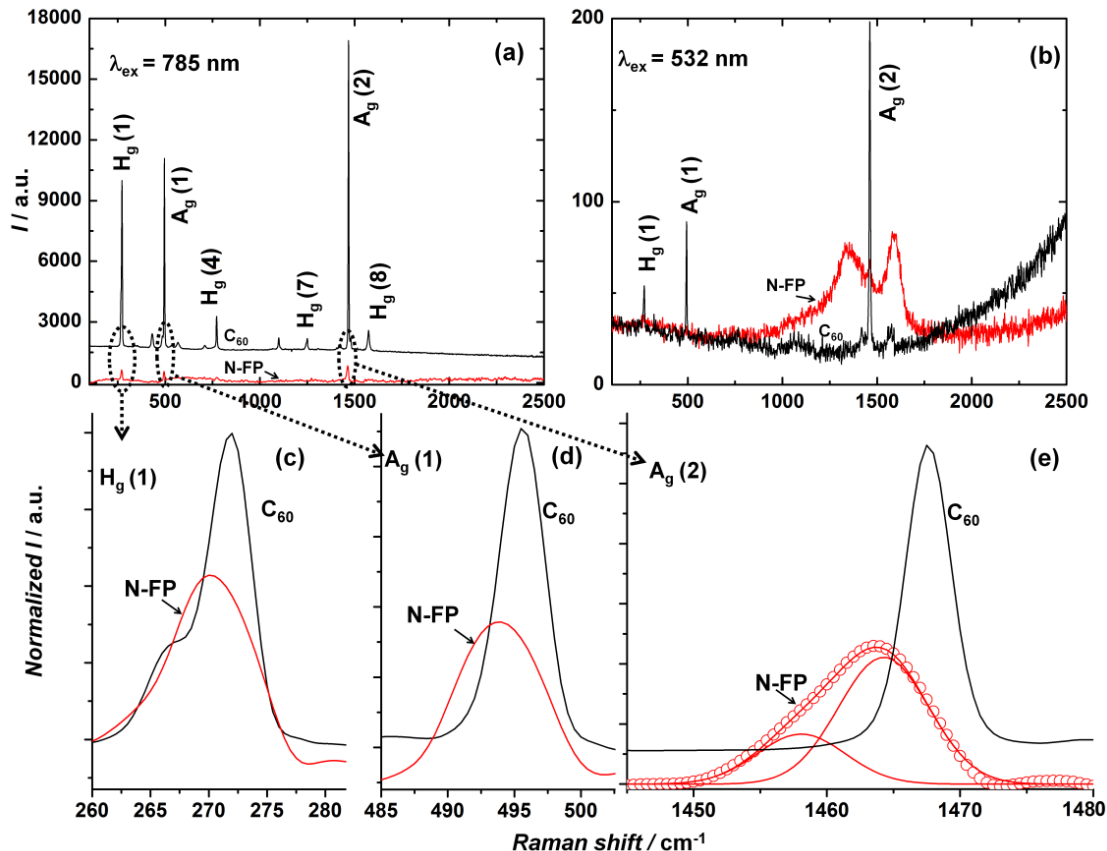
Figure 3.1 Raman spectra of neat fullerene and N-methyl fulleropyrrolidine (N-FP) recorded at laser excitation wavelengths of: (a) 785 and (b) 532 nm and enlarged views of the spectra at λ_{ex} = 785 nm for the (c) $H_g(1)$, (d) $A_g(1)$ and (e) $A_g(2)$ modes. Deconvoluted $A_g(2)$ components for N-FP are shown in (e).

On comparing the spectrum of neat fullerene with N-methyl fulleropyrrolidine (at λ_{ex} = 785 nm), we find that while neat fullerene shows a split for the $H_g(1)$ mode with two components poised at 266 and 272 cm^{-1}, the derivative shows a single peak at 270 cm^{-1}. The $A_g(1)$ mode appears at 497 cm^{-1} for neat fullerene, and at 493 cm^{-1} for the derivative, but it is the $A_g(2)$ mode which is most sensitive to the chemical environment, as this mode is seen as a singular sharp peak at 1467 cm^{-1} in neat fullerene, whereas it acquires a highly asymmetric profile upon derivatization. Deconvolution of this broadened peak in N-methyl fulleropyrrolidine, yielded twin components at 1464 and 1458 cm^{-1}, signifying photopolymerization in the fcc C_{60} crystal. But noteworthy was the difference between the spectrum of neat C_{60} and the derivative recorded at 532 nm. Except for the $A_g(2)$ mode at 1458 cm^{-1}, the derivative shows no other characteristic modes of C_{60}, but produces two broad peaks at 1340 and 1583 cm^{-1}, plainly contrasting the structure of the derivative from that of the parent molecule.

Further evidence differentiating N-FP from fullerene was also obtained through XRD studies (Figure 3.2). X-ray diffractograms of a neat fullerene and N-methyl fulleropyrrolidine are shown in Figure S1a. Neat fullerene shows three high intensity distinctive peaks at d = 8.20, 5.01 and 4.28 Å corresponding to (111), (220) and (311) reflections of face centered cubic (fcc) lattice of C_{60} molecules which concurs well with the PDF file number: 82-0505. In addition, five low intensity lines are also observed for neat fullerene, which are not observed for the derivative. Albeit an overall decrease in the intensity of the peaks, the derivative: N-methyl fulleropyrrolidine, also showed the main diffraction lines at d = 8.22, 5.01 and 4.28 Å, indicating that the fcc crystal structure of neat fullerene is preserved upon derivatization. However, the enlarged views of these peaks, shown in Figure 3.2b, c and d, reveal that these three main peaks have split with additional components at d = 8.39, 5.12 and 4.37 Å, suggestive of some alterations at the lattice level. The modified XRD pattern is an indirect indicator of successful derivatization.
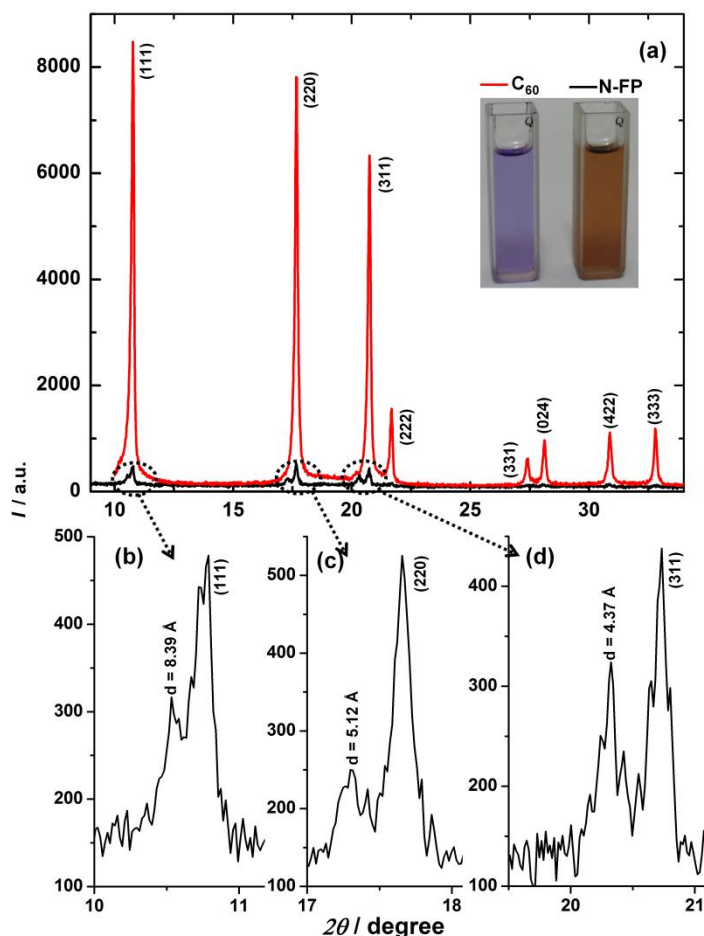
Figure 3.2 X-ray diffractograms of (a) neat fullerene and N-methyl fulleropyrrolidine (N-FP), (b), (c) and (d) are enlarged views of the XRD patterns of N-FP showing the emergence of new d lines in addition to the contributions from neat C_{60}; with hkl enclosed in parentheses.

Raman spectra of the control PEDOT/PDDA and PEDOT/PDDA/N-FP films measured at excitation wavelengths of 785 and 532 nm are displayed in Figure 3.3a and b. The control film (at λ_{ex} = 785 nm) shows low intensity peaks at 569 and 987 cm^{-1}, ascribable to the oxyethylene ring deformation, and at 702 and 1262 cm^{-1}, due to symmetric C-S-C deformation and C_α–$C_{\alpha'}$ (inter-ring) stretching modes [18,19]. The PEDOT/PDDA/N-FP film also shows similar peaks, as the strong absorptions of the conducting polymer PEDOT supersede the contributions from the fullerene derivative. But it is the 1440-1550 cm^{-1} region, which provides direct evidences for the reduction of PEDOT induced by PDDA. The enlarged view of the control film and fullerene derivative incorporated PEDOT/PDDA film (Figure 3.3b), reveals three peaks which, upon Gaussian deconvolution were found to be centered at 1366, 1434 and 1510 cm^{-1} for the control film and downshifted slightly to 1361, 1426 and 1496 cm^{-1} for the PEDOT/PDDA/N-FP film. When irradiated by a laser of 532 nm wavelength, these peaks were seen at ~1364, 1433 and 1511 cm^{-1} for both samples. The high intensity band observed in the 1430-1440 cm^{-1} range is assigned to the C_α=C_β(−O) stretching mode [18]. This band shows maximum intensity (among all peaks in a given sample) for both control PEDOT/PDDA and PEDOT/PDDA/N-FP films at both excitation wavelengths of 785 and 532 nm, is a clear indicator of the dominance of reduced C_α=C_β groups in the films. In the past, for oxidized PEDOT films, this peak was found to be almost non-existent, when irradiated with a laser beam equipped with a wavelength of 514 nm [20]. Authors propounded that since the oxidized PEDOT film shows a strong absorption only at wavelengths above 850 nm, corresponding to bi-polaronic transitions, the oxidized film does not show any Raman peaks when excited with 514 nm. They further found that only the reduced film, which showed a $\pi-\pi^*$ transition peak at a photopic wavelength of 514 nm, showed Raman peaks upon excitation at 514 nm. Authors concluded that the intensities of Raman bands were enhanced for reduced PEDOT, because of a resonance effect as the electronic transition within PEDOT matched with the impinging laser's wavelength [20].

Here, if the PEDOT film had been predominantly in the oxidized state, it would not have responded to a green laser with a λ_{ex} of 532 nm. Since both PEDOT/PDDA and PEDOT/PDDA/N-FP films show distinct Raman signals (especially the most intense one in the 1430-1440 cm^{-1} range due to C_α=C_β(−O) stretch), when excited by a wavelength of 532 nm, it is reasonable to conclude that the film exists in a partially reduced state. But how the reduced state of PEDOT is rendered stable in air is baffling. Nonetheless it is obvious that PDDA plays a crucial role in completely modifying the absorption behavior of PEDOT. The two peaks found in the 1360-1370 cm^{-1} and 1495-1515 cm^{-1} regions are ascribable to C–C stretch and the asymmetric C=C stretching vibrations and the preponderance of the latter mode at both λ_{ex} = 785 and 532 nm (for both films), reiterates the prevalence of high π-bond character in the as-fabricated films.
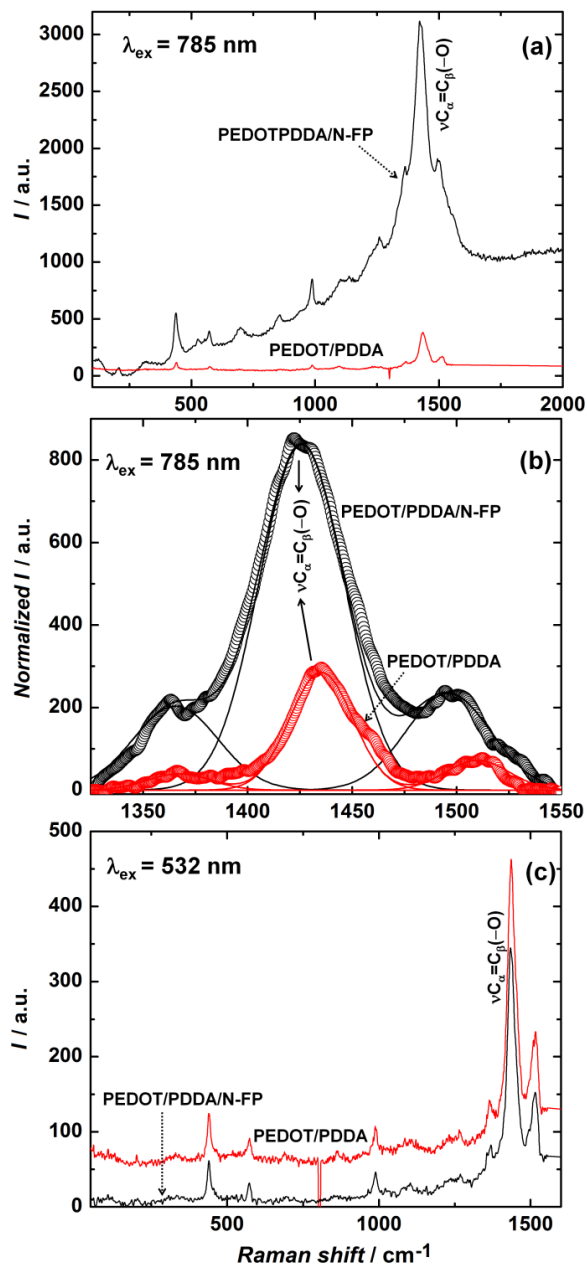
Figure 3.3 Raman spectra of PEDOT/PDDA and PEDOT/PDDA/N-FP films recorded at laser excitation wavelengths of: (a) 785 nm in the 400 – 2000 nm wavelength range and (b) enlarged deconvoluted views of the $\nu\{C_\alpha=C_\beta(-O)\}$ modes; the solid lines represent the fits and (c) comparison at λ_{ex} = 532 nm.

3.3.2 C-AFM and KPFM

Simultaneous topography and current images of PEDOT/PDDA and PEDOT/PDDA/N-FP films acquired by conducting-AFM are shown in Figure 3.4. The corresponding section profiles are displayed as insets. The topography shows globular structures with randomly distributed protrusions (bright regions in Figure 3.4a and a′) of various dimensions typically a few hundred nanometers in height. The root-

mean-square (rms) roughnesses were 43.5 and 48.7 nm for the PEDOT/PDDA and PEDOT/PDDA/N-FP films respectively. The concurrently acquired current images furnish a nanoscale map of differences in current conduction for each sample (Figure 3.4b and b′). At the nanoscale, the both surfaces exhibits relatively uniform but low electronic conductivity, as dark regions corresponding to low current pre-dominate in both films. The bright areas or the protrusions arise from the dopant species and these domains are few but more conductive. The maximum current values were 70 pA and 1.1 nA for the PEDOT/PDDA and PEDOT/PDDA/N-FP films. The current maps reveal that incorporation of N-FP in PEDOT/PDDA enhances the nanoscale current carrying ability of the film and this attribute facilitates charge transport during redox switching which accounts for the larger optical contrast attained by the PEDOT/PDDA/N-FP film (seen later). To quantify the variation of the local conductance, current-voltage (I-V) plots were performed as a function of the applied voltage, which was linearly scanned between +3 and −3 V. Representative curves obtained by averaging 15 curves recorded at fifteen equally spaced out spots in Figure 3.9b and b′ are shown in Figure 3.4c and c′. While the current response is quasi-linear with an almost negligible slope in the voltage window of -3 to +2 V (marked as region I in Figure 3.4c), current rises steeply but linearly as a function of bias in the +2 to +3 V range (region II in Figure 3.4c). The average nanoscale conductivity deduced from Ohm's law for the film in region II is 6×10^{-7} S cm^{-1}. For the PEDOT/PDDA-N-FP film, prior to current saturation, there are three linear zones with different slopes, and the conductivity averaged over regions I, II and III is 8.09×10^{-2} S cm^{-1}. The nanoscale conductivity of the PEDOT/PDDA-N-FP film is greater by five orders of magnitude, and this infers a more conductive matrix thus implying the presence of less hindered pathways for electron movement during oxidation and reduction which effectively translates into a higher optical contrast relative to the PEDOT/PDDA film.
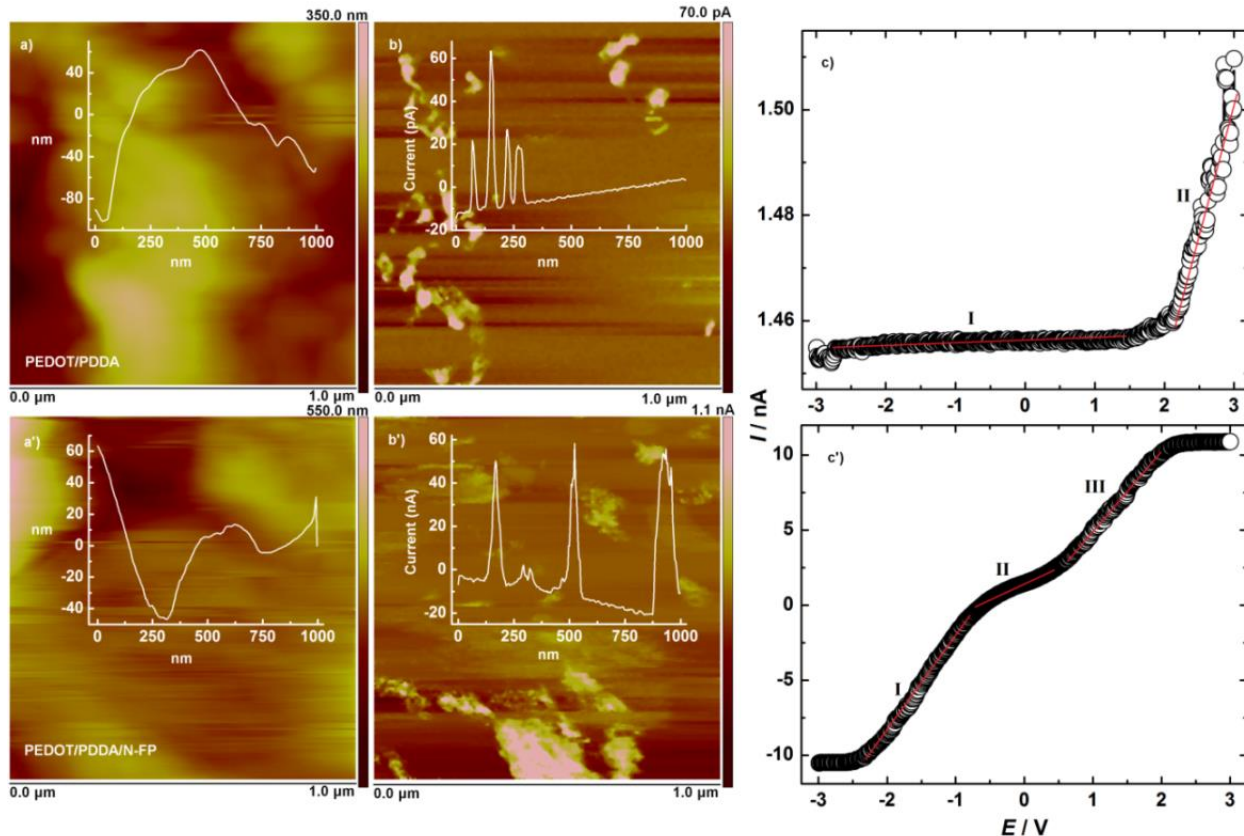
Figure 3.4 Representative simultaneous topography and current images of (a,b) PEDOT/PDDA and (a′,b′) PEDOT/PDDA/N-FP films measured over a scanned area of 1 μm × 1 μm. Corresponding cross-sectional profiles are shown in the insets of the images. Follow-on I-V plots generated by averaging 15 I-V curves recorded at 15 equally spaced points (on each current image shown in (b) and (b′)) are shown in panels: (c) PEDOT/PDDA and (c′) PEDOT/PDDA/N-FP films.

Topography and surface potential maps of PEDOT/PDDA and PEDOT/PDDA/N-FP films were generated consecutively and these are shown in Figure 3.5. The surface potential images were obtained at two different lift heights (Δz: distance between the metallized tip and the sample surface) of 50 and 100 nm for both samples (Figure 3.5a′, b′, c′ and d′). Broadly, greater the separation between tip apex and the sample surface smaller would be the surface potential or the contact potential difference (V_{CPD}), because of the decreased strength of interaction between the two materials. The quantitative profiling of the surface potential variation as a function of distance for given magnitude of Δz are shown in the insets of the surface potential maps. These were obtained along the mid-section of each image. We used the KPFM result for Δz = 50 nm, for deducing the work function of the two films, as it has been established in the past that errors increase with increasing lift height. We too observed a lowering of surface potential ongoing from Δz = 50 nm to a Δz = 100 nm, for both films.

45
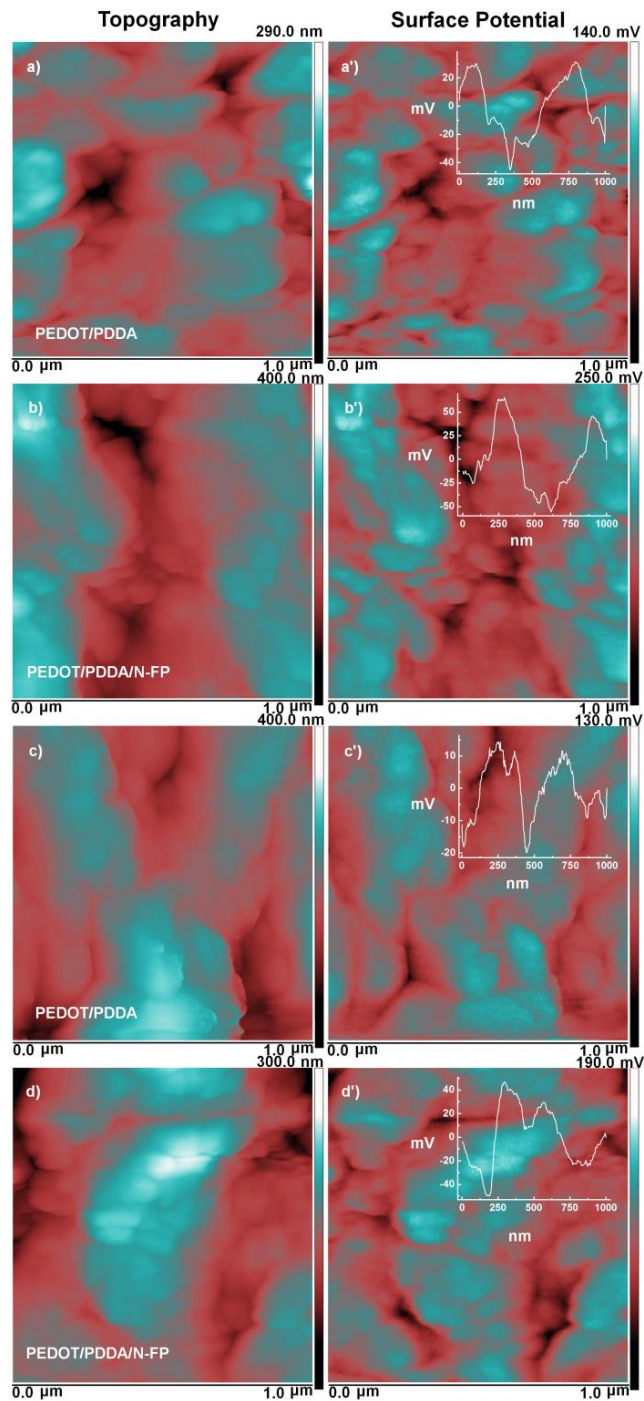
Figure 3.5 Topography and surface potential maps of (a,a′) and (c,c′): PEDOT/PDDA and (b,b′) and (d,d′): PEDOT/PDDA/N-FP films recorded over a scanned area of 1 μm × 1 μm. Corresponding cross-sectional profiles are shown in the insets of the images. Sample to tip distance was fixed at 50 nm in a′ and b′ and 100 nm in c′ and d′.

The work functions of PEDOT/PDDA and PEDOT/PDDA/N-FP films are 4.76 and 4.65 eV respectively and these are lower than the reported work function of PEDOT:PSS which is 5.0 eV [20]. A reduced work function registered here for the PEDOT/PDDA film implies that removal of an electron or oxidation of PEDOT is relatively easier as compared to conventional PEDOT, and this property can be of advantage even in an organic photovoltaic cell, wherein a cheaper and low work function material is sought to replace the expensive and high work function In_2O_3:Sn electrode. Further since the PEDOT/PDDA/N-FP film has a lower work function as compared to PEDOT/PDDA, possibly due to the inclusion of N-methylfulleropyrrolidine in the former, it is apparent that the energetics of the PEDOT/PDDA/N-FP film favors the oxidation/reduction in this film, in comparison to the PEDOT/PDDA film. This is also illustrated through an energy band diagram shown in Figure 3.6. The band gaps in Figure 3.6 were deduced from the absorption edges shown in Figure 3.7. Thus KPFM indirectly shows that the much larger optical contrast achieved in the PEDOT/PDDA/N-FP film as compared to the PEDOT/PDDA film is imposed by the positions of conduction band levels.
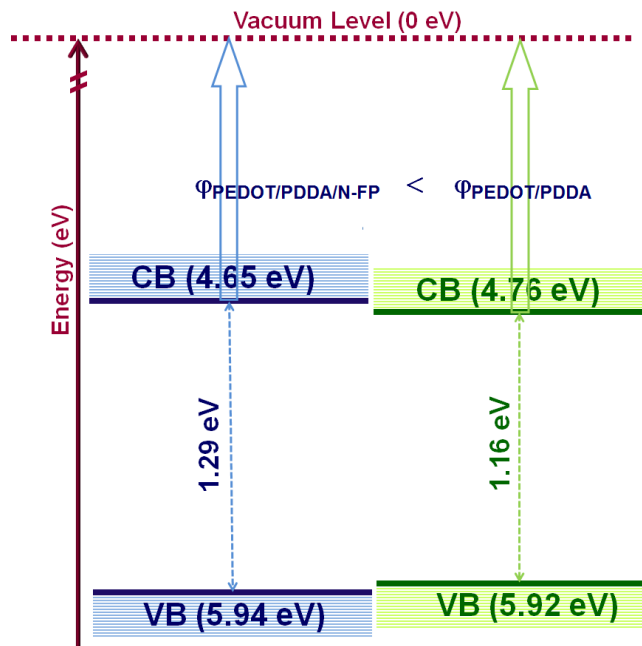
Figure 3.6 Energy band diagram of PEDOT/PDDA/N-FP and PEDOT/PDDA films; band gaps deduced from absorption spectra and conduction band positions determined by KPFM analyses (not drawn to scale: displays the relative positions in the two samples).
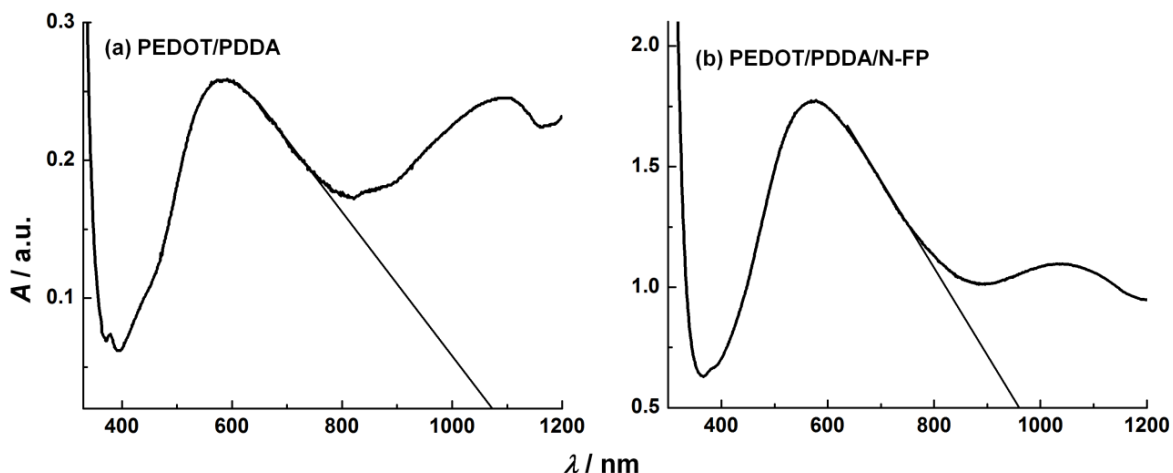
Figure 3.7 Absorption edges for determination of band gap of as fabricated (a) PEDOT/PDDA and (b) PEDOT/PDDA/N-FP films.

3.3.3 Cyclic voltammetric studies of PEDOT/PDDA and PEDOT/PDDA/N-FP films

Cyclic voltammograms of PEDOT/PDDA and PEDOT/PDDA/N-FP films were compared within a voltage window of ± 1 V at different scan rates and these plots are shown in Figure 3.8. At a scan rate of 5 mV s^{-1}, the difference between the redox activities of the two films becomes apparent. For the PEDOT/PDDA/N-FP film, a broad oxidation peak is registered at +0.27 V ascribable to the egress of cations from the polymer film and the second oxidation peak seen at +0.69 V is attributed to further oxidation, as the positive charges on the polymer chain surpass the number of bound anions and therefore electro-neutrality is attained by compensation with trifluoromethanesulfonate ions of the electrolyte. In the reverse scan, the reduction peak at –0.19 V corresponds to the movement of the electrolyte anions out of the film matrix leading to the formation of neutral PEDOT. In case of the PEDOT/PDDA film, no oxidation peak was observed at any scan rate and only a single reduction peak was seen at –0.23 V, corresponding to the formation of neutral PEDOT. At any given scan rate, the area under the voltammogram is larger for the PEDOT/PDDA/N-FP film as compared to the PEDOT/PDDA film, which confirms that N-methyl fulleropyrrolidine, increases the charge storage capacity of PEDOT/PDDA film during redox switching. The response of both films shows a capacitive behavior at high scan rates of 50 and 100 mV s^{-1}.
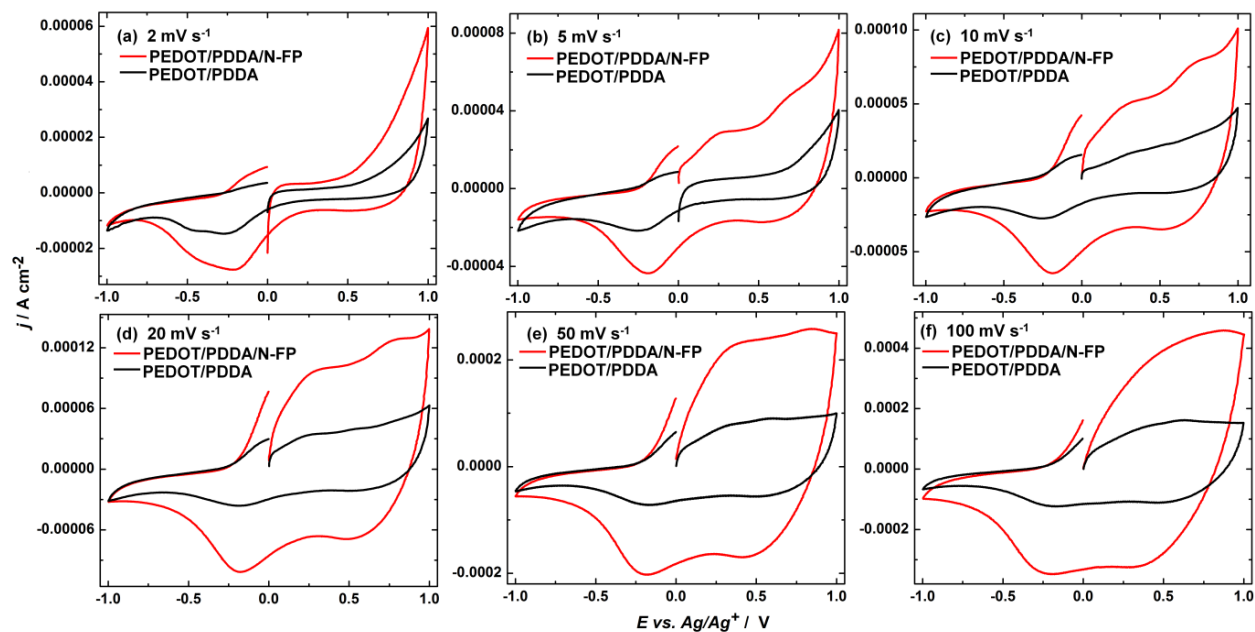
Figure 3.8 Cyclic voltammograms of PEDOT/PDDA and PEDOT/PDDA/N-FP films recorded within a voltage window of ± 1.0 V at scan rates of (a) 2, (b) 5, (c) 10, (d) 20, (e) 50 and (f) 100 mV s^{-1} in the ionic liquid: 1-butyl-1-methyl pyrrolidinium trifluoromethanesulfonate.

CV plots of PEDOT/PDDA however do not reflect the role of PDDA in controlling the optical behavior of PEDOT, as the CV curve obtained herein is quite similar to cyclic voltammograms obtained in the past for PEDOT films doped by conventional anions. This indicates that although the optical absorption or band gap of the as-fabricated PEDOT/PDDA film is different from that of conventional PEDOT, nonetheless, the film does undergo oxidation and reduction in potential ranges similar to that shown by PEDOT doped with perchlorate ions.

3.3.4 Absorption and dynamic spectroelectrochemistry

The electrochromic response of PEDOT doped by conventional anions such as perchlorate or a polyanion like poly(styrene sulfonate) is very well-understood [1,21]. The stepwise oxidation of neutral reduced PEDOT (−1.0 V) to fully oxidized state (+0.9 V) is accompanied by a color change from deep blue to sky blue with intermediate shades of blue, corresponding to an optical absorption in the same visible range of wavelength albeit a lowering of intensity. Irrespective of the type anion used for charge balancing in fully oxidized PEDOT, the film typically shows a broad absorption band at wavelengths above 800 nm, characteristic of the bipolaronic transitions in the polymer, and thus ratifying its' oxidized status. As an illustrative example, the absorption spectrum of fully oxidized PEDOT doped by camphor sulfonate ions is shown in Figure 3.9d. Upon reducing this film in a liquid electrolyte, an intense band in the visible region with a λ_{max} at ~598 nm attributable to $\pi-\pi^*$ transitions appears thereby confirming the conversion of oxidized PEDOT to neutral insulating PEDOT. The absorption spectrum of an as-fabricated

49

PEDOT/PDDA film, however showed a marked digression from this predictable trend (Figure 3.9a). Instead of the bipolaronic band in the NIR region, this polymer film showed a broad absorption peak with a λ_{max} at ~582 nm, which is supposedly the signature peak of reduced PEDOT. Neutral PEDOT is unstable in air, and the $\pi-\pi^*$ absorption peak in the 500-650 nm wavelength range is usually obtained under *in-situ* conditions. On the contrary, a $\pi-\pi^*$ absorption peak in the visible region for an as-fabricated PEDOT/PDDA film was obtained in air. It is evident that the counter ion source: PDDA which was used herein for oxidative electropolymerization of EDOT played a key role in controlling the band gap of the polymer formed and as a consequence its' optical absorption.

The absorption behavior of the PEDOT/PDDA film was followed by studying the spectroelectrochemistry in 1-butyl-1-methyl pyrrolidinium trifluoromethanesulfonate ionic liquid electrolyte under (a) anodic potentials varied from +0.4 V to +2.6 V in steps of +0.2 V and (b) cathodic potentials varied from –0.4 to –2.6 V in steps of –0.2 V (Figure 3.9a). Since the optical changes in the film were rather small for potential intervals less than 0.2 V and consequently were difficult to distinguish with naked eye, intervals of ± 0.2 V were used. On increasing the potential in the positive direction, the $\lambda_{max(ox)}$ showed a progressive redshift from 582 nm (E = 0 V) to 650 nm (E = +2.6 V) and the peak intensity increased as a function of potential between these two extreme points. The PEDOT/PDDA film acquired a deep blue color in the fully oxidized state which is in stark contrast to the pale blue hue acquired by fully oxidized PEDOT doped by conventional anions like perchlorate.

Under cathodic potentials, as potential is raised from –0.4 to –2.6 V, the peak with a λ_{max} at 582 nm (at E = 0 V) loses intensity, while a new peak is seen at ~458 nm and this peak splits into two components at 429 and 459 nm, especially under high negative potentials (–1.9 V ≤ E ≤ –2.6 V), due to vibronic coupling [1]. The color of the film under negative potentials changes from blue to brown. In addition to studying the effect of PDDA on the optical switching response of PEDOT, we also examined the effect of incorporating a fullerene derivative: N-FP in the PEDOT/PDDA film (Figure 3.9c). For the PEDOT/PDDA/N-FP film, the absorption change as a function of applied potential and wavelength is akin to that shown by the PEDOT/PDDA film, but one significant advantage was realized in terms of a larger change in the overall optical modulation.
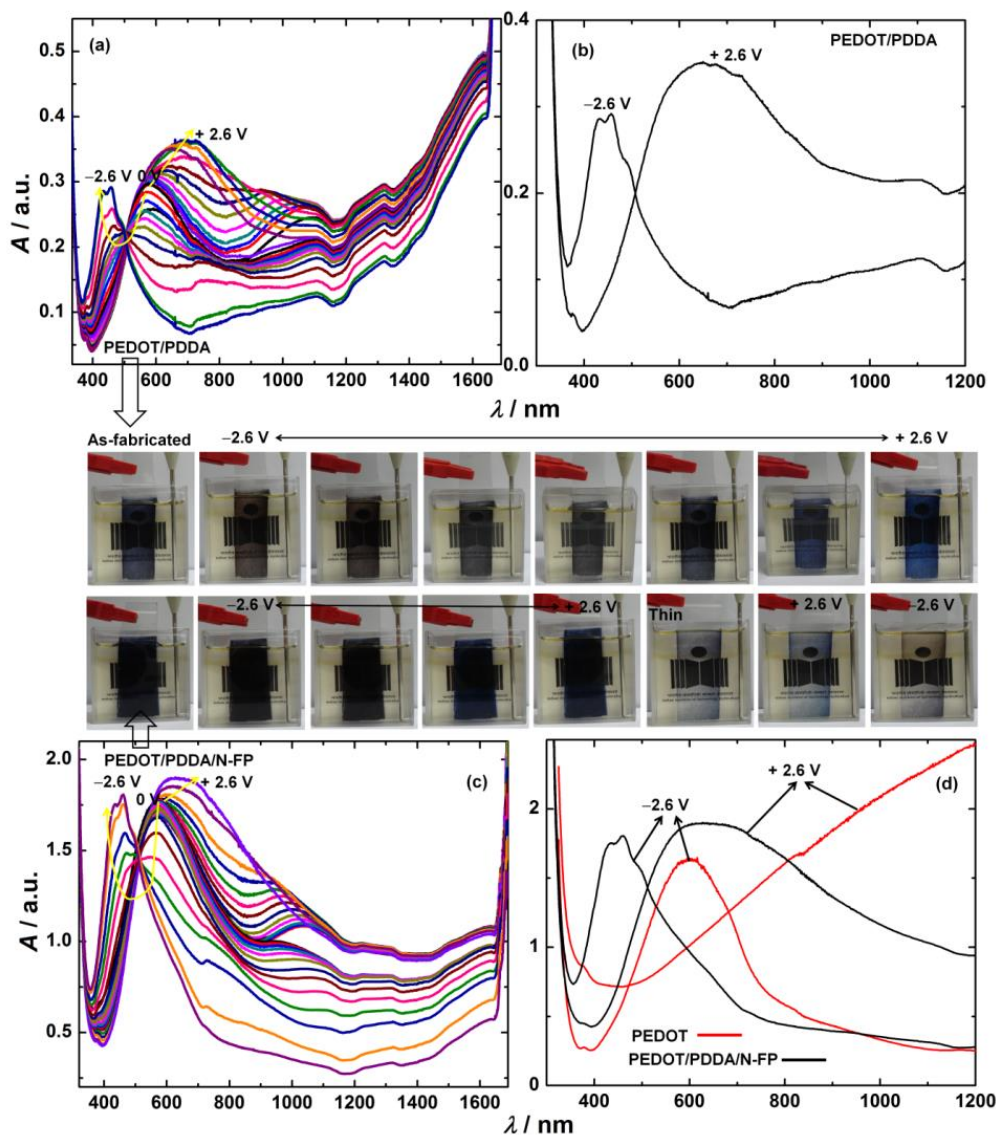
Figure 3.9 *In-situ* absorbance spectra of a (a) PEDOT/PDDA and (c) PEDOT/PDDA/N-FP films in the wavelength range of 350–1650 nm recorded under different potentials of –2.6 V to +2.6 V in steps of 0.2 V, applied for 90 s each. Absorbance spectra under –2.6 V and +2.6 V of (b) PEDOT/PDDA and (d) PEDOT/PDDA/N-FP film; (d) also shows the optical response of a conventional PEDOT film doped with camphorsulfonate ions. First row of photographs of a PEDOT/PDDA film: As-fabricated film followed by a progressive change from a fully reduced (–2.6 V) to fully oxidized (+2.6 V) state and second row of photographs: As-fabricated PEDOT/PDDA/N-FP film followed by a progressive change from a fully reduced (–2.6 V) to fully oxidized (+2.6 V) state; the last three photographs are for a thin PEDOT/PDDA film: as-fabricated, fully reduced (–2.6 V) and fully oxidized (+2.6 V) states. All measurements were performed in the ionic liquid: 1-butyl-1-methylpyrrolidinium trifluoromethanesulfonate.

51

For a given value of applied potential, the optical density change produced by a PEDOT/PDDA/N-FP film was substantially greater than that achieved for its PEDOT/PDDA counterpart. Here too, $\lambda_{max(ox)}$ showed a bathochromic shift from 564 nm (E = 0 V) to 650 nm (E = +2.6 V) as a function of increasing oxidation potential. With increasing reduction potential, this peak at 564 nm (E = 0 V) gave way to twin peaks at 429 and 459 nm, which preponderate at E = –2.6 V.

The optical density change is defined as: $\Delta OD_{max} = OD$ (λ_{max} for E_{max} in oxidized state/reduced state) – OD (λ_{max} for E_{max} in reduced state/oxidized state) for a given film, where $E_{max} = \pm 2.6$ V and $\lambda_{max(ox)}$ was fixed at ~650 nm for the PEDOT/PDDA film in the oxidized state and at 630 nm for the PEDOT/PDDA/N-FP film in the same state. In the reduced state of either of the two films, since we observed two $\lambda_{max(red)}$ peaks in the 420-460 nm wavelength range, we fixed $\lambda_{max(red)}$ at a wavelength of 460 nm, for both films. The ΔOD_{max} under an oxidation potential of +2.6 V, at a $\lambda_{max(ox)} = 630$ nm is 1.05 for the PEDOT/PDDA/N-FP film and for the same potential at a $\lambda_{max(ox)} = 650$ nm, the PEDOT/PDDA film shows a ΔOD_{max} of 0.27, which is only about 25% of the maximum absorptive contrast acquired by the film with the N-fulleropyrrolidine incorporated within. Similarly, under a reduction potential of –2.6 V, at a $\lambda_{max(red)}$ of 460 nm, the PEDOT/PDDA film was able to produce a ΔOD_{max} of 0.19, which is only 18% of the maximum contrast achieved by the PEDOT/PDDA/N-FP film ($\Delta OD_{max} = 1.07$). The large differential in the absorptive contrast between the two films also extends to the NIR region, as at a NIR wavelength of 1000 nm, a ΔOD of 0.82 was registered for the PEDOT/PDDA/N-FP film in contrast to a ΔOD of 0.15 generated by the film without the fullerene derivative.

On comparing the optical contrast of the PDDA based film with that of the PEDOT film doped by camphorsulfonate ions; the later film shows a ΔOD of 0.62 at a $\lambda_{max(red)}$ of 600 nm, and this $\lambda_{max(red)}$ is observed for conventional PEDOT film in the reduced state. In the oxidized state, the film does not show any $\lambda_{max(ox)}$ in the visible region. Even here, for the PEDOT/PDDA or PEDOT/PDDA/N-FP films, the twin $\lambda_{max(red)}$ peaks centered at 429 nm and 459 nm can be exploited for modulating visible radiation. We, therefore, have the advantage of modulating a wider portion of the visible spectrum as the film (with or without the fullerene derivative) absorbs strongly in the 580–700 nm range in the oxidized state and this absorption shifts to extreme blue (or 420–460 nm) in the reduced state. Since both these absorptions are rather pronounced, and strikingly different from what is shown by conventional PEDOT, this opens up new possibilities for preparing similar poly(ion)/conducting polymer films capable of absorbing differently from the parent polymer. Furthermore we also found that on integrating an electron conducting carbon nanostructure like N-fulleropyrrolidine with the PEDOT/PDDA film, the ensuing films show a dramatic improvement in contrast ratio. The coloration efficiency of the PEDOT/PDDA/N-FP film was

deduced to be 386 cm^2 C^{-1} (E = +2.6 V, $\lambda_{max(ox)}$ = 630 nm) and it is 113 cm^2 C^{-1} (E = +2.6 V, $\lambda_{max(ox)}$ = 650 nm) for the PEDOT/PDDA film. Likewise it was 118 cm^2 C^{-1} and 370 cm^2 C^{-1} at (E= –2.6 V, $\lambda_{max(red)}$ = 460 nm) for the PEDOT/PDDA and PEDOT/PDDA/N-FP films respectively. These values compare well with reported values of coloration efficiency for PEDOT doped by perchlorate ions or PEDOT derivatives [21,22].

To corroborate these results, the absorption behavior of PEDOT/PDDA and PEDOT/PDDA/N-FP films was also followed by dynamic measurement of absorption with varying applied potential and wavelength (Figure 3.10). The instrument takes 1 ms to scan the wavelength span of 400 – 800 nm and each spectrum therefore is a cumulative response recorded over a time span of 3 s under a fixed value of applied bias. For the PEDOT/PDDA film, the broad absorption band with a λ_{max} at ~582 nm is seen under E = +0.5 V, and it shows a slight shift to about 590 nm as E is raised to +2.6 V (Figure 3.10a). On reversing the potential polarity, i.e. at –0.5 V, the absorption peak profile acquires a flat shape in the visible region, and upon further increasing the applied bias in a stepwise manner to E = –2.6 V, the intensity of a new peak at 465 nm also increases, which concurs with the spectrophotometric results.

Here, since the mode of measurement is fiber-optic based, the noise levels are rather high, and consequently the 465 nm peak split could not be resolved. For the PEDOT/PDDA/N-FP film, the broad absorption peak with a λ_{max} poised in the range of 580-600 nm, is observed under an E = +0.5 V and the intensity of this peak does not increase much even upon increasing the potential to +1.5 V (Figure 3.10b). The absorption profile under E = +1.5 V almost retraces the curve observed under +0.5 V. On applying a cathodic bias of –0.5 V, the absorption peak downshifts, with a λ_{max} at ~469 nm, and the intensity of this peak also does not increase, even upon increasing the bias to –1.5 V. These results show that (a) the magnitude of optical density change for a given value of applied potential (E = ± 0.5 V) is much larger for the PEDOT/PDDA/N-FP film as compared to the PEDOT/PDDA film and (b) the PEDOT/PDDA/N-FP film is able to acquire the desired level of coloration with a smaller magnitude of applied potential or injected charge density in contrast to the PEDOT/PDDA film which requires a higher value of applied potential to acquire the same coloration density. It is therefore pertinent to infer that the N-methylfulleropyrrolidine derivative promotes rapid electron injection/ejection and ensures a better utilization of inserted charge, for had it been otherwise the two films would have responded in a similar manner to applied bias.
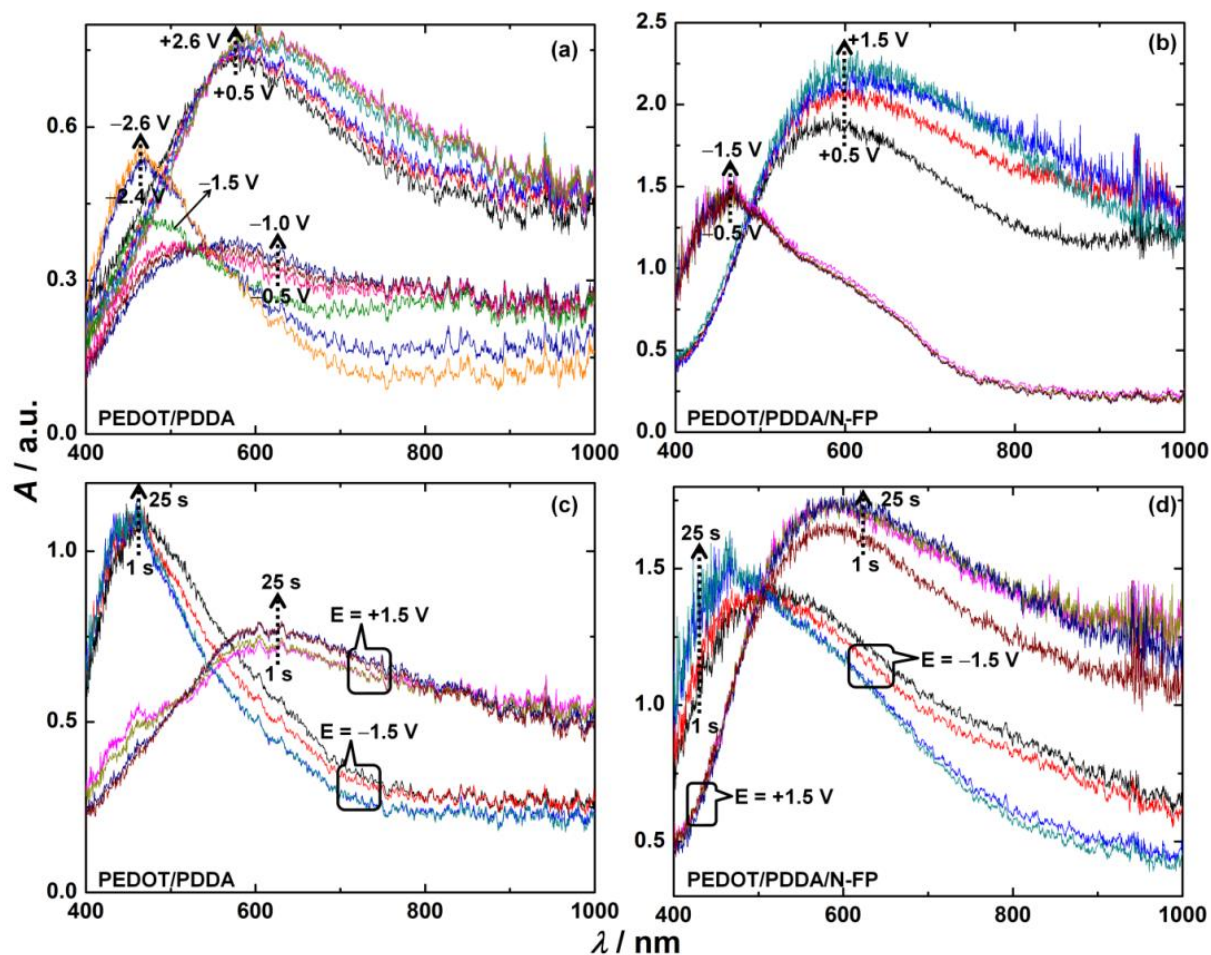
Figure 3.10 Dynamic absorbance spectra recorded in the ionic liquid: 1-butyl-1-methyl pyrrolidinium trifluoromethanesulfonate: (a) PEDOT/PDDA under +0.5, +0.8, +1.0, +1.5, +2.4 and +2.6 V (for oxidation) and –0.5, –0.8, –1.0, –1.5, –2.4 and –2.6 V (for reduction) and (b) PEDOT/PDDA/N-FP films under +0.5, +0.8, +1.0 and +1.5 V (for oxidation) and –0.5, –0.8, –1.0 and –1.5 V (for reduction); all potentials applied for a fixed duration of 3 s, (c) PEDOT/PDDA and (d) PEDOT/PDDA/N-FP films under E = ±1.5 V, each anodic/cathodic bias applied for time duration of 1, 3, 10 and 25 s.

To ratify this conjecture, the absorption variation of PEDOT/PDDA and PEDOT/PDDA/N-FP films under a fixed bias of ± 1.5 V, applied for different durations (1 s, 3 s, 10 s and 25 s) was studied. Under an oxidation potential of +1.5 V, when applied for a time span of 1 s, the PEDOT/PDDA film showed a broad λ_{max} ranging between 590-600 nm (Figure 3.10c). The λ_{max} shift was accompanied by a small increase in peak intensity, thus implying that the film is able to acquire 91 % of the total contrast within 1 s (at λ = 590 nm). Under a reduction potential of –1.5 V, the λ_{max} shifted to 465 nm. In the reduction cycle, the total contrast could be achieved in 1 s as no increase in peak intensity was attained with increasing time (at λ = 465 nm). On the contrary, on subjecting the PEDOT/PDDA/N-FP film to an E =

+1.5 V for different time spans ranging from 1 s to 25 s (Figure 3.10d), the absorption curve did not change significantly, indicating that the film acquires the maximum coloration hue within 1 s. Similarly on applying a cathodic potential of -1.5 V, the absorption peak with a λ_{max} at ~463 nm is attained within 1 s and the intensity of the peak remains unaltered even upon increasing the time period to 30 s. These results reiterate the ability of the PEDOT/PDDA/N-FP film to undergo larger optical change in response to lower values of external bias applied for shorter time spans, relative to the PEDOP/PDDA film. On the basis of these results, we propose a mechanism for formation of partially reduced PEDOT/PDDA film, involving the abstraction of a labile hydrogen radical from PDDA and regeneration of the thiophene double bond after oxidative electropolymerization and this is shown in Figure 3.11.
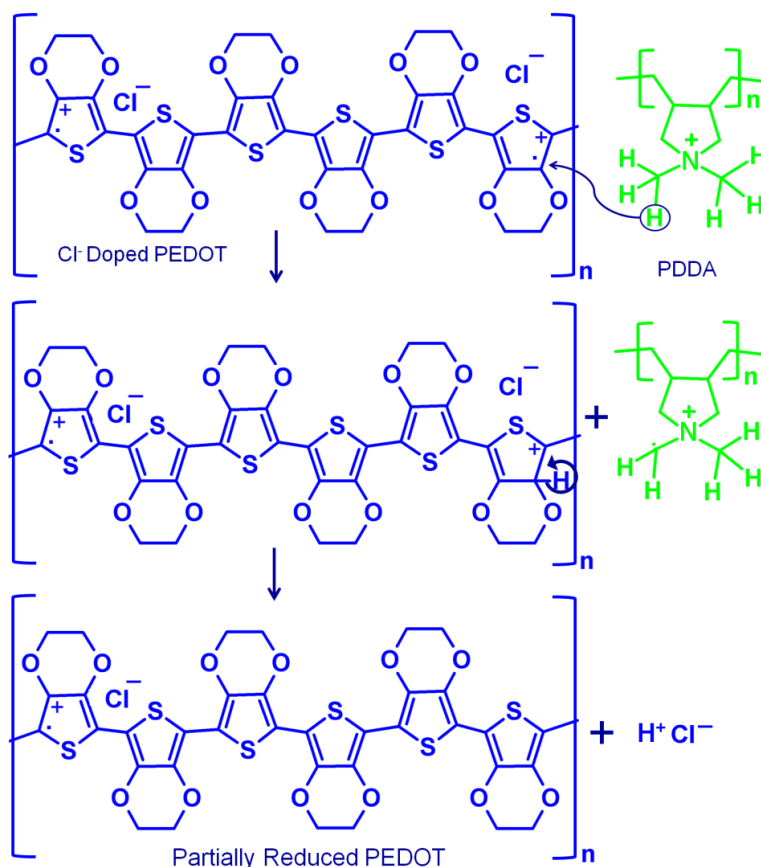
Figure 3.11 Schematic for a possible mechanism for partial reduction of PEDOT by PDDA during film formation.

The absorbance *versus* time transients for PEDOT/PDDA and PEDOT/PDDA/N-FP films recorded under a square wave dc amplitude of ± 2.5 V at a monochromatic wavelength of 460 nm, under a step time of 3 s are shown in Figure 3.12. When subjected to the same magnitude of dc potential and frequency and at $\lambda = 460$ nm, the full optical contrast attained by the PEDOT/PDDA film is only 48.5 %

of the full contrast acquired by the PEDOT/PDDA/N-FP film, again indicating that the latter is more electroactive than the former. Similarly, at λ = 630 nm, the total optical contrast attained by the PEDOT/PDDA film is only 60.5 % of the total contrast acquired by the PEDOT/PDDA/N-FP film (Figure 3.13).
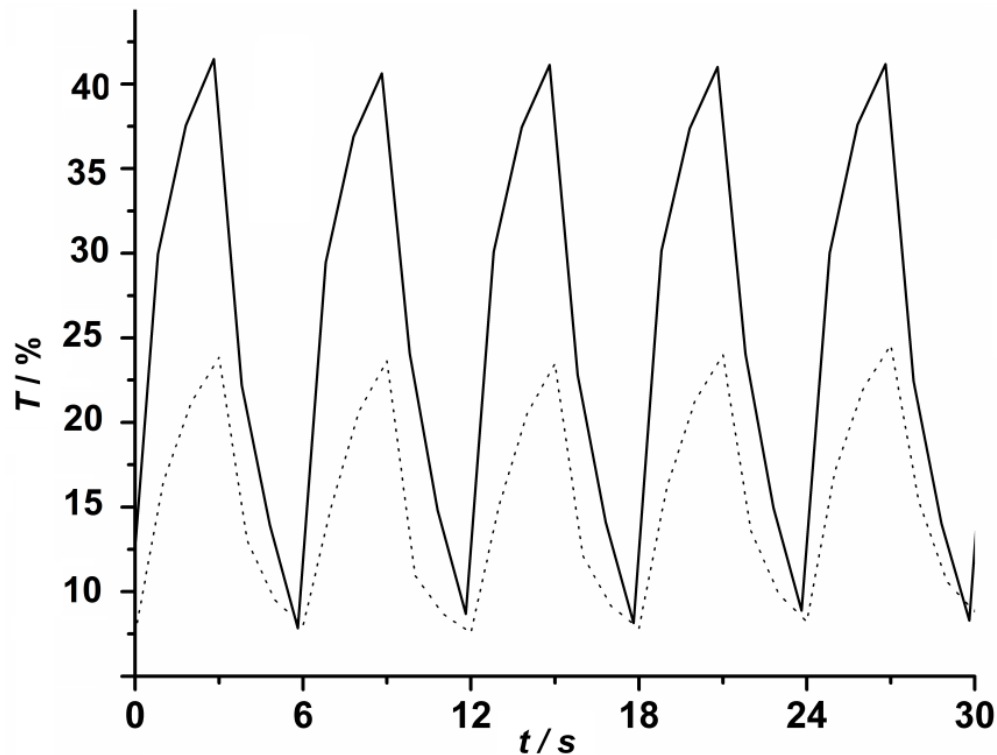
Figure 3.12 Color-bleach kinetics of PEDOT/PDDA (---) and PEDOT/PDDA/N-FP (−) films at a $\lambda_{max(red)}$ = 460 nm under a square wave pulse of ± 2.5 V with a step time of 3 s in 1-butyl-1-methylpyrrolidinium trifluoromethanesulfonate.
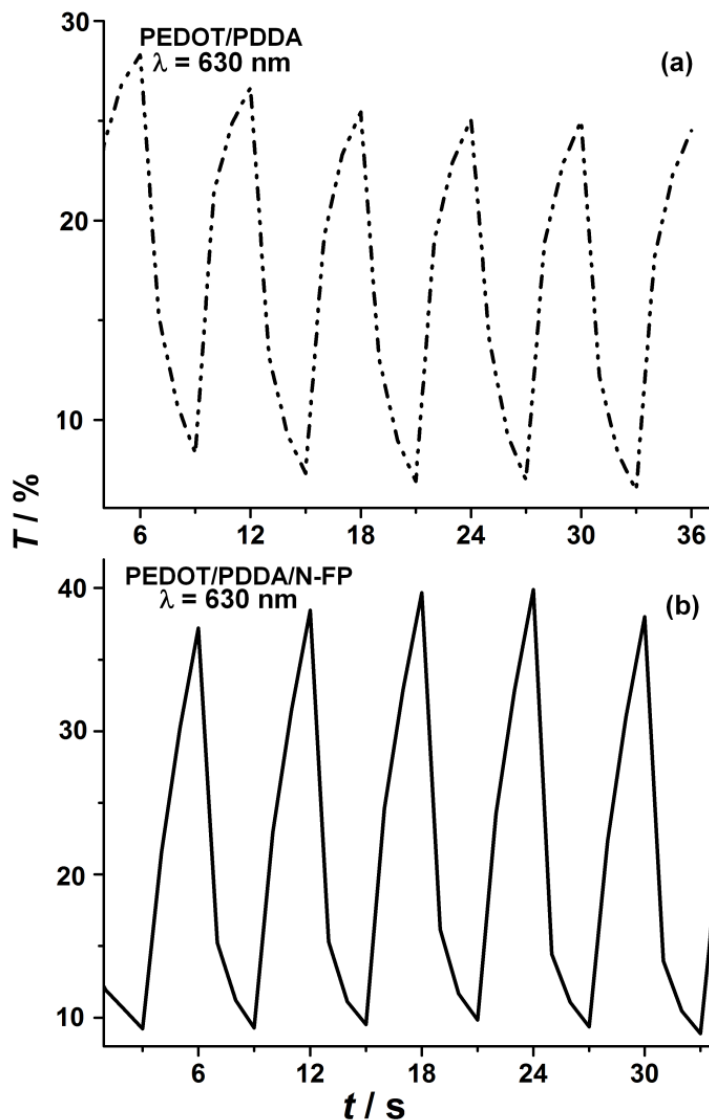
Figure 3.13 Color-bleach kinetics of (a) PEDOT/PDDA and (b)PEDOT/PDDA/N-FP films at a $\lambda_{max(ox)} =$ 630 nm; all measurements performed under a square wave pulse of $\pm$ 2.5 V with a step time of 3 s in 1-butyl-1-methyl pyrrolidinium trifluoromethanesulfonate.

3.4 Summary

Composite films of PEDOT/PDDA and PEDOT/PDDA/N-FP have been electrophoretically synthesized and contrary to the expected reversible color switching between dark blue and sky blue hues, here the films showed a transition between deep blue and bright brown colors, which was accompanied by a $\lambda_{max(ox)}$ shift from 630 nm to ~460 nm, in the reduced state, thus enabling the ability to absorptively modulate a wider span of visible range contrasting the conventional PEDOT films. Both dynamic and static *in-situ* absorption measurements provided unambiguous proofs for the ability of PEDOT/PDDA

57

film to show two coloration efficiency maxima, as the film absorbs different parts of the visible spectrum in oxidized and reduced states. By incorporating N-methyl fulleropyrrolidine in PEDOP/PDDA, the utility of the polymer is augmented as N-FP imparts high nanoscale electronic conductivity and reduces the work function of the PEDOP/PDDA, thus improving the overall optical density change, coloring efficiency and ion ingress-egress capacity during electrochemical probing. Our fortuitous but reproducible findings on PEDOT/PDDA capable of unparalleled brown and blue hues commensurate with different absorption ranges of the visible spectrum, and the stabilization of the blue hue in air, opens up new avenues for exploiting the ability of PEDOT to perform electronic, optical and redox functions differently from what is known till date in the realm of PEDOT films.

References

[1] A. Kumar, D.M. Welsh, M.C. Morvant, F. Piroux, K.A. Abboud, J.R. Reynolds, Chem. Mater. 10 (1998) 896.
[2] M.G. Han, S.H. Foulger, Small 2 (2006) 1164.
[3] S. Bhandari, M. Deepa, S.N. Sharma, A.G. Joshi, A.K. Srivastava, R. Kant, J. Phys. Chem. C 114 (2010) 14606.
[4] G. Sonmez, P. Schottland, J.R. Reynolds, Synth. Met. 155 (2005) 130.
[5] L. Groenendaal, F. Jonas, D. Freitag, H. Pielartzik, J. R. Reynolds, Adv. Mater. 12 (2000) 481.
[6] F. Jonas, L. Schrader, Synth. Met. 41 (1991) 831.
[7] H.J. Ahonen, J. Lukkari, J. Kankare, Macromolecules 33 (2000) 6787.
[8] S. Kirchmeyer, K. Reuter, J. Mater. Chem. 15 (2005) 2077.
[9] C. Qiu, Chunchang Qiu, J. Wang, S. Mao, W. Guo, S. Cheng, Y. Wang, Polym. Adv. Technol. 21 (2010) 651.
[10] R.R. Smith, A.P. Smith, J.T. Stricker, B.E. Taylor, M.F. Durstock, Macromolecules 39 (2006) 6071.
[11] G. Sonmez, Chem. Commun. 42 (2005) 5237.
[12] F. Giacalone, N. Martan, Adv. Mater. 22 (2010) 4220.
[13] T. Hasobe, P.V. Kamat, M.A. Absalom, Y. Kashiwagi, J. Sly, M.J. Crossley, K. Hosomizu, H. Imahori, S. Fukuzumi, J. Phys. Chem. B 108 (2004) 12865.
[14] H. Imahori, S. Fukuzumi, Adv. Func. Mater. 14 (2004) 525.
[15] M. Sathish, K. Miyazawa, T. Sasaki, Chem. Mater. 19 (2007) 2398.
[16] C.H. Choi, M. Kertesz, J. Phys. Chem. A 104 (2000) 102.
[17] G.P. Lopinski, J.R. Fox, J.S. Lannin, Chem. Phys. Lett. 239 (1995) 107.
[18] S. Garreau, G. Louarn, J.P. Buisson, G. Froyer, S. Lefrant, Macromolecules 32 (1999) 6807.
[19] A. Schaarschmidt, A.A. Farah, A.Aby, A.S. Helmy, J. Phys. Chem. B 113 (2009) 9352.
[20] X. Crispin, F.L.E. Jakobsson, A. Crispin, P.C.M. Grim, P. Andersson, A. Volodin, C.V. Haesendonck, M.V. derAuweraer, W.R. Salaneck, M. Berggren, Chem. Mater. 18 (2006) 4354.
[21] C.L. Gaupp, D.M. Welsh, R.D. Rauh, J.R. Reynolds, Chem. Mater. 14 (2002) 3964.
[22] J-H. Kang, Y-J. Oh, S-M. Paek, S-J. Hwang, J-H. Choy, Sol. Energy Mater. Sol. Cells 93 (2009) 2040.

Chapter 4A

Electrochromic device response controlled by an *in-situ* polymerized ionic liquid based gel electrolyte

4A.1. Introduction

In the previous chapter, we studied the electrochromism and the electrochemical behavior of films of PEDOT. For device fabrication, the electrolyte is of extreme importance and therefore in this chapter the electrolyte was optimized first and then high quality PEDOT and viologen based ECDs were fabricated. The electrolyte or the ion conducting medium is an important component of an ECD, and the use of solid polymer electrolytes aids in the formation of leakage free devices. In the past, few reports have either focused largely on the properties of polymer electrolytes or evaluated the EC response of ECDs or films, [1-4] but a combination of electrolyte properties and how it affects the darkening/bleaching phenomena in ECDs is relatively less investigated. In this chapter, polymer electrolytes were synthesized by two different approaches and applied to ECDs based on electrodeposited PEDOT films as the cathode, and a PB film as the anode. The first method involved the entrapping of an ionic liquid (IL) in a polymer host (poly(methylmethacrylate) or PMMA) and the second approach relied on the *in-situ* thermal polymerization of methylmethacrylate (MMA) monomer in the hydrophobic IL, yielding a solidified transparent gel. In the second approach, the electrolyte containing the monomer is injected into a pre-sealed ECD in the liquid state and subjected to *in-situ* thermal polymerization, to bring about the solidification of the electrolyte solution. The strategy of introducing an electrolyte to the ECD in a liquid state and then subjecting the same to gradual polymerization allows greater accessibility of the electrolyte ions to the active sites on the EC electrodes and superior interfacial contact. Despite the complexity of the comparison, owing to the multiple components of the device, our study attempts to provide an understanding of how the electrolyte incorporation method can alter the EC response of the devices. Comparison of the EC performance characteristics of the PEDOT–PB ECDs based on the *in-situ* polymerized gel electrolyte *versus* a conventional polymeric electrolyte were studied in terms of absorbance/reflectance modulation, coloration efficiency (CE), redox response and charge transport characteristics.

4A.2. Experimental

4A.2.1. Synthesis of EC films: PEDOT and PB

Dissolution of 0.1 M of EDOT, 0.1 M LiCF$_3$SO$_3$, 1.2 M camphorsulfonic acid (CSA) in 15 mL of deionized water and 10 mL of isopropanol resulted in a colorless solution. The solution was magnetically stirred for thirty minutes at room temperature. The clear sol was used for the oxidative electropolymerization of EDOT onto transparent conducting FTO coated glass substrates under potentiostatic conditions (+1.2 V), in a three electrode system with another FTO coated glass substrate as counter electrode and Ag/AgCl/KCl as reference electrode, for three minutes. Films were rinsed in methanol and stored in air. PB films were grown from a solution of 10 mM K$_3$[Fe(CN)$_6$] and 10 mM FeCl$_3$ in 0.01 N HCl in a three electrode electrochemical cell using Ag/AgCl/KCl as reference electrode by applying a fixed potential of +1.5 V for 300 s to a FTO coated glass substrate. Films were washed in a solution of 0.01 N HCl and deionized water mixed in a 2:3 volume ratio and stored in air.

4A.2.2 Synthesis of ionogel electrolytes and ECD fabrication

In the first approach, an acrylic adhesive tape (640 μm thick and 3 mm wide) was applied along the four edges of the glass on the cathodically coloring electrode (PEDOT) and the complementary electrode (PB) was then placed above this electrode and two 1 mm wide openings were grafted in the tape along one edge. Except for the two openings, the remainder of this assembly was sealed with an epoxy. MMA was passed through an activated neutral alumina column, to remove the inhibitor. To the IL: 1–butyl–1-methyl pyrrolidinium bis(trifluoromethylsulfonyl)imide, 30 wt.% of MMA was added and benzoyl peroxide (1 wt.% relative to MMA) was used as an initiator. The electrolyte was injected using a glass syringe through one of the open ports in the device, and the device was then placed vertically in an oven for *in-situ* thermal polymerization at 60−70 °C for 24−36 h. Upon polymerization of the liquid in the device, the open ports were sealed with an epoxy. In the second approach, PMMA powder was dissolved in the IL (in terms of wt.%: 20−25) by continuous stirring at 50–60 °C for 8 to 10 h till a clear homogeneous transparent gel was obtained. An open faced cavity was fabricated on the PEDOT electrode using an adhesive acrylic tape and it was filled with the gel electrolyte, and heated in the oven at 60 °C, till a bubble free electrolyte was obtained. The counter electrode (PB) was then fixed onto this electrode and the whole configuration was held in place with binder clips. The device was sealed along the entire periphery of the device using epoxy and cured at room temperature. The ECDs based on the *in-situ* polymerized gel have been designated as PEDOT−PB (MMA) and the ECDs prepared by the direct application of the polymeric gel electrolyte were named as PEDOT−PB (PMMA).

4A.2.3 Fabrication of ECDs

In an ECD, an ion conducting electrolyte separates the two EC layers, and together the layers and the electrolyte allow the transport of electrons and ions. A pyrrolidinium ion based IL was preferred as the electrolyte, as, due to its' non-aromatic character (in comparison to an imidazolium ion), the pyrrolidinium electrolyte is known to be electrochemically more stable than the imidazolium electrolyte and is therefore more suitable for EC or electrochemical devices [5,6]. In the device, one layer acts as the positive electrode (e.g. PB) and another layer (e.g. PEDOT) serves as the negative electrode. A schematic illustrating the differences in fabrication of MMA and PMMA based ECDs is shown in Figure 4A.1a and b. For fabricating the MMA based ECDs, the injection filling technique was used. Two open ports of about 2 mm each were created on the spacer strip affixed to a PB film (Figure 4A.1c) and the red adhesive tape was removed, as shown in the Figure 4A.1. The PEDOT coated glass substrate, with the electroactive layer facing inwards, was placed on the acrylic tape and allowed to cure. The MMA electrolyte in the liquid state was then injected through one of the open ports using a syringe, and then the whole device assembly was heated for *in-situ* thermal polymerization. Upon solidification of the electrolyte, the two ports were sealed with an epoxy and the ECD was ready for use.
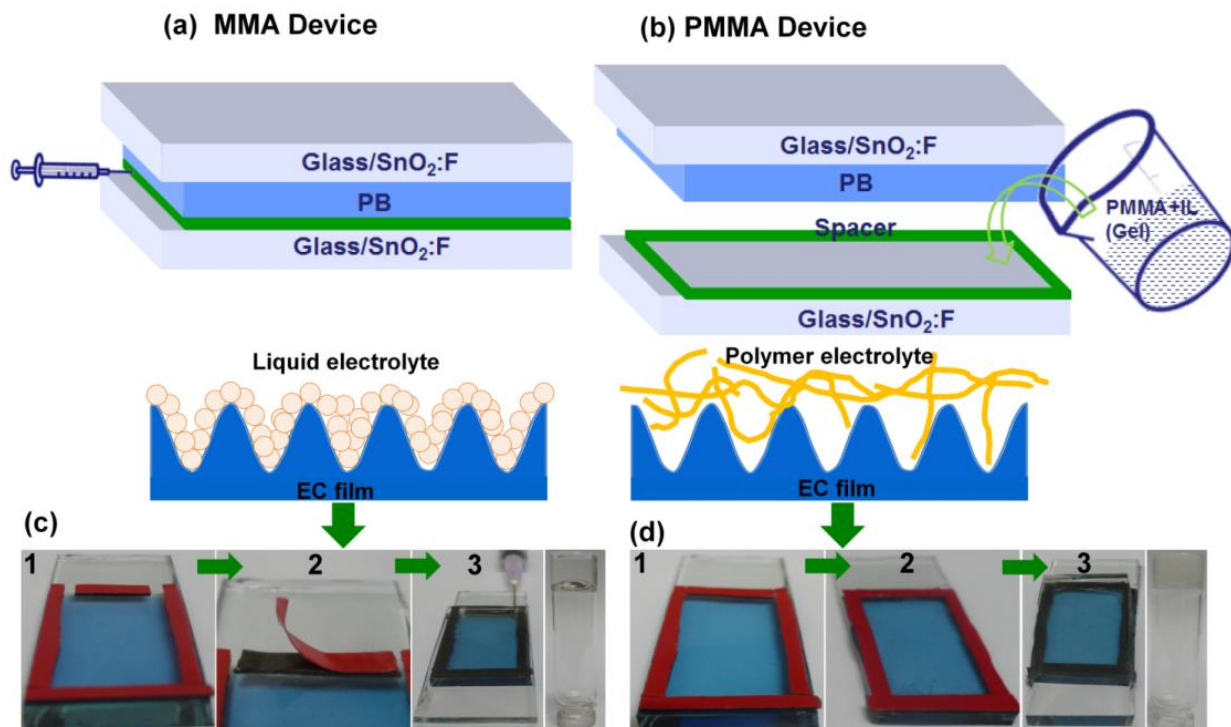
Figure 4A.1 Schematics of protocols used for ECD fabrication in (a) MMA and (b) PMMA based ECDs and the corresponding electrode/electrolyte interface in each case. The sequence of steps followed in the fabrication of (c) MMA based ECDs: (1) open ports on a PB layer with a spacer, (2) removal of adhesive

tapes and (3) fabrication of device and injection of electrolyte and (d) PMMA based ECDs: (1) creation of cavity with a spacer on a PB layer, (2) cavity filled with PMMA electrolyte and (3) removal of red adhesive tape and device fabrication. The inverted vials in (c) and (d) are photographs of MMA and PMMA electrolytes.

For synthesizing PMMA based ECDs, the spacer was applied along all four edges of the PB film without leaving any gaps (Figure 4A.1d). The PMMA based gel electrolyte was carefully filled into the cavity with a glass rod, and the assembly was heated until a bubble free electrolyte layer was obtained (Figure 4A.1d). At this juncture, the red overlying tape was removed and the complementary EC film (PEDOT) was placed on this assembly. Upon curing at room temperature, the ECDs were sealed with epoxy prior to use. Both MMA and PMMA based gels have hardly any flow properties at room temperature, as can be seen from their photographs shown in Figure 4A.1c and d. The gels do not flow even when the vials are turned upside-down.

4A.3. Results and Discussion

4A.3.1 Electrolyte characteristics

Figure 4A.2a shows the comparison of transmittance of the MMA and PMMA based electrolytes as a function of wavelength. The percent transmission of the MMA based electrolyte in a Glass/SnO_2:F/MMA electrolyte/SnO_2:F/Glass configuration is slightly less than 60% with respect to air in the reference beam in the visible region, but it is higher than that of the PMMA based ECD, in the same region. The values are possibly lower than actual due to multiple layers in both cases. Figure 4A.2b shows the cyclic voltammograms of the two electrolytes in the same configuration recorded between +3 and −3 V at a scan rate of 10 mV s^{-1}. While the MMA based electrolyte shows no peaks and is electrochemically stable approximately between ±2.5 V, the PMMA based electrolyte shows a broad peak of a small amplitude at −1.5 V, indicating some decomposition reaction. In the anodic branch, however this electrolyte is stable upto +2.5 V.
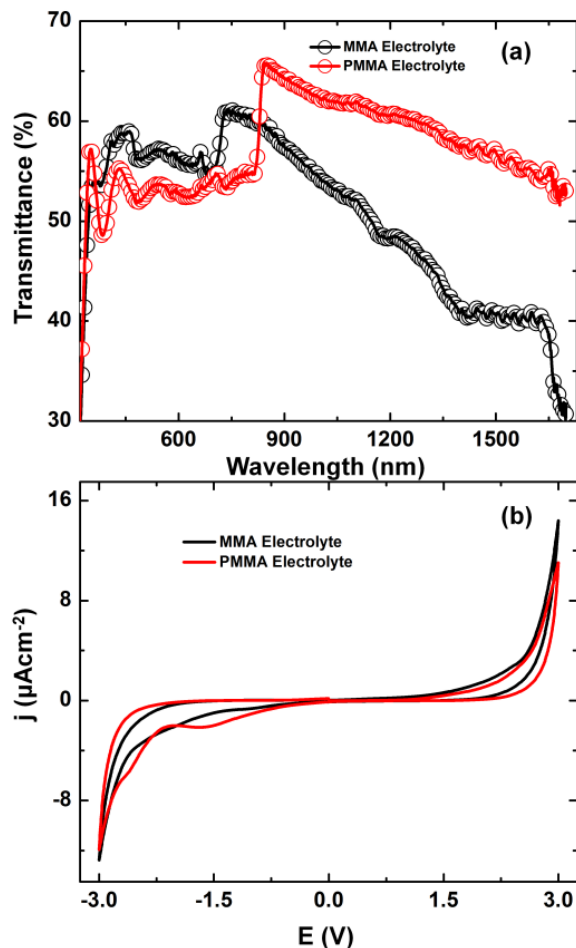
Figure 4A.2 (a) Percent transmission *versus* wavelength and (b) cyclic voltammograms of the MMA and PMMA based electrolytes in the Glass/SnO$_2$:F/Electrolyte/SnO$_2$:F/Glass configuration.

4A.3.2 Redox behavior of ECDs

Cyclic voltammograms of PEDOT−PB (MMA) and PEDOT−PB (PMMA) ECDs (with PEDOT functioning as working electrodes) recorded at scan rates of 2 and 20 mV s^{-1} are shown in Figure 4A.3 The redox response of the MMA based ECD showed a pronounced dependence on scan rate, (Figure 4A.3a), as at 2 mV s^{-1}, two distinct cathodic peaks were seen at +0.06 V (due to anion extraction) and at −0.48 V. These can be ascribed to the charged domains embedded in the matrix of an insulating film. In the reverse sweep, a broad peak at ~+0.03 V attributed to the release of positive charge and anion intercalation is seen. This is accompanied by a dark blue to pale blue color transition. For the PEDOT−PB (PMMA), (Figure 4A.3b) a voltammogram without any distinct peak was observed (at 20 mV s^{-1}) suggestive of the highly capacitive nature of PEDOT film.

$$PEDOT^{(x+\cdot)}: ((CF_3SO_2)_2N)^-_x + x\ e^- \underset{Ox}{\overset{Red}{\rightleftharpoons}} PEDOT + x\ ((CF_3SO_2)_2N^-) \quad\text{————}\quad (4A.1)$$

63
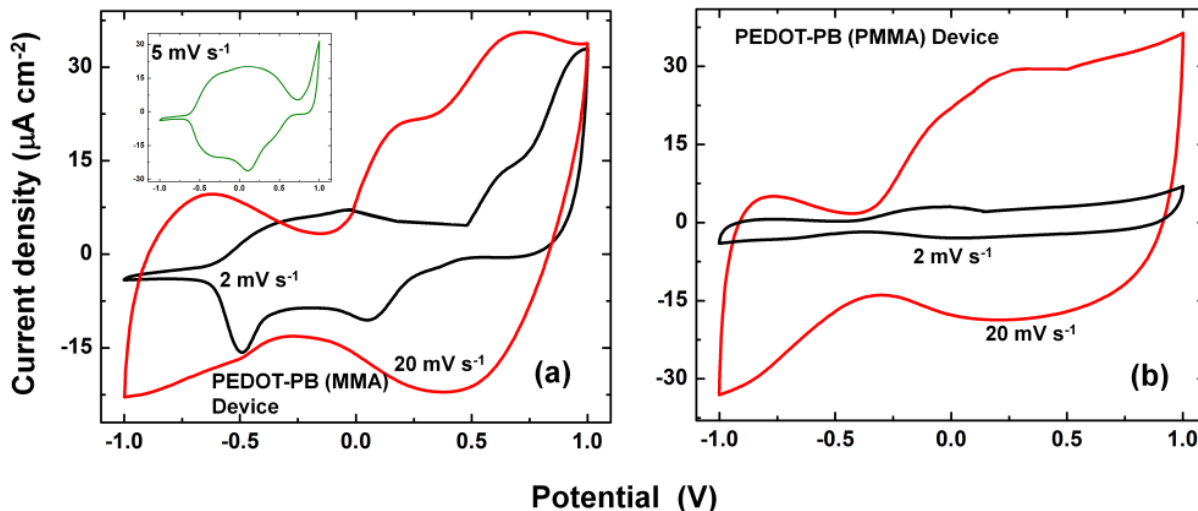
Figure 4A.3 Cyclic voltammograms of (a) PEDOT–PB (MMA) and (b) PEDOT–PB (PMMA) ECDs within ±1.0 V recorded at scan rates of 2 and 20 mV s^{-1}; inset of (a) shows a CV plot of PEDOT–PB (MMA) device measured at 5 mV s^{-1}.

4A.3.3 Spectral response of PEDOT–PB ECDs

4A.3.3.1 *In-situ* absorption studies for the MMA and PMMA based ECDs

The absorbance variation and CE plots as a function of wavelength and applied potential for PEDOT–PB (MMA) and PEDOT–PB (PMMA) ECDs are shown in Figures 4A.4 and 4A.5. The *in-situ* absorbance spectra of PEDOT–PB (MMA) ECD measured under different oxidation potentials (applied to PEDOT) of +0.5 to +1.5 V (in steps of 0.5 V) and reduction potentials of –0.5 V to –2.9 V, in steps of 0.2 V and from –3.0 to –3.4 V, in steps of 0.1 V are shown in Figure 4A.4a. All ΔOD_{max} for the devices were determined from the difference between fully colored and bleached states. The PEDOT–PB (MMA) device remains slightly blue even in the bleached state (Figure 4A.4b) due to the highly absorptive nature of oxidized PEDOT in the visible region. All ΔOD_{max} for the ECDs were determined from the difference between fully colored and bleached states. A maximum absorbance change of 0.65 was registered for the MMA based ECD at a λ_{max} of 600 nm (Figure 4A.4a). The broad absorption in the NIR region in the oxidized form of PEDOT is due to the bipolaronic transitions which, loses intensity at the expense of π-π* transition peak (at 600 nm) with increasing reduction potential. Photographs of the PEDOT–PB (MMA) device of ~4 cm × 5 cm dimensions in dark blue, and transparent states are shown in Figure 4A.4b.
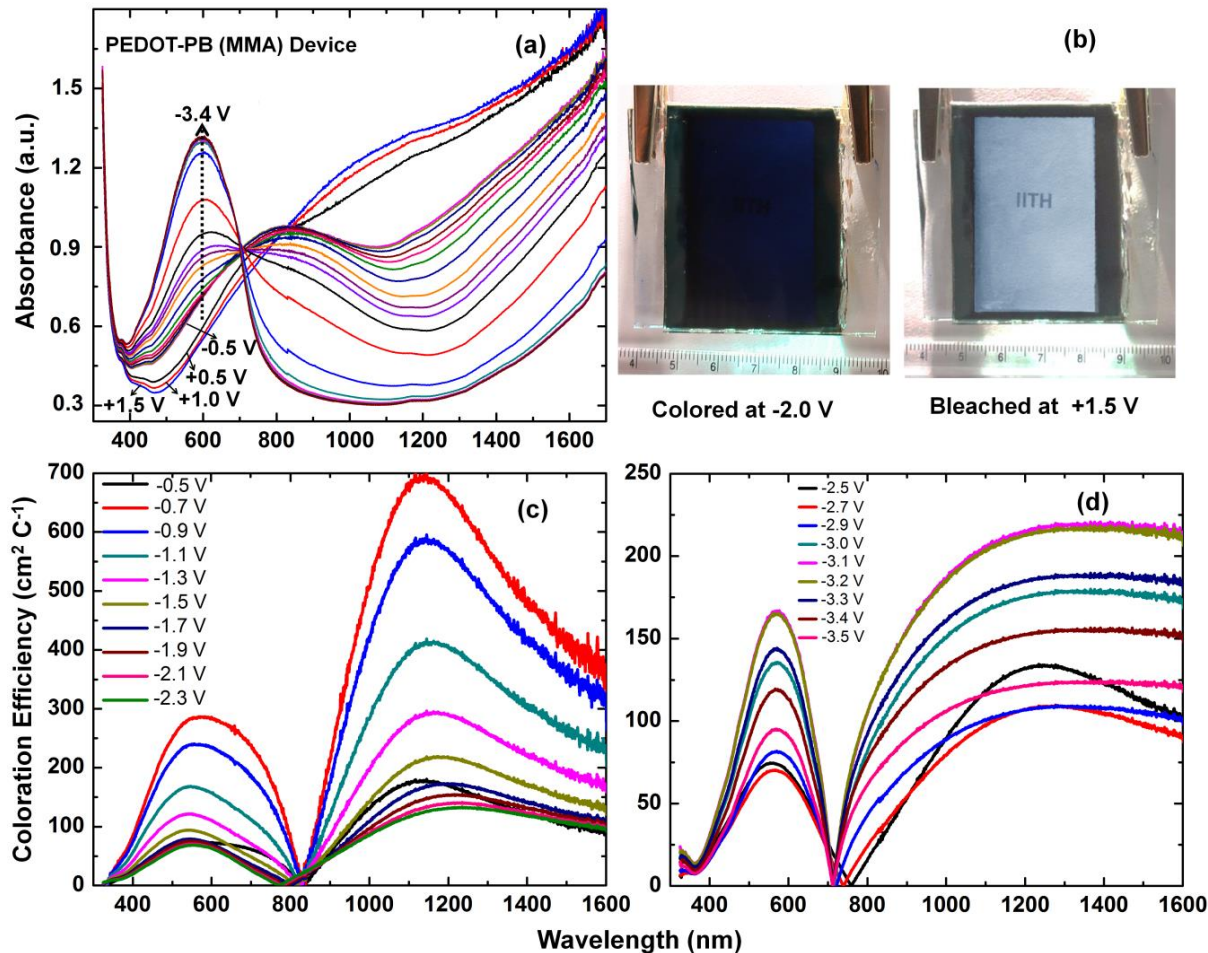
Figure 4A.4 (a) *In-situ* absorbance spectra of a (a) PEDOT−PB (MMA) ECDs in the wavelength range of 350−1700 nm recorded under oxidation potentials of +0.5, +1.0 and +1.5 V and under reduction potentials of −0.5 V to −2.9 V, in steps of 0.2 V and from −3.0 to −3.4 V, in steps of 0.1 V, applied for 90 s each. (b) Photographs of a PEDOT−PB (MMA) ECD in colored and bleached states, CE plots of PEDOT−PB (MMA) ECD as a function of wavelength for reduction potentials between (c) −0.5 and −2.3 V and (d) −2.5 and −3.5 V; the optical state under +1.5 V in (a) was chosen as reference.

A similar trend for OD variation was observed for the PEDOT−PB (PMMA) device. A ΔOD_{max} of 0.45 (with +1.5 V as the reference potential) was achieved at λ_{max} of 610 nm (Figure 4A.5). The PEDOT−PB ECDs also retained a large optical change in the NIR region. CE plots for the PEDOT−PB (MMA) device as a function of wavelength and at different reduction potentials are shown in Figure 4A.5b. The reference potential was chosen as +1.5 V for the calculations. A CE maximum of 287 cm^2 C^{-1} was registered for this device at a λ_{max} of 567 nm, under a fairly low reduction potential of −0.7 V which, is most beneficial for maximizing the operation lifetime of the device. Under the same potential, at 550 nm, the CE was 283 cm^2 C^{-1} and at 633 nm, the CE was 274 cm^2 C^{-1}, clearly demonstrating the applicability of this device to

65

EC applications, which do not require a colorless bleached state. A second CE_{max} of 706 cm^2 C^{-1} at 1145 nm was also registered at the same potential of –0.7 V. The second highest CE was observed under a potential of –0.9 V; it was 240 cm^2 C^{-1} at 567 nm, and at all other potentials the CE was lower than what was achieved under –0.7 V. The lowest CE_{max} was observed under a potential of –2.3 V; it was 68 cm^2 C^{-1} at a λ_{max} of 560 nm. CE does not follow a systematic trend of decreasing values as a function of potential, owing to the varying (i) spectral changes and (ii) charge with potential. For a poly(propylenedioxythiophene)-(Et)$_2$/PB device, an unusually high CE of 1214 cm^2 C^{-1} was obtained [7]. For a PEDOT/In$_2$O$_3$:Sn/PET film, a CE of 124 cm^2 C^{-1} and a ΔOD of ~0.26 was observed at 540 nm [8]. However, in both these reports, the values were achieved in a liquid electrolyte: LiClO$_4$/PC. In another report, for a PEDOT/Gel/PB device, prepared using PET substrates, with a gel containing Li(CF$_3$SO$_2$)$_2$N, 1-butyl-3-methyl imidazolium imide and PMMA, a CE of 335 cm^2 C^{-1} (640 nm) was attained and a ΔOD of ~0.77 was observed [9]. The CE plot for the PEDOT–PB (PMMA) device in Figure 4A.5b shows this device to have a CE_{max} of 267 cm^2 C^{-1} at ~695 nm (under E = –1.5 V). Under the same bias at 600 nm, the CE was 176 cm^2 C^{-1} and at 550 nm, the CE was 108 cm^2 C^{-1}. CE values were lower at other potentials. It is obvious that the PMMA based device requires a higher potential (E = –1.5 V) to acquire a CE_{max}, whereas an external bias of only –0.7 V, was sufficient for reaching a higher value of CE_{max} in its MMA counterpart. A lesser amount of charge suffices to generate a greater EC efficiency in the MMA based devicewhich, is beneficial for prolonging the functional lifetime of the device.
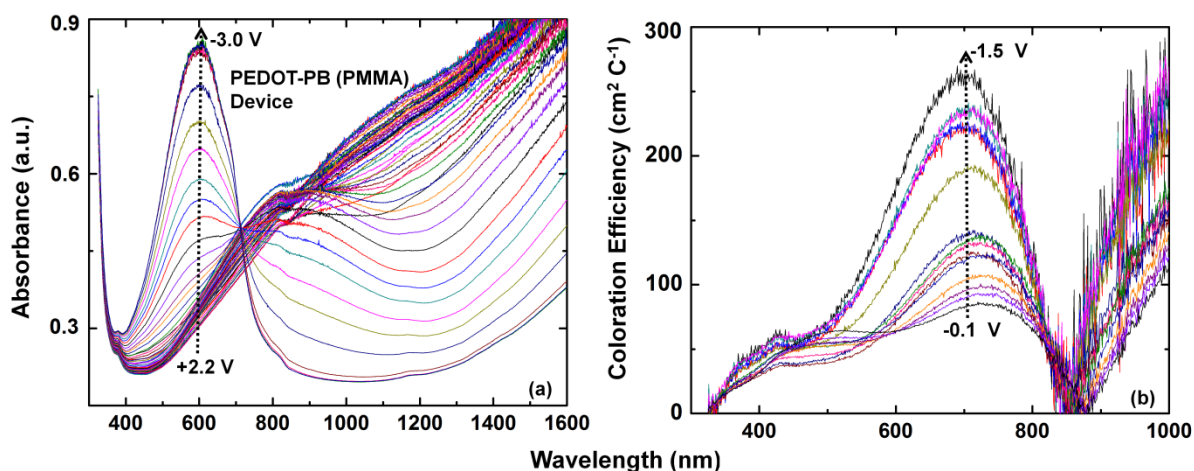
Figure 4A.5 (a) *In-situ* absorbance spectra of a (a) PEDOT–PB (PMMA) device recorded under potentials of +2.2 V to –3.0 V, in steps of 0.1 V, applied for 90 s each and (b) CE of a PEDOT–PB (PMMA) device as a function of wavelength for reduction potentials between –0.1 and –1.5 V; the optical state under +1.5 V in (a) was chosen as reference.

4A.3.3.2 *In-situ* **specular reflectance studies for the MMA and PMMA based ECDs**

The specular reflectance variation as a function of wavelength in the visible region of the ECDs was measured under oxidation potentials of +1.0, +2.0 and +2.5 V and under reduction potentials of −1.0 to −3.5 V. The PEDOT−PB (PMMA) device showed extremely small changes in reflectance with potential, (Figure 4A.6b), due to a low transparency even in the oxidized state. ΔR showed very little change as a function of wavelength in the visible region for this device. A ΔR value of 21.1% at a λ_{max} of 550 nm was registered for the PEDOT−PB (MMA) device (Figure 4A.6a). Although the magnitude of reflectance modulation is lower than the corresponding absorptive modulation of these ECDs, nevertheless this ΔR value is reasonably high for their application to reflective ECDs. Again, ΔR at λ_{max} was larger for the MMA based ECDs as compared to the PMMA based devices. The superiority of electrolyte filling by injection and *in-situ* thermal polymerization method is obvious. Our values are comparable to values reported in literature for ECDs of smaller dimensions. In the past, for a PEDOT based device, a reflectance contrast of 40% was achieved at a photopic wavelength of 573 nm [10].
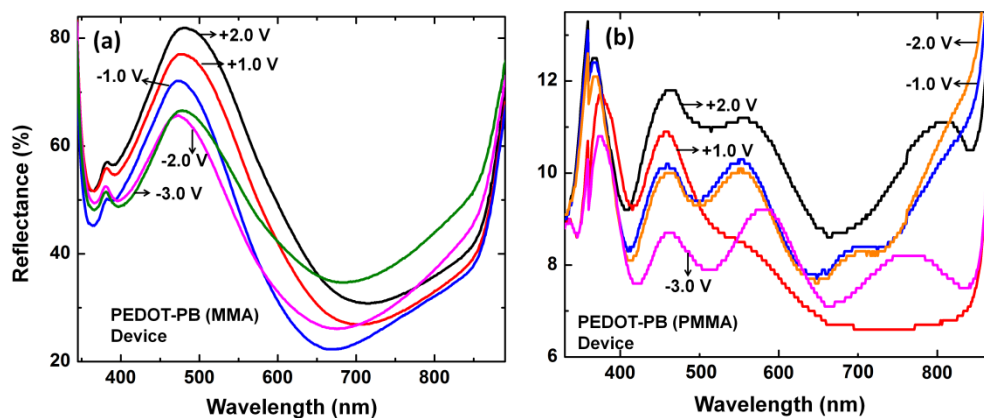
Figure 4A.6 *In-situ* specular reflectance of (a) PEDOT−PB (MMA) and (b) PEDOT−PB (PMMA) ECDs *versus* wavelength recorded with respect to a standard mirror/control device assembly under different dc potentials in the range of +2.5 V to –3.5 V.

4A.3.3.3 Switching kinetics

Coloration-bleaching characteristics of PEDOT−PB (MMA) ECDs recorded at monochromatic wavelengths (λ_{max}) of 585 and 685 nm, with 3 and 5 s as step times, under a square wave potential of ± 2.0 V, are shown in Figure 4A.7a and b. Under a step time of 3 s (Figure 4A.7a) a coloration time of 2.0 s and a bleaching time of 2.2 s was observed for the PEDOT−PB (MMA) ECD. Coloration kinetics is faster than bleaching for the PEDOT based device. In the PEDOT based ECDs, it is the anion insertion and extraction from the polymer film which, controls switching rates. Coloration of PEDOT is accompanied by the transition from the conducting doped state to the neutral state, the ease of electron injection into the

matrix of a not yet insulating film promotes faster color kinetics. The PMMA based ECDs showed slower kinetics and a smaller magnitude of optical density change (Figure 4A.7c) for the same values of applied potential as used for the MMA based ECDs. While MMA and PMMA based ECDs show comparable response times, MMA device acquires a more saturated hue than PMMA device for the same step time. For the PEDOT−PB (PMMA) device coloration and bleaching times are 3.5 and 2.6 s respectively.
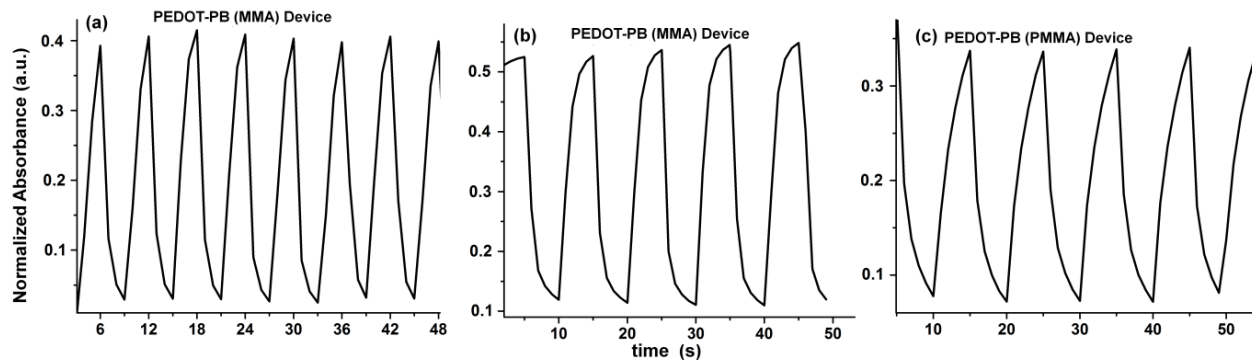
Figure 4A.7 Color-bleach kinetics of a PEDOT−PB (MMA) device recorded at a λ_{max} of 585 nm with step times of (a) 3 s and (b) 5 s. Color-bleach kinetics of a (c) PEDOT−PB (PMMA) (λ_{max} = 585 nm) ECD recorded under a step time of 5 s and under a square wave potential of ±2V.

To further confirm that absorbance in the visible region indeed changes rapidly in PEDOT film, the dynamic change in absorbance was measured during redox switching. The films were subjected to an oxidation potential of +1.0 V for 3 s and the dynamic absorbance, wherein the instrument scans 300−1000 nm wavelength range within 1 ms was measured. In a similar manner, dynamic spectral responses of the same film were recorded under a reduction potential of −1.0 V for durations of 10, 15, 20, 25 and 30 s (Figure 4A.8). The film acquires a saturated blue color within 25 s, as the dynamic response measured for a 30 s duration re-traces the curve obtained in the 25 s cycle. From the curves it is obvious, that the film acquires ~69% of the total absorption change that it is capable of attaining, within 5 s. This is a clear indicator of the fact that film shows fast kinetics. Bleaching is also fast, as the peak due to π-π* absorption vanishes in a span of 3 s.
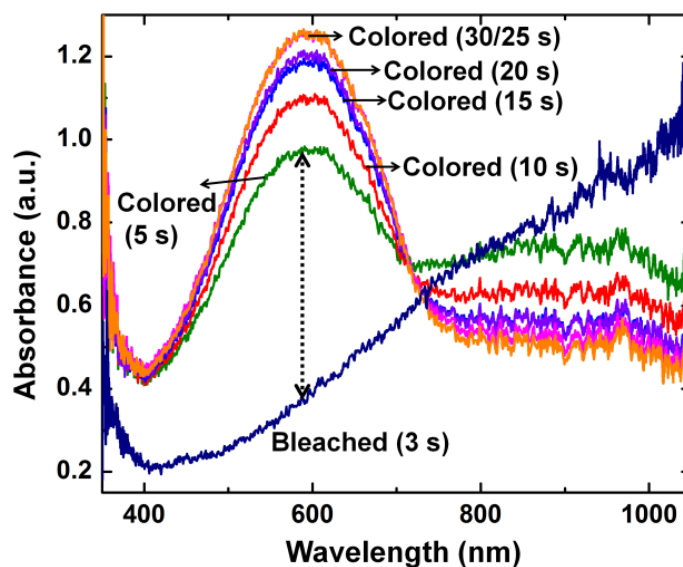
Figure 4A.8 Dynamic absorbance spectrum of a PEDOT film, recorded in a liquid electrolyte, wherein the wavelength range of ~400 to 800 nm is swept within 1 ms, under dc potentials of +1.0 V (for bleaching) and −1.0 V (for coloration).

4A.3.4 Electrochemical impedance spectroscopy

Nyquist plots of PEDOT−PB (MMA) and PEDOT−PB (MMA) ECDs are shown in Figure 4A.9 and Bode plots are shown in the corresponding insets. The equivalent circuit displayed in Figure 4A.9a was found to give excellent fits for all Z'' *versus* Z' curves and the fitted/calculated parameters are summarized in Table 4A.1. The PEDOT−PB (MMA) ECD shows an arc in the high frequency region, whereas only a slight curvature is observed for the PEDOT−PB (PMMA) ECD. As can be seen from the Bode plots, the magnitude of impedance ($|Z|$) is larger for the MMA based ECDs, in comparison to the PMMA based ECDs. Ionic conductivities of the two electrolytes were determined from the impedance plots and for the MMA based gel, it is 1.6×10^{-4} S cm^{-1}. The PMMA based gel shows an ionic conductivity of 4.2×10^{-5} S cm^{-1}. In the past, a poly(ethyl methacrylate)-LiClO$_4$/PC based electrolyte, showed a room temperature ionic conductivity of 6.9×10^{-4} S cm^{-1} [11], and a dried polyelectrolyte film of poly(ethylene imine)/poly(acrylic acid)/LiCF$_3$SO$_3$, prepared by layer-by-layer assembly method was characterized by an ionic conductivity greater than 10^{-5} S cm^{-1} at ambient temperature [12]. The charge transfer resistances (R_{CT}) for the MMA based ECDs are smaller in magnitude as compared to the PMMA based ECDs (Table 4A.1). It is apparent that the MMA based electrolyte forms a more intimate contact with the electrode (PEDOT) surface as it is introduced in the ECD in a liquid state in contrast to the PMMA based electrolyte which, is incorporated in a semi-solid state and therefore does not attach to the electrode as effectively as the MMA electrolyte does. This inference is also supported by the fact that both exchange current density and diffusional pseudocapacitance (the measure of charging in the bulk of

the film in the low frequency region) have larger values for the MMA based ECDs in contrast to the PMMA based ECDs (Table 4A.1).
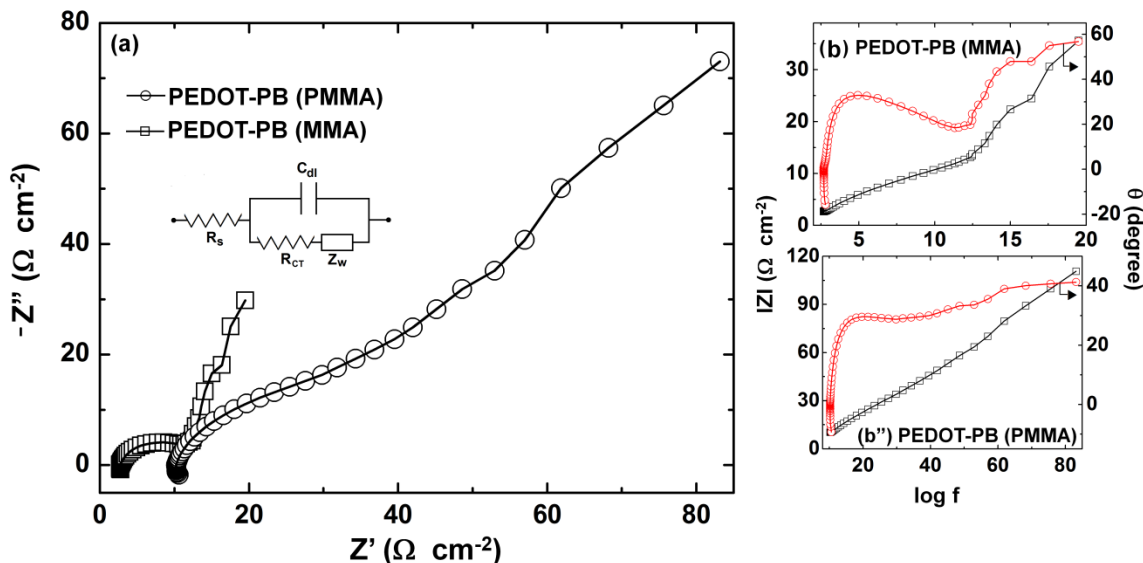
Figure 4A.9 Nyquist plots of (a) PEDOT−PB (MMA) (□) and PEDOT−PB (PMMA) (O) ECDs recorded under an ac amplitude of 10 mV; (b) the corresponding Bode plots (□) |Z| *versus* log (frequency) and (O) θ *versus* log (frequency). Symbols represent the experimental data and the solid lines (—) are obtained by fitting the experimental data in the model shown in (a).

Table 4A.1: Electrochemical impedance spectroscopy results for PEDOT as working electrodes, obtained by fitting the experimental data in the model shown in Figure 4A.9a.

Device	R_{CT} (Ω cm^{-2})	C_{dl} (F cm^{-2})	C_D (F cm^{-2})	j_o (mA cm^{-2})
PEDOT−PB (MMA)	11.5	0.013	0.13	2.2
PEDOT−PB (PMMA)	32.0	0.005	0.009	0.4

4A.4 Summary

Two methods were used for synthesizing and applying polymer electrolytes to ECDs of PEDOT−PB. In the first approach, a homogeneous transparent gel formed by the immobilization of PMMA in an IL was applied to the devices whereas in the second method, direct *in-situ* thermal polymerization of the monomer in the devices was performed after injecting the MMA-IL solution in the devices. The *in-situ* polymerized gel, by the virtue of being introduced into the device in a liquid state, allows the formation of better interfacial contacts which, reduces the charge transfer resistance and thus enables faster intercalation-deintercalation reactions at the EC electrode. It also allows a greater number of electrolyte ions to access the redox active sites in the EC films which results in a high contrast. ECDs prepared by the direct incorporation of the gel electrolyte, do not have either of the above mentioned two advantages

and therefore the EC performance is adversely affected. The i*n-situ* based ionogel is found to be superior to conventional gel for a PEDOT based ECD.

References

[1] C.A. Nguyen, S. Xiong, J. Ma, X. Lu, P.S. Lee, J. Phys. Chem. B 113 (2009) 8006.
[2] J. Reiter, O. Krejza, M. Sedlarkova, Sol. Energy Mater. Sol. Cells 93 (2009) 249.
[3] E.D.C. Rios, A.V. Rosario, A.F. Nogueira, L. Micaroni, Sol. Energy Mater. Sol. Cells 94 (2010) 1338.
[4] C.A. Nguyen, A.A. Argun, P.T. Hammond, X. Lu, P.S. Lee, Chem. Mater. 23 (2011) 2142.
[5] M. Dobbelin, I. Azcune, M. Bedu, A.R. de Luzuriaga, A. Genua, V. Jovanovski, G. Cabanero, I. Odriozola, Chem. Mater. 24 (2012) 1583.
[6] T. Sato, G. Masuda, K. Takagi, Electrochim. Acta 49 (2004) 3603.
[7] K.-C. Chen, C.-Y. Hsu, C.-W. Hu, K.-C. Ho, Sol. Energy Mater. Sol. Cells 95 (2011) 2238.
[8] R.M. Osuna, V. Hernandez, J.T. L. Navarrete, E.I. Kauppinen, V. Ruiz, J. Phys. Chem. Lett. 1 (2010) 11367.
[9] S. Duluard, A.C. -Cochet, I. Saadeddin, A. Labouret, G. Campet, G. Schottner, U. Posset, M.-H. Delville, New J. Chem. 35 (2011) 2314.
[10] P.-H. Aubert, A.A. Argun, A. Cirpan, D.B. Tanner, J.R. Reynolds, Chem. Mater. 16 (2004) 2386.
[11] J. Reiter, O. Krejza, M. Sedlarkova, Sol. Energy Mater. Sol. Cells 93 (2009) 249.
[12] C.A. Nguyen, A.A. Argun, P.T. Hammond, X. Lu, P.S. Lee, Chem. Mater. 23 (2011) 2142.

Chapter 4B

Development of fast switching electrochromic devices using *in-situ* polymerization

4B.1 Introduction

In the recent times, ECRA mirrors, which is a mirror in automobiles and other vehicles designed to allow the driver to see rearward through the vehicle's backlight (rear windshield or windscreen), are currently being used for the safety driving in the night time [1-5]. Viologen based materials are used for the commercial ECRA mirror applications [6-9]. Since, in this thesis, both PEDOT and viologens were synthesized, the applicability of the *in-situ* ionogel was extended to viologen based ECDs. The same strategy of *in-situ* ionogel fabrication was applied to heptyl viologen (HV) based ECDs with PB as a counter electrode. Large area HV−PB (~8 cm × 6 cm) ECDs were fabricated. Their ability to color and bleach uniformly and reversibly was demonstrated.

4B.2 Experimental

4B.2.1 Synthesis of HV

4,4′-bipyridine (0.025 mol) and n-heptyl bromide were refluxed in 50 mL of acetonitrile for 24 h at 75−80 °C. The resulting turbid yellow solution was filtered and cooled in an ice-bath, and yellow crystals of heptyl viologen bromide were formed after recrystallization from an acetone-methanol solvent mixture.

4B.2.2 Synthesis of solid polymeric electrolyte and ECD fabrication

Methylmethacrylate (MMA) monomer in an ionic liquid (IL): 1-butyl-1-methyl pyrrolidinium bis(trifluoromethylsulfonyl)imide was used as a polymerization solvent. Prior to polymerization, the monomer was made inhibitor free by passing through an activated alumina column. The MMA monomer was taken as 25−30% by volume of the polymerizing solvent and benzoyl peroxide (1% based on MMA) was used as an initiator. 0.01 M HV and the monomer were then mixed with the IL. The electrolyte was filled by injection filled technique, where the electrolyte was injected into the cavity through the port with the help of a syringe and was then set for *in-situ* polymerization at 60 °C for 20−24 h. For this type of filing technique, the empty cell included more than one port, one for filling and another for venting air as the cell is filled. The ports were sealed with an epoxy based sealant, which cured at room temperature. The device is hereafter referred to as the HV−PB ECD.

4B.3 Results and discussion

4B.3.1 Cyclic voltammetric studies of HV−PB ECD

   The cyclic voltammogram of the HV−PB ECD was recorded within the potential limits between −1.5 to +0.2 V at a scan rate of 10 mV s^{-1} and is shown in Figure 4B.1. In the cathodic branch, the first reduction peak was observed at −0.82 V, and it is assigned to the formation of the dark blue radical cation salt on the FTO surface, which is followed by the oxidation to the di-cation and its' dissolution in the electrolyte at −0.71 V in the reverse sweep. We observed a second reduction peak at −1.34 V. These two peaks correspond to the monovalent radical cation formation followed by formation of the neutral viologen, upon further increasing the reduction potential. In the anodic branch, the first oxidation peak at −1.25 V corresponds to the radical cation formation and the second peak at −0.73 V is attributed to the di-cation formation.
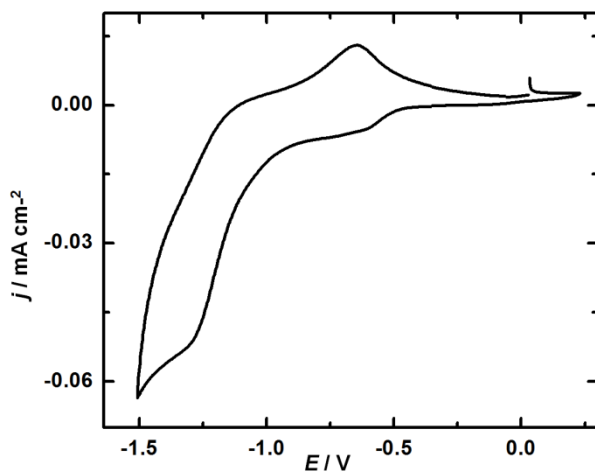
Figure 4B.1 Cyclic voltammogram of the HV−PB ECD recorded between potential limits of −1.5 and +0.2 V at a scan rate of 10 mV s^{-1}.

4B.3.2 *In-situ* transmittance spectra of HV−PB ECDs

   The *in-situ* transmittance spectra of the HV−PB ECD under different applied potentials in the wavelength range of 300 to 1700 nm are shown in Figure 4B.2a and the transmission modulation (ΔT) plot in the visible range is shown in Figure 4B.2c. The ECD shows a maximum transmission modulation of 50.5% at 550 nm (green, the wavelength at which human eye is most responsive), and a ΔT of 54% at λ_{max} of 603 nm, under a reduction potential of −2.9 V and an oxidation potential of +1.0 V; these values are acceptable for ECRA mirror applications.
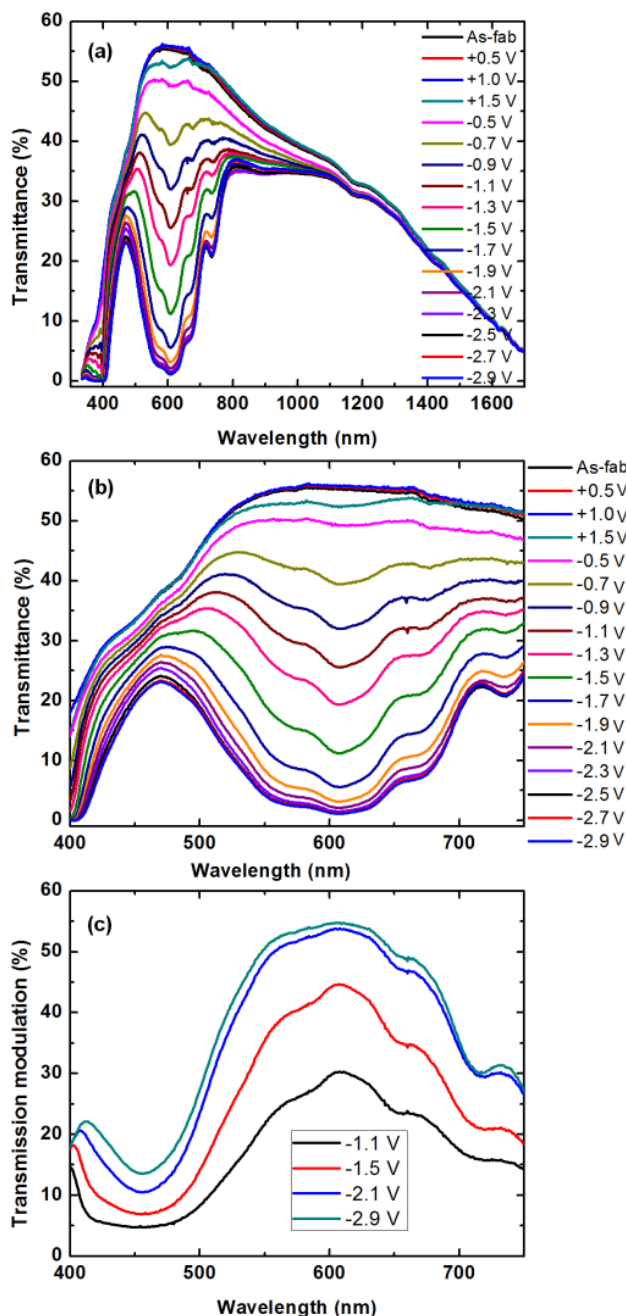
Figure 4B.2 (a) Transmittance spectra of the HV−PB ECD recorded under different potentials and (b) enlarged view of the transmittance change in the visible region, and (c) transmission modulation *versus* wavelength (reference oxidation potential : +1.0 V).

Coloration efficiencies (CE) of the HV−PB ECD were obtained (using equation 2.3) at 550 nm, 633 nm and at a λ_{max} of 603 nm. The values are given in Table 4B.1. In the past, a CE of 196 cm^2 C^{-1} was obtained for a 1 cm^2 viologen-ZnO based device [10]. In yet another report, CE values of 270 and 197 cm^2 C^{-1} were obtained at 450 and 650 nm respectively [11].

74

Wavelength	CE (-1.1 V) ($cm^2 C^{-1}$)	CE (-1.5 V) ($cm^2 C^{-1}$)	CE (-2.1 V) ($cm^2 C^{-1}$)	CE (-2.9 V) ($cm^2 C^{-1}$)
550 nm	73.06	113.10	206.49	223.11
633 nm	99.00	146.15	258.87	274.57
603 nm	111.48	172.29	312.25	334.62

Photographs of the HV–PB ECDs of dimensions (~8cm × 6 cm) under coloration (deep blue, −2.0 V) and bleached (transparent, +1.5 V) states are shown below in Figure 4B.3.
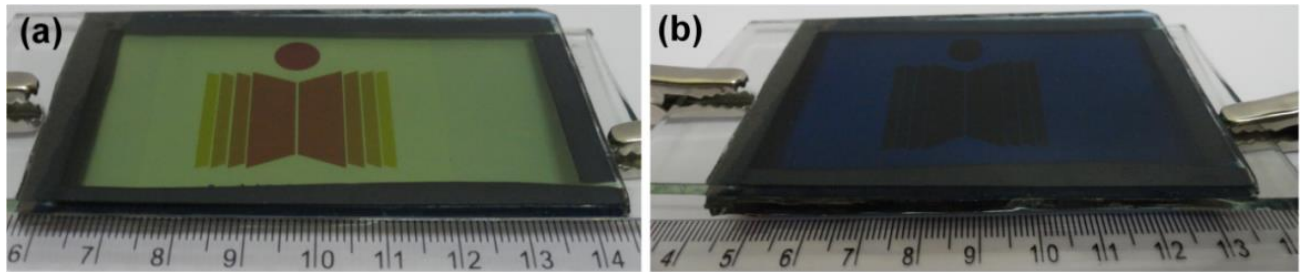
Figure 4B.3 (a) Prototype HV–PB ECDs colored by the application of −2.0 V and bleached by the application of +1.5 V to the cathode.

4B.3.3 Reflectance studies for HV–PB ECD

The *in-situ* reflectance spectra of ECDs were recorded in specular reflectance mode, at different potentials and these are shown in Figure 4B.4.
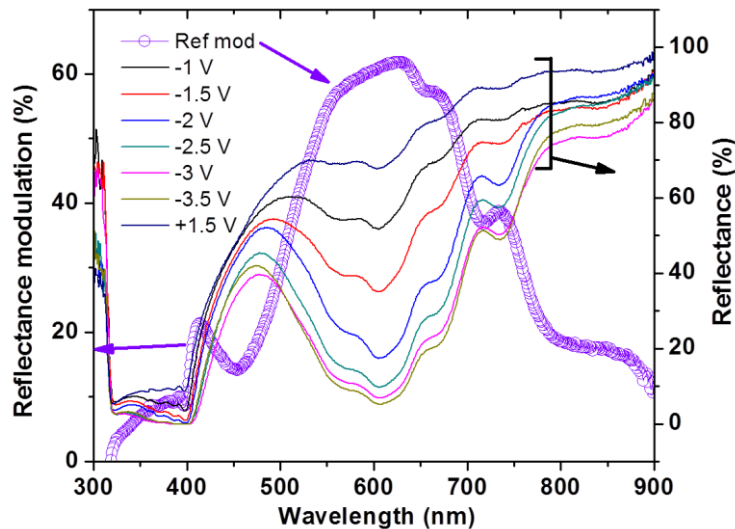
Figure 4B.4 Reflectance spectra of HV–PB ECD recorded under different potentials and reflectance modulation *versus* wavelength (reference oxidation potential: +1.5 V and reduction potential: −3 V).

The reflectance modulation (ΔR) shown by the ECD was 54% (at 550 nm) and 62% at a λ_{max} of 618 nm under a reduction potential of -3.0 V. Under a potential of -2 V, the reflection modulation at 618 nm was 50%. The oxidation potential was fixed at +1.5 V for this calculation.

The photographs of the HV−PB ECRA mirror under switch on and off modes are shown in the figure below. Photographs of HV−PB ECRA of dimensions ($\sim$ 8 cm $\times$ 6 cm) under coloration (-2.0 V) and bleached (+1.5 V) and are shown below in Figure 4B.5. Our pictures can be favourably compared with that of commercially available ECRA mirrors, as can be seen from the pictures below (Figure 4B.6).
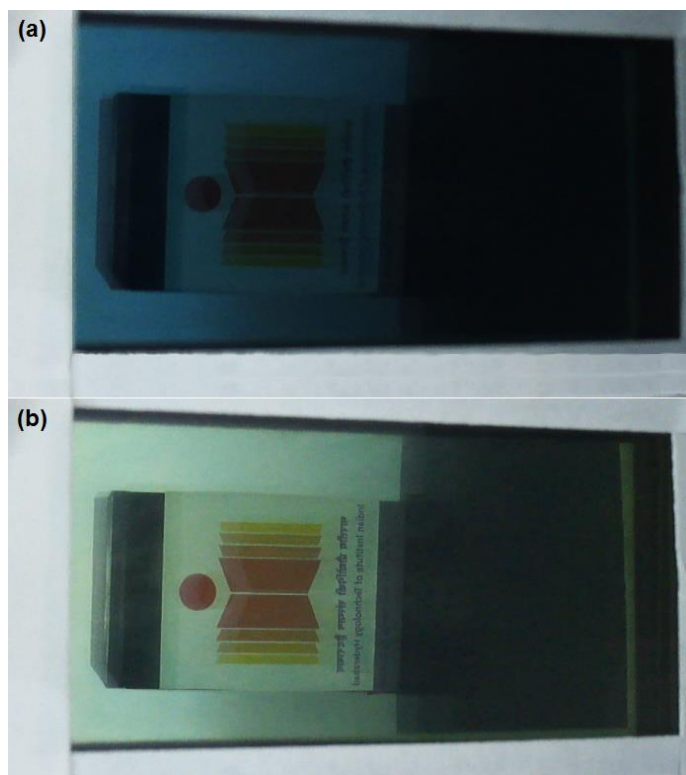
Figure 4B.5 Prototype ECRA mirror based on the HV−PB ECD in colored and bleached states with a mirror at the rear; the IITH logo is a reflection.

Figure 4B.6. A commercial electrochromic rear view mirror in bleached and colored states (source: wwwhttp://www.youtube.com/watch?v=PXFvnfi5t94&feature=player_detailpage).

4B.3.4 Switching behavior of ECDs

Color-bleach characteristics of the HV−PB ECD were measured under a step time of 5 s, under a square wave potential of ± 2.5 V, at a monochromatic wavelength of 610 nm. The device switched between blue and transparent states, within 5 s, as can be seen in Figure 4B.7 and the progressive coloration of a HV−PB ECD is shown in Figure 4B.8. A coloration time of 3.7 s and a bleaching time of 3.1 s were observed for the ECD under a step time of 5 s. The switching times are moderately fast and are acceptable for practical applications.
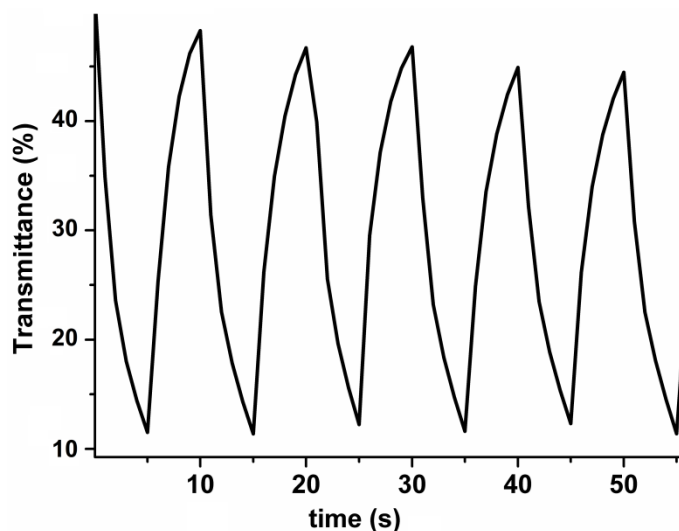
Figure 4B.7 Color-bleach kinetics of a HV−PB ECD recorded with a step time of 5 s.
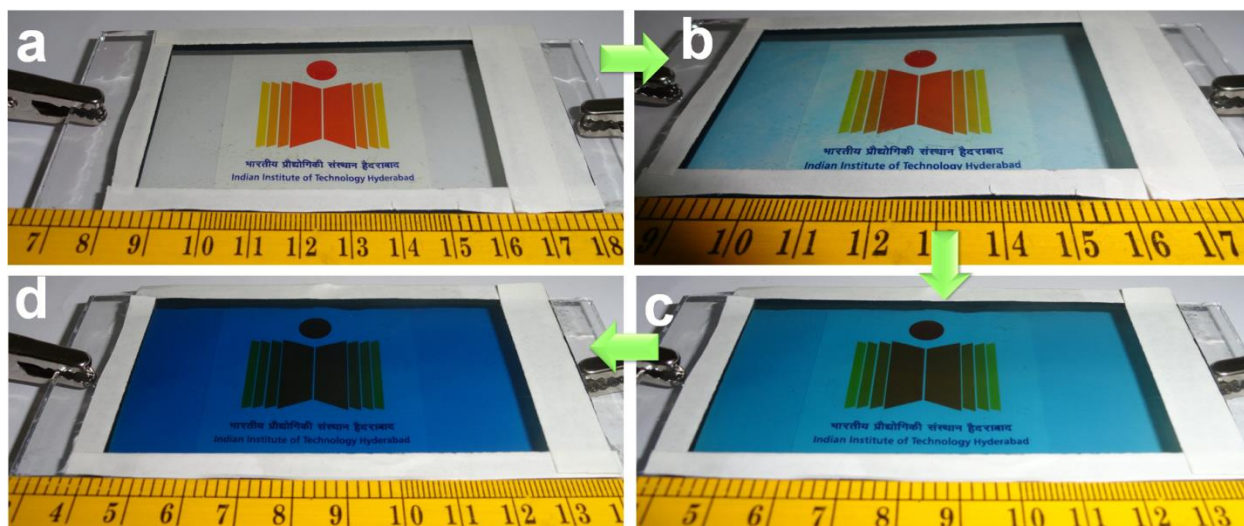
Figure 4B.8 HV−PB ECD (7 cm × 5 cm) developed at IITH; a to d shows the color deepening with increasing reduction potential.

4B.3.5 Cycling and temperature effect

The HV−PB ECD was subjected to reptitive cycling. The reflectance modulation of the device in the as-fabricated state and after 1000 cycles is shown below. The initial ΔR was 60% and it was 43% after 1000 cycles under potentials of +1.5 V and −3.0 V at 600 nm. This device was also heated to 70−80 $^{\circ}$C to evaluate the effect of temperature on performance and the reflectance modulation was measured. Similarly it was kept in a salt-ice mixture for thirty minutes and its' performance was monitored. After exposure to hot or cold conditions, the device either showed a slight increase (hot) or a small decrease (under cold) in reflectance relative to its performance under reduction potentials at room temperature (rt). Reflectance modulation upon heating was 62% and upon cooling, it was 52% at 600 nm. The devices

were found to exhibit no significant change in their modulation, upon storing them in air for about 12 months.
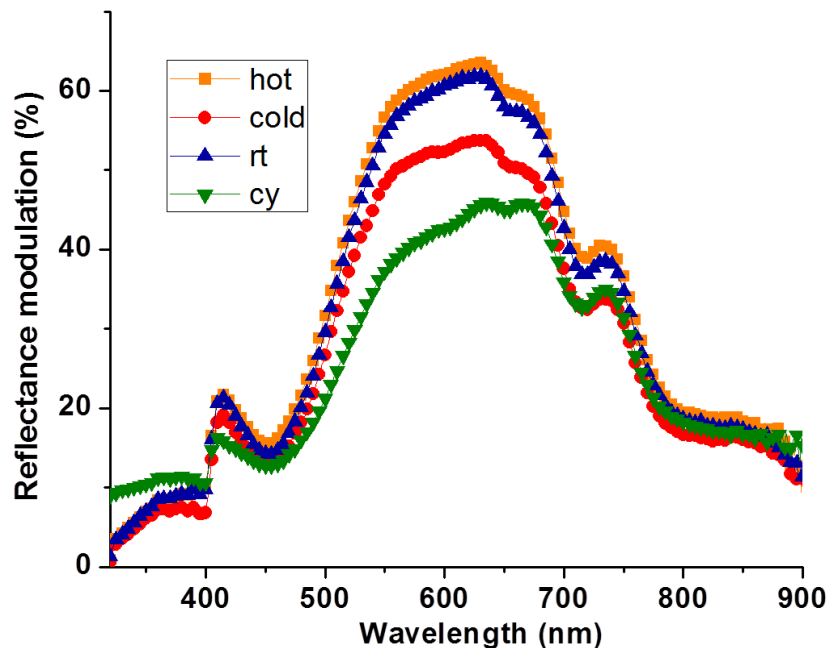
Figure 4B.8 Comparison of reflectance modulation of the ECD: at rt, after having been heated or cooled and also at rt after 1000 cycles (cy). The oxidation potential was fixed at +1.5 V and the reduction potential was fixed at −3 V.

4B.4 Summary

We fabricated prototype HV−PB ECDs and demonstrated their suitability for ECRA mirror applications. Viologen based ECDs can be up-scaled for energy efficient smart window applications as well, as these are less expensive than transition metal oxide based electrochromic coatings. The *in-situ* fabrication technique can be applied to large area devices which have tremendous potential as facades or windows in buildings.

References

[1] C.M. Lampert, A. Agrawal, C. Baertlien, J. Nagai, Sol. Energy Mater. Sol. Cells 56 (1999) 449.
[2] A. Pennisi, F. Simone, G. Barletta, G. Di Marco, M. Lanza, Electrochim. Acta 44 (1999) 3237.
[3] C.M. Lampert, IEEE Circuits Devices Mag. 8 (1992) 19.
[4] A. Pennisi, F. Simone, Sol. Energy Mater. Sol. Cells 39 (1995) 333.
[5] P. van Konynenburg, S. Marsland, S. McCoy, Sol. Energy Mat. 19 (1989) 27.
[6] H. Byker, Proc. Electrochem. Soc. 94 (2) (1994) 3.
[7] S.A. Agnihotry, Pradeep, S.S. Sekhon, Electrochim. Acta 44 (1999) 3121.
[8] A.W. Czandema, C.M. Lampert, SERI (NREL) Report, TP-255-3537, 1990.
[9] P.R. Somani, S. Radhakrishnan, Mater. Chem. Phys. 77 (2002) 117.
[10] X. W. Sun, J. X. Wang, Nano Lett. 8 (2008) 1884.
[11] P. Bonhote, E. Gogniat, F. Campus, L. Walder, M. Gratzel, Displays 20 (1999) 137.

Chapter 5

Preparation of conducting PET flexible electrodes using PEDOT and a study of a flexible ECD

5.1 Introduction

In the last two chapters, the focus was on preparing and characterizing PEDOT based films and devices on rigid substrates. Optically transparent conducting electrodes (ITO or FTO) are at the forefront of research in electronic devices, due to their application in flat panel displays and organic light emitting diodes (OLEDs). ITO is the widely used current collectors in these devices, but the exorbitant cost of In and the brittle nature of these materials (both FTO and ITO), inhibits the fabrication of these devices in stretchable, bendable, flexible forms, and from these serious limitations, arises the need for a cost-effective, distensible alternate [1-3]. PEDOT, by replacing the expensive ITO as the transparent conductive layer in optoelectronic devices, yields an excellent compromise between cost and performance [4-8]. In the recent times, there is a huge research thrust on developing flexible conducting films for electronic devices such as flat panel displays and organic light emitting diodes (OLEDs). Therefore, in continuation on my work on PEDOT, flexible PEDOT films were fabricated by a novel approach. Despite the significant strides made in the synthesis and characterization of PEDOT coatings or dispersions, much room still remains for developing facile methods to fabricate high performance PEDOT coatings of good optical transparency and low sheet resistance on large area plastic or poly(ethylene terephthalate) or PET substrates. In this chapter, PEDOT films were grown on PET substrates by a novel continuous stirring process using a reverse micellar precursor solution containing EDOT, the monomer, $FeCl_3$ as the oxidant and dopant and sodium bis(2-ethylhexyl) sulfosuccinate or AOT as the surface wetting surfactant. Furthermore, to irrefutably illustrate the practical utility of these films, a flexible electrochromic device (ECD) was assembled, with a PEDOT/PET as the cathodic colorant, an ionic liquid (1-Ethyl-3-methylimidazolium bis(trifluoromethylsulfonyl)imide) as the electrolyte and an anodically coloring Prussian blue or PB film layer as the counter electrode. In an ECD, the application of an external bias

80

yields a color change due to the generation of new electronic absorption transitions in the visible region within a material (PB or PEDOT) [9,10]. Our results show that the highly conductive, PEDOT coated PET films have the potential to replace conventional ITO or fluorine doped tin oxide (FTO) in optoelectronic and electrochemical devices.

5.2 Experimental

5.2.1 Chemical bath deposition of PEDOT on PET

In a typical synthesis, AOT (13.5 mmol) was dissolved in 300 mL of n-hexane in a beaker of 500 mL capacity and a solution of $FeCl_3$ (6.2 mmol) in 1.0 mL of water was added. The resulting orange-colored mixture was gently stirred for 5 min., followed by slow addition of EDOT liquid monomer (2.5 mmol). A 20 cm × 6 cm PET substrate was immersed in the reaction mixture (step 1 in Figure 5.1) and the solution was magnetically stirred for a pre-defined duration between 1−5 h at room temperature.
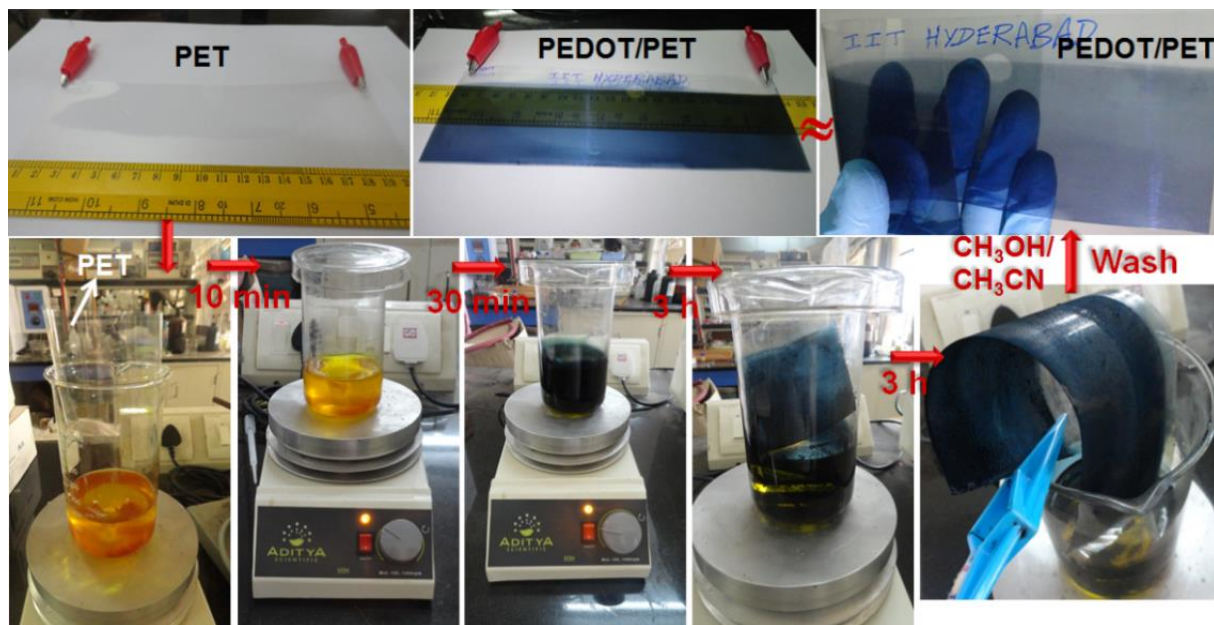
Figure 5.1 Photographs illustrating the step-wise formation of PEDOT/PET electrodes.

A uniform deposit of pale blue colored PEDOT on PET, referred to as PEDOT/PET, was obtained at the end of 1 h stirring. The PEDOT/PET film was washed with excess amounts of methanol and acetonitrile and dried at 30 °C for 1 h. The formation of PEDOT/PET from the polymerization bath is shown as a function of time in Figure 5.1. Using the same above-mentioned method, PEDOT thin films of different thicknesses were also prepared on PET, by extending the stirring duration in the bath to 2, 3, 4 and 5 h, and extracting the film from the bath, washing and drying at the end of each time period.

5.2.2 Electrochemical deposition of PB films on PEDOT/PET

PB films were grown from a solution of $K_3[Fe(CN)_6]$ (10 mM) and $FeCl_3$ (10 mM) in HCl (0.01 N) in a three electrode cell, using an Ag/AgCl/KCl as a reference electrode and Pt as the counter electrode and by applying a fixed potential of +1.5 V for 360 s to PEDOT/PET, which served as the working electrode. Bright blue colored PB films were deposited over pale blue colored PEDOT/PET electrodes. The PB-PEDOT/PET films were washed in a solution of 0.01 M HCl and deionized water mixed in a 2:3 v/v ratio and stored in air.

5.2.3 Construction of a PEDOT- PB flexible device

A PEDOT/PET film was used as a cathode and a PB/PEDOT/PET film was used as the anode. A 0.64 mm thick and 2 mm wide adhesive acrylic tape was employed as the spacer, which prevented the shorting of the two electrodes and also held the device assembly together. Two open ports 1 mm wide were created along the length of spacer between two electrodes, which were in sandwich configuration, for filling the electrolyte. A clear liquid electrolyte containing 1-Ethyl-3-methylimidazolium bis(trifluoromethylsulfonyl) imide (IL) and propylene carbonate (PC) in a 1:1 v/v ratio was used and injected through a port to fill the device. A transparent, pale blue colored device was obtained and all the four edges were sealed with an epoxy sealant. The device, hereafter is referred to as the PEDOT-PB flexible device and the active area of the device was about 2 cm × 4 cm.

5.3 Results and Discussion

5.3.1 Mechanism of PEDOT/PET and PB/PEDOT/PET formation

The growth of PEDOT over PET, as a function time (Scheme 5.1), occurs by a chemical bath solution phase polymerization and deposition. Initially, in the solution containing the monomer: EDOT, oxidant: $FeCl_3$ and surfactant: AOT, $FeCl_3$ oxidizes the monomer, which forms radical cations, and these are charge compensated by the Cl^- ions in solution. The radical cations have greater electron density at the α-position and they dimerize, which is followed by oligomerization, nucleation and growth of polymer chains (Scheme 5.1). The polymer clusters tend to deposit on the PET surface, which is aided by the continuous stirring of the solution and also by AOT, which acts as a wetting reagent. The stirring of the formulation allows uniform tethering of the polymer on PET, assisted by the presence of the homogenously distributed AOT surfactant in the solution, and as a consequence, a PEDOT film of uniform pale blue color is obtained at the end of 1 h. PEDOT/PET films of higher thicknesses were obtained by extending the stirring duration to 2, 3, 4 and 5 h, with the maximum value of uniform deposit thickness achieved at the end of 5 h. For stirring durations in excess of 5 h, the PEDOT film was patchy, non-uniform and also began to peel off from the PET substrate.
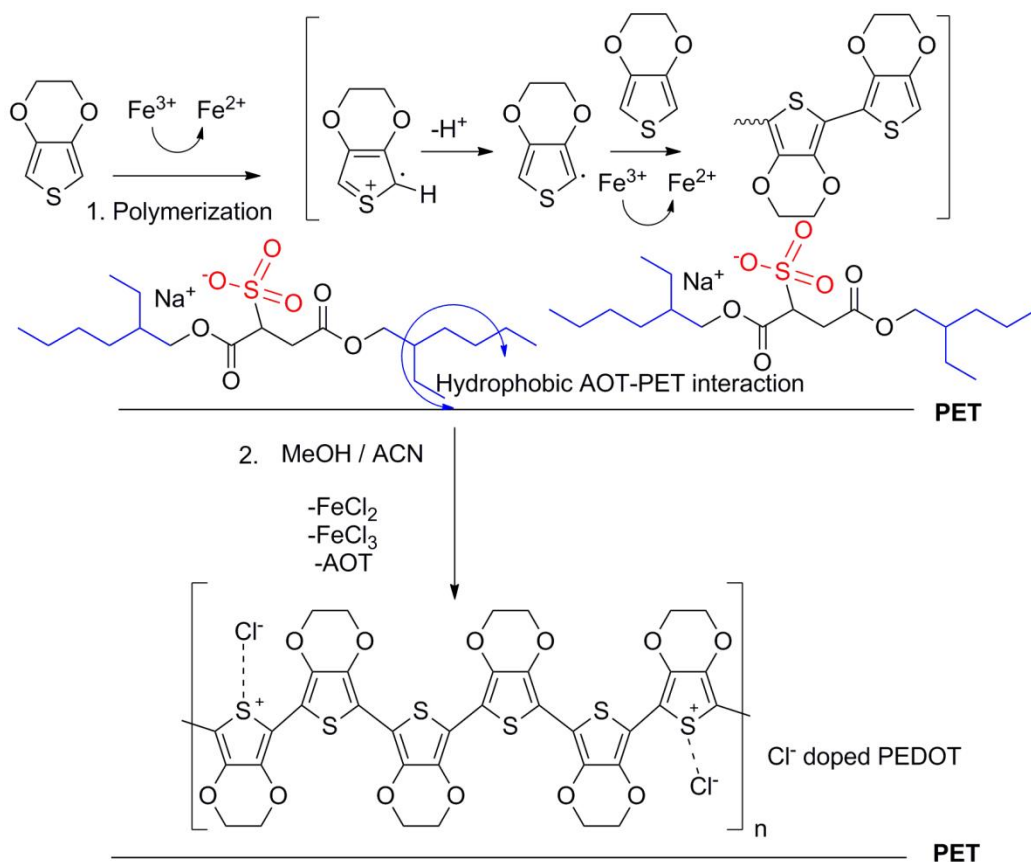
Scheme 5.1: Mechanism of formation of PEDOT on PET

PB films were then grown by an electrochemical route, on the PEDOT/PET substrate, wherein the thickness of PEDOT was ~300 nm. The current-time transient curve corresponding to the formation of the PB film over the PEDOT/PET substrate is shown in Figure 5.2. At t = 0 s, the initial current density is high (0.254 mA cm^{-2}), ascribable to the double layer capacitance charging, followed by a gradual decline. This depleting current region corresponds to the formation of PB film, by the following reaction (5.1). The formation of a turquoise blue colored PB film over the PEDOT/PET electrode, clearly shows the ability of PEDOT/PET to function as an electron conductor.

$$Fe^{3+} + [Fe(CN)_6]^{3-} + e^- \rightarrow Fe^{III}[Fe^{II}(CN)_6]^- \ x.H_2O \quad\quad\quad (5.1)$$

$$(PB)$$
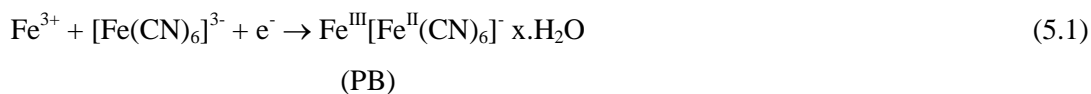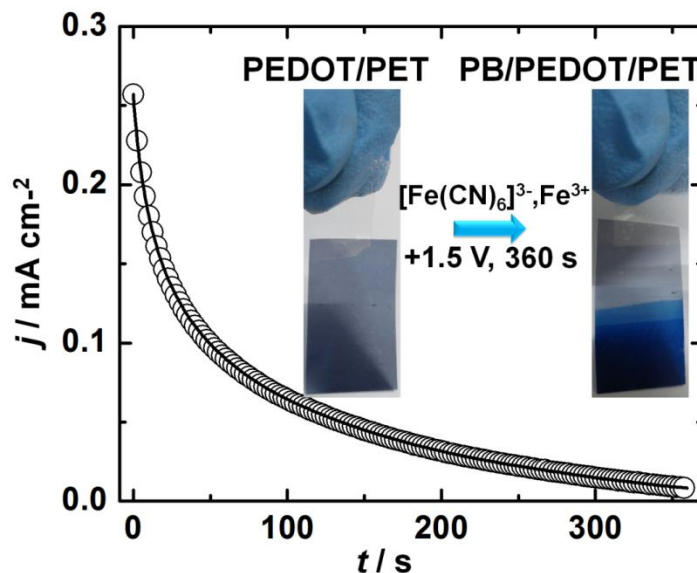
Figure 5.2 Current density *versus* time plot for the deposition of a PB film on PEDOT/PET from a precursor solution containing 10 mM K$_3$[Fe(CN)$_6$] and 10 mM of FeCl$_3$ using 0.01 M HCl as the medium. Insets are the photographs of the PEOT/PET and PB/PEDOT/PET films.

5.3.2 Optical and electrical properties of PEDOT/PET and PB/PET

5.3.2.1 FTIR, FESEM, transmittance and thickness studies for flexible films

The ATR-FTIR spectra of the PEDOT/PET and PB-PEDOT/PET films recorded in the frequency region of 500 to 4000 cm^{-1} are displayed in Figure 5.3a. Signals from 1521 to 1352 cm^{-1} arise from the ν(C=C) stretching vibrations of the thiophene ring for the Cl$^-$ doped PEDOT [11]. The peaks at 1098 and 1030 cm^{-1} correspond to the stretching modes in the ethylenedioxy group ν(C-O-C) and the peaks at 983 and 878 cm^{-1} can be attributed to the C-S interaction in the thiophene ring ν(C-S) [11,12]. The FTIR spectrum of the PB/PEDOT/PET film (Figure 5.3b), in addition to the peaks of the Cl$^-$ doped PEDOT, showed a strong and broad absorption band peaking at 2058 cm^{-1}, which is attributable to the –C≡N groups of iron(III) hexacyanoferrate(II). The absorptions at ~3410 and ~1610 cm^{-1} are attributed to O–H stretching and bending vibrational frequencies of water molecules that prevail in the PB film, KFe[Fe(CN)$_6$] x.H$_2$O [13]. FE-SEM images of PEDOT/PET film and PB/PEDOT/PET film are displayed in Figure 5.3c and d. The SEM image of PEDOT shows the film to be composed of uniformly distributed, interlinked spherical particles, 40-60 nm in dimensions. The EDX plot of the same film shows the presence of the following elements: C, O, S and Cl, thus confirming the formation of Cl$^-$ doped PEDOT on PET. The SEM image of the PB/PEDOT/PET shows the film to be composed of compactly packed grains of irregular shapes, with indistinguishable grain boundaries. The film is dense, and the morphology

84

is visibly different from that of the PEDOT/PET substrate. The EDX plot of the PB film shows the presence of C, N, O, S and Fe elements; the Fe–(CN) groups originate from PB.
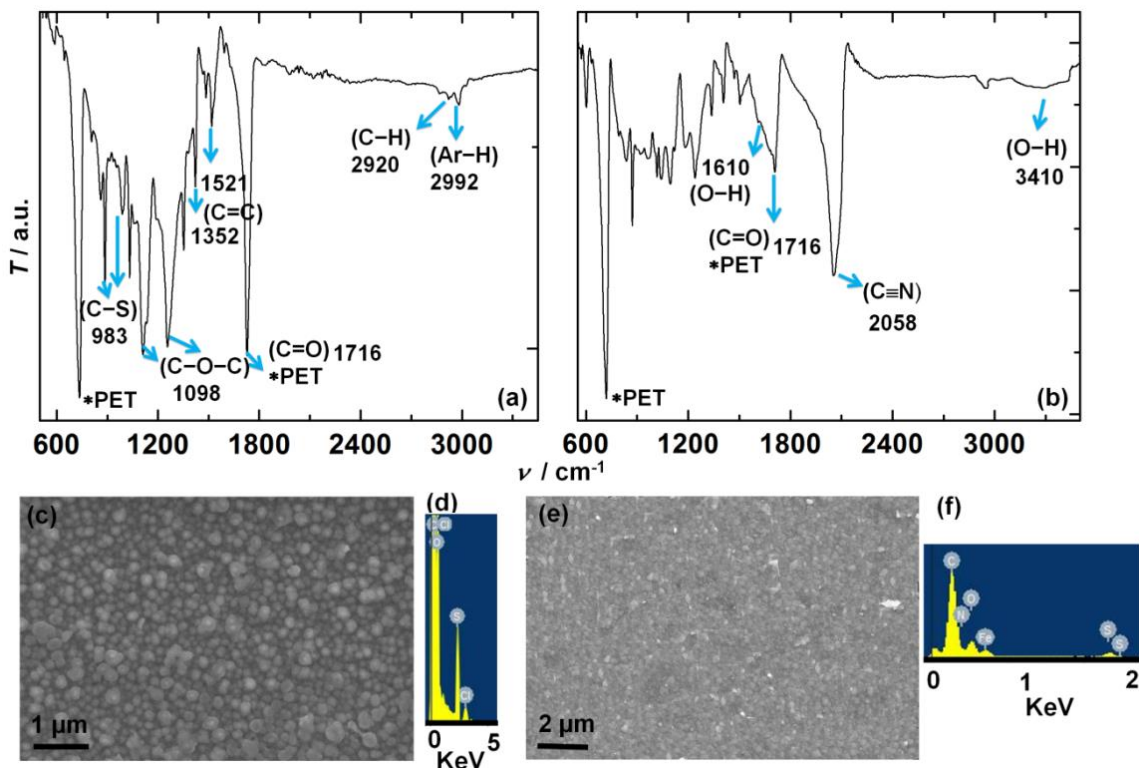
Figure 5.3 FTIR spectra of (a) PEDOT/PET and (b) PB/PEDOT/PET films, SEM micrographs of (c) PEDOT/PET and (e) PB/PEDOT/PET films and EDX plots of (d) PEDOT/PET and (f) PB/PEDOT/PET films.

The thicknesses of the PEDOT/PET films deposited for different durations were measured by AFM technique by running an AFM tip over a step of PEDOT/blank PET. The thickness of the PEDOT/PET film obtained at the end of 1 h stirring, was found to be $\sim 80 \pm 20$ nm and the one obtained after a stirring period of 5 h, was found to have a thickness of $\sim 480 \pm 80$ nm. Representative sectional profiles of the steps for the PEDOT/PET films obtained after stirring spans of 1 and 5 h are shown in Figure 5.4 and the thicknesses are summarized in Table 5.1.
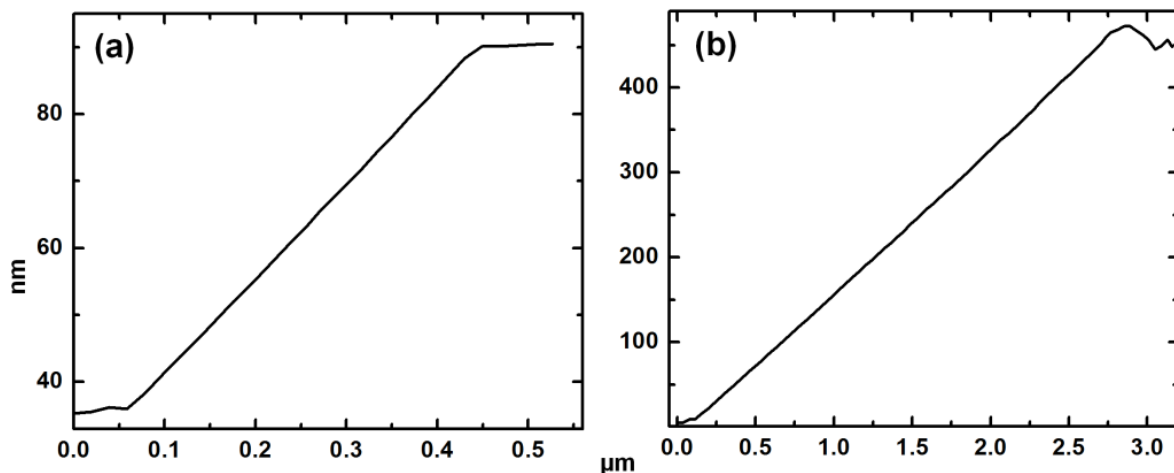
Figure 5.4 Representative sectional profiles of the steps for the PEDOT/PET films obtained after stirring spans of (a) 1 and (b) 5 h.

Table 5.1: Thickness of the PEDOT/PET films deposited at different stirring times.

PEDOT/PET	Stirring Time (h)	Film Thickness (nm)
Sample 1	1	80±20
Sample 2	2	170±30
Sample 3	3	285±45
Sample 4	4	340±65
Sample 5	5	400±80

Transmittance spectra of the PEDOT/PET films of different thicknesses recorded in the wavelength region of 300 to 1200 nm are shown in Figure 5.5a. For a thin film of PEDOT/PET (~80 nm), a maximum transmittance of 93% and %T of about 85% was observed in the bulk of the visible spectrum. For a film of moderate film thickness (~300 nm) and for a still thicker film (~400 nm), the transmittance values were in the ranges of 73% and 61% respectively. The surface resistances of PEDOT films were measured by a four-probe method. The surface resistance values of the PEDOT films as a function of thickness are shown in Figure 5.5b. The surface resistance was in the range of 2-4 KΩ cm^{-2} at ~80 nm thin films and it decreased to ~600 Ω cm^{-2}, for a ~400 nm thick film. It was observed that the PEDOT film formation takes place slowly under the said experimental conditions and the sheet resistance decreases significantly and attains a limiting value of 600 Ω cm^{-2} in about 5 h.
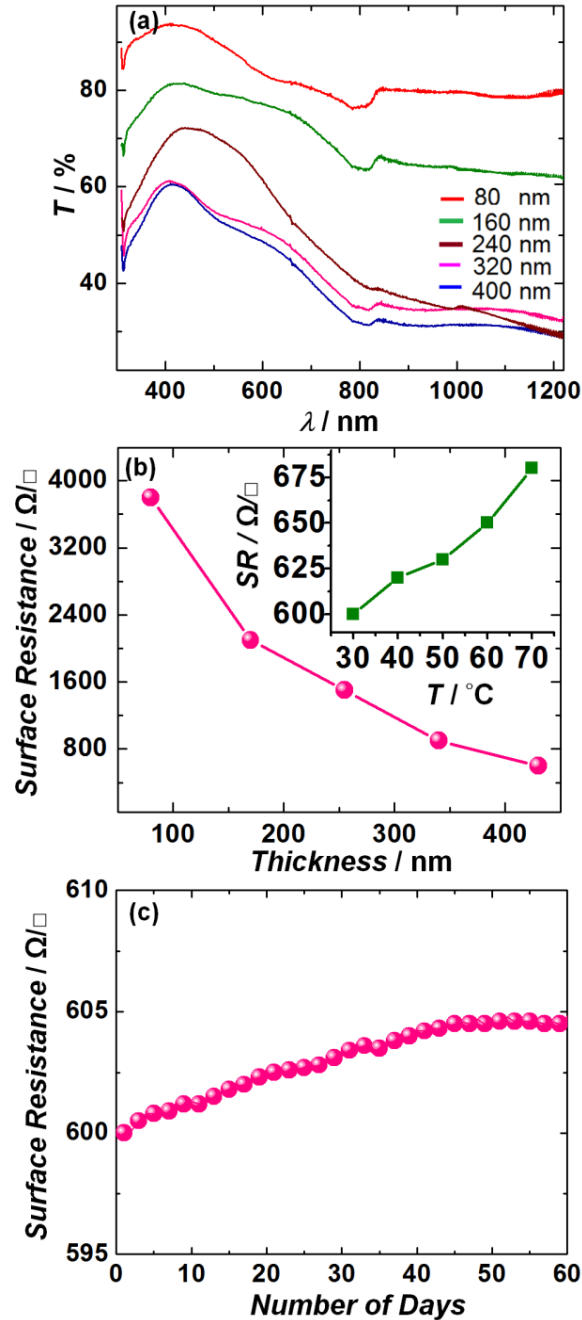
Figure 5.5 (a) Variation of transmittance as a function of film thickness for the PEDOT/PET film in the wavelength region of 300 to 1200 nm and (b) surface resistance of PEDOT/PET films as a function of film thickness. Inset of (b) shows the variation of surface resistance of a 400 nm thick film with temperature. (c) Surface resistance variation of a 400 nm thick PEDOT/PET electrode as a function of time.

Thus, electrical conductivity is also affected by deposition time or film thickness. For deposition periods in excess of 5 h, the PEDOT film was non-uniform; it pulverized and detached from the PET

substrate. For a 400 nm thick PEDOT film, the effect of temperature on sheet resistance was measured at different temperatures of 30, 40, 50, 60 and 70 °C and at each temperature, the film was heated for 30 min. in air. In a previous report, a PEDOT film was heat-treated for about 1000 h at 100 °C and it showed no change in conductivity [14]. We too observed an insignificant change in surface resistance (~600 $\Omega/\square$) for the PEDOT/PET film with increase in temperature (the inset of Figure 5.5b), which indicates that they can be used in devices which operate at temperatures above room temperature. To determine the shelf-life of the PEDOT film, the surface resistance of a PEDOT film (initial resistance = 600 $\Omega/\square$) stored in a container was measured intermittently, over a period of two months (Figure 5.5c). At the end of two months, the film showed only a 1.66% increase in surface resistance, which implied that the film is air-stable.

5.3.2.2 C-AFM and KPFM studies for flexible PEDOT/PET films

The CAFM images (with a tip bias of 50 mV) of topography and current of the PEDOT/PET film (with PEDOT thickness ~ 400 nm), concurrently acquired during scanning are displayed in Figure 5.6a and b, respectively. The corresponding cross-sectional profiles of height and current are shown in Figure 5.6a' and b'. The topography of the film is relatively featureless, as a few large irregular shaped grains with fuzzy grain boundaries are only seen. In the current image, the bright and the dark regions correspond to regions of high and low currents respectively, and the current magnitude is scaled on the right side of the image. The nanoscale current image of PEDOT/PET reveals the film to be constituted predominantly by bright domains of high current, extending to more than a micron in length, and the regions of relatively low currents are very few. These low current phases appear as spots embedded in the high current regions. Since the high current carrying domains are almost continuous, and even in the dark regions, bright spots due to high currents are embedded; it is obvious that this film is capable of carrying high electronic currents. The maximum current that the film can sustain is 22 nA. The homogeneous granular morphology of conducting PEDOT is responsible for the film's ability to transport currents. The cross-sectional profile of current also shows that current varies over a narrow range of 17 to 20 nA, on an average, over a length scale of 2 μm. The nanoscale electrical conductivity of the PEDOT/PET film, was determined by measuring point scale I-V characteristics at nine equidistant points on the current image, and the average I-V profile is shown in Figure 5.6c. A quasi-linear dependence of current on swept potential was confined to a voltage window of about −1.5 to +1.1 V, for this film. At applied voltages, outside of this range, the current saturates, acquires a steady state, at ~12.3 nA, and remains invariant with potential. From the straight-line fit, the ambient temperature nanoscale electronic conductivity was determined by using equation (5.2).

$$\sigma_{RT} = (I/V) \times (d/\pi r^2) \tag{5.2}$$

In equation (5.2), r is the radius of the conducting tip (~ 10 nm) and d is the thickness of the PEDOT film. The average nanoscale electronic conductivity for the PEDOT/PET film, deduced from the ohmic regime, was found to be 0.103 S cm^{-1}. Our value is comparable to literature values of PEDOT: PSS conductivity for a film formed by spin-coating from aqueous solution (Baytron PV4071 from Bayer Corporation) has a conductivity of about 0.4 S cm^{-1} [15]. Also for a spin-coated pristine PEDOT:PSS film conductivity was measured to be about 0.20 S cm^{-1} [16]. In the past, it was found that the PEDOT-PSS films after secondary doping with some inert solvents, such as sorbitol, N-methylpyrrolidone, polyethylene glycol, dimethyl sulfoxide undergo a conductivity increase of 2-3 orders of magnitudes to reach up to 80 S cm^{-1} [17,18]. The large value of PEDOT/PET's nanoscale conductivity shows this film can be easily applied to electrochemical or photovoltaic devices, wherein a high conductivity will permit facile charge transport, which can have a positive impact on device performance.
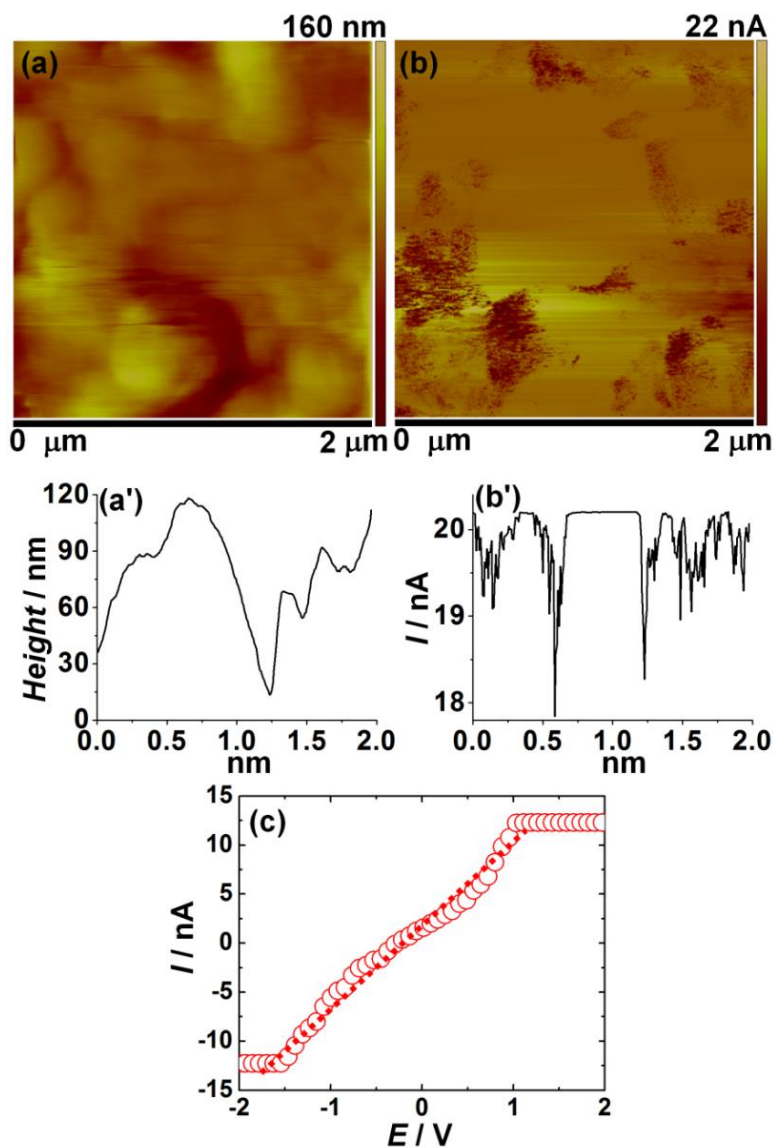
Figure 5.6 Concurrent topography (a) and current (b) images of a PEDOT/PET film, recorded over a scanned area of 2 μm × 2 μm. Corresponding cross-sectional profiles are shown in (a') and (b'). (c) Resultant current-voltage curve of PEDOT/PET, averaged over 9 I-V curves recorded at 9 spots on the current image in (b). The dashed line in (c) represents the linear fit.

The work function (Φ) of a PEDOT/PET film (400 nm thick) was determined by a Kelvin probe force microscopy (KPFM) measurement. At lower thicknesses, due to lower conductivity, surface potential images of good quality could not be obtained. In KPFM, the topography of the film (PEDOT/PET) surface is measured in tapping mode and the surface potential (SP) variation is measured with a conducting tip. Representative topography and the corresponding surface potential map of the PEDOT/PET electrode are shown in Figure 5.7a and b. The tip was held at ~100 nm above the PEDOT

surface, and it is charged due to the applied ac potential. The sample surface is also charged since it is in the vicinity of the charged tip. An ac bias is applied to a conducting Pt/Ir tip of a known work function; it scans the sample surface and the localized contact potential difference (V_{CPD}) that arises between the conducting tip and the sample surface, is used for generating the SP map, as shown in the following equation (5.3).

$$V_{CPD} = (\Phi_{tip} - \Phi_{sample}) / e^-$$ (5.3)

Φ_{tip} is the work function of the conducting Pt/Ir coated Si cantilever (5.5 eV) and Φ_{sample} is the work function of the PEDOT/PET electrode. The work function of Pt/Ir tip was first calibrated with highly ordered pyrolytic graphite (HOPG) ($\Phi_{HOPG} = 4.6$ eV) to convert the measured V_{CPD} to absolute surface work function. The absolute surface work function of PEDOT/PET was calculated with equation (5.4).

$$\Phi_{sample} = 4.6 \text{ eV} + V_{CPDHOPG} - V_{CPDsample}$$ (5.4)
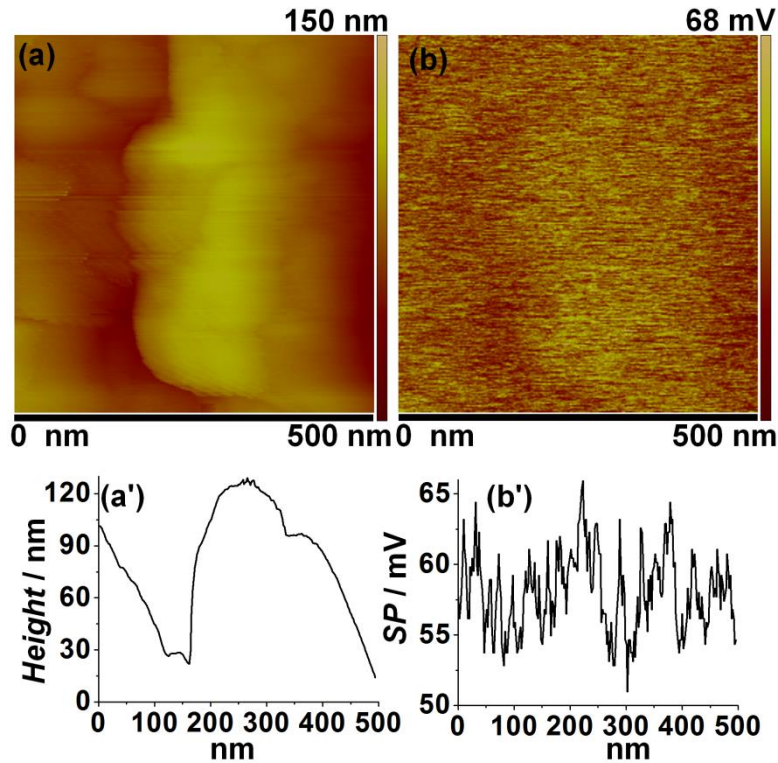
Figure 5.7 (a) Topography and (b) surface potential maps a PEDOT/PET film recorded over a scanned area of 500 nm × 500 nm. Corresponding cross-sectional profiles are shown in (a') and (b').

The topography of the PEDOT/PET again showed the presence of large irregular shaped grains of a few hundred nanometer dimensions, and the corresponding SP map showed dark and bright spots distributed uniformly across a length scale of 500 nm. The cross sectional profile of SP shows this potential, lies in the range of 50 to 68 mV, thus indicating that the SP varies moderately across the film surface. The SP of

the PEDOT/PET electrode was taken as 68 mV (maximum value attained in the SP map) and the corresponding work function calculated from equation (5.4) is 4.9 eV.

5.3.3 Electrochromic PEDOT-PB flexible device

5.3.3.1 Cyclic voltamograms of PEDOT-PB device

The cyclic voltammograms for the PEDOT-PB device recorded between +1.5 and −1.5 V with PEDOT/PET (of ~400 nm thickness) as the working electrode at different scan rates of 2, 5, 10, 20, 50 and 100 mV s^{-1} are shown in Figure 5.8. In the cathodic branch of the CV plot, for the device recorded at 2 mV s^{-1} (Figure 5.8a), a reduction peak is observed at −0.41 V. This peak is assigned to the formation of the deep blue PEDOT in "neutral state" on the PET surface, by dedoping of imide anions. It is followed by oxidation to the doped PEDOT (pale blue), evidenced from a broad peak observed at +0.34 V, in the reverse sweep. Upon increasing the scan rate, from 2 to 100 mV s^{-1}, the reduction peak shifted to higher negative potentials and the broad oxidation peak also flattened out in the anodic branch (Figure 5.8b). The peak shift to more negative potentials is due to the sluggish de-doping process, at higher scan rates. It was also observed that within applied potential window of ± 1.5 V, the redox process of the PEDOT/PET film in the IL/PC electrolyte is reversible and also stable, as no over-oxidation peaks were detected [19].
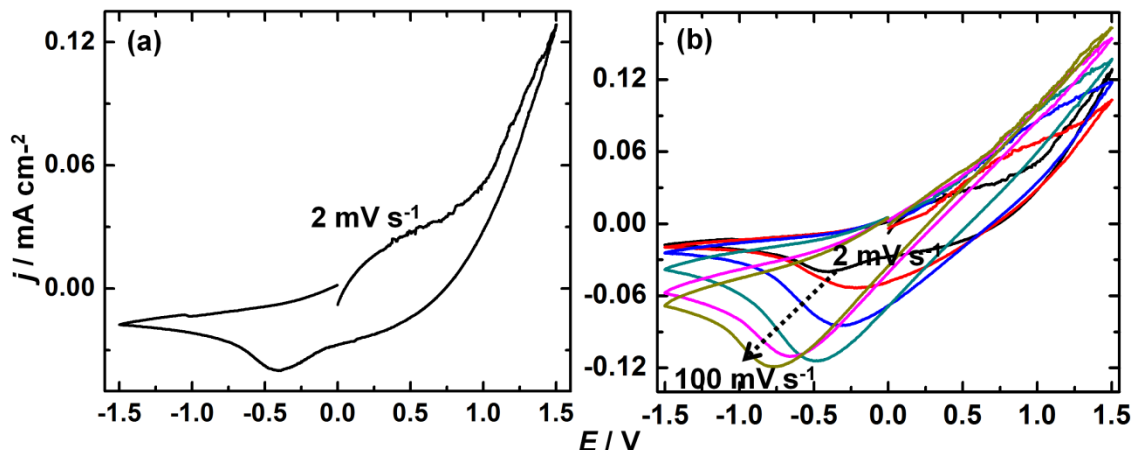
Figure 5.8 Cyclic voltammograms of a PEDOT-PB device recorded between the potential limits of −1.5 and +1.5 V, at different scan rates of (a) 2 and (b) 2, 5, 10, 20, 50 and 100 mV s^{-1}.

5.3.3.2 Spectroelectrochemistry of PEDOT-PB device

The *in-situ* UV-visible-near infrared (NIR) absorption spectra of the PEDOT-PB device recorded under different dc reduction potentials (applied to the PEDOT/PET electrode) in the range of −0.5 to −1.5 V, in steps of 0.2 V, and under different oxidation potentials of +0.5, +1.0 and +1.5 V are shown in Figure 5.9a and b. The thickness of the PEDOT/PET film, employed in this device as cathode, was ~400 nm. Under reduction potentials, with increasing negative potential, the sky blue hue of the device slowly changes to a deep blue-violet hue, a typical electrochromic response of PEDOT [20]. This deep color reverted back to

pale blue, when positive potentials of +0.5, +1.0 and +1.5 V were applied. The device attains an appreciable violet color at −1.0 V which deepens to a deep violet-blue state at −1.5 V. The absorption spectrum for the device in the extreme reduced state (at −1.5 V) reveals a λ_{max} at 580 nm. This peak is assigned to the $\pi \rightarrow \pi^*$ charge transfer in the reduced PEDOT, signifying the formation of the neutral polymer. The maximum optical density change for the device in the visible region was observed under potentials of ± 1.5 V (ΔOD = 0.4). PEDOT, upon applying oxidation potentials, readily converts to its' doped form and absorbs strongly in the NIR region [21]. These absorptions are due to the formation of polarons and bipolarons in oxidized PEDOT. The absorption spectra of the PEDOT-PB device in the NIR region, from 900 to 1650 nm (Figure 5.9b), showed that this device is capable of NIR modulation, as well. It must be noted that the visible and NIR energies are absorbed by the device in colored and bleached states respectively. When the device is bleached, it absorbs NIR radiation, and thus prevents "heat" from entering into a room or an automobile, when employed as a smart window. When the device is colored, it modulates visible radiation, and enables viewing, without turning opaque. A ΔOD = 0.7 was observed at ~1190 nm under +1.5 V, by taking the spectral response at −1.5 V for the device as reference. *In-situ* absorption studies were also performed for the anodically coloring PB/PEDOT/PET electrode in the IL/PC electrolyte using a Pt rod as counter electrode (Figure 5.9c). The absorption spectrum of the as-deposited PB/PEDOT/PET film contains a broad intense band, centering at ~720 nm and upon applying increasing magnitudes of positive potentials (+1.0 and +1.5 V) to the PB film, the intensity of this band also increases. The contribution of PEDOT/PET to the color change shown by PB, is minimized, as in this case, a thin film of this underlying substrate was used (~300 nm). The origin of color in PB is attributed to the charge transfer mechanism between Fe^{2+} and Fe^{3+} centers within the PB film. Upon application of negative potentials to the PB film, from −0.7 to −1.5 V, the intensity of the absorption band at ~720 nm decreases and this can be explained in terms of decreased proportion of Fe^{3+} species in the PB film [22,23].
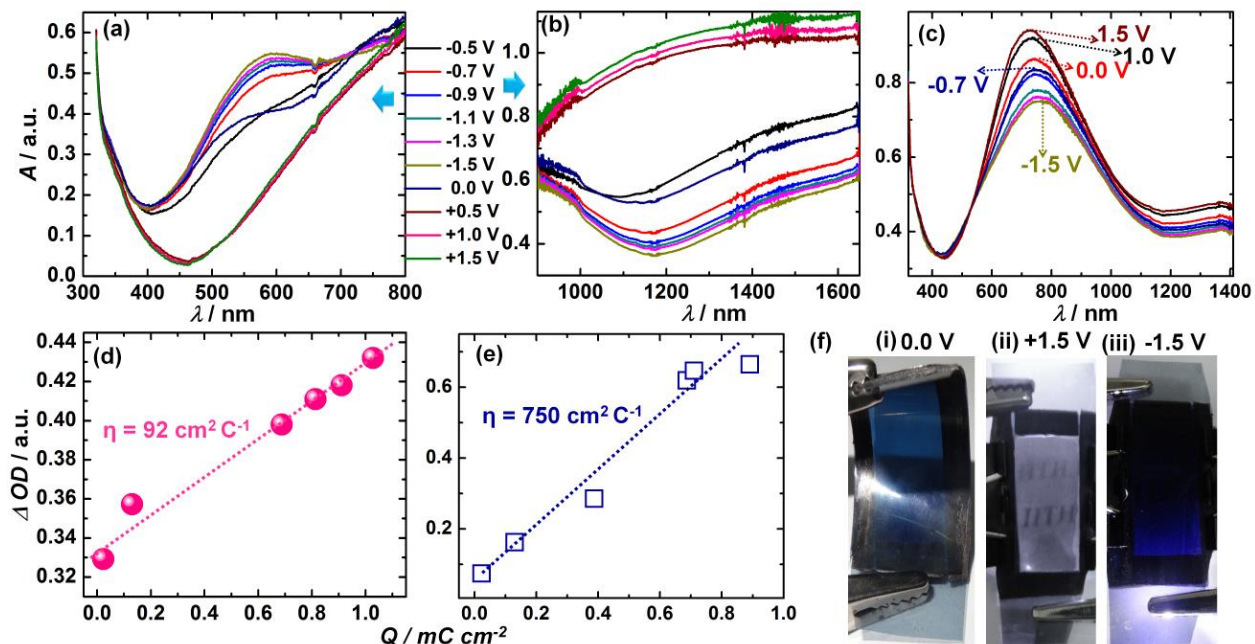
Figure 5.9 *In-situ* absorption spectra of the PEDOT-PB device recorded in the wavelength region of (a) 330-800 nm and (b) 900-1650 nm under different reduction potentials starting from −0.5 V and in steps of 0.2 V to −1.5 V and under oxidation potentials of +0.5, +1.0 and +1.5 V; all potentials applied to the PEDOT electrode of the device. (c) *In-situ* absorption spectra of the PB/PEDOT/PET electrode recorded under different reduction potentials starting from −0.7 V and in steps of 0.2 V to −1.5 V, at 0.0 V and under oxidation potentials of +1.0 and +1.5 V. ΔOD *versus* charge density plots at monochromatic wavelengths of (d) 580 nm with OD response under +1.5 V used as reference for ΔOD calculation and (e) 1190 nm with OD response under −1.5 V used as reference for ΔOD calculation for the PEDOT-PB device. (f) Digital photographs of the PEDOT-PB device in: (i) as fabricated (0.0 V), (ii) bleached (E= −1.5 V) and (iii) fully colored (E = −1.5 V) states.

When a series of negative voltages was applied, the PEDOT-PB device colored and the values of injection charge were determined at each bias by chronoamperometry and these values were used for plotting the ΔOD *versus* inserted charge per unit area (Q/A). The slope of the ΔOD *versus* intercalated charge per unit area profile yields the CE of the device at a monochromatic wavelength. We used a λ = 580 nm in the visible region and λ = 1190 nm in the NIR region as λ_{max}, for determining the CE (η) for the PEDOT-PB device (Figure 5.9d and e). In the visible region, the reference potential for estimating the ΔOD values was fixed at +1.5 V, and, in the NIR region, the reference potential for estimating the ΔOD values was fixed at −1.5 V. CE was therefore deduced from the equation 2.2.

94

The CE values for the device at λ = 580 and 1190 nm were calculated using the ΔOD plots, and these are shown the Figure 5.9d and e. At 580 nm, the CE for the PEDOT-PB device is calculated to be 92 cm^2 C^{-1} and at 1190 nm, it is 750 cm^2 C^{-1} for the same device. The high CE obtained for the device in the NIR region, demonstrates that the flexible device can work as a heat modulator and can reduce air-conditioning requirements. The digital photographs of the (i) as-fabricated, (ii) fully bleached (E = +1.5 V) and (iii) fully colored (E= −1.5 V) PEDOT-PB device are shown in Figure 5.9f. In the past, a PEDOT/PB couple was used to fabricate an ECD and it showed a CE of ∼300 cm^2 C^{-1} [24]. In a previous study, an ECD of two conducting polymers, polyaniline (PANI) and PEDOT based ECD showed a CE of 285 cm^2 C^{-1} at 570 nm [25].

5.3.3.3 Switching kinetics of PEDOT-PB device

The color-bleach characteristics for the PEDOT-PB device were recorded at half-cycles of 10 s and by using a square wave potential of ±1.5 V (Figure 5.10). The kinetic response was recorded at a λ_{max} of 580 nm. Coloration time, defined as the time required for the device to acquire a 90% of the total transmission change, was observed to be 5.8 s under step time of 10 s. Bleaching time, defined as the time taken by the device to undergo a 90% decrease (of the complete transmission change) was 5.5 s for 10 s half-cycle. Previously, for a patterned solid- state ECD developed using ITO-coated plastic substrates, PEDOT was deposited via a solvent less oxidative chemical vapor deposition technique and the device showed optical switching speeds of 13 and 8.5 s, for light-to-dark and dark-to-light transitions, respectively [26]. Our kinetics is comparable to that observed in plastic ECDs. The device herein was subjected to continuous cycling at a scan rate of 20 mV s^{-1}, between −1.5 to +1.5 V and the CV plots for the 1st and 1000th cycles are displayed in Figure 5.10a. In the cathodic branch, the peak current densities at −0.32 V for 1st and 1000th cycles are −0.10, −0.08 mA cm^{-2} respectively. After 1000 repetitive cycles, the current density at −0.32 V, decreased only by 10% of its' original value. To re-affirm the cycling stability of the device, color-bleach kinetics were measured with a step time of 10 s, under an applied potential of ± 1.5 V, for 1000 times in transmittance mode, at a λ_{max} of 580 nm (Figure 5.10b). The transmittance change, offered by the device in the 1st cycle is 19.5, and after 1000 cycles, it is 16.5; the device shows high stability up to 1000 cycles, since 84.6% of the original ΔT change is retained.
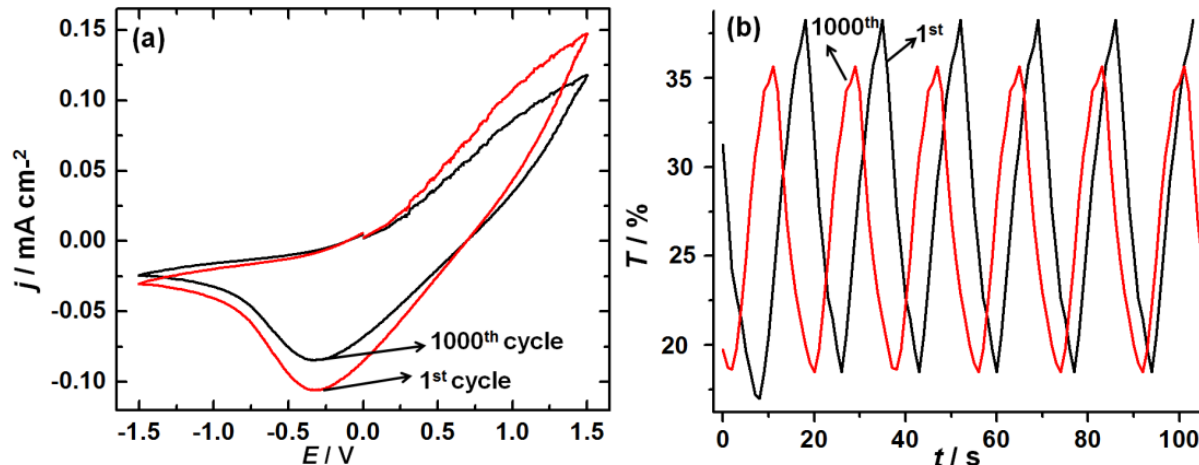
Figure 5.10 Cyclic voltammograms of the PEDOT-PB device for 1st and 1000th cycles recorded over potential ranges of (a) −1.5 V to +1.5 V at 20 mV s^{-1} and (b) kinetics of the same device measured after 1st and 1000th cycles at a monochromatic wavelength of 580 nm under a square wave dc potential of ±1.5 V, under a step time of 10 s.

5.4 Summary

A solution-phase chemical bath polymerization method involving the use of an oxidant and an anionic surfactant, AOT, was developed for the deposition of highly uniform, pin-hole free optically see-through conducting PEDOT films at nano-level thicknesses over large area plastic flexible substrates of PET. This conductive film demonstrated a variation in sheet resistance from 2×10^3 - 3.8×10^3 Ω/□ at ~80 nm thickness to 600 Ω/□ at ~400 nm thickness. The film showed a maximum of 93% optical transmission at ~80 nm thickness and 61% at 400 nm thickness, in the visible region. CAFM studies showed the film to be characterized by an average nanoscale conductivity of ~0.1 S cm^{-1} and the film to be constituted by high current carrying domains spanning over a micron length dimensions. The ability of PEDOT/PET to work as a transparent conducting electrode was confirmed by the successful electrochemical deposition of PB films of good cosmetic quality over PEDOT/PET. A flexible electrochromic PEDOT-PB device was fabricated and the device exhibited a remarkable optical contrast as it changed from pale blue to deep-blue violet upon redox switching between the potential limits of ± 1.5 V. The device showed CEs of 92 cm^2 C^{-1} and 750 cm^2 C^{-1} in the visible and NIR regions and optical switching times of about 5 s. The device endured ~1000 cycles of reversible dark to pale blue transitions without appreciable degradation in optical response, which reiterated the functional value of the device as a low cost, solar tuning smart window. KPFM analysis revealed a work function for PEDOT/PET to be ~4.93 eV. The high uniformity of the PEDOT coating achieved over multiple length scales, the excellent tradeoff achieved between electrical properties and optical transparency and the ability of PEDOT/PET to serve as an electrochrome

and as an electron conducting electrode for any device, exemplifies the potential this electrode has for application in futuristic flexible electronic devices.

References

[1] D. Kaduwal, B. Zimmermann, U. Würfel, Sol. Energy Mater. Sol. Cells 120 (2014) 449.
[2] C. Qiu, J. Wang, S. Mao, W. Guo, S. Cheng, Y. Wang, Polym. Adv. Technol. 21 (2010) 651.
[3] N. Fukuri, N. Masaki, T. Kitamura, Y. Wada, S. Yanagida, J. Phys. Chem. B 110 (2006) 25251.
[4] K. Gurunathan, A.V. Murugan, R. Marimuthu, U.P. Mulik, D.P. Amalnerkar, Mater. Chem. Phys. 61 (1999) 173.
[5] Y. Li, X. Hu, S. Zhou, L. Yang, J. Yan, C. Sun, P. Chen, J. Mater. Chem. C 2 (2014) 916.
[6] Y. Lei, H. Oohata, S. Kuroda, S. Sasaki, T. Yamamoto, Synth. Met. 149 (2005) 211.
[7] J. Kim, E. Kim, Y. Won, H. Lee, K. Suh, Synth. Met. 139 (2003) 485.
[8] N. Perinka, C.H. Kim, M. Kaplanova, Y. Bonnassieux, Phys. Procedia 44 (2013) 120.
[9] C.-F. Lin, C.-Y. Hsu, H.-C. Lo, C.-L. Lin, L.-C. Chen, K.-C. Ho, Sol. Energy Mater. Sol. Cells 95 (2011) 3074.
[10] P.R. Somani, S. Radhakrishnan, Mater. Chem. Phys. 77 (2002) 117.
[11] C. Kvarnstro, H. Neugebauer, S. Blomquist, H.J. Ahonen, J. Kankare, A. Ivaska, Electrochim. Acta 44 (1999) 2379.
[12] H. Chelawat, S. Vaddiraju, K. Gleason, Chem. Mater. 22 (2010) 2864.
[13] P.J. Kulesza, Anal. Chem. 68 (1996) 2442.
[14] W.H. Kim, G.P. Kushto, H. Kim, Z. H. Kafafi, J. Polym. Sci., Part B: Polym. Phys. 41 (2003) 2522.
[15] J. Ouyang, C.-W. Chu, F.-C. Chen, Q. Xu, Y. Yang, J. Macromol. Sci. Part A 41 (2004) 1497.
[16] H.J. Lee, J. Lee, S. Park, J. Phys. Chem. B 114 (2010) 2660.
[17] X. Crispin, F.L.E. Jakobsson, A. Crispin, P.C.M. Grim, P. Andersson, A. Volodin, C. Van Haesendonck, M.V.D. Auweraer, W.R. Salaneck, M. Berggren, Chem. Mater. 18 (2006) 4354.
[18] T.-Y. Chiang, M.-C. Huang, C.-H. Tsai, RSC Adv. 4 (2014) 21201.
[19] P. Tehrani, A. Kanciurzewska, X. Crispin, N. Robinson, M. Fahlman, M. Berggren, Solid State Ionics 177 (2007) 3521.
[20] R. Sydam, M. Deepa, A. K. Srivastava, RSC Adv. 2 (2012) 9011.
[21] E.E. Havinga, C. M. J. Mutsaers, Chem. Mater. 8 (1996) 769.
[22] R.J. Mortimer, T.S. Varley, Sol. Energy Mater. Sol. Cells 99 (2012) 213.
[23] T.-H. Kuo, C.-Y. Hsu, K.-M. Lee, K.-C. Ho, Sol. Energy Mater. Sol. Cells 93 (2009) 1755.
[24] A.A. Argun, P. Aubert, B.C. Thompson, I. Schwendeman, C.L. Gaupp, J. Hwang, N.J. Pinto, D.B. Tanner, A.G. Macdiarmid, J.R. Reynolds, Chem. Mater. 16 (2004) 4401.
[25] T.-H. Lin, K.-C. Ho, Sol. Energy Mater. Sol. Cells 99 (2006) 506.
[26] J.P. Lock, J.L. Lutkenhaus, N.S. Zacharia, S.G. Im, P.T. Hammond, K.K. Gleason, Synth. Met. 157 (2007) 894.

Chapter 6A

Influence of a butyl imidazole in a viologen on its' electrochromic characteristics

6A.1 Introduction

In the last few chapters, fresh insights into PEDOT based films, electrolytes, and devices were provided and discussed, since the objective was to work on organic electrochromes, new viologens were also developed and the electrochromism in these viologens was studied in detail. The need for developing new viologens stems from the fact that traditional viologens like di-heptyl viologen are planar molecules, and when reduced to radical cations, they re-arrange themselves on the electrode surface to form a stack like assembly (aging process), wherein each molecule lies directly above the other. Such a compact structure is resistive to oxidation and within a few cycles, the redox process becomes irreversible and the device acquires a permanently colored state. One approach attempted to prevent the non-erasure of films of $HV^{+\bullet}$ salt, was to add redox mediators such as hydroquinones, ferrous ions or hexacyanoferrate(II) species [1,2]. Other strategies to improve the write–erase efficiency of viologen based ECDs include: (i) chemical tethering of the viologen to the surface of an electrode or by immobilizing the viologen species within a semi-solid electrolyte [3] and (ii) by choosing asymmetric viologens, which yield solid radical cations [4]. To circumvent this, bulky substituents are attached to the N,N'- positions of the bipyridyl, which coerce the radical cation out of planarity, prevent re-arrangement, thus inhibit stacking and make the process reversible and therefore rendering them conducive for switchable electrochromic devices [5-7]. To address these issues, we have selected 5,6-dimethylbenzimidazole (chapter 6A) and indole moieties (chapter 6B), as both these moieties can offer steric hindrance and also can act as ligands which can donate electron density or interact with the electron deficient 4,4'-bipyridinium core within the viologen derivative. Thus new derivatives of viologen salts containing the 5,6-dimethylbenzimidazole moiety connected by a butyl chain and also containing the indole moiety connected by an ethyl chain were synthesized and characterized. The electrochromic characteristics of these two materials in a device are discussed in detail in this chapter.

The performance attributes of the viologen based electrochromic device coupled with the ease of synthesis of a stable polymeric semi solid electrolyte and facile device fabrication, serve as a paradigm for

developing enhanced contrast, durable and rapid switching electrochromic devices for display and smart window applications.

6A.2 Experimental

6A.2.1 Synthesis of 1-(4-bromobutyl)-5,6-dimethyl-1H-benzimidazole (2)

To 1.0 g of 5,6-dimethyl-1H-benzimidazole (**1**) (6.8 mmol), 1.4 g of K_2CO_3 (10.2 mmol) was added and dissolved in 30 mL of dried acetonitrile and stirred for 30 minutes under ice cold conditions. 1.77 g of 1,4-dibromobutane (8.2 mmol) was added drop-wise under N_2 atmosphere and the reaction was stirred at 60 °C for 6-8 h. The reaction mixture was filtered and the filtrate was concentrated under reduced pressure. Crude product was purified through the column chromatography (dichloromethane/ethyl acetate**:** 95:5 to 85:15) as pale yellow viscous liquid (**2**). Yield (0.86 g, 45%) for (**2**). This compound is unstable and the next reaction was implemented immediately. [TLC control (dichloromethane/ethyl acetate 7:3, R_f(**1**) = 0.50, R_f(**2**)=0.60, UV detection]. IR (MIR-ATR, 4000–600 cm^{-1}): ν_{max} = 3075, 2923, 2853, 1627, 1563, 1498, 1469, 1218, 1142, 1022, 870, 841, 720,621 cm^{-1}. ^{1}H NMR (CDCl$_3$, 400 MHz): δ = 7.76 (s, 1H, Ar-H), 7.55 (s, 1H, Ar-H), 7.15 (s, 1H, Ar-H), 4.13–4.17 (t, 2H, -CH$_2$), 3.36–3.40 (t, 2H, -CH$_2$), 2.37 (s, 3H, Ar-CH$_3$), 2.39 (s, 3H, ArCH$_3$), 2.00-2.05 (m, 2H,-CH$_2$) and 1.84-1.89 (m,2H,-CH$_2$) ppm. ^{13}C NMR (CDCl$_3$, 100 MHz): δ=142.5 (s, Ar-C), 142.0 (d, Ar-C), 132.2 (s, 2C, Ar-C), 131.1 (s, Ar-C), 120.4 (d, Ar-CH), 109.7 (d, Ar-CH), 44.2 (t, -CH$_2$), 32.6 (t, -CH$_2$), 29.7 (t, -CH$_2$), 28.4 (t, -CH$_2$) and 20.6 (q, Ar-CH$_3$), 20.3 (q, Ar-CH$_3$) ppm. HR-MS (APCI+) m/z calculated for $[C_{13}H_{18}BrN_2]^+ = [(M+H)]^+$: 281.0648; found: 281.0640.

6A.2.2 Synthesis of 1,1′-bis[4-(5,6-dimethyl-1H-benzimidazole-1-yl)butyl]-4,4′-bipyridinium dibromide (IBV) salt (3)

To 1.0 g of 1-(4-bromobutyl)-5,6-dimethyl-1H-benzimidazole (**2**) (3.56 mmol), added 0.221 g of 4,4′-bipyridyl (1.42 mmol), dissolved in dried acetonitrile (50 mL) and continued stirring under N_2 atmosphere at 45-50 ^{0}C for 72 h. The crude precipitate was washed with ethyl acetate to remove unreacted 4,4′-bipyridyl. The precipitate was purified by repeated precipitation using methanol/acetone. The product was washed with n-hexane and with dry diethyl ether, and vacuum dried at 60 °C for 4 h. This viologen salt (**3**) (IBV) is a pale yellow powder. Yield (0.845 g, 83%) and it was calculated with respect to 4,4′-bipyridyl. Melting point: Decomposed at 170 °C. IR (MIR-ATR, 4000–600 cm^{-1}): ν_{max} = 3018, 2980, 2944, 1637, 1563, 1488, 1447, 1362, 1218, 1175, 1022, 1001, 864, 817, 720, 603 cm^{-1}. ^{1}H NMR : (CD$_3$OD, 400 MHz): δ=9.06-9.09 (dd, 2H, Ar-H), 8.92-8.93 (d, 1H, Ar-H), 8.70-8.74 (m, 2H, Ar-H), 8.33-8.42 (m, 2H, Ar-H) 7.97 (d, 1H, Ar-H), 7.86-7.89 (m, 2H, Ar-H), 7.45-7.49 (t, 1H, Ar-H), 7.23-7.27 (m, 2H, Ar-H), 7.15 (d, 1H, Ar-H) ppm. ^{13}C NMR (CD$_3$OD, 100 MHz): δ=151.8 (d, 2C Ar-CH), 151.2 (s, 2C, Ar-C), 138.7 (d, 2C, Ar-CH), 131.4 (d, 2C, Ar-CH), 127.2 (s, 2C, Ar-C), 127.0 (d, 2C, Ar-

CH), 123.6 (d, 2C, Ar-CH), 123.5 (s, 2C, Ar-C), 123.2 (s, 2C, Ar-C), 120.2 (d, 2C, Ar-CH), 114.1 (s, 2C, Ar-C), 111.5 (d, 2C, Ar-CH), 47.6 (t, 2C, N-CH$_2$), 45.3 (t, 2C, N-CH$_2$), 27.1 (t, 2C, N-CH$_2$-CH_2), 26.8 (t, 2C, -CH_2-CH$_2$-N) and 20.5 (q, 4C, 4×Ar-CH$_3$) ppm. HR-MS (ESI+) m/z calculated for $[C_{36}H_{42}Br_2N_6]^+$ = [M+2Na]$^+$: 762.2; found: 762.2.
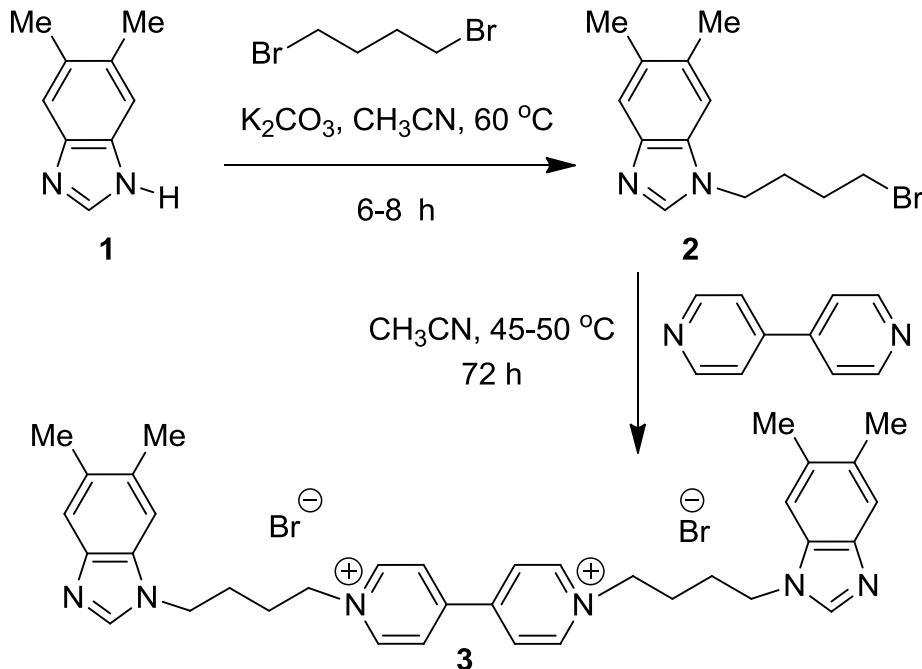
Scheme 6A.1: Two step synthesis of IBV salt (**3**).

6A.2.3 Fabrication of ECD with IBV salt

The monomer HEMA was passed through a neutral alumina column to remove the inhibitor. The ionic liquid (EtMeIm$^+$N(CN)$_2^-$) and N,N-dimethylformamide were taken in a 1:2 weight ratio, and 20-25 wt% of HEMA and 3-4 wt % of benzoyl peroxide were added. For preparing an electrochromic device, 0.025 M IBV salt was dissolved in the electrolyte solution. All the contents were sonicated for 15 minutes. A cavity was created between two electrodes; the cathode was a blank FTO coated glass substrate and the anode was a Prussian blue film coated on FTO/glass. A 0.64 mm thick and 3 mm wide adhesive acrylic tape was employed as the spacer, which prevented the shorting of the two electrodes and also held the device assembly together. The electrolyte solution containing the monomer (HEMA) and the IBV salt was injected into the device. *In-situ* thermal polymerization of the monomer was carried out by heating the above prepared electrolyte solution at 60 °C for 12 – 15 h in an oven. A transparent, pale blue colored device encompassing the electrolyte in the form of a gel was obtained and all the edges were sealed with epoxy. The device, hereafter is referred to as the IBV/P(HEMA)/EtMeIm$^+$N(CN)$_2^-$/PB device.

6A.3 Results and discussion

6A.3.1 XPS studies

The survey spectrum of the IBV salt and the core level spectra are shown in Figure 6A.1. The survey spectrum shows distinct peaks from C1s, Br3p, Br3d, N1s and O1s, indicating the presence of these elements in the sample. The deconvoluted C1s spectrum shows two peaks at 284.5 and 285.8 eV, which are attributed to the C-C and C-N groups in the salt. The deconvoluted N1s spectrum shows three peaks at 403.4, 401.1 and 396.3 eV, which can be attributed to the quaternary nitrogen ($-N^+$), the $-N=$ bonds and the tertiary nitrogen groups respectively. The Br3d core level spectrum shows an intense, symmetric peak centered at 67 eV, which is slightly downshifted in comparison to the Br3d peak typically observed at 70 eV for covalently bonded bromine [8-10]. This shift to a lower binding energy is suggestive of ionic Br^-, implying the formation of N^+-Br^- ionic bonds or salt formation. Similarly, an enlarged view of the two components of the Br3p spin-orbit split doublet is shown as an inset of Figure 6A.1a.
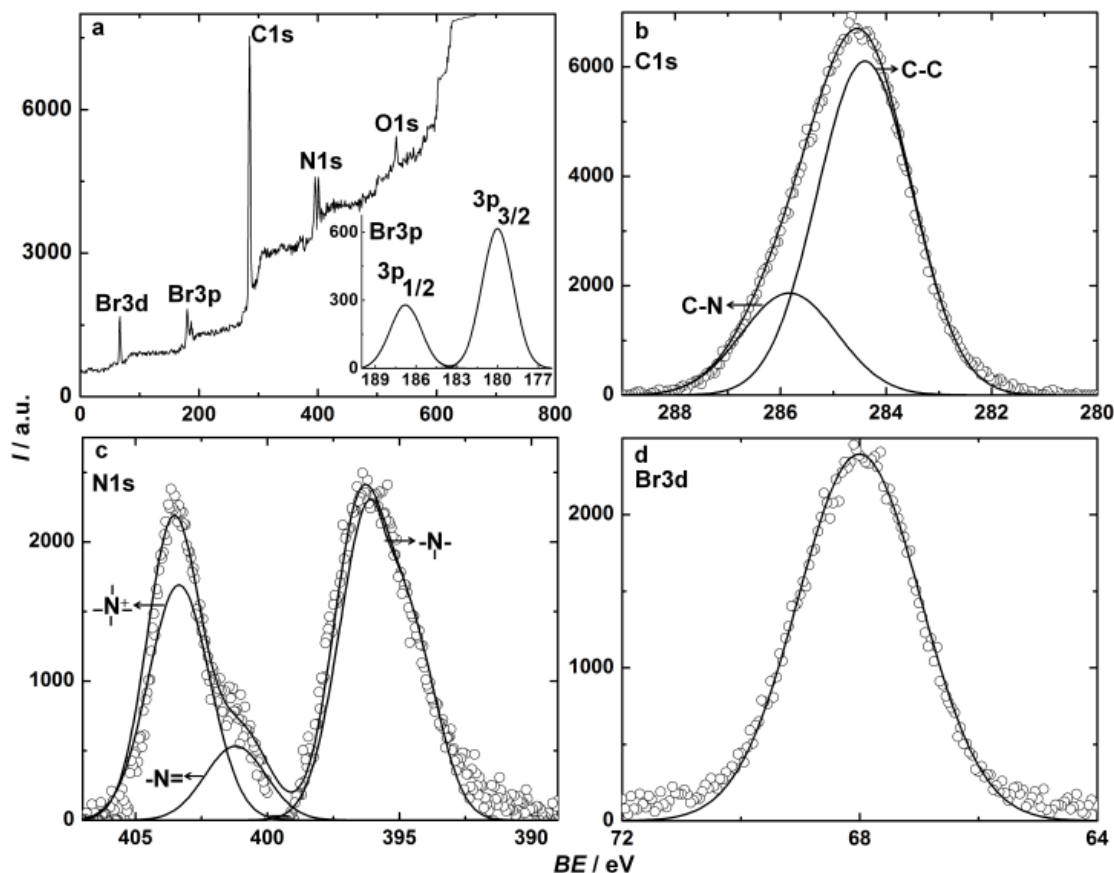
Figure 6A.1 (a) XPS survey spectrum, and deconvoluted core level spectra of (b) C1s and (c) N1s and (d) Br3d of the IBV salt. Inset of (a) shows the enlarged view of the Br3p peak from IBV salt.

The peaks at 180 and 187 eV with an almost 2:1 intensity ratio, are ascribed to the $Br3p_{3/2}$ and $Br3p_{1/2}$ components. Since these two peaks appear at positions, downshifted relative to the positions of 183 and 190 eV for covalently bonded Br in literature [8], this implies that the nature of the bond formed by Br in the IBV salt is ionic and not covalent. The lack of evidence for the existence of covalently bonded Br, also indicates that the final product (or IBV salt) contains no traces of unreacted precursor (containing covalently bound Br). Thus, XPS data analysis provides evidences in support of the formation of the IBV salt as proposed in Scheme 6A.1.

6A.3.2 Electrolyte and IBV salt characteristics

TGA plots of the *in-situ* polymerized gel electrolyte (semi-solid), IL (ionic liquid) and IBV salt (solid powder) in the 30–600 °C temperature range are shown in Figure 6A.2a and 6A.3 (Figure 6A.3 is the TGA plot of the IBV solid). The figure shows the weight losses in the samples as a function of temperature. For in-situ gel, the initial weight loss upto 60 °C is attributed to the evaporation of adsorbed moisture from the sample; thereafter, a plateau was observed till 270 °C, indicating that the gel undergoes decomposition only at high temperatures and therefore can be incorporated in an electrochromic device (for which usually the upper limit of operational temperature is stipulated to be ~ 90 °C). The pristine ionic liquid was found to be stable upto 290 °C. The IBV salt decomposed only at ~270 °C (Figure 6A.3), which illustrates its' suitability for any electrochemical device application. The photographs of the electrolyte solution (prior to temperature induced polymerization) with and without the IBV salt are shown as insets in Figure 6A.3. The IBV salt completely dissolves in the liquid electrolyte to yield a yellow transparent solution, indicating good compatibility with organic solvents like DMF and the ionic liquid. The ability of the IBV salt to form radical cations by chemical reduction was also confirmed by using sodium hydrosulfite in ammonia, and a deep blue color was obtained in solution phase (Figure 6A.2, inset c). The linear sweep voltammogram of the *in-situ* polymerized gel is shown in Figure 6A.2b, and the gel was observed to be electrochemically inert in the voltage range of −2 V to +2 V, indicating a potential stability window of about ~4 V, which is adequate for electrochromic device application. The transmittance of the gel electrolyte in the visible region (Figure 6A.2c) was found to vary between 60-65%. Since the electrolyte is optically transparent in the 400-750 nm wavelength region, it can be employed for fabricating transmissive electrochromic devices. The ionic conductivity of the gel electrolyte was found to be 0.26 mS cm^{-1} at room temperature and it varied insignificantly with temperature; as conductivity increased from 0.21 to 0.27 mS cm^{-1} on raising temperature from −5 and 10 to 70 °C in steps of 10 °C (Figure 6A.2d). Previously, electrochromic devices employing methacrylate-based polymer electrolytes exhibited good ionic conductivity of 0.7 mS cm^{-1} at 20 °C, which is comparable to our observed value [11]. For any electrochemical device, ideally, the ionic conduction

capability of the electrolyte should be invariant within the operational temperature window of the device. The *in-situ* polymerized gel fulfills this pre-requisite, thereby justifying its' use as the electrolyte in a solid-state electrochromic device.
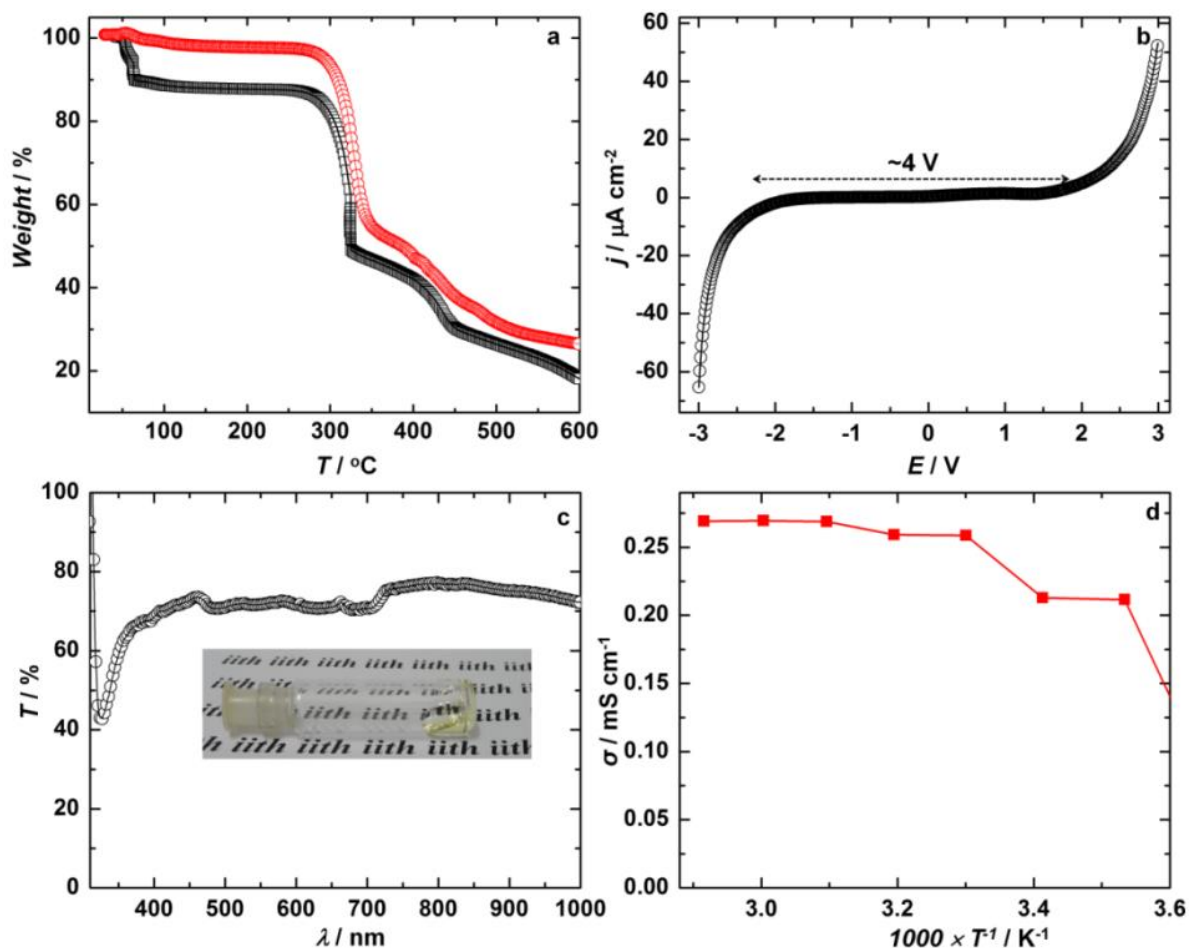
Figure 6A.2 (a) TGA curves for the pristine ionic liquid: [EtMeIm$^+$N(CN)$_2$$^-$] (○) and the P(HEMA)/EtMeIm$^+$N(CN)$_2$$^-$/DMF gel electrolyte (□), (b) LSV plot of the P(HEMA)/EtMeIm$^+$N(CN)$_2$$^-$/DMF gel electrolyte recorded at a scan rate of 20 mV s^{-1} between two Pt electrodes, (c) variation of transmittance as a function of wavelength and (d) ionic conductivity *versus* reciprocal absolute temperature curve for the P(HEMA)/EtMeIm$^+$N(CN)$_2$$^-$/DMF gel electrolyte. Inset of (c) shows a photograph of the semi-solid gel.
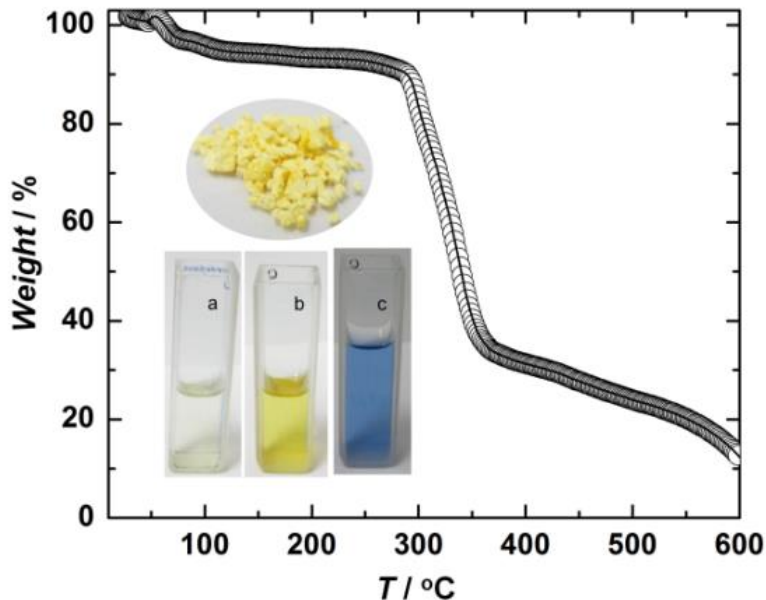
Figure 6A.3 TGA plot of the IBV salt in the 30 – 600 °C temperature range. Digital photographs of the as-synthesized yellow colored IBV salt, and solutions of (a) blank electrolyte: HEMA-DMF-IL (b) IBV salt in electrolyte and (c) IBV salt dissolved in a solution of sodium hydrosulfite in ammonia, showing the chemical reduction of IBV^{2+} to IBV$^{+\bullet}$ (blue).

6A.3.3 Cyclic voltammetry

   "Type II" electrochromes, undergo a soluble to insoluble transition on an electrochemical reduction from aqueous solutions [2]. Similarly, the IBV salt prepared herein is a "type II" electrochrome. The cyclic voltammograms for the IBV/P(HEMA)/EtMeIm^{+}N(CN)$_2$$^{-}$/PB device, recorded within the potential limits of −0.8 to +0.2 V and between −1.5 to +0.2 V are shown in Figure 6A.4a and b. In the cathodic branch, the reduction peak observed at −0.62 V (Figure 6A.4a) is assigned to the formation of the dark blue radical cation salt on the FTO surface, which is followed by the oxidation to the di-cation and its' dissolution in the electrolyte at −0.53 V, in the reverse sweep. The peak separation was 0.09 V. The one electron oxidation and reduction reaction occurs as shown in the first step of the equation (6A.1).

104

$$\text{IBV}^{2+} \underset{-e^-}{\overset{+e^-}{\rightleftharpoons}} \text{IBV}^{+\cdot} \underset{-e^-}{\overset{+e^-}{\rightleftharpoons}} \text{IBV(0)} \quad\text{------} \quad (6A.1)$$

IBV is

$X^- = Br^-$ or $N(CN)_2^-$

The cyclic voltammogram shown in Figure 6A.4b illustrates the two redox states of the IBV salt. We observed a second reduction peak at −1.08 V. These two peaks correspond to the monovalent radical cation formation followed by formation of the neutral viologen, upon further increasing the reduction potential, as shown in the second step of equation (6A.1). In the anodic branch, the first oxidation peak at −1.06 V corresponds to the radical cation formation and the second peak at −0.65 V is attributed to the di-cation formation. The neutral viologen is colorless or is expected to have a pale color. However, we did not observe any pale colored deposit on the electrode in the cathodic branch, thus providing evidence for comproportionation reaction. Also, the ratio of peak currents represented by i_{pc}/i_{pa} is 1.6 for the first pair of redox peaks and it is considerably skewed for the second pair of redox peaks. The fact that it is very much greater than unity for the second pair of redox peaks indicates that a comproportionation reaction, as shown in equation (6A.2), involving the fully oxidized di-cation and the fully reduced neutral viologen occurs at the electrode surface at higher potentials [12,13].

$$\text{IBV}^{2+} + \text{IBV(0)} \rightarrow 2\text{IBV}^{+\bullet} \qquad\qquad (6A.2)$$

The dimer formation is generally not feasible in non-aqueous solvents [14,15]. However, in a previous study, Sammells *et al.* observed a deep violet color as the product of mono-reduction of a heptyl viologen, and a more intense violet color (of the same hue) was the product of di-reduction [16]. Here, we too observed the deep blue hue for IBV/P(HEMA)/EtMeIm$^+$N(CN)$_2^-$/PB device, even when the negative bias was increased to −2.6 V, indicating that the neutral viologen exists probably as a transition state entity.

Figure 6A.4 Cyclic voltammograms of the IBV/P(HEMA)/EtMeIm$^+$N(CN)$_2$$^-$/PB device recorded between potential limits of (a) −0.8 and +0.2 V and (b) −1.5 and +0.2 V at a scan rate of 2 mV s^{-1} and (c) between −0.8 and +0.2 V at different scan rates of 2, 5, 10, 20, 50 and 100 mV s^{-1}.
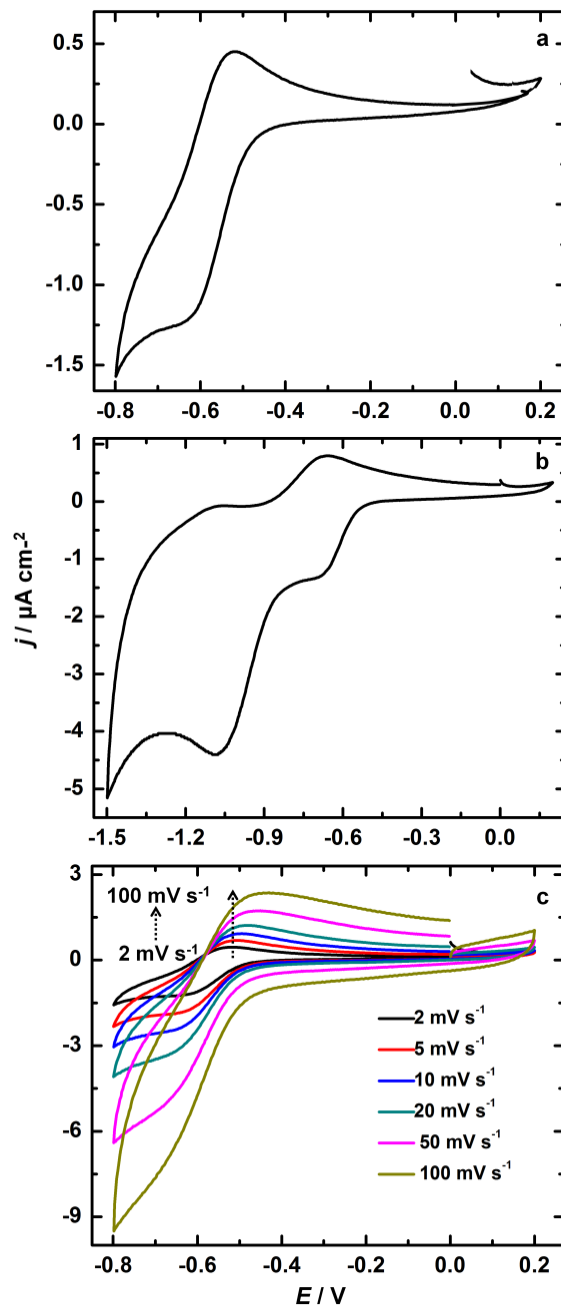
Since the reversible transition between the deep blue and colorless hues was easily achieved within the voltage limits of −0.8 to +0.2 V, the effect of scan rate on the redox response of the IBV salt was examined within these limits (Figure 6A.4c). With increasing scan rate (from 2 to 100 mV s^{-1}) , the

oxidation peak shifts to less negative potentials, the reduction peak shifts to more negative potentials, and the peak separation increases.

6A.3.4 Spectroelectrochemistry of IBV based device

The *in situ* UV–vis absorption and transmittance spectra of the IBV/P(HEMA)/EtMeIm$^+$N(CN)$_2^-$/PB device measured under different dc reduction potentials (applied to the blank electrode) in the range of -0.5 to -2.6 V and under oxidation potentials of $+0.5$ and $+1.0$ V, are shown in Figure 6A.5. The device encompasses the semi-solid state electrolyte with the ionic liquid: EtMeIm$^+$N(CN)$_2^-$ and 25 wt.% of the polymer P(HEMA) and 25 mM IBV salt dissolved therein. A PB film served as the charge balancing counter electrode layer in the device. Under oxidation potentials of $+0.5$ and $+1.0$ V and in the as-fabricated state, the device shows an absorption peak at 385 nm, which is attributed to the charge transfer between the IBV^{2+} cation and the Br$^-$ anion [17]. No strong absorption is seen in the visible region (Figure 6A.5a). Upon applying a reduction potential of -1.0 V to the device, a blue film of the IBV radical cation (which is insoluble in the electrolyte) is formed on the FTO surface corresponding to the IBV^{2+} to IBV$^{+\bullet}$ transition. The blue color deepens and an absorption peak (λ_{max} at around 605 nm) reflecting the corresponding increase in the number of color centers or the radical cation proportion, progressively gains intensity with increasing potential. This peak is assigned to the intra-molecular charge transfer in the bipyridyl moiety of the IBV radical cation. The device attains a deep blue color in the fully reduced state (E $= -2.6$ V), and a photograph showing the blue device is also shown in Figure 6A.5c. Two satellite peaks at 562 and 664 nm, on either side of the main absorption peak are also observed and these have pronounced intensities in the fully reduced state (E $= -1.0$ to -2.6 V). Whilst reduction of IBV^{2+} to IBV$^{+\bullet}$ occurs at the cathode, at the anode, the Prussian white (PW) oxidizes to form Prussian blue (PB). The two processes are complementary and a dark blue hue is achieved for the device. The reason for the retention of the deep blue hue even at a high cathodic potential of -2.6 V, is the comproportionation reaction, which causes the neutral viologen to react with a di-cation and form the radical cation, as expressed in equation (6A.2) [18]. The spectral peak below 410 nm also experiences an intensity enhancement as the applied reduction potential is raised from -0.5 V to -2.6 V; this could be due to an increased interaction between the positively charged IBV$^{+\bullet}$ moieties and the negatively charged dicyanamide ions from the electrolyte gel [19]. However, upon further increasing the cathodic potential to values above -2.6 V, air-bubbles were formed in the device, and the absorption intensity acquired saturation. On the other hand, in the fully oxidized state ($+1.0$ V applied to the blank FTO electrode in the device), the device acquires an almost transparent hue which can also be perceived in the inset of Figure 6A.5c.
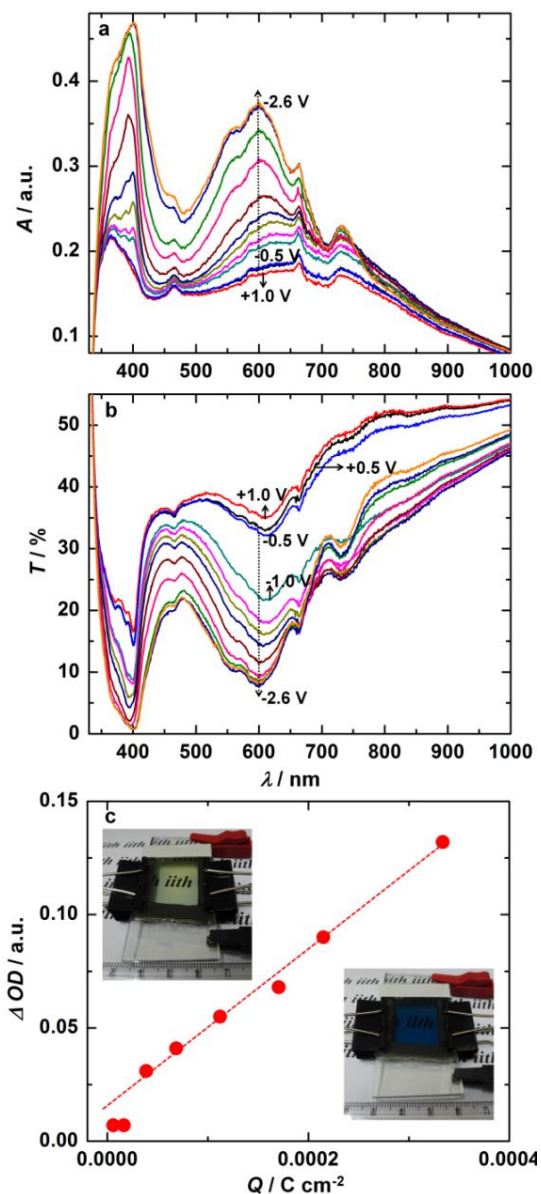
Figure 6A.5 *In-situ* (a) absorption spectra and (b) normalized transmission spectra of the IBV/P(HEMA)/EtMeIm$^+$N(CN)$_2^-$/PB device recorded under different reduction potentials of: –0.5 V and from –1 to –2.6 V in steps of 0.2 V, and under oxidation potentials of +0.5 and +1.0 V; all potentials applied to the blank FTO electrode or cathode of the device. (c) ΔOD *versus* charge density plot at a monochromatic wavelength of 605 nm (●) for the IBV/P(HEMA)/EtMeIm$^+$N(CN)$_2^-$/PB device with OD response under +1 V in (a) used as reference for determination of ΔOD. Digital photographs of the electrochromic device in fully colored (E = –2.6 V) and fully bleached (E = +1.0 V) states are shown as an inset of (c).

In the reduced state, the deposited viologen radical cations are somewhat stabilized as mono-cation radical species on the FTO surface possibly due to the steric hindrance offered by the bulky imidazole groups attached to the bi-pyridinium radical cations, which prevents radical couplings. Evan et al., previously observed that mesityl viologens, do not undergo radical dimerization even at low temperatures [20]. But here, the steric crowding engendered by the benzimidazole groups, does not allow the two mono radical cations or $IBV^{+\bullet}$ to approach close enough for the spin-pairing interaction to overcome the repulsion energy. This can be observed in the UV-visible spectra, Figure 6A.5a, as there were no absorptions around 900 nm region, which are generally observed whenever viologen dimers are formed [21,22]. The transmittance *versus* wavelength plots for the device, under the same reduction/oxidation potentials are displayed in Figure 6A.5b. The bleached state transmittance of the device is 65.5% at 605 nm when an external bias of 0 V was applied. The maximum transmission modulation ($\Delta T = T (+1.0 \text{ V}) - T (-2.6 \text{ V})$) offered by the device, at photopic wavelengths of 500 and 605 nm are 19.4 and 30.5% respectively, which are sufficient for electrochromic window applications. In the past, Lin et al., observed a transmission modulation of 59% at 609 nm, for a PB and a heptyl viologen ($HV(BF_4)_2$) solution based electrochromic device [23].

When a series of voltages (from -1.0 to -2.6 V) are applied, the device gets colored; the values of injection charge were determined at each bias by chronoamperometry and these values were used for plotting the optical density change (ΔOD) *versus* inserted charge per unit area (Q/A) (Figure 6A.5c). The slope of the ΔOD versus intercalated charge per unit area profile yields the coloration efficiency (CE) of the device at a monochromatic wavelength (Equation 2.2). We used 605 nm or λ_{max} for calculating the coloration efficiency and the reference potential for estimating the ΔOD values was $+1.0$ V. The CE at 605 nm is calculated to be 725 $cm^2 C^{-1}$ for the $IBV/P(HEMA)/EtMeIm^+N(CN)_2^-/PB$ device which is adequate for ECDs. In a previous report, Hu et al., observed a CE of 342.2 $cm^2 C^{-1}$ (at 610 nm) for an all-solid-state electrochromic device with heptyl viologens [14] and in yet another study, a CE of 163 $cm^2 C^{-1}$ (at 650 nm) was observed for a device based on poly(butyl viologen) [24]. A composite of In/Sn oxide nanoparticles and heptyl viologen showed a CE of 912 $cm^2 C^{-1}$ [25].

6A.3.5 Switching kinetics of IBV based device

The color-bleach characteristics for the $IBV/P(HEMA)/EtMeIm^+N(CN)_2^-/PB$ device were recorded at half-cycles corresponding to 3.0 s and 5.0 s and by switching potentials of ±2.0 V (Figure 6A.6a). The kinetic responses were recorded at the λ_{max} of 605 nm. Coloration time was observed to be 2.1 and 2.5 s (when subjected to step times of 3 and 5 s respectively). Bleaching time was 2.2 and 3.3 s for 3 and 5 s half-cycles. Our color-bleach times are comparable to values of 1.3 and 4.7 s reported for viologen based devices [14,24]. The device was subjected to continuous cycling at a scan rate of 100 mV s^{-1}, between –

0.8 to +0.2 V and the CV plots for the first and thousandth cycle are displayed in Figure 6A.6b. The cathodic peak current decreased only by 18.9% of its original value after 1000 cycles, indicating that the IBV salt based device can endure repetitive transparent ↔ blue transitions without undergoing degradation. Such a robust, high contrast device is most conducive for electrochromic window applications.
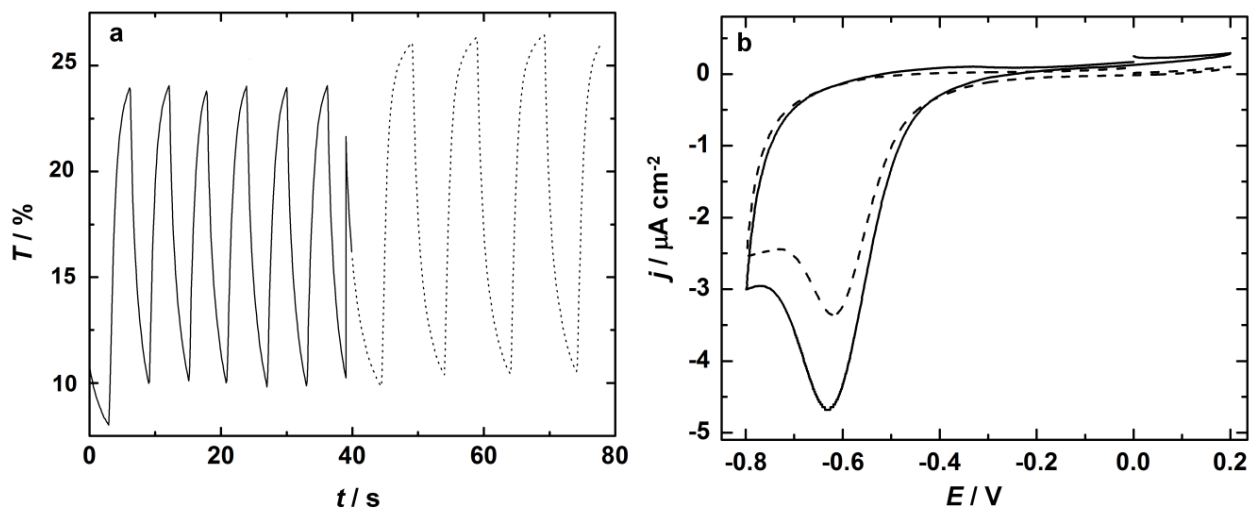
Figure 6A.6 (a) Normalized absorbance *versus* time curves for the IBV/P(HEMA)/EtMeIm$^+$N(CN)$_2^-$/PB device at a λ_{max} of 605 nm, under a square wave dc potential of ±2.0 V and under step times of 3 (—) and 5 (.....) s. (b) Cyclic voltammograms of the IBV/P(HEMA)/EtMeIm$^+$N(CN)$_2^-$/PB device recorded in the 1st cycle (—) and after 1000 cycles (----) (scan rate = 100 mV s^{-1}).

6A.3.6 Electrochemical impedance spectroscopy

To understand how transmission modulation and coloration efficiency are controlled by the internal circuit elements of the device, EIS spectra of the IBV/P(HEMA)/EtMeIm$^+$N(CN)$_2^-$/PB device were recorded by superimposition of voltage of 10 mV over different magnitudes of dc potentials. All potentials were applied to the blank FTO electrode of the device. The equivalent circuit displayed in the inset of Figure 6A.7 was found to give excellent fits almost over the entire frequency range of 1 MHz to 0.1 Hz under consideration. The Z″ *versus* Z′ curve for the device, under all dc potentials shows an inclined line profile, except for the curve at −2.0 V, which comprises of a semicircle followed by the straight line response. The point of commencement of the Z″ *versus* Z′ curve, corresponds to the bulk resistance of the ionic liquid based solid polymer electrolyte which lies in the range of ~50 – 60 Ω (over different applied potentials), and its' value was largely independent of the applied dc bias. The subsequent curvature is explained by a parallel combination of resistance due to charge transfer (R$_{CT}$) at the IBV^{2+} gel/FTO interface and the corresponding electrical double layer capacitance (C$_{dl}$). The magnitude of R$_{CT}$

110

increases (from 7.7 μΩ to 26.0 μΩ) with increasing reduction potentials, i.e., ongoing from −0.5 to −1.0 V and in this range, the profile is quasi-linear. The curve tilts towards the real (resistive component, Z') axis, at −2.0 V and the R_{CT} has a value of 35.3 Ω while C_{dl} decreases from 34 to 18 μF (ongoing from −0.5 to −2.0 V).
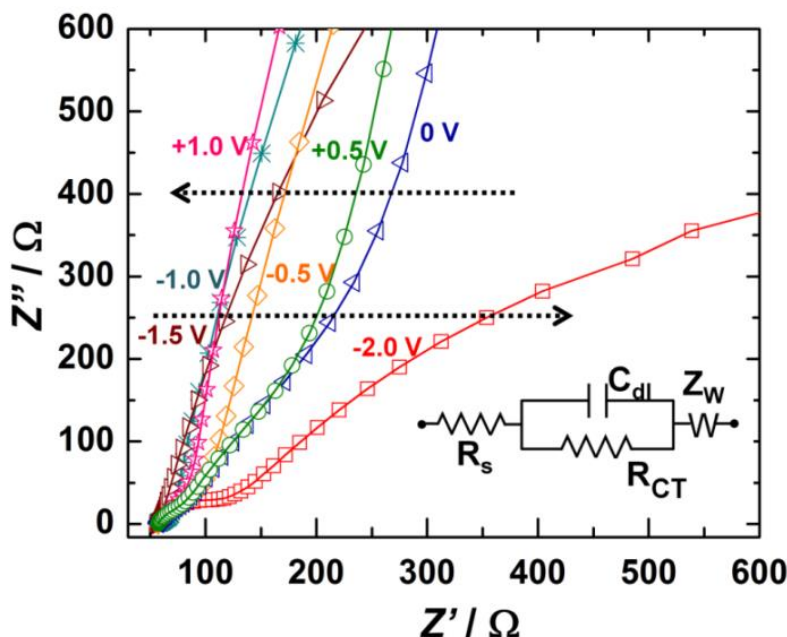
Figure 6A.7 Electrochemical impedance spectra of the IBV/P(HEMA)/EtMeIm$^+$N(CN)$_2^-$/PB device recorded under dc potentials of: 0 (△), +0.5 (○), +1.0 (✳) V and −0.5 (◇), −1 (✳), −1.5 (▽) and −2.0 (□) V, over a frequency range of 0.1 to 10^6 Hz; dc potential applied to the blank FTO electrode/cathode. Inset shows the equivalent circuit used for fitting the experimental data.

The magnitude of charge transfer resistance is a measure of the ease with which ions are transferred across the electrode/electrolyte interface. Here the value of R_{CT} is extremely low under low reduction potentials of −0.5 to −1.0 V. It varies between 7.7 to 26 μΩ. Coloration in this potential range is therefore induced by a capacitive Faradaic charging mechanism rather than resistive charge transfer. However, once the insoluble radical cation (IBV$^{+\bullet}$) forms a blue layer over the FTO surface, further insertion of electrons from the external circuit and release of anions from the viologen backbone into the gel electrolyte are hindered by the bulk of this film and therefore the profile acquires a dominant resistive component than capacitive. On subjecting this electrode to potentials of +0.5 and +1.0 V, the curve again reverts to a capacitive response, primarily because the IBV$^{+\bullet}$ film dissolves in the gel by undergoing oxidation to the IBV^{2+} di-cation, and therefore only the double layer of charge encompassing the negative charges from the dicyanamide and bromide anions in the gel and the positive charges on FTO surface contributes to impedance. It is apparent that both the resistive and capacitive charging- charge transfer

mechanisms operative at negative potentials, commensurate with the high ΔOD achieved for the device which effectively translates into a high CE of 725 cm^2 C^{-1}.

6A.4 Summary

A novel 1,1′-bis[4-(5,6-dimethyl-1*H*-benzimidazole-1-yl)butyl]-4,4′-bipyridinium dibromide (viologen) (IBV) was synthesized and characterized. XPS studies ascertained the formation of the IBV salt as distinctive contributions from quaternary and neutral nitrogens and electrostatically bonded bromide were obtained. The viologen was incorporated in an electrochromic device, by dissolution in a dicyanamide based ionic liquid-gel electrolyte having a large ionic conductivity, good thermal stability upto 200 ^{o}C and wide electrochemical potential stability window (of ~4 V) and moderately high optical transparency in the visible region. The device exhibited reversible switching between colorless and dark blue states. It shows a high transmission modulation of 30.5% at 605 nm, an outstanding CE of 725 cm^2 C^{-1} (at 605 nm), good color homogeneity and rapid response times of 2-3 s. The high electrochemical activity of the IBV (viologen) salt was retained even after 1000 repeated switches between the transparent and colored states. The excellent performance attributes of the electrochromic device with this new viologen/novel ionic liquid based gel electrolyte opens up avenues to develop variants of dimethylbenzimidazole based derivatives of 4,4′-bipyridyl, for application in both transmissive and reflective electrochromic devices.

References

[1] P.M.S. Monk, J. Electroanal. Chem. 432 (1997) 175.
[2] P.M.S. Monk, R.J. Mortimer, D.R. Rosseinsky, Electrochromism and Electrochromic Devices, Cambridge University Press, Cambridge, U.K., 2007.
[3] D.C. Bookbinder, M.S. Wrighton, J. Electrochem. Soc. 130 (1983) 1080.
[4] J.A. Barltrop, A.C. Jackson, J. Chem. Soc. Perkin Trans. 2 (1984) 367.
[5] P.R. Somani, S. Radhakrishnan, Mater. Chem. Phys. 77 (2002) 117.
[6] C.L. Bird, A.T. Kuhn, Chem. Soc. Rev. 10 (1981) 49.
[7] H.T. Van Dam, J.J. Ponjee, J. Electrochem. Soc. 121 (1974) 1555.
[8] I. Mazov, D. Krasnikov, A. Stadnichenko, V. Kuznetsov, A. Romanenko, O. Anikeeva, E. Tkachev, J. Nanotech. 2012 (2012) 1.
[9] Z. Jian, H.-T. Liu, B. Wu, C.-A. Di, Y.-L. Guo, T. Wu, G. Yu, Y.-Q. Liu, D.-B. Zhu, Sci Rep. 2 (2012) 662.
[10] Y.P. Zhang, J.H. He, G.Q. Xu, J. Phys. Chem. C 116 (2012) 8943.
[11] J. Reiter, O. Krejza, M. Sedlarkova, Sol. Energy Mater. Sol. Cells 93 (2009) 249.
[12] D.R. Rosseinsky, P.M.S. Monk, J. Chem. Soc. Faraday Trans. 89 (1993) 219.
[13] D.R. Rosseinsky, P.M.S. Monk, J. Chem. Soc. Faraday Trans. 86 (1990) 3597.
[14] C.-W. Hu, K.-M. Lee, K.-C. Chen, L.-C. Chang, K.-Y. Shen, S.-C. Lai, T. -H. Kuo, C.-Y. Hsu, L.-M. Huang, R. Vittal, K.-C. Ho, Sol. Energy Mater. Sol. Cells 99 (2012) 135.
[15] G. Chidichimo, M.D. Benedittis, J. Lanzo, B.C.D. Simone, D. Imbardelli, B. Gabriele, L. Veltri, G. Salerno, Chem. Mater. 19 (2007) 353.
[16] A.F. Sammells, N.U. Pujare, J. Electrochem. Soc. 133 (1986) 1270.
[17] R.J. Mortimer, T.S. Varley, Sol. Energy Mater. Sol. Cells 99 (2012) 213.

[18] P.M.S. Monk, The Viologens: Physicochemical Properties, Synthesis and Applications of the Salts of 4,4′-Bipyridine, J. Wiley & Sons: Chichester, U.K., 1998.

[19] P. Cea, S. Martin, A. Villares, D. Mobius, M.C. Lopez, J. Phys. Chem. B 110 (2006) 963.

[20] J.C. Evans, C.C. Rowlands, C.R. Morris, J. Chem. Soc. Perkin Trans. II 9 (1987) 1375.

[21] R.J. Mortimer, Electrochim. Acta 44 (1999) 2971.

[22] P.M.S. Monk, R.D. Fairweather, J. A. Duffy, M.D. Ingram, J. Chem. Soc. Perkin Trans. II (1992) 2039.

[23] C.-F. Lin, C.-Y. Hsu, H.-C. Lo, C.-L. Lin, L.-C. Chen, K.-C. Ho, Sol. Energy Mater. Sol. Cells 95 (2011) 3074.

[24] T.-H. Kuo, C.-Y. Hsu, K. -M. Lee, K. -C. Ho, Sol. Energy Mater. Sol. Cells 93 (2009) 1755.

[25] Y. Rong, S. Kim, F. Su, D. Myers, M. Taya, Electrochim. Acta 56 (2011) 6230.

Chapter 6B

Effect of ethyl indole in a viologen on its' electrochromic response

6B.1 Introduction

   Use of bulky substituents on viologen's nitrogen atoms can lead to less dimerization and therefore fast switching can be observed [1]. In the last chapter, a new organic viologen with butyl imidazole derivative was studied. In this chapter, a novel cathodically coloring viologen electrochrome: 1,1'-bis(2-(1H-indol-3-yl)ethyl)-4,4'-bipyridinium diperchlorate (IEV), comprising of a 4,4′-bipyridyl core, sandwiched between two indole moieties, was synthesized using 3-(2-bromoethyl)-indole. The indole moieties of the IEV^{2+} salt owing to their electron donating tendency can act like bleaching agents and bleach the viologen faster $(IEV^{+\bullet} \rightarrow IEV^{2+})$ and this hypothesis was used for explaining the improved write–erase efficiency of ECD. The IEV viologen was dissolved in the electrolyte based on an ionic liquid and PB was used as the anodic electrochrome. The synthetic routes for viologen derivatives are time-consuming, typically involving long reflux periods [2,3]. Here, microwave irradiation was used to facilitate the viologen synthesis. This viologen with its bulky ethylindole group and its' effect on the write erase efficiency of the ECD is presented in this chapter.

6B.2 Experimental

6B.2.1 Microwave-assisted synthesis of (1) and preparation of (2) (IEV (ClO$_4$)$_2$)

   3-(2-bromoethyl)-indole (0.3 g, 1.3 mmol), 4,4′-bipyridyl (0.07 g, 0.5 mmol) and dried acetonitrile (2.5 mL) were irradiated in a quartz vessel of 10 mL capacity in a microwave reactor at 300 W for 15 min at 130 °C. The precipitate was filtered and washed with plenty of acetonitrile to remove unreacted reactants and dried under vacuum at room temperature. The organic viologen salt (1) was isolated in the form of a brown colored solid powdery material. Yield (0.22 g, 81%). Melting point: Decomposed at 305 °C. FTIR (4000–600 cm^{-1}): ν_{max} = 3172, 3004, 2853, 1633, 1551, 1498, 1340, 1221, 1168, 1022, 816, 748, 701,632 cm^{-1}. ^{1}H NMR : (DMSO-d$_6$, 400 MHz): δ=10.97 (br. s, 2H, 2 × Ar-NH), 9.11-9.13 (d, 4H, 4 × Ar-H), 8.54-8.56 (d, 4H, 4 × Ar-H), 7.51-7.53 (d, 2H, 2 × Ar-H) 7.36-7.37 (d, 2H, 2 × Ar-H), 7.14-7.15 (d, 2H, 2 × Ar-H), 7.08-7.10 (m, 2H, 2 × Ar-H), 6.94-6.98 (m, 2H, 2 × Ar-H), 4.92-4.95 (t, 4H, 2 × N-CH$_2$), 3.42-3.45 (t, 4H, 2 × Ar-CH$_2$) ppm. ^{13}C NMR (DMSO-d$_6$, 100 MHz): δ=148.99 (s, 2C 2 × Ar-C), 146.01 (d,

4C, 4 × Ar-CH), 136.55 (s, 2C, 2 × Ar-C), 127.07 (s, 2C, 2 × Ar-C), 126.60 (d, 4C, 4 × Ar-CH), 124.57 (d, 2C, 2 × Ar-CH), 121.92 (d, 2C, 2 × Ar-CH), 119.24 (d, 2C, 2 × Ar-CH), 118.43 (d, 2C, 2 × Ar-CH), 112.12 (d, 2C, 2 × Ar-CH), 108.66 (s, 2C, 2 × Ar-C), 62.06 (t, 2C, 2 × N-CH$_2$), 27.27 (t, 2C, 2 × N-CH$_2$-CH_2) ppm. HR-MS (ESI$^+$) m/z value calculated for $[C_{30}H_{28}Br_2N_4]^+$ = $[M+Na]^+$: 625.057; found: 625.060. The viologen of perchlorate salt (IEV (ClO$_4$)$_2$) was obtained by re-precipitation of IEV Br$_2$ (~50 mM) in an aqueous solution of 0.3 M LiClO$_4$ (Scheme 6B.1). The precipitate was filtered and washed with plenty of water, ethanol and dried under vacuum at room temperature, and a brownish orange solid powder (**2**) was obtained. HR-MS (ESI+) m/z value calculated for $[C_{30}H_{28}Cl_2N_4O_8]$ = $[M+Na]^+$: 665.118; found: 665.116.
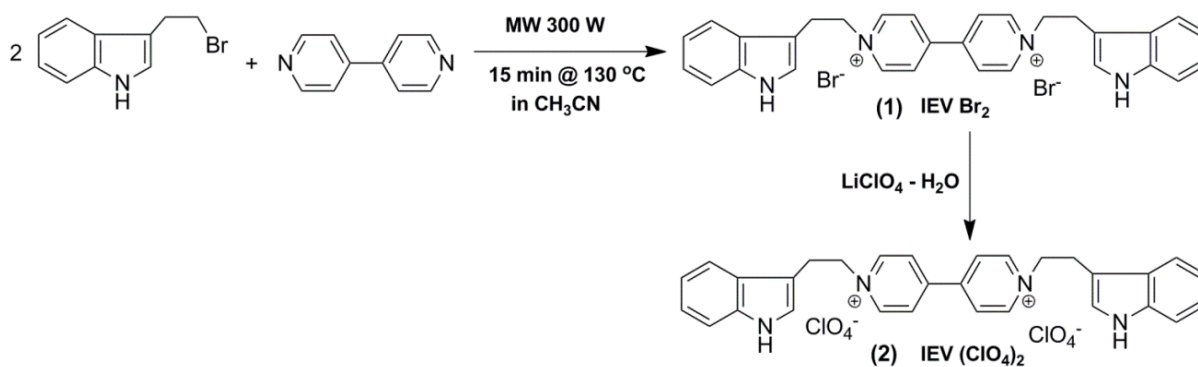
Scheme 6B.1: Synthesis of electrochromic viologen: IEV (ClO$_4$)$_2$.

6B.2.3 Construction of an ECD containing IEV (ClO$_4$)$_2$

For preparing an ECD, a 10 mM IEV (ClO$_4$)$_2$ solution was prepared in a liquid electrolyte solution of DMF and IL in a 1:1 volume ratio and sonication was done for 10 min for complete dissolution. An acrylic adhesive tape (0.64 mm thick and 3 mm wide) was applied along the four edges of the a FTO coated glass plate (cathode). Two 1 to 2 mm wide openings were grafted in the tape along one edge and the complementary electrode (PB) was then placed above this electrode. Except for the two openings, the remainder of this assembly was sealed with an epoxy. The adhesive strip plays the role of a spacer and inhibits the cathode and anode from coming in contact with each other. The IEV (ClO$_4$)$_2$ solution was filled into the device with a syringe through one of the open ports. The four edges and the two open ports were sealed with an epoxy sealant. The ECD was labeled as IEV−PB, and it appears as a transparent, pale yellow colored device of about 2 cm × 3 cm dimensions.

6B.3 Results and discussion

6B.3.1 Features of IEV (ClO$_4$)$_2$ and the ionic liquid electrolyte

The percentage weight loss *versus* temperature profiles of the ionic liquid and the IEV salt are displayed in Figure 6B.1a. A flat contour was observed for the pure IL upto 400 °C, suggesting that the IL is suitable for application to an ECD. Similarly, the IEV salt decomposed only at ~300 °C (Figure 6B.1a), which justifies its' use in an ECD. The formulation of the electrolyte contains DMF, and therefore the ECD electrolyte can be expected to be stable up to 156 °C (its boiling point), sufficient for practical use. The IEV salt completely dissolves in the electrolyte of IL-DMF and a light-yellow clear solution is obtained, for it is highly miscible with non-aqueous high polar solvents like DMF and DMSO. The electrolyte (IEV-IL-DMF) was also found to exhibit 96% transmittance in the visible region, which validates its' incorporation in ECDs such as smart windows. The electrolyte was found to be electrochemically stable in the applied bias range of −1.8 V to +1.8 V, which amounts to a stable voltage window of ~3.6 V, which is sufficient for use in an ECD (Figure 6B.1b). The electrical ionic conductivity of the electrolyte was calculated to be 4.7 mS cm^{-1}, at ambient temperature and it changed insignificantly as a function of temperature, i.e., it varied from 4.5 to 9.3 mS cm^{-1}, when the temperature was changed from 10 to 70 °C (Figure 6B.1c). Previously, ECDs employing imide IL based electrolytes in combination with organic solvents like methanol, acetonitrile exhibited good ionic conductivities in the range of 5-20 mS cm^{-1} at room temperature, which is comparable to our observed value [4]. The increase in the conductivity with temperature is due to higher ionic mobility and reduced viscosity of the medium at higher temperatures. The electrolyte solution of IL-DMF with its' high electrochemical, good thermal stability and large ionic conductivity is a suitable choice for a solution phase organic electrochromic viologen device.
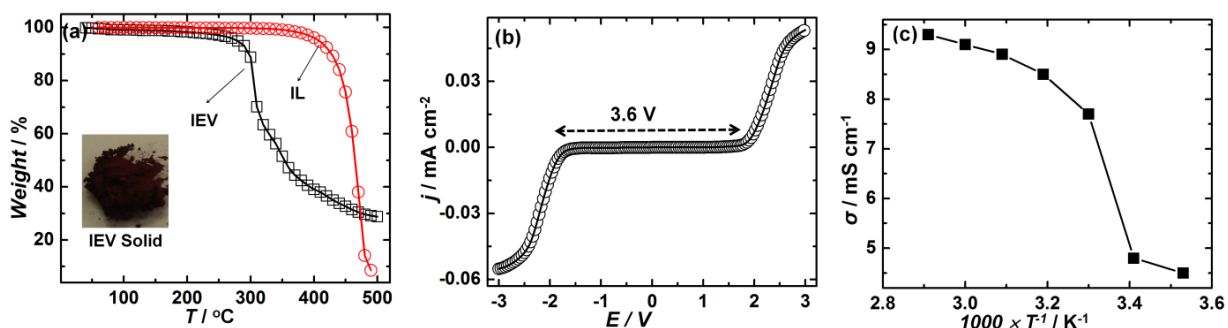
Figure 6B.1 (a) TGA curves for the pristine ionic liquid: 1-Ethyl-3-methylimidazolium bis(trifluoromethylsulfonyl) imide (○) and IEV salt (□), (b) LSV plot of the IL−DMF electrolyte recorded at a scan rate of 20 mV s^{-1} between two Pt electrodes and (c) ionic conductivity *versus* reciprocal absolute temperature curve for the IL−DMF electrolyte. Inset of (a) shows the IEV solid powder.

6B.3.2 Cyclic voltammetry for IEV and IEV based device

The cyclic voltammograms for the viologen (IEV, 10 mM) salt solution in IL and DMF (1:1/v/v) within the voltage window of −1.2 to +0.2 V (using a Ag/Ag$^+$ reference electrode) are shown in Figure 6B.2a. The CV plot shown in Figure 6B.2a illustrates the two redox states of the IEV salt, and corresponds to the monovalent radical cation (IEV$^{+\bullet}$) formation, followed by the formation of the neutral viologen (IEV(0)) as shown in equation (6B.1). The first reduction peak, in the cathodic sweep, is seen at −0.46 V which is attributed to the reduction of the IEV salt to the deep blue colored insoluble radical cationic species, formed uniformly over the transparent conducting substrate (cathode). Another peak is obtained at a higher cathodic potential of −0.94 V, which corresponds to further reduction leading to the formation of the neutral viologen (IEV(0)) (inset of Figure 6B.2a). On changing the sweep direction, the first and second anodic peaks at −0.81 V and at −0.38 V are due to oxidation of (i) neutral IEV(0) to IEV$^{+\bullet}$ and (ii) IEV$^{+\bullet}$ to IEV^{2+} salt respectively. The separations between the anodic and cathodic peaks were 0.11 and 0.13 V for the 1st and 2nd redox pairs respectively.
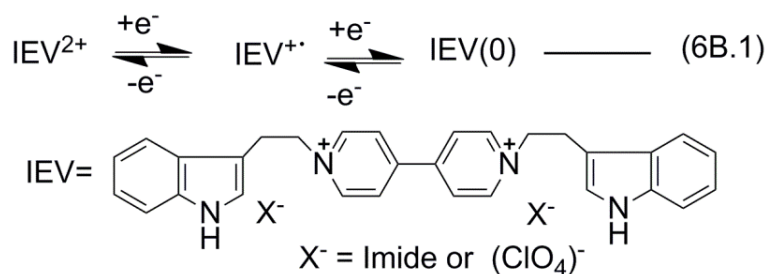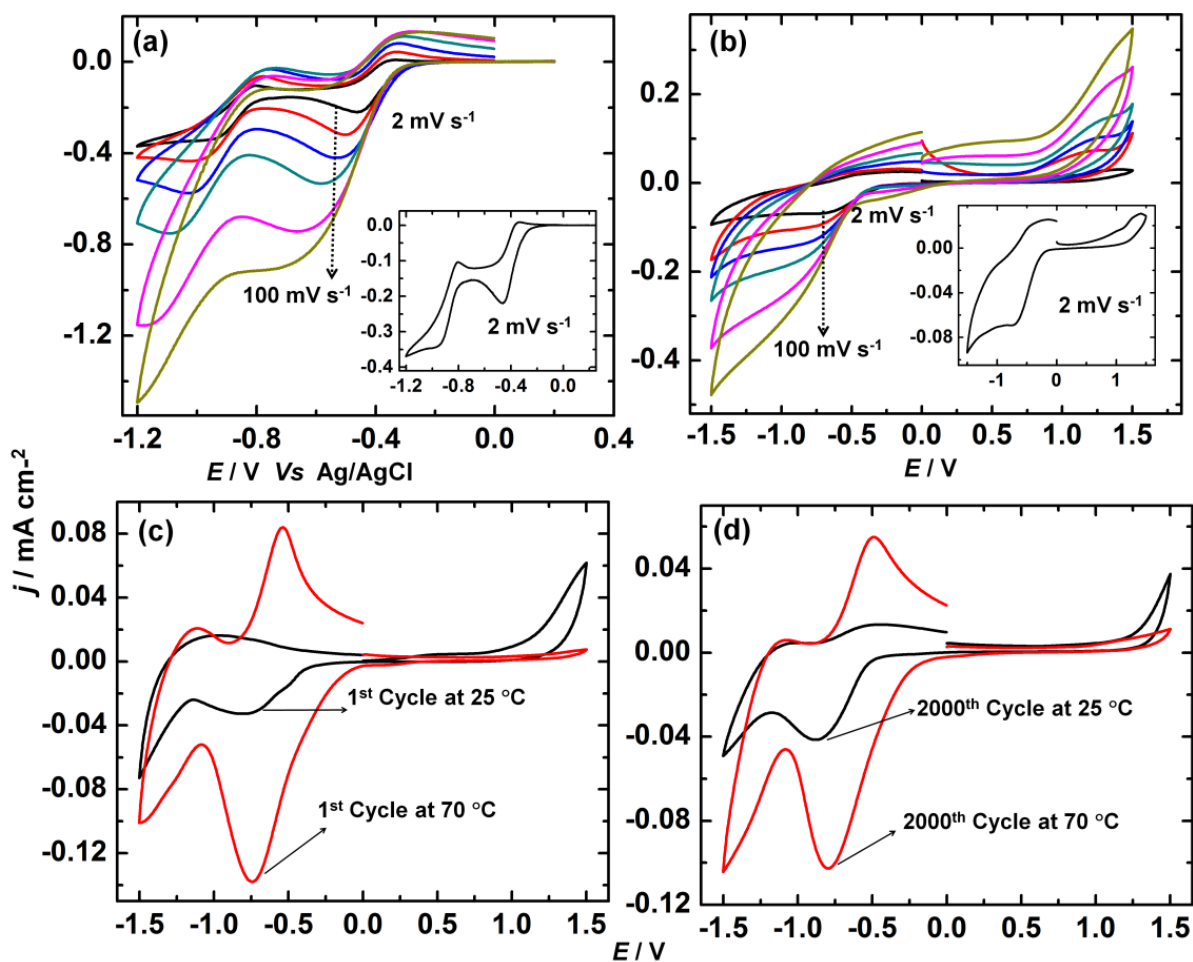
Figure 6B.2 Cyclic voltammograms of the 10 mM IEV salt in the IL−DMF recorded between potential limits of (a) −1.2 and +0.2 V and (b) CV plots of the IEV−PB device at different scan rates of 2, 5, 10, 20, 50 and 100 mV s⁻¹ respectively. CV plots of the 1ˢᵗ and 2000ᵗʰ cycles of the same ECD at temperatures of (c) 25 and (d) 70 °C, recorded at a scan rate of 20 mV s⁻¹ respectively.

Since the transitions between the dark blue and colorless states were achieved in the applied bias ranging from −1.2 to +0.2 V, the influence of sweep rate on the electrochemical switching behavior of the IEV dicationic salt was recorded for the same IEV solution (Figure 6B.2). Upon increasing the scan rate (from 2 to 100 mV s⁻¹), while the oxidation peak shifts to less negative potentials, the reduction peak shifts to more negative potentials, and the peak separation increases. These plots indicate that the reversible process is retained even for the second reduction peak indicating that this new viologen has high redox reversibility for the di-reduced viologens. The CVs recorded for the IEV−PB ECD within the applied voltage range of −1.5 to +1.5 V at various sweep rates in the range of 2 to 100 mV s⁻¹ are shown in Figure 6B.2b. A cathodic peak at −0.70 V (inset of Figure 6B.2b) is attributed to the reduction of IEV²⁺

118

to IEV$^{+\bullet}$ species and the anodic peak at −0.43 V, is ascribed to the conversion of IEV$^{+\bullet}$ to the dicationic IEV salt.

The effect of temperature on the stability of redox species generated by IEV^{2+} was studied by recording CV plots for the IEV−PB ECD at room temperature (25 °C) and at a moderately high temperature of 70 °C, between the potential limits of −1.5 to +1.5 V, at a scan rate of 20 mV s^{-1} (Figure 6B.2c,d). The current densities achieved for the device were higher at 70 °C compared to that of the ECD operating at room temperature. This can due to the increased mobility of the ionic species and also due to an increased contribution from more number of electroactive species of IEV, available for reduction/oxidation, when the temperature is raised. The conductivity of the electrolyte is also slightly increased with temperature, which also contributes to the increased electroactivity of the IEV salt (Figure 6B.1c). The CV of the IEV−PB ECD recorded at 70 °C showed well resolved redox peaks, whereas broad peaks were observed in the case of the room temperature device. The appearance of well resolved CV peaks of IEV at a high temperature indicates that the redox activity is increased at high temperatures, but the viologen is stable, as there are no peaks corresponding to decomposition, seen in the CV plots. In order to further confirm the stability of IEV redox species at high temperatures, the same device was cycled for 2000 cycles, by maintaining the device at 70 °C and the device was found to retain its' characteristic response. The stability of the cycled device is discussed in the later section.

6B.3.3 Spectroelectrochemistry of IEV−PB device

In-situ absorption and percent transmission spectra of the IEV−PB ECD obtained under various magnitudes of negative dc bias (applied to the transparent conducting electrode) ranging from −0.5 to −1.5 V and at three positive dc voltages of +0.5, 1.0 and +1.5 V are displayed in Figure 6B.3. The ECD contains a liquid electrolyte of 10 mM IEV salt dissolved in IL−DMF and a PB layer as the anodic electrochrome. Under oxidation potentials of +0.5, +1.0 and +1.5 V and under zero bias, the ECD produces a peak at λ_{max} = 378 nm, corresponding to charge transfer between the IEV^{2+} di-cation and the ClO$_4^-$ anion or imide ion (from the IL). Upon applying reduction potentials from −0.5 V to −1.5 V, the device showed a typical absorption peak of viologens, with a λ_{max} at ~605 nm. A blue colored insoluble layer of the IEV$^{+\bullet}$ species develops on the transparent conducting substrate (cathode) of the ECD. The observed blue color is due to the intramolecular charge transfer between the two nitrogen atoms (bipyridyl) within the radical cation IEV$^{+\bullet}$. The blue color of the device deepens, as the applied negative potential on blank FTO increases from −0.9 V and thus a trend of gradual increase in intensity of the peak at λ_{max} of 605 nm, was observed. The intensity increases in the visible region (with λ_{max} at 605 nm) with increasing potential, indicating the gradual rise in the population of the blue colored IEV$^{+\bullet}$ species. The

device acquires a dark blue hue in the reduction potential region from −1.1 V to −1.5 V. Additional peaks with high intensities were seen at 568 and 665 nm, especially when the ECD was completely reduced. At the cathode, IEV^{2+} converts to $IEV^{+\bullet}$, and simultaneously, PB is formed by the oxidation of Prussian white (PW) at the anode. These two complementary coloring phenomena work in tandem and as a consequence a dark blue colored ECD is obtained. The photographs of the device at 0 V (as-fabricated), under +1.5 V (bleached state) and −1.5 V (colored state) are shown in Figures 6B.3d, e and f.
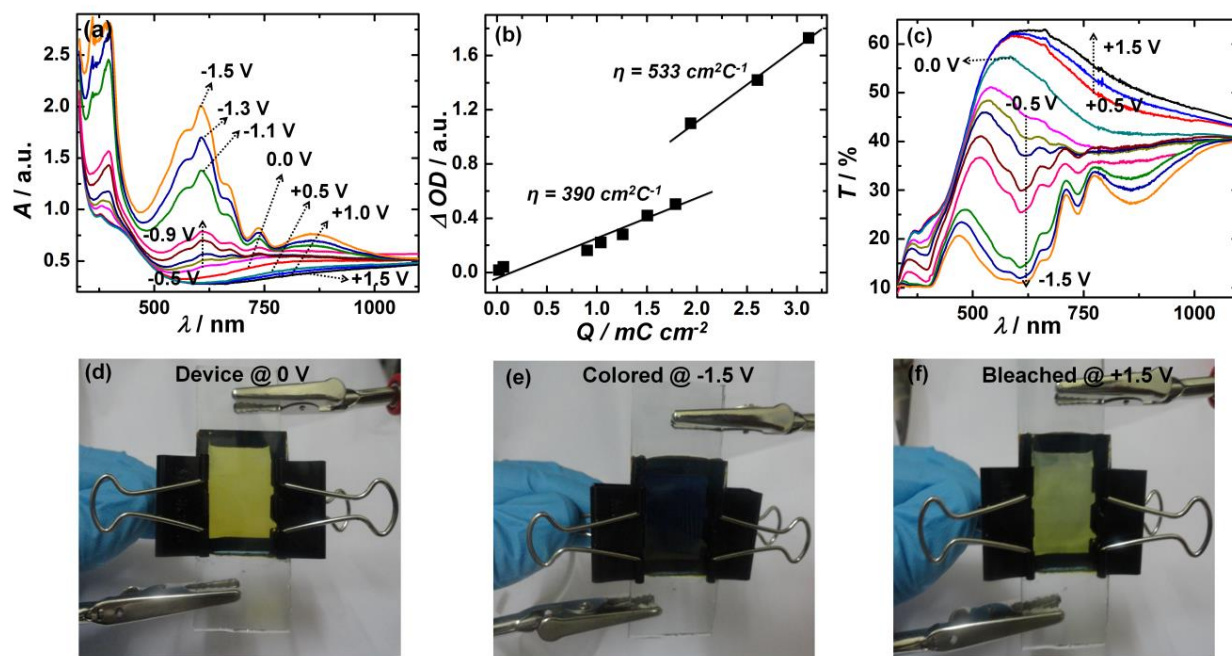
Figure 6B.3 (a) *In-situ* absorption spectra of the IEV−PB device recorded under different reduction potentials of: −0.5 V to −0.9 V in steps of 0.1 V, −0.9 V to −1.5 V in steps of 0.2 V and under oxidation potentials of +0.5, +1.0 V and +1.5 V; all potentials applied to the blank FTO electrode or cathode of the device and (b) ΔOD *versus* charge density plot at a monochromatic wavelength of 605 nm (■) for the IEV−PB device with OD response under +1.5 V in (a) used as reference for determination of ΔOD. (c) The *in-situ* transmission spectra of the same device under same applied potentials as in absorption spectra of (a). Digital photographs of the ECD: (d) as fabricated (0 V), (e) in fully colored (E = −1.5 V) and (f) fully bleached (E = +1.5 V) states respectively.

When the viologen salt is reduced, the insoluble radical cations formed are stable, perhaps, due to the bulkiness of the ethylindole moieties linked to the bi-pyridilium species, which tend to decrease the coupling of the radical cations. Bulkier groups attached to 4,4′−bipyridyl, generally, do not favor dimerization due to steric hindrance to some extent. In literature, various types of aggregate species and dimers of different viologens formed upon reduction were studied by Lee et al., and from the UV-visible

NIR spectra they assigned the different NIR absorption bands corresponding to the aggregates. We also did not observe any intense band near 900 nm, in the *in-situ* spectra of IEV−PB device (Figure 6B.3a). Although non-aqueous solvents do not favor dimerization [5], and since the solution phase electrolyte contains DMF, the dimerization process will be inhibited to some extent.

The ECD was subjected to a series of negative voltages, and the magnitudes of the charge densities intercalated were determined by chronoamperometry (for each value of applied bias). The (ΔOD) *versus* charge density (Q/A) plot is shown in Figure 6B.3b and the slope of this graph directly gives the CE of an ECD. A wavelength of 605 nm, which is λ_{max}, was used for the determination of CE (η) and the OD plot of the ECD obtained under +1.5 V was used as a reference.

The ΔOD plot shows two slopes, in the low applied reduction potential region, the CE is calculated to be 390 $cm^2\ C^{-1}$ and in the high reduction potential region, it is 533 $cm^2\ C^{-1}$ for the IEV−PB ECD. The value of CE obtained herein is greater than the CEs obtained in the past for other viologens. The bulky substituents on the bipyridyl prevent the undesirable monomer radical cations couplings, at low to moderate reduction potentials, leading to radical mono cations which offer high molar extinction coefficients. Hu et al., obtained a CE of 342.2 $cm^2\ C^{-1}$ (at 610 nm) for an ECD in solid state with heptyl viologen as the cathodic electrochrome [5]. A η of 163 $cm^2\ C^{-1}$ (at 650 nm) was achieved for a poly(butylviologen) based ECD [6]. A device based on star-shaped 4,4′-bipyridine derivative (1,3,5-tri(1-methyl-4,4′-bipyridinium bromide)-2,4,6-trimethyl benzene) showed a CE of 279 $cm^2\ C^{-1}$ [7].

The plots of transmittance *versus* wavelength for the IEV−PB ECD, obtained at different potentials are shown in Figure 6B.3c. The ECD, in the completely bleached state (under +1.5 V) exhibits a transmittance of 62.2% at 605 nm. The highest transmission contrast (ΔT = T (+1.5 V) − T (−1.5 V)) delivered by the ECD, in the visible region, i.e., at 500 and 605 nm are 46 and 52 %, respectively, which are suitable for transmissive ECDs such as smart windows. A contrast of 59% at 609 nm, was achieved for a heptyl viologen- PB device, in an earlier study [8]. For a star-shaped 4,4′-bipyridine derivative (1,3,5-tri(1-methyl-4,4′-bipyridinium bromide)-2,4,6-trimethyl benzene) based device, a contrast ratio of 55% at 530 nm was reported [9].

6B.3.4 Write−erase efficiency of the IEV−PB device

In the present study, the viologen contains a bulkier indole group which is separated by just two carbon atoms from the 4,4′−bipyridyl system, and therefore can easily donate π-electron density of C_2-C_3 bond of indole to the bipyridyl system. The π-electrons of carbon atoms belong to the π-electron pool of the highly conjugated indole molecule. The high electron density renders these individual C atoms to be good "local" donors [10]. This electron rich character of the viologen can make the bleaching process or re-oxidation of IEV$^{+\bullet}$ species faster. Usually, the radical cations of bipyridyl system upon reduction are more likely to form

radical dimers due to aging process and the re-oxidation process is slow. However, here, due to the presence of electron donating indole groups (Scheme 6B.2), the re-oxidation is easier and therefore, the radical cation forms the dicationic viologen upon oxidation (colorless form). This effect makes the viologen a fast bleaching system.
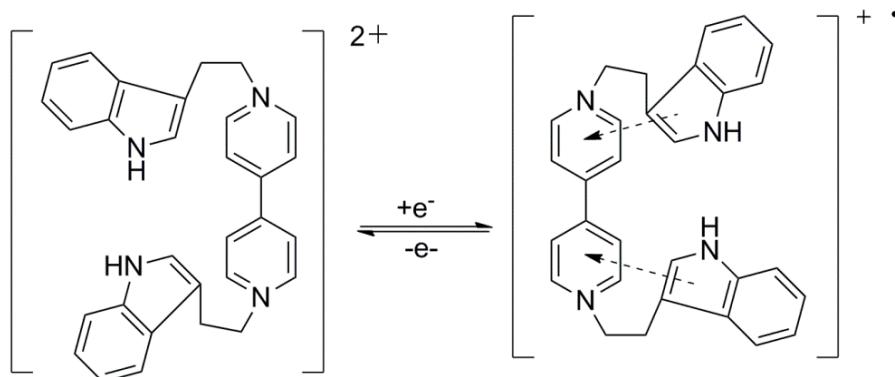
Scheme 6B.2: A depiction of the electron donating tendency of the indole groups in the viologen.

The color-bleach characteristics for the IEV–PB ECD were obtained under step times of 3.0 s, 5.0 s, 10 s and 20.0 s and by using a square wave potential of ± 1.5 V (Figure 6B.4a). The kinetic responses were recorded at a λ_{max} of 605 nm. Coloration times of 2.1 and 2.5 s were obtained for the ECD at frequencies of 0.33 and 0.2 Hz respectively. Bleaching times, of 2.2 and 3.3 s, were observed at frequencies of 0.33 and 0.2 Hz respectively. The switching times of the IEV–PB ECD are comparable to other viologen based devices. Previously, for a PBV–PB device containing a solid-state electrolyte, the switching times for the bleaching and darkening processes, were calculated to be 9.4 and 2.0 s, respectively [6]. For a liquid state based heptyl viologen in propylene carbonate [11], the bleaching and darkening times were calculated to be 6.6 and 1.8 s, respectively.
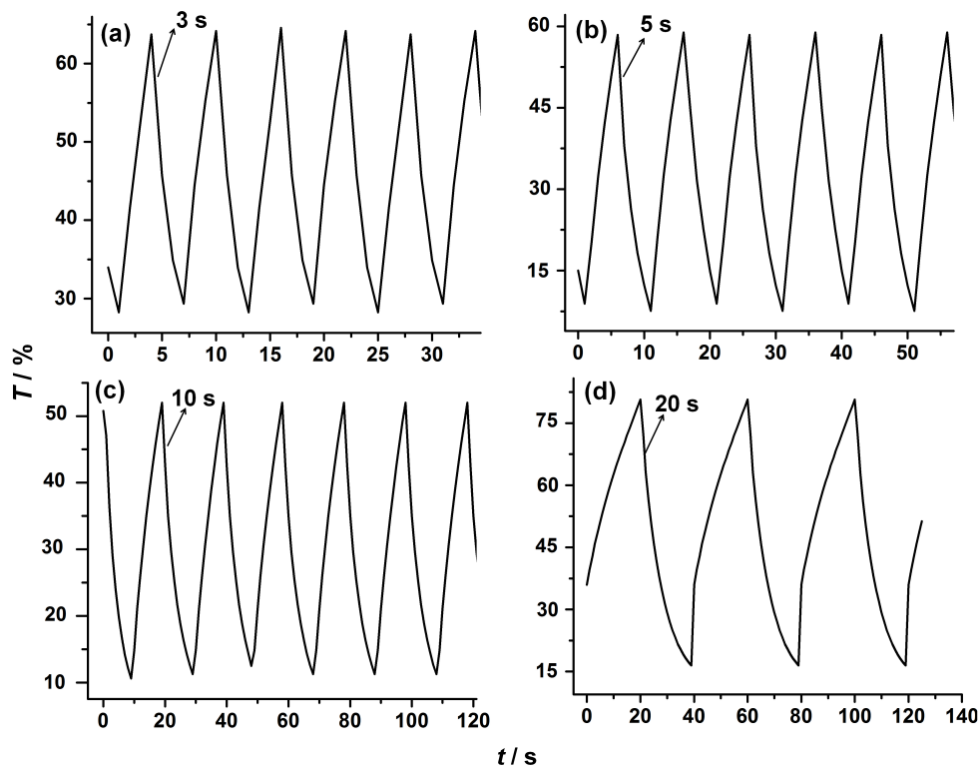
Figure 6B.4 Transmittance *versus* time curves for the IEV−PB device at a λ_{max} of 605 nm, under a square wave dc potential of ±1.5 V and under step times of (a) 3, (b) 5, (c) 10 and (d) 20 s.

The write−erase efficiency of the device for 3 s, 5 s and 10 s switch durations are calculated to be 95 %, 86 % and 79 % respectively. It became less for the 20 s switch, indicating that the device works well in the fast switching mode. For shorter switch durations, the device offers a highly reversible modulation, at the onset of applied potential, but upon increasing the applied potential span or cycle time, color bleaching takes longer time compared to colorless to color transition. For devices, wherein a sharp and abrupt change in OD is required, this device is apt as it can offer a large modulation within 3 s, with a write−erase efficiency of 95 %.

6B.3.5 Durability of IEV-PB Device

The ECD was evaluated for cycling stability, by subjecting it to contiguous cycling at a sweep rate of 100 mV s^{-1}, between −1.5 to +1.5 V and the voltammograms obtained in the 1st, 1000th and 2000th are shown in Figure 6B.5a. The cathodic peak current densities at −0.71 V for 1st, 1000th and 2000th are −0.071, −0.067 and −0.058 mA cm^{-2} respectively. After 2000 repetitive cycles, the current density at −0.71 V, reduced by 18.3% relative to its' value in the first cycle. To re-affirm the cycling stability of the device, color-bleach kinetics were measured with a step time of 5 s, under an applied potential of ± 1.5 V, for 2000 times in absorbance mode at a λ_{max} of 605 nm (Figure 6B.5b). The absorbance change, offered

by the device in the 1st cycle is 0.73, and after 2000 cycles, it is 0.64; the device shows high stability up to 2000 cycles, since 87.6 % of the original absorbance change is retained. The transmittance plots recorded for the IEV−PB device after 1st and 2000th CV cycles are shown in the Figure 6B.5c. The optical transmittance change (ΔT) for the device was calculated to be 52 % after the 1st CV cycle and it was 46 % after 2000 cycles. The device retained 88.4 % of the original transmittance change even after 2000 cycles, which further confirms that the device is stable for 2000 cycles. Previously, a star-shaped 4,4′-bipyridine derivative (1,3,5-tri(1-methyl-4,4′-bipyridinium bromide)-2,4,6-trimethyl benzene) based device was found to be stable for 500 cycles [7]. For an imidazole based viologen with a PB film as counter electrode, a cycle life time of 1×10^3 was reported [1]. An operational life of about 4000 cycles was observed previously for a device containing PB and Poly(butyl viologen) and a succinonitrile containing electrolyte [6]. Here, we observed that the IEV-PB ECD can tolerate a large number of repetitive colorless to dark blue switches, and is therefore apt for electrochromic applications.
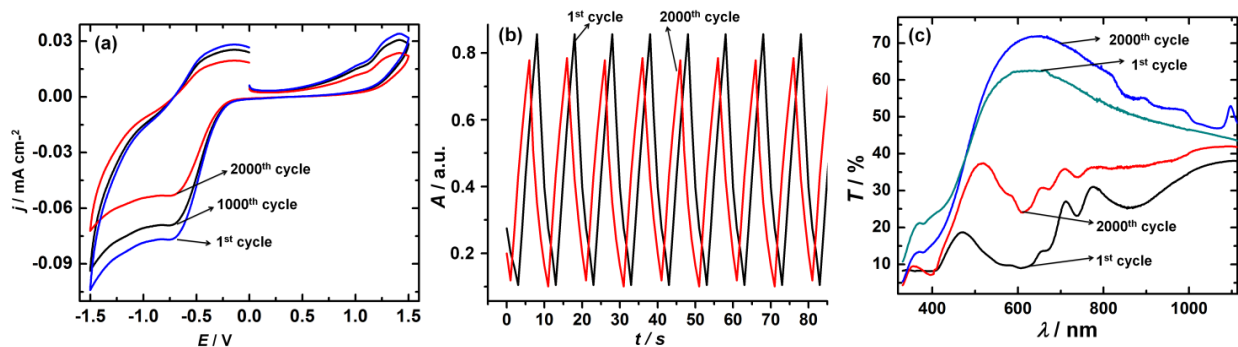
Figure 6B.5 (a) Cyclic voltammograms of the IEV−PB device recorded in the 1st, 1000th and 2000th cycles between the potential limits of −1.5 V to +1.5 V at a scan rate of 20 mV s^{-1}. (b) Kinetics of the same device measured after 1st and 2000th cycles at a monochromatic wavelength of 605 nm under a square wave dc potential of ±1.5 V at a step time of 5 s. (c) Transmittance plots recorded for the IEV−PB device at +1.5 V (fully bleached state) and −1.5 V (fully colored state) after 1st and 2000th CV cycles respectively.

6B.4 Summary

A new viologen, namely, 1,1'-bis(2-(1H-indol-3-yl)ethyl)-4,4'-bipyridinium diperchlorate (IEV), was synthesized and characterized. An ECD was constructed containing the IEV viologen salt dissolved in a solution of 1-ethyl-3-methylimidazolium bis(trifluoromethylsulfonyl) imide ionic liquid and DMF. The electrolyte was characterized by a large ionic conductivity almost invariant with temperature, good thermal stability upto 150 °C and a stable redox potential range of ~3.6 V, and was ideal for a solution phase ECD. The IEV-PB ECD switched reversibly between colorless and dark blue states, and showed a

high transmission contrast of 52% and an outstanding CE of 533 cm^2 C^{-1} (at 605 nm), good color uniformity, rapid response times of ~2 s and also excellent write−erase efficiency. The IEV viologen due to the presence of pendant indole based electron donors, minimizes the radical cation coupling effects and thus makes color bleach kinetics a rapid process. The excellent redox response of the IEV salt did not diminish as a function of repeated cycling between the colored and bleached states. The redox activity was slightly enhanced when the ECD was maintained at higher temperatures, indicating the thermal stability of the device. The remarkable electrochromic response of the device containing the hitherto unexplored IEV viologen is a good choice for fast responsive transmissive and reflective display/window applications.

References

[1] R. Sydam, M. Deepa, A.G. Joshi, Org. Electron. 14 (2013) 1027.

[2] H.M. Chawla, N. Pant, B. Srivastava, S. Upreti, Org. Lett. 8 (2006) 2237.

[3] M. Lamberto, E.E. Rastede, J. Decker, F.M. Raymo, Tetrahedron Lett. 51 (2010) 5618.

[4] Q.-G. Zhang, S.-S. Sun, S. Pitula, Q.-S. Liu, U. Welz-Biermann, J.-J. Zhang, J. Chem. Eng. Data 56 (2011) 4659.

[5] C.-W. Hu, K.-M. Lee, K.-C. Chen, L.-C. Chang, K.-Y. Shen, S.-C. Lai, T.-H. Kuo, C.-Y. Hsu, L.-M. Huang, R. Vittal, K.-C. Ho, Sol. Energy Mater. Sol. Cells 99 (2012) 135.

[6] T.-H. Kuo, C.-Y. Hsu, K.-M. Lee, K.-C. Ho, Sol. Energy Mater. Sol. Cells 93 (2009) 1755.

[7] G. Wang, X. Fu, J. Huang, C. Wu, L. Wu, Q. Du, Org. Electron. 12 (2011) 1216.

[8] C.-F. Lin, C.-Y. Hsu, H.-C. Lo, C.-L.; Lin, L.-C. Chen, K.-C. Ho, Sol. Energy Mater. Sol. Cells 95 (2011) 3074.

[9] G. Wang, X. Fu, J. Huang, C. Wu, L. Wu, Q. Du, Org. Electron. 12 (2011) 1216.

[10] S.-G. Albert, I. Irvin, Biochemistry 46 (1960) 1334.

[11] G. Chidichimo, M. De Benedittis, J. Lanzo, B.C. De Simone, D. Imbardelli, B. Gabriele, L. Veltri, G. Salerno, Chem. Mater. 19 (2007) 353.

Chapter 7

Effect of inclusion of a hexacyclic phoshonitrillic core in a viologen on its' electrochromic behavior

7.1 Introduction

   In the previous chapter, I had developed new organic viologens, to further improve the EC performance, an organo-inorganic hybrid viologen was synthesized and studied. Here an innovative design for synthesizing an electrochromic organo-inorganic hybrid material endowed with remarkable redox switching and optical properties is presented. Phosphazene inorganic polymers and in organic synthesis [1,2]. Similarly two/three-dimensional covalent structures derived by treating phosphonitrilic chloride with bridging 1,4-phenylenediamine and benzidine units have been synthesized and characterized in the past[3]. Previously, formation of polymeric material from hexachlorotriphosphazene $(PNCl_2)_3$, and quinone precursors directly at the electrode surface was studied by Li et al. [4]. Similarly, viologen-phosphorus dendrimers have in the past found applications in biology particularly in view of their ability to reduce cytotoxicity and hemotoxicity and for their antimicrobial and antifungal activities [5]. In view of the above developments, a new organo-inorganic hybrid, a polymeric cyclophosphazene–4,4′-bipyridinium chloride salt (PPBP) was synthesized, the hybrid salt (PPBP) was incorporated in an ECD as the cathodically coloring species by its' dissolution in an ionic liquid based gel electrolyte and a PB film was used as the anodic electrochrome.

7.2 Experimental

7.2.1 Synthesis of compound 3 (PPBP)

   0.5 g of hexachlorotriphosphazene (1) (1.4 mmol) was dissolved in 30 mL of dry dichloromethane and stirred for 5 minutes at room temperature under N_2. Then a solution containing 1.57 g (10.06 mmol) of 4,4′-bipyridyl in 10 ml dry dichloromethane was added slowly under N_2 atmosphere, and stirred at room temperature for 24 h. The reaction mixture was filtered and purified by washings with excess dichloromethane, and a white solid powder (3) was obtained (Scheme 7.1). Yield (0.86 g). Melting point: decomposed at 205 °C. FT-IR (neat, 4000–600 cm^{-1}): v 3087, 3036, 1629, 1594, 1578, 1485, 1455, 1342,

1221, 1192, 839, 792, 739 and 712 cm^{-1}. ^{1}H NMR (DMSO-d6, 400 MHz): δ 9.03–9.02 (dd, 4H, Ar-H), 8.36–8.35 (dd, 4H, Ar-H) ppm. ^{13}C NMR (DMSO-d6, 100 MHz): δ 148.3 (q, 2C, Ar-C), 145.4 (d, 4C, Ar-C), 124.2 (d, 4C, Ar-C) ppm, ^{31}P {^{1}H} NMR (162 MHz, DMSO-d6) δ 12.7 ppm. HR-MS (MALDI+): Higher molecular weight fragments or PPBP aggregates are found in mass spectrum with m/z values of 989.2, 986.9, 828.6, 824.9, 668.7 and 432.9.
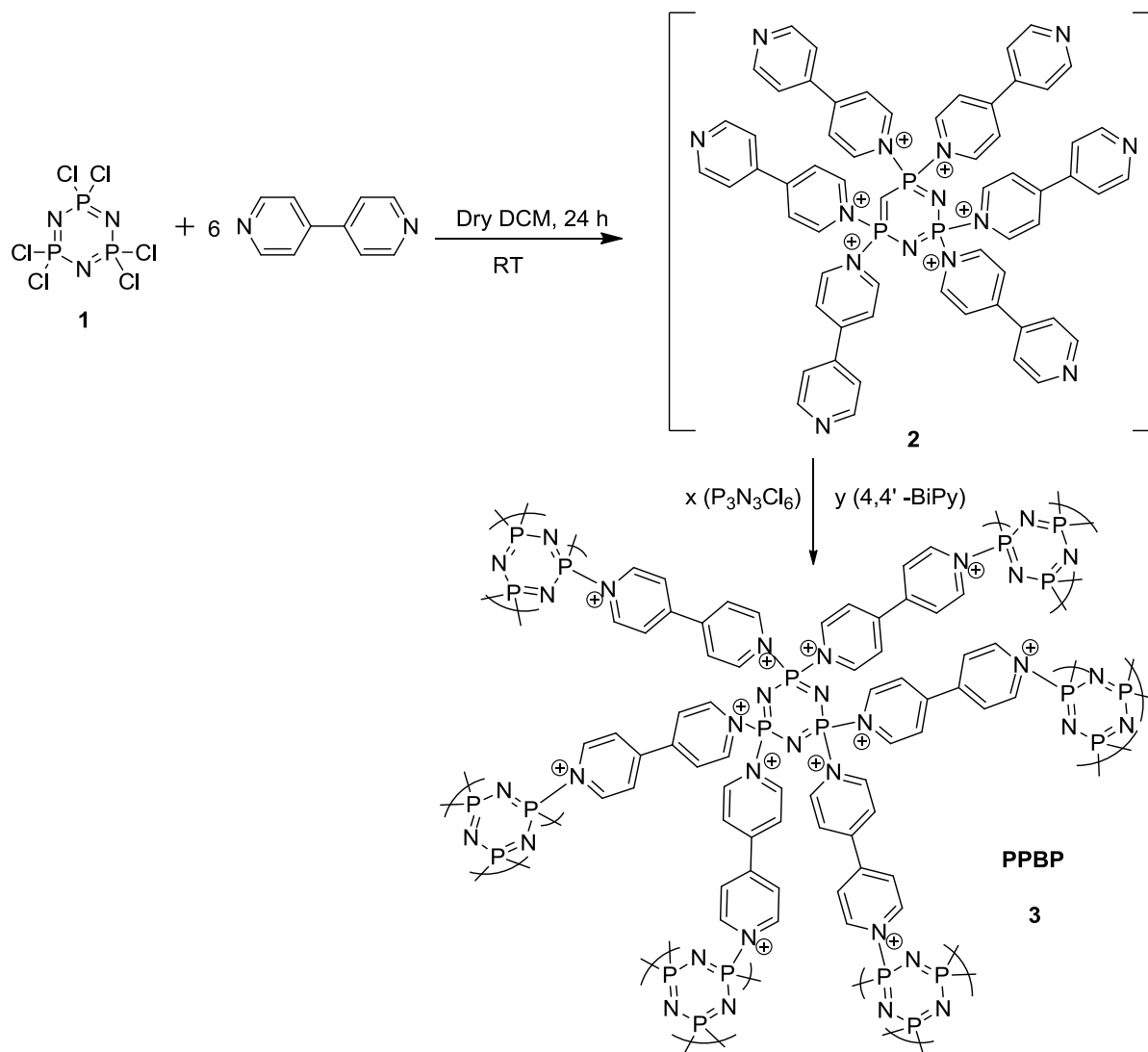
Scheme 7.1: Synthesis of PPBP.

7.2.2 Construction of ECD with PPBP

A polymeric ionic-gel electrolyte was prepared by dissolving poly(methylmethacrylate) (PMMA) in 10 wt% ionic liquid [1-ethyl-3-methylimidazolium tetracyanoborate, (EMIB(CN)$_4$)] and DMSO in a 2:1 weight ratio respectively. The dissolution of the polymer was achieved by heating the contents with

continuous stirring for 6 h at 60 °C and a transparent, colorless gel electrolyte (pictures of blank electrolyte are shown in Figure 7.4) was formed. For preparing an ECD, 50 mg of PPBP salt was dissolved in the electrolyte containing 10 wt% PMMA in an IL/DMSO, 2:1 w/w mixture; all the contents were sonicated for 5 minutes and a polymeric gel electrolyte was obtained, in a similar way as described for the blank PMMA gel. A cavity was created between two electrodes; cathode was a blank FTO coated glass substrate and the anode was a PB coated on FTO/glass. A 0.64 mm thick and 3 mm wide adhesive acrylic tape was employed as the spacer, which prevented the shorting of the two electrodes and also held the device assembly together. A transparent, pale blue colored ECD encompassing the electrolyte in the form of a gel was obtained and all the edges were sealed with epoxy. The ECD, hereafter is referred to as the PPBP-PB ECD.

7.3 Results and discussion

7.3.1 XPS Studies

^{1}H, ^{13}C-NMR and HRMS studies showed that the polymer PPBP is formed (Section 7.2.1). XPS studies were done to re-affirm these inferences. The XPS survey spectra of $(PNCl_2)_3$ trimer and PPBP polymer and the corresponding deconvoluted core level spectra are shown in Figure 7.1 and Figure 7.2. The survey spectra of the $(PNCl_2)_3$ trimer and PPBP show distinct signals from C1s, O1s, P2p, N1s, and Cl2p; indicating the retention of the PN ring and the presence of bipyridyls in PPBP. Since the trimer does not contain C or O, signals from C and O were not expected; however as these two elements are omnipresent, the C1s and O1s peaks were also observed. The core level spectrum of C1s from PPBP was deconvoluted into two main peaks at 284.6 and 285.6 eV corresponding to the C-C and C-N bonds in PPBP respectively. A broad π-π* shake up peak, which arises from the bipyridyl rings in PPBP was also observed at 291.6 eV. The $(PNCl_2)_3$ trimer shows a broad P2p peak centered at ~135.2 eV corresponding to neutral phosphorus on the PN rings which agrees well with a standard reported value of 135.3 eV observed for this trimer previously [6]. For PPBP, this peak downshifts by 2.5 eV. The P2p envelope was observed at a lower binding energy of 132.7 eV and it could also be deconvoluted into the $P2p_{3/2}$ and $P2p_{1/2}$ components at 132.5 and 133.5 eV respectively. The $P2p_{3/2}$ and $P2p_{1/2}$ components have an intensity ratio of about 1:2 and arise from spin-orbit coupling. The downshift in the P2p position on moving from the $(PNCl_2)_3$ trimer to PPBP, clearly indicates a change in the chemical environment of the trimer, and this shift is induced by the formation of new P-N[+] bonds, formed after the bipyridyl nitrogens (N[+]) link to the phosphorus on the trimer (as shown in Scheme 7.1). The change in the N1s profile ongoing from the $(PNCl_2)_3$ precursor to PPBP also provided evidence for the formation of P-N[+] bonds. The $(PNCl_2)_3$ trimer showed a single broad symmetric N1s peak at 400 eV corresponding to neutral nitrogen which exists in the form of =N-P=N- groups that constitute the PN ring. In an earlier study [7],

the N1s peak was observed at 400.3 eV for the same trimer. On the other hand, an asymmetric N1s curve was registered for PPBP. It was deconvoluted into two components, the low energy one at 400.1 eV is attributed to the neutral nitrogens on the $(PNCl_2)_3$ trimer, but the high energy one at 402.1 eV originates from the positively charged nitrogens in bipyridyl, which attain a positive charge upon forming covalent bonds with the phosphorous atoms on $(PNCl_2)_3$, as shown in Scheme 7.1.
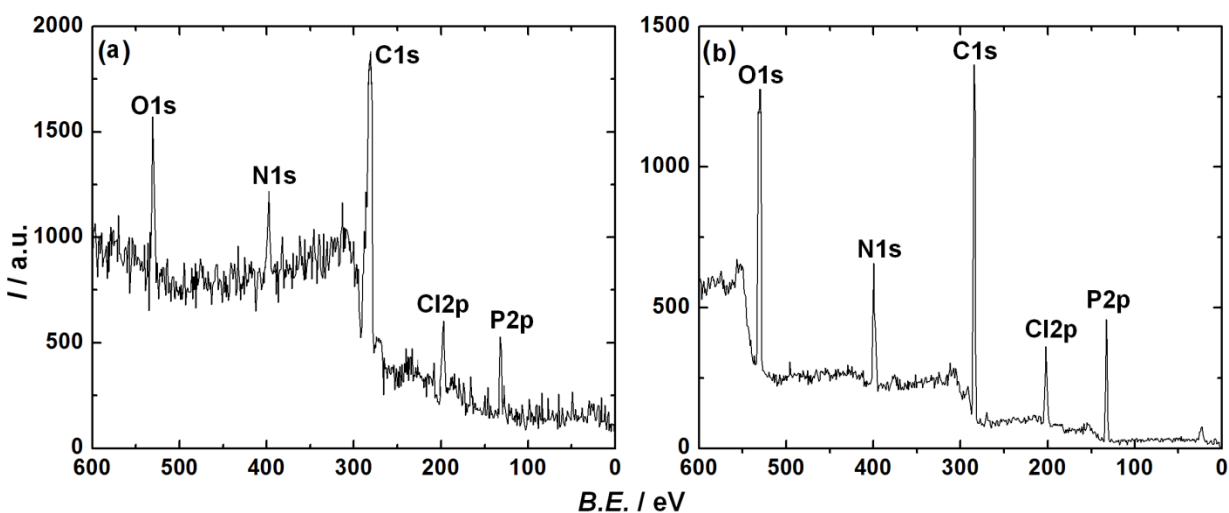
Figure 7.1 XPS survey spectra of (a) $(PNCl_2)_3$ trimer and (b) PPBP material.

Further proof for the successful formation of PPBP was achieved from the shift in the Cl2p peak position. The Cl2p peak was observed at 200.15 eV in the $(PNCl_2)_3$ trimer and it downshifted to 197 eV in PPBP. Cl atoms are covalently bound to phosphorous atoms in the $(PNCl_2)_3$ trimer whereas they are ionic in PPBP, as they serve as counter ions to the positively charged nitrogens on the bipyridyl rings. Covalently bound Cl is therefore expected to appear at higher binding energy relative to ionic Cl, and this is evident in Figure 7.1d, thus implying the conversion of $(PNCl_2)_3$ to PPBP. A similar difference in the Cl2p binding energy was observed for chlorobutyl sulfonate based ionic liquids, when the mode of chloride bonding changed from covalent to ionic [8].
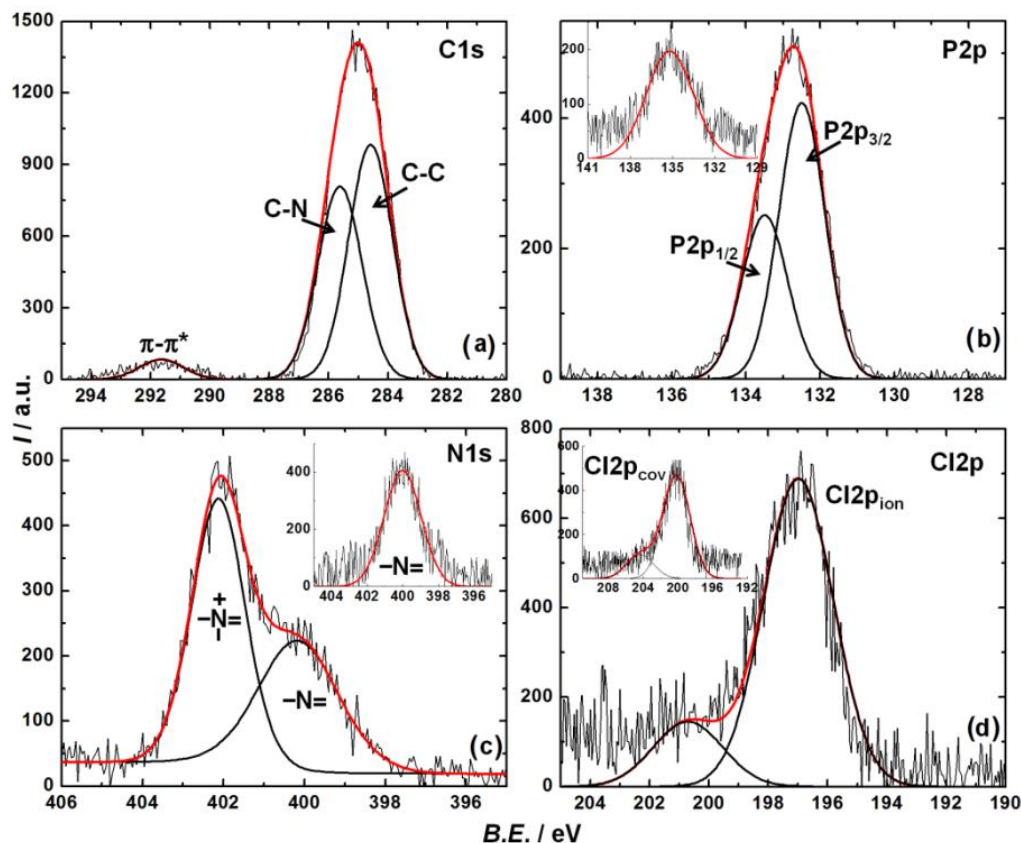
Figure 7.2 Deconvoluted core level spectra of (a) C1s, (b) P2p, (c) N1s and (d) Cl2p from PPBP. Insets of (b), (c) and (d) are the P2p, N1s and Cl2p core level spectra of $(PNCl_2)_3$ trimer. The jagged lines represent the raw data; the solid lines denote the fitted envelopes (red) and the deconvoluted components (black).

7.3.2 Structural analysis

The SEM micrograph and the corresponding EDX plot of the PPBP solid are shown in Figure 7.3. The solid has a granular texture and exists in form of irregular shaped agglomerates. The elemental composition in terms of atomic percentages is: C: 60.49%, N: 26.93%, P: 5.95% and Cl: 6.63%. While the proportions of C and Cl are close to the atomic make-up of the repeating unit of the polymeric material $(P_3N_3(4,4'-BiPy)_6Cl_6)_n$ or $(C_{60}H_{48}Cl_6N_{15}P_3)_n$, the proportion of N is significantly higher possibly due to the aggregation of nitrogen rich functionalities on the surface.
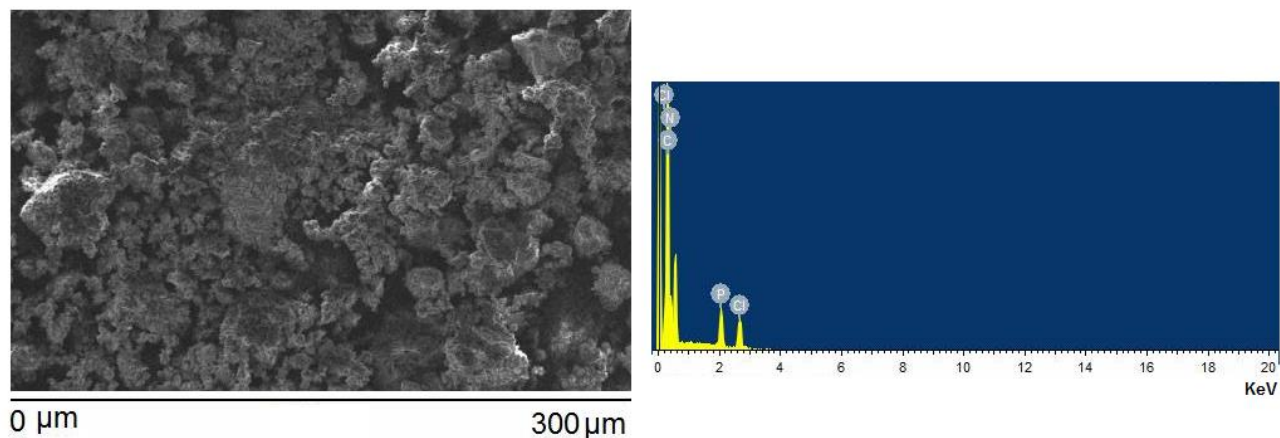
Figure 7.3 SEM micrograph and the corresponding EDX plot of the PPBP solid.

The FTIR spectra of the PPBP solid and the precursor $(PNCl_2)_3$ are displayed in Figure 7.4. A broad band spanning from 980 to 1260 cm^{-1} and peaking at 1180 cm^{-1} is ascribed to asymmetric ν_a(PNP) ring stretching modes and peaks at 870 cm^{-1} and 596 cm^{-1} are ascribed to symmetric ν_s(PNP) and P-Cl stretching modes respectively in the precursor $(PNCl_2)_3$ [9,10]. The asymmetric ν_a(PNP) peaks are observed at ~1160 and ~960 cm^{-1} and the symmetric ν_s(PNP) peak is seen at 790 cm^{-1} for the PPBP solid. For PPBP, the P=N stretching values are downshifted; this can be explained in terms of decreased positive charge around phosphorous. During the formation of P-N bond between the phosphazene trimer and bipyridyl molecules, the bipyridyl nitrogens donate a lone pair of electrons, as a result the electron density around phosphorus will increase and thus P=N strength decreases in the phosphazene trimer of PPBP.

131
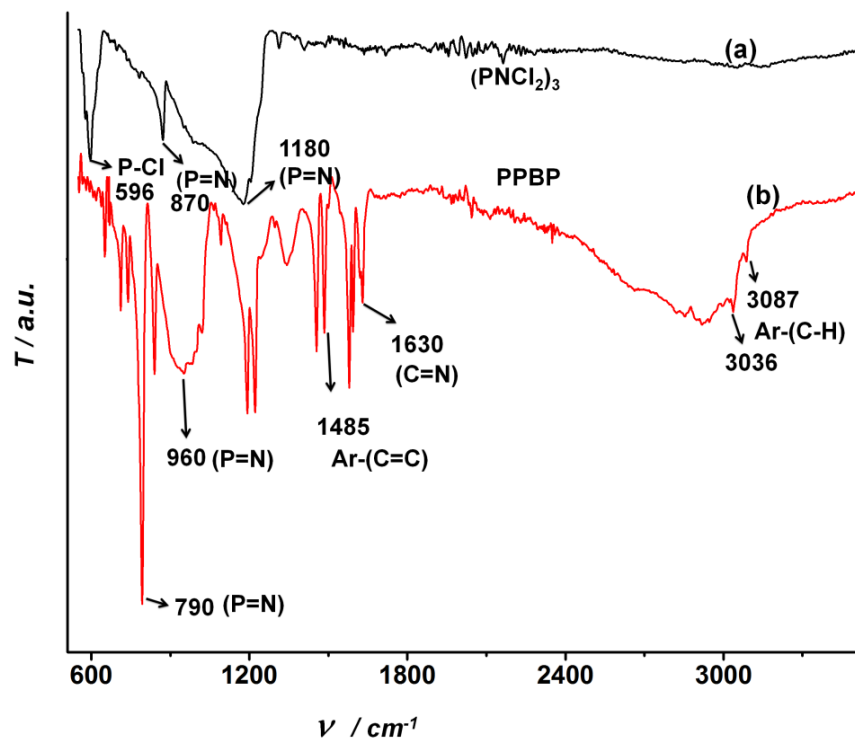
Figure 7.4 FTIR spectra of (a) precursor $(PNCl_2)_3$(**1**) and (b) PPBP solid (**3**).

7.3.3 Electrolyte and PPBP salt characteristics

The TGA of the neat IL is provided in Figure 7.5 in the 30–600 °C temperature range and it was found to be stable up to 430 °C. TGA plots of the PMMA, PPBP-PMMA gel and PPBP solid in the 30–400 °C temperature range are shown in Figure 7.6. The pristine PPBP solid salt showed a high thermal decomposition temperature of ~190 °C, as only above this temperature a continuous and an appreciable weight loss was registered for this compound. The PMMA-IL-DMSO gel however decomposed at 160 °C, owing to the presence of the low boiling DMSO and as a result, the thermal stability window of the PPBP/PMMA-IL-DMSO gel was restricted to 160 °C, which is acceptable for ECD operation.

132
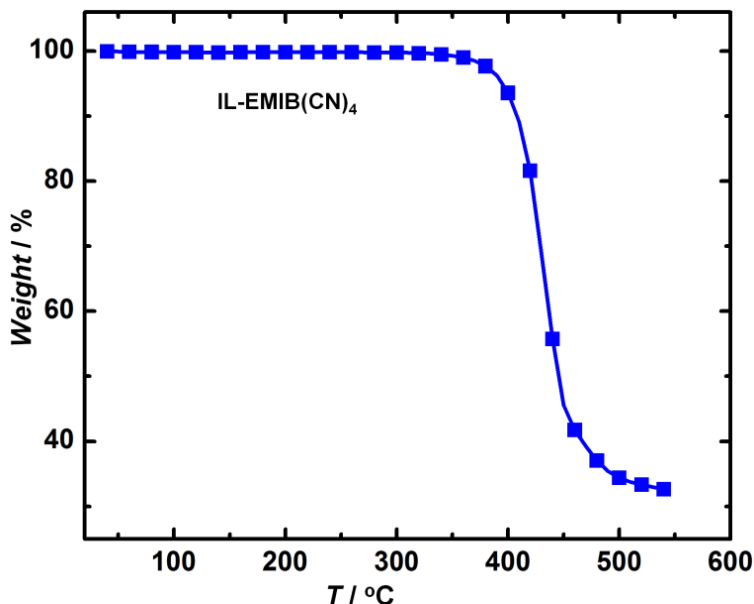
Figure 7.5 TGA of neat IL (EMIB(CN)$_4$) recorded in the 30–600 °C temperature range under N$_2$.

The photographs of the PPBP-PMMA electrolyte and the PPBP salt are shown as insets of Figure 7.6. The off-white colored PPBP salt completely dissolved in the liquid electrolyte (IL+DMSO) to yield a transparent solution, indicating good compatibility with organic solvents like DMSO and the IL. The gel obtained after dissolution of PMMA is observed to be transparent and homogeneous, thus appropriate for use in a device. The linear sweep voltammogram of the PMMA-IL-DMSO gel recorded at a scan rate of 2 mV s^{-1} in the −3.0 to +3.0 V potential range is shown in Figure 7.6c, and the gel was observed to be electrochemically inert in the voltage range of −2.5 to +2.5 V, confirming a voltage stability window of about ~5 V, which is again adequate for ECDs. The PMMA-IL-DMSO gel (Figure 7.6d) showed high transmittance in the visible region as % T varied between 80-85 % in the 400-750 nm wavelength region, which is advantageous for constructing transmissive ECDs. The thermal dependence of ionic conductivity of the PMMA-IL-DMSO gel electrolyte is shown in Figure 7.6b. The gel showed a reasonably high ambient temperature (25 °C) ionic conductivity of 0.19 mS cm^{-1} which did not alter much with temperature. Conductivity increased marginally from 0.192 to 0.198 mS cm^{-1} on raising the temperature from 0 °C to 70 °C in steps of 10 °C (Figure 7.6b). Previously, ECDs employing methacrylate-based polymer electrolytes exhibited good ionic conductivity of 0.707 mS cm^{-1} at room temperature, which is comparable to our observed value [11]. An invariant ionic conductivity profile within the operational temperature range of the device (typically between 0 to 60 °C) is ideal and the PMMA-IL-DMSO gel satisfies this criterion, thereby validating its' use as the electrolyte in a solid-state ECD.

133

Figure 7.6 (a) TGA curves for the PPBP solid (■), PPBP/EMIB(CN)₄/DMSO gel electrolyte (●) and PPBP/PMMA/EMIB(CN)₄/DMSO gel electrolyte (▲) and inset of (a) shows the PPBP solid powder and gel electrolyte, (b) ionic conductivity *versus* reciprocal absolute temperature curve for the PMMA/EMIB(CN)₄/DMSO gel electrolyte, (c) LSV plot of the PMMA/EMIB(CN)₄/DMSO gel electrolyte recorded at a scan rate of 5 mV s⁻¹ between two Pt electrodes, (d) variation of transmittance as a function of wavelength for PMMA/EMIB(CN)₄/DMSO gel electrolyte and Inset of (d) shows a photograph of the gel electrolyte.

7.3.4 Redox behavior of PPBP

The linear sweep voltammogram of a solution of the PPBP solid in DMSO (5 mg/mL), recorded with two Pt electrodes, in the potential range of +2 to −2 V is shown in Figure 7.7a. The solution is colorless in the oxidation potential regime of +2 to 0 V and the j-V profile is flat and devoid of any distinct feature, indicating that the PPBP salt is electrochemically stable under oxidation potentials. The first reduction peak is observed at −0.41 V, which is followed by a second peak at −1.02 V. This peak was accompanied by the appearance of a uniform blue coating over the cathodic Pt electrode, which confirmed the

134

Figure 7.6 (a) TGA curves for the PPBP solid (■), PPBP/EMIB(CN)$_4$/DMSO gel electrolyte (●) and PPBP/PMMA/EMIB(CN)$_4$/DMSO gel electrolyte (▲) and inset of (a) shows the PPBP solid powder and gel electrolyte, (b) ionic conductivity *versus* reciprocal absolute temperature curve for the PMMA/EMIB(CN)$_4$/DMSO gel electrolyte, (c) LSV plot of the PMMA/EMIB(CN)$_4$/DMSO gel electrolyte recorded at a scan rate of 5 mV s^{-1} between two Pt electrodes, (d) variation of transmittance as a function of wavelength for PMMA/EMIB(CN)$_4$/DMSO gel electrolyte and Inset of (d) shows a photograph of the gel electrolyte.

7.3.4 Redox behavior of PPBP

The linear sweep voltammogram of a solution of the PPBP solid in DMSO (5 mg/mL), recorded with two Pt electrodes, in the potential range of +2 to −2 V is shown in Figure 7.7a. The solution is colorless in the oxidation potential regime of +2 to 0 V and the j-V profile is flat and devoid of any distinct feature, indicating that the PPBP salt is electrochemically stable under oxidation potentials. The first reduction peak is observed at −0.41 V, which is followed by a second peak at −1.02 V. This peak was accompanied by the appearance of a uniform blue coating over the cathodic Pt electrode, which confirmed the

134

formation of the radical cation. Subsequent to the second reduction peak, current increased monotonically with potential. The j-V dependence was observed to be quasi-linear which corresponds to an ohmic dependence of voltage on current in the oxidation potential regime of +0.6 and +1.4 V and in the reduction potential regime of −0.8 V and −1.5 V. The conductivity (σ) for the PPBP salt in the neutral oxidized state was found to be 0.009 S cm^{-1}, from the corresponding j-V slope (j/V) using ($\sigma = (j/V) \times l$), where l is the distance between the electrodes. The conductivity of the radical cationic form of PPBP was determined to be 0.42 S cm^{-1}; it is 46 times greater than that of the salt, clearly indicating that the electronic conductivity of the derivative dominates, after formation of the blue film. Since we did not use any supporting electrolyte in this experiment, the calculated conductivity solely arises from the PPBP salt. The radical cation formed *in-situ* during reduction is expected to be electronically conducting, as opposed to the neutral PPBP salt formed upon oxidation. Of particular interest is the high bias non-linear regime of −1.5 to −2 V, wherein the blue radical cation exists, and electronic conduction in the derivative in this voltage domain, in all likelihood corresponds to a trap-free space charge limited current (SCLC), if it obeys the Mott-Gurney law [12].

$$j_{SCLC} = 9/8 \ (\varepsilon_r \varepsilon_o \mu \ V^2/l^3) \tag{7.1}$$

In equation (7.1), ε_r is the dielectric constant of the radical cation, μ is the charge carrier mobility and l is the sample thickness. We plotted log j *versus* log V for the blue radical cation for the voltage range of −1.5 and −2 V (inset of Figure 7.7a) and we observed an almost log j $\propto$ 2 log V dependence, which ratified that charge transport in this regime is dominated by the injected electrons controlled by space charge. Under an applied field, the free carrier concentration is increased due to the injected electrons in the vicinity of an interface formed by the blue radical cation film and the Pt electrode support. When the injected carrier concentration is larger than its thermal equilibrium value, the space-charge effect is said to occur. The current produced due to the presence of a space-charge effect is called the SCL and this current is responsible for the electronic conduction in the PPBP radical cation at high negative potentials.
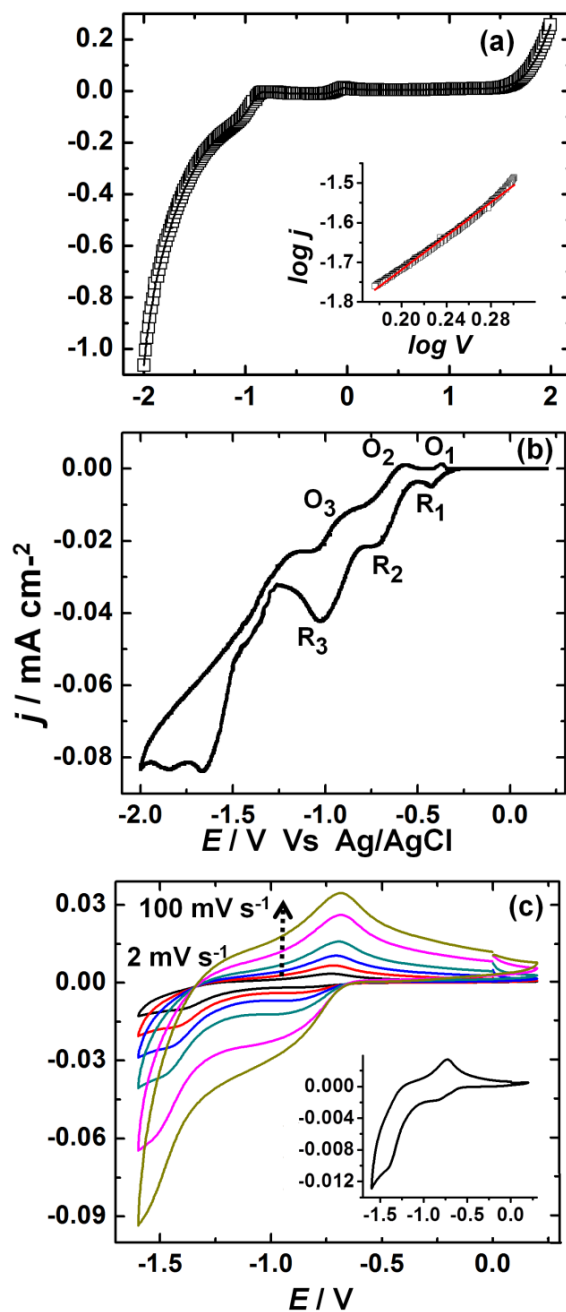
Figure 7.7 (a) LSV plot of 100 mg PPBP salt in 10 mL of DMSO recorded between potential limits of +2.0 and −2.0 V at a scan rate of 2 mV s^{-1} and inset of (a) shows log j *versus* log V for the blue radical cation for the voltage range of −1.5 and −2 V, (b) Cyclic voltammograms of the PPBP salt (10 mM) in EMIB(CN)$_4$–DMSO recorded between potential limits of −2.0 and +0.2 V and (c) PPBP/PMMA/EMIB(CN)$_4$/DMSO/PB ECD recorded between potential limits −1.6 and +0.2 V at different scan rates of 2, 5, 10, 20, 50 and 100 mV s^{-1} and the inset of (c) shows the CV plot at scan rate of 2 mV s^{-1}.

136

To understand the redox switching behavior of the PPBP derivative, a cyclic voltammogram of PPBP (50 mg) was measured in a DMSO:BMIB(CN)$_4$ solution, mixed in 1:2 weight ratio at a scan rate of 2 mV s^{-1} (Figure 7.7b). In the cathodic branch, the first reduction peak labeled as R$_1$ was observed at −0.42 V, followed by a second peak at −0.70 V (R$_2$) and finally a third reduction peak at −1.02 V (R$_3$). These were followed by twin reduction peaks above −1.2 V, which were found to be irreversible. Only the first three reduction peaks served as redox couples, for in the anodic branch, their corresponding oxidation peaks were observed at −0.38 V (O$_1$), −0.60 V (O$_2$) and −0.94 V (O$_3$). It is apparent that the PPBP salt undergoes a three step reversible redox process and the mechanism is illustrated in Scheme 7.2. At R$_1$, the PPBP salt converts to a single mono radical cationic bipyridyl species and at R$_2$, two mono radical cationic bipyridyl moieties are generated and these are deposited in the form of a uniform violet-blue coating on the Pt electrode. The radical cationic species are stable and immobilized on the electrode surface due to the delocalization of electrons within the PPBP molecule. At R$_3$ (~ −1.02 V), the PPBP takes up one more electron and three mono radical cationic bipyridyl moieties are formed in the PPPB molecule which even at this juncture continues to appear as a violet-blue film. However above −1.2 V, two irreversible reduction peaks are observed, but these cannot be ascribed to further reduction of the radical cation, which is confirmed by the absence of the corresponding oxidation peaks. Alternately and in all likelihood, they may arise from the entrapment of imidazolium ions (of the ionic liquid) in the radical cation film matrix. This is also supported by the presence of a pre-peak at −1.14 V in the anodic branch, which could probably originate from the release of the positively charged imidazolium ions trapped in the radical cation films, prior to the removal of an electron from the radical cation species. Further ahead in the anodic cycle, the violet-blue film gets detached from the Pt electrode by step-wise regeneration of the PPBP salt (Scheme 7.2), which eventually dissolves completely in the electrolyte to yield a colorless solution [13]. Cyclic voltammograms of a PPBP-PB quasi solid state ECD recorded in the range of −1.6 to +0.2 V at different scan rates of 2, 5, 10, 20, 50 and 100 mV s^{-1} are shown in Figure 7.7c. An enlarged view of the CV plot recorded at a scan rate of 2 mV s^{-1} is shown as an inset. For the ECD, only two reduction peaks were seen, with R$_1$ at −0.82 V and R$_2$ at −1.36 V. In the anodic branch, one shoulder and one peak corresponding to oxidation were observed at −0.73 V (O$_1$) and at −1.25 V (O$_2$). The reduction peaks correspond to the step-wise formation of mono radical cationic bipyridyls in PPBP, which are highly reversible, as the ECD acquired a deep blue state in the reduced state in the cathodic branch and turned transparent and colorless in the anodic sweep. A three-step redox process was not observed in the ECD, possibly because of the use of a polymeric electrolyte, a two electrode cell configuration and the presence of a redox active counter electrode.
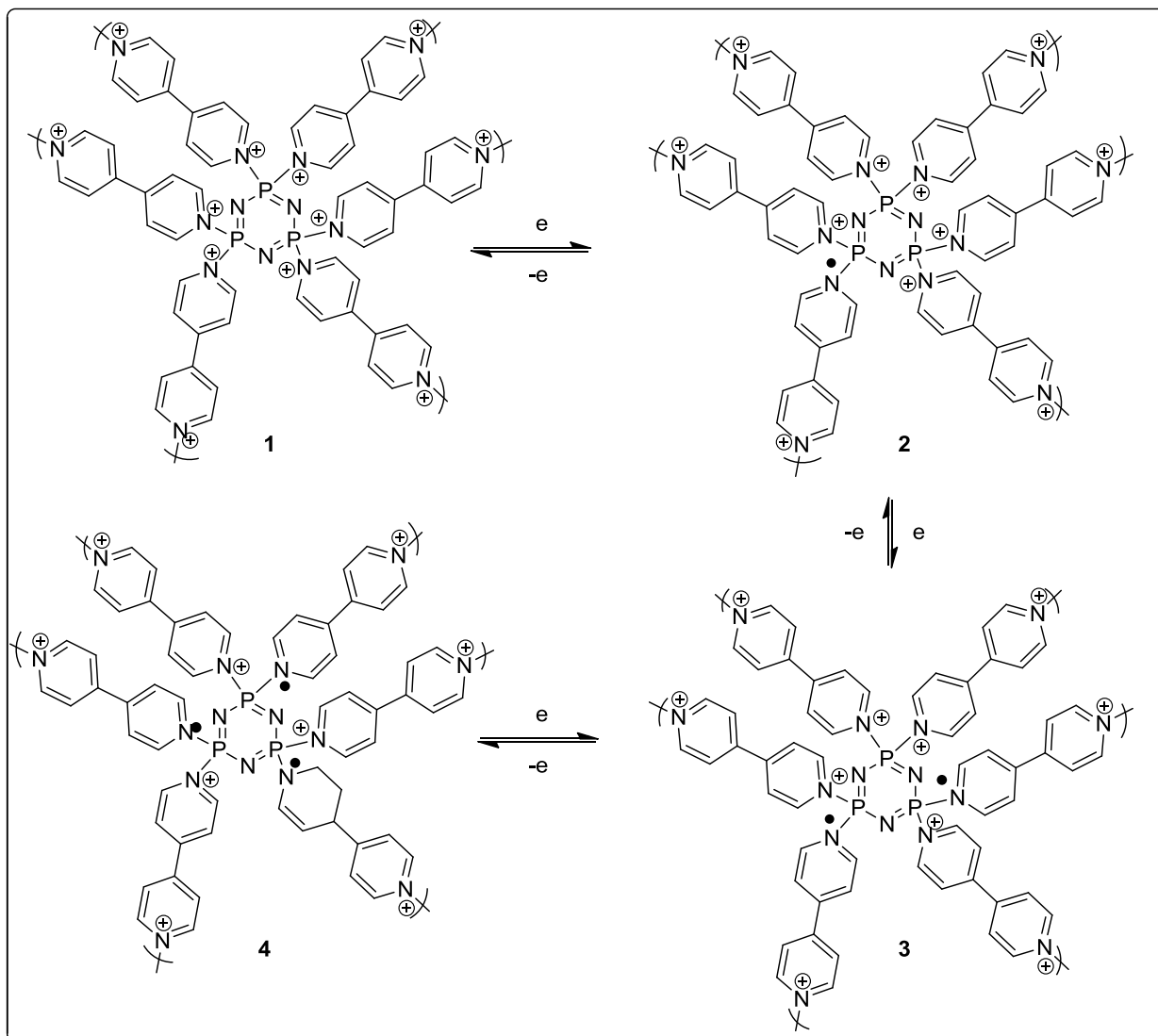
Scheme 7.2: Redox switching of PPBP.

7.3.5 Spectroelectrochemistry of the PPBP-PB ECD

7.3.5.1 *In-situ* absorption spectra of the PPBP-PB ECD

The *in-situ* absorption spectra of PPBP-PB ECD recorded under different dc reduction potentials (applied to the blank FTO electrode) in the range of −0.5 to −2.0 V and under different oxidation potentials of +0.5, +1.0 and +1.5 V are shown in Figure 7.8a. The ECD was subjected to negative potentials starting from −0.5 V and in steps of 0.2 V upto −1.1 V and then in steps of 0.1 V up to −2.0 V. Under reduction potentials, the ECD showed an electrochromic response similar to viologens [14], whereby an electrode supported violet-blue film is deposited on the FTO coated glass, which bleached when positive potentials were applied. The ECD attains an appreciable violet color at −1.2 V which deepens to a blue state at −2 V; the origin of color centers in PPBP can be explained by the generation of

radical cations of di-quaternized 4,4'-bipyridyls in PPBP. The absorption spectrum for the ECD in the extreme reduced state (at −2 V) reveals a λ_{max} at ~590 nm and a second shoulder peak at 550 nm in the visible region. This peak is assigned to the intra-molecular charge transfer within the bipyridyl moiety upon reduction in PPBP. In addition, highly intense peaks were seen at ~382 and ~372 nm, and these peaks are attributed to intra-molecular coupling between radical cation species and the di-quaternized bipyridyls in PPBP [15]. The systematic increase in the intensity of the absorption peaks as a function of increasing negative potential, indicates a greater degree of reduction of PPBP (formation of radical cations in PPBP) and a higher delocalization of the charge over the bipyridyls in PPBP cation with potential. However, we observed that the absorption peak intensity tends to saturate at −2 V, as at −2.1/−2.2 V, the curve retraces the profile obtained at −2 V and at potentials above −2.5 V, the absorption peak intensity decreased possibly due to the decomposition of PPBP. The ECD bleached upon application of a positive potential of +0.5 V, simultaneously accompanied by the disappearance of the absorption peaks in the visible region, indicating the oxidation of the PPBP radical cation and its' transformation into the PPBP neutral salt. Higher oxidation potentials of +1.0 and +1.5 V were applied to ensure complete oxidation.

$$\text{CE (or) } \eta(\lambda)=\Delta OD(\lambda)/Q \tag{7.2}$$

$$\Delta OD(\lambda)=OD_{col}(\lambda)-OD_{bleach}(\lambda) \tag{7.3}$$

where OD_{col} at −0.5 to −2 V and OD_{bleach} at +1.5 V

The ΔOD values of the ECD were determined using the optical density data obtained at +1.5 V as reference, at λ_{max} of 590 nm and also at 550 nm, the wavelength at which the human eye is most responsive. At both the monochromatic wavelengths shown in Figure 7.8b and c, the ΔOD *versus* charge inserted profiles are similar; upto −1.1 V, the magnitude of ΔOD is not large, but above this voltage, ΔOD increases steeply, signalling the formation of the violet-blue hue. In this deeply colored state, from the slopes of the ΔOD *versus* Q plots, the coloration efficiency of the ECD in the higher potential regime of −1.3 to −2 V is deduced to be 504 cm^2 C^{-1} at 590 nm and 414 cm^2 C^{-1} at 550 nm. In the lower potential regime of −0.5 to −1.1 V, the ECD is pale blue colored and the corresponding coloration efficiencies are also low: 36 cm^2 C^{-1} (at 590 nm) and 23 cm^2 C^{-1} (at 550 nm). In the past, for all-solid-state ECD with 2,2,6,6-tetramethyl-1-piperidinyloxy (TEMPO), heptyl viologen, and succinonitrile, a high coloration efficiency of 342.2 cm^2 C^{-1} was obtained at 610 nm [16]. In another study on a star-shaped 4,4′-bipyridine derivative (1,3,5-tri(1-methyl-4,4′-bipyridinium bromide)-2,4,6-trimethyl benzene), a coloration efficiency of 279 cm^2 C^{-1} was observed [13].

Figure 7.8 (a) *In-situ* absorption spectra of the PPBP−PB ECD recorded under different reduction potentials starting from −0.5 V and in steps of 0.2 V up to −1.1 V and then in steps of 0.1 V up to −2.0 V, and under oxidation potentials of +0.5, +1.0 and +1.5 V; all potentials applied to the blank FTO electrode or the cathode of the ECD. Digital photographs of the ECD (i) in fully colored (deep blue, E = −2.0 V), (ii) purple color (~ −1.1 V) and (iii) fully bleached (E = +1.0 V) states are shown. ΔOD *versus* charge density plot at monochromatic wavelengths of (b) 590 nm and (c) 550 nm for the ECD with OD response under +1.5 V used as reference for determination of ΔOD.

7.3.5.2 *In-situ* transmittance spectra of the PPBP-PB ECD

The transmittance *versus* wavelength plots for the ECD, under the same reduction/oxidation potentials are displayed in Figure 7.9a. The bleached state transmittance of the ECD is 84.6% at 590 nm when an external bias of +1.5 V was applied and the colored state transmittance of the ECD is 14.1% at 590 nm. A maximum transmission modulation of 70.5% at 590 nm was registered for the ECD (Figure 7.9b), one of the highest reported transmittance modulation in organic electrochromics ($\Delta T = T$ (+1.5 V) − T (−2.0 V)).

Figure 7.9 (a) The *in-situ* transmittance spectra of PPBP-PB ECD recorded under different dc reduction potentials (applied to the blank FTO electrode) in the range of −0.5 to −2.0 V and under different oxidation potentials of +0.5, +1.0 and +1.5 V and (b) the corresponding transmission modulation (ΔT) plots are shown. The ECD was subjected to negative potentials starting from −0.5 V and in steps of 0.2 V upto −1.1 V and then in steps of 0.1 V upto −2.0 V. The maximum transmission modulation ΔT_{max} ($\Delta T = T_{bleach}(+1.5$ V$) − T_{col}$), T_{bleach} at +1.5 V and T_{col} at −0.5 to −2 V;) offered by the ECD was 70.5 % at λ_{max} of 590 nm by using T_{col} at −2 V and it was 68.9 % at 550 nm. The transmittance data recorded under +1.5 V was used as reference for all ΔT plots.

7.3.5.3 Specular reflectance spectra of the PPBP-PB ECD

Specular reflectance spectra for the PPBP-PB ECD as a function of wavelength were recorded under different dc potentials within the range of +1.5 to −2.0 V (Figure 7.10a). The ECD was supported over a highly polished mirror to enable reflectance measurements and the zero-line calibration was performed using the same mirror. A high specular reflectance modulation (ΔR, where $\Delta R(\lambda) = R_{bleach}(\lambda) − R_{col}(\lambda)$, R_{bleach} at +1.5 V and R_{col} at −0.5 to −2 V) is essential for using ECD for anti-glare rearview mirrors in vehicles [17]. The plots of ΔR *versus* wavelength in the visible region for the ECD, by using the reflectance data obtained under a voltage of +1.5 V as reference, are shown in Figure 7.10b. With increasing reduction potential, the magnitude of ΔR increases in the visible region and two unresolved peaks at 545 and 590 nm appear at −1.2 V. The intensities of the peaks increase as potential is raised from −1.2 to −2 V and these amalgamate into a composite peak at ~ 540 nm at −2 V. Akin to the CE trend deduced from absorbance variations, here too ΔR is high for the extreme reduced violet-blue state of the ECD (at −2.0 V, with respect to the bleached state of the ECD at +1.5 V) with values of 59.2 and 52.4% at 545 and 590 nm respectively. The ability of the quasi-solid state PPBP-PB ECD to offer such a high value of reflectance change in the visible region close to 60%, unambiguously validates its' use for

141

electrochromic mirror applications. The ΔR magnitudes are however, lesser at low reduction potentials, for instance at -1.1 V, with respect to the bleached state of the ECD at $+1.5$ V, ΔR values are 8.9 (at 590 nm) and 7.4% (at 545 nm).
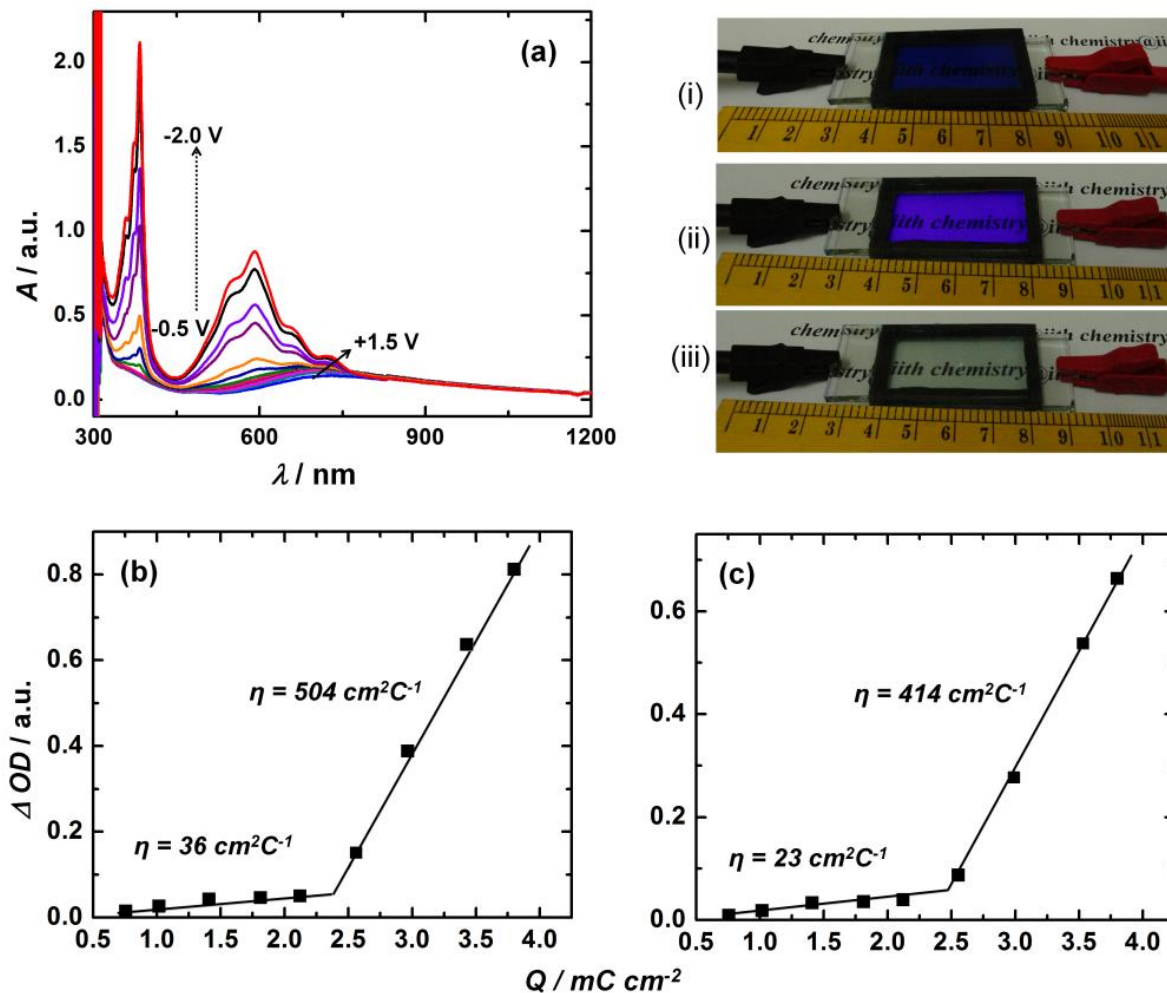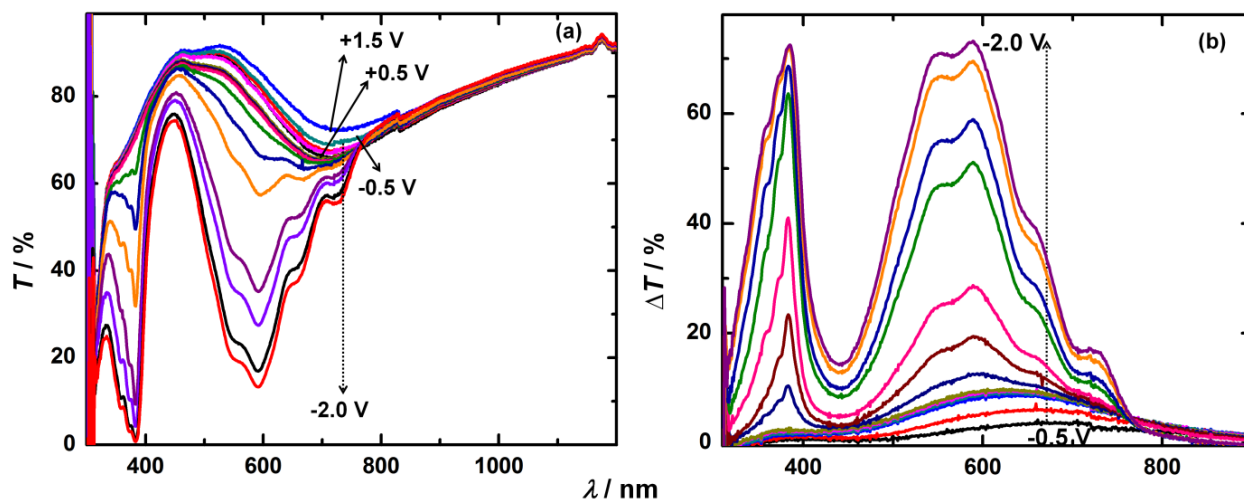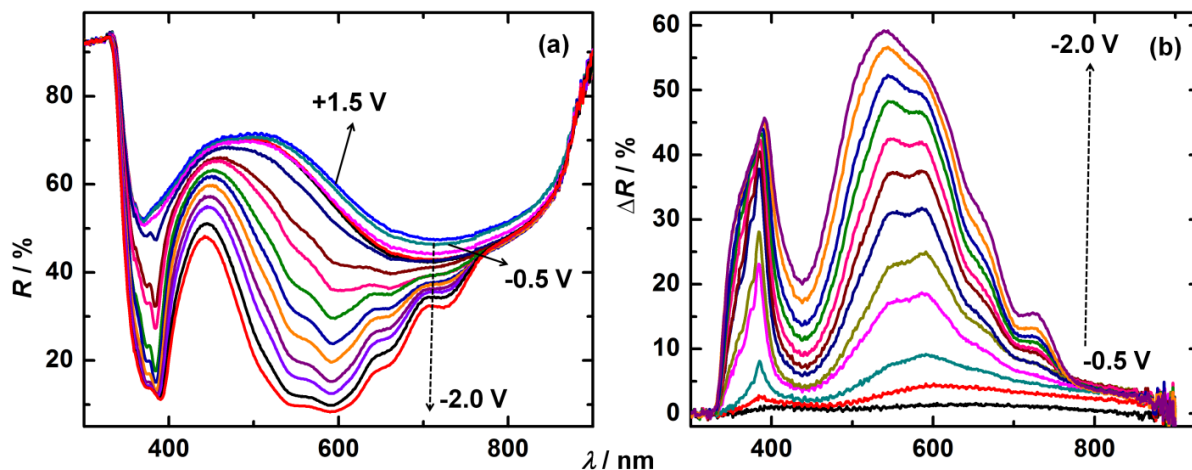

Figure 7.10 (a) *In-situ* specular reflectance spectra of the PPBP−PB ECD recorded under different reduction potentials starting from -0.5 V and in steps of 0.2 V upto -1.1 V and then in steps of 0.1 V up to -2.0 V, and under oxidation potentials of $+0.5$, $+1.0$ and $+1.5$ V; all potentials applied to the blank FTO electrode or cathode of the ECD and (b) the corresponding reflectance modulation (ΔR) plots for the ECD with reflectance response under $+1.5$ V used as reference for determination of ΔR for all the negative potentials from -0.5 V to -2.0 V.

7.3.5.4 Switching kinetics of the PPBP-PB ECD

Switching kinetics of the PPBP-PB (PMMA) ECD were measured at λ_{max} of 590 nm in transmittance mode with 3, 5 and 20 s as step-times, and under a square wave potential of $\pm$ 1.5 V (Figure 7.11). The time required for %T change to increase from 10% to 90% of its full switch in a half cycle is bleaching time and for %T to decrease from 90% to 10% of its total magnitude is the coloration time. Under a step time of 3 s a coloration time of 0.8 s and a bleaching time of 1.1 s were observed for the PPBP-PB ECD. The magnitude of transmittance change increased as a function of cycle time, as prolonged application of a given potential, affords either the generation of more number of blue colored bipyridyl radical cations on the PPBP moiety (during reduction at -1.5 V) or the conversion of more number of the bipyridyl radical cations to the colorless neutral PPBP salt (during oxidation at $+1.5$ V). However, a maximum transmittance change (ΔT) of 47.8% was attained under a step time of 20 s, and from the plot it is obvious that ΔT acquires saturation after 10.8 s, indicating that further increase in step-time, will lead to no further amplification of ΔT. Color and bleach times determined from this 40 s cycle are 7.4 s and 8.2 s, these values are a measure of time required to induce a full optical switch under an applied potential of $\pm$ 1.5 V.

142

Coloration kinetics is faster than bleaching for the PPBP based ECD, this is due to the generation of radical cation on the FTO, which involves mainly the intercalation of cation from IL within the deposit as a charge balancing ion, which could be faster under cathodic potentials, but in case of bleaching due to very low diffusion rates or diffusion coefficients measured for the PPBP salt, the de-intercalation mechanism will become slower. There are also possibilities of formation of radical cation dimers on FTO due to which there will not be a quick reversible process and the bleaching process becomes slow.
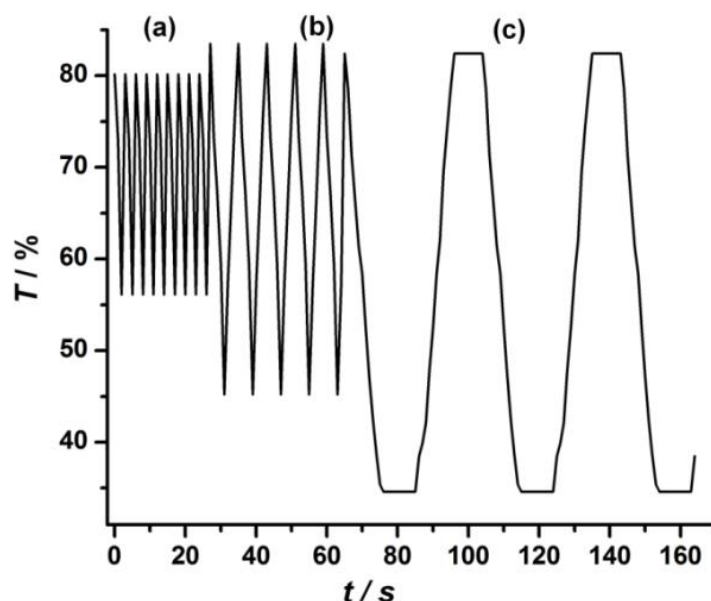

Figure 7.11 Transmittance *versus* time curves for the PPBP–PB ECD at a λ_{max} of 590 nm, under a square wave dc potential of ±1.5 V at different step times of (a) 3 s, (b) 5 s and (c) 20 s.

7.3.6 Charge transport dynamics

Charge transfer phenomena in the PPBP-PB ECD were elucidated by recording impedance spectra of the PPBP-PB ECD, by superimposing a sinusoidal ac voltage of 10 mV over a fixed dc potential of different magnitudes. The experimental and fitted impedance spectra of the ECDs are shown in Figure 7.12 and a tabulation of the parameters is provided in Table 7.1. The equivalent circuit displayed in the insets was found to give good fits almost over the entire frequency range of 1 MHz to 0.01 Hz under consideration. The start of the first semicircle is ascribed to the uncompensated bulk resistance (R_S) of the IL based solid polymer electrolyte which lies in the range of 29-31 Ω; its' value was found to be largely independent of the applied dc bias. A parallel combination of interfacial resistance due to charge transfer (R_{CT}) and the corresponding electrical double layer capacitance (C_{dl}) or constant phase element (Q) and/or a warburg diffusional impedance (Z_w) was used for fitting the data. At zero dc bias, the overall magnitude of impedance was higher than at any finite value of dc voltage. We observed that the impedance was higher under oxidation potentials relative to impedance under reduction potentials. The diameter of the

impedance arc obtained at −2 V is 25 times smaller than that observed at +0.5 V. Lower impedance to charge transfer and transport during reduction is probably caused by the formation of an electronically conducting PPBP radical cation film, immobilized on the transparent conducting substrate. Under oxidation potentials, the film disintegrates into the gel, and at this point, the PPBP molecule is ion-conducting and electron-insulating. The charge transfer resistance was 300 Ω at +0.5 V, and it is 157 and 3.5 Ω at −0.5 and −2 V, implying that the migration of the PPBP from the electrolyte on to the substrate is a facile process whereas the conversion of the radical cation to the cation is not. This was also reflected in the switching kinetics, as coloration was found to be faster than bleaching. Once the mono-radical cation of PPBP is formed on the electrode, this species is electronically conductive, which further promotes electron injection from the external circuit and these are readily taken by the PPBP radical cation to form two or three mono-radical cations. But upon oxidation, the electronically conducting radical cation converts to a bulky ion conducting cation, the overall conductivity of the species decreases and migration of the cation to the gel becomes a resistive process, which accounts for the considerable disparity in the R_{CT} values for reduction and oxidation.

In the low frequency regime, it is the diffusional impedance which governs charge propagation and the parameter Y_o gives the measure of the ease of ion diffusion. Higher the value of Y_o, faster is the diffusion of the ionic species. We observed that Y_o at −2 V was sixteen times greater than the Y_o at −0.5 V, thus indicating an applied potential activated diffusion, during coloration which also facilitates the PPBP blue film formation.
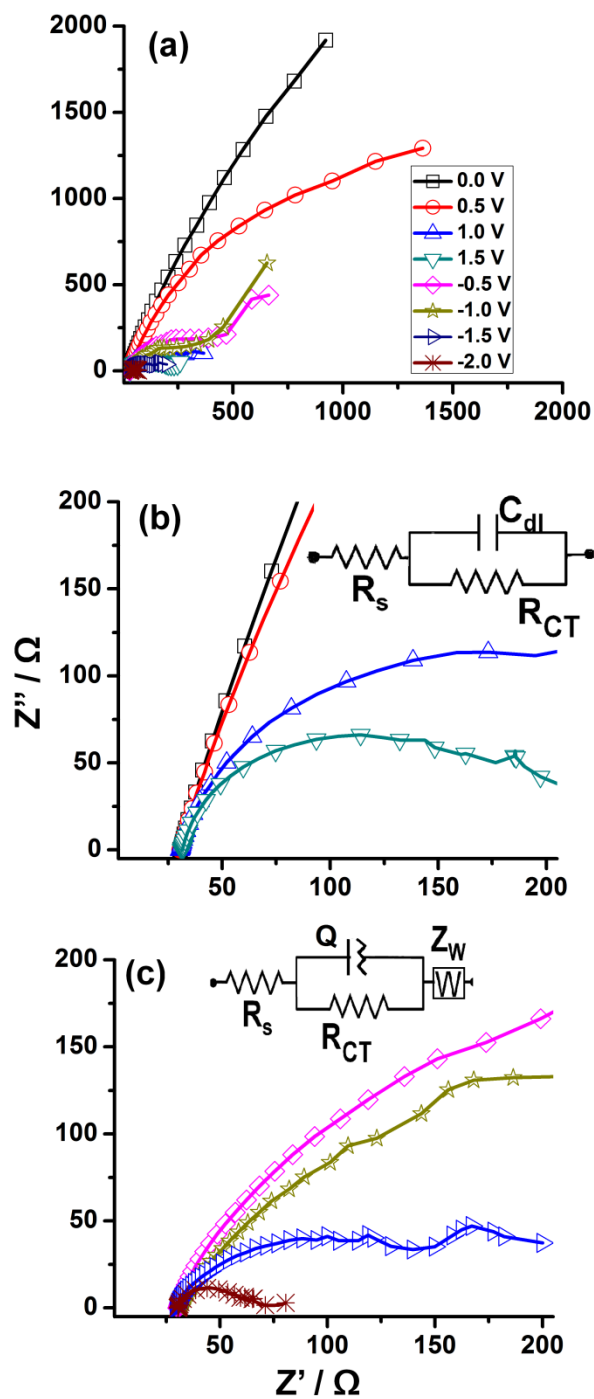
Figure 7.12 Nyquist plots of PPBP-PB ECD recorded under an ac amplitude of 10 mV, at different dc potentials: (a) 0.0 (□), 0.5 (○), +1.0 (△), +1.5 (▽), -0.5 (◇), -1.0 (✶), -1.5 (▷) and −2 (✳) V, over a frequency range of 1 MHz to 0.01 Hz; (b) and (c) are the enlarged views of the high frequency response under positive and negative potentials respectively. Symbols represent the experimental data and the solid lines are obtained by fitting the experimental data in the models shown in the insets of (b) and (c).

Table 7.1: Electrochemical impedance spectroscopy results for PPBP-PB ECD, obtained by fitting the experimental data in the models shown in Figure 7.12.

Applied E / V	R_{CT} / Ω	C_{dl} / μF	Y_o / μS
0	390	0.52	–
+0.5	300	0.54	–
+1.0	121	0.56	–
+1.5	44	0.48	–
–0.5	157	1.42	193
–1.0	31	0.68	201
–1.5	14	0.22	2360
–2.0	3.5	1.4	3030

7.3.7 Durability of PPBP-PB ECD

The ability of the PPBP-PB ECD to resist degradation upon repetitive cycling between the transparent and blue states was examined by cyclic voltammetry and multi-step chronoamperometry. Cyclic voltammograms of the PPBP-PB ECD were recorded over two potential ranges of (i) −2.0 and +2.0 V and (ii) −1.2 V to +0.2 V at 5 mV s^{-1} for 1000 cycles. The voltammograms for the 1st and the 1000th cycle are shown in Figure 7.13. The current densities decrease slightly with cycling. In the cathodic sweep, the broad peak at −0.89 V is assigned to formation of radical cations and the peak current densities are 0.088 and 0.074 mA cm^{-2} for the 1st and 1000th cycle respectively. Similarly, in the anodic branch, a distinct peak signaling the regeneration of the neutral PPBP salt is seen at −0.86 V, and the peak current densities are 0.011 and 0.013 mA cm^{-2} for the 1st and 1000th cycle respectively. The insignificant drop in current densities indicates that PPBP endures the repeated redox switching between the colored and bleached states without deteriorating and is therefore apt for electrochromic applications. To re-affirm the cycling stability of the ECD, color-bleach kinetics were measured with a step time of 5 s under an applied potential of ± 1.5 V for 1000 times in transmittance mode at λ_{max} of 590 nm. The transmittance change (ΔT) offered by the ECD in the first cycle is 37.8% and after thousand cycles, ΔT is 32.6%. The ECD shows no significant degradation, since 96.2% of the original ΔT is retained even at the end of 1000 cycles. Furthermore, color-bleach times are 3.2 and 3.4 s for a 80% switch in the initial cycles, and these remain almost unchanged after 1000 cycles, again illustrating that the PPBP based solid-state ECD is most conductive for practical electrochromic applications like smart windows and anti-glare mirrors.
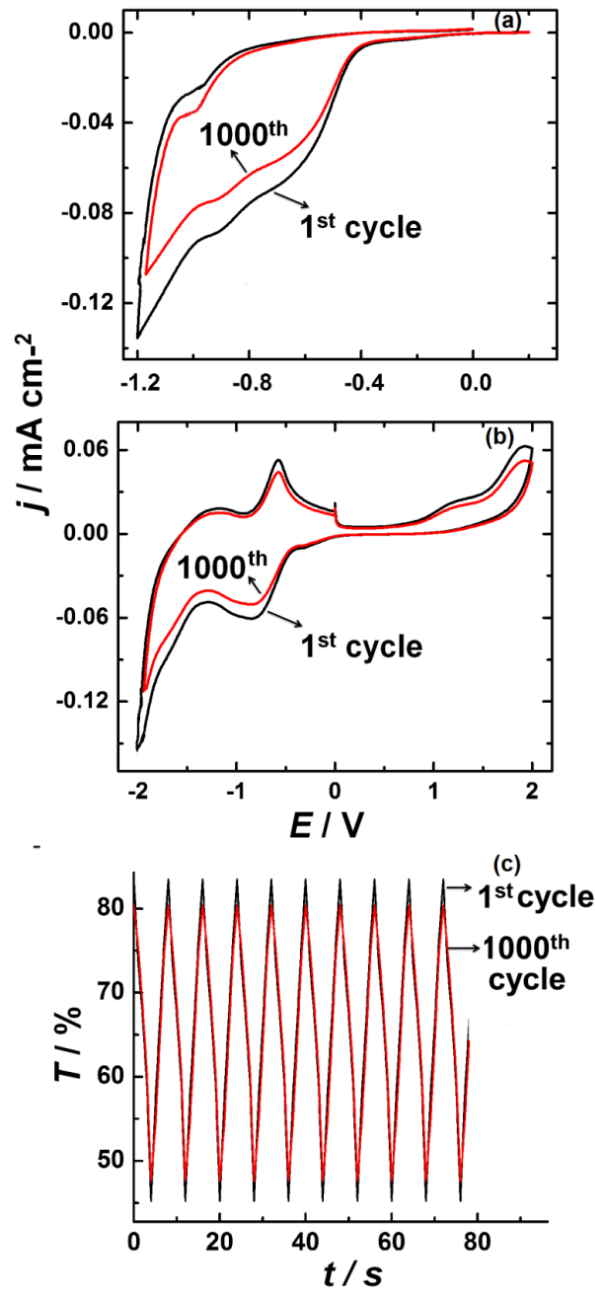
Figure 7.13 Cyclic voltammograms of the PPBP - PB ECD for 1st and 1000th cycles recorded over two potential ranges of (a) −1.2 V to +0.2 V (b) −2.0 and +2.0 V at 5 mV s^{-1} and (c) kinetics of the same ECD measured after 1st and 1000th cycles at a monochromatic wavelength of 590 nm under a square wave dc potential of ±1.5 V at a step time of 5 s.

7.4 Summary

A novel organo-inorganic hybrid polymeric material, poly(cyclotriphosphazene–4,4′-bipyridinium) chloride (PPBP) encompassing a phosphonitrilic trimer as the core, encapsulated by six di-quaternized

4,4′-bipyridyls via covalent bonds was synthesized and characterized by ^{31}P NMR, FTIR and XPS. The presence of both P-N$^+$ and P-N linkages in the PPBP molecule and the conversion of the covalently attached Cl in the precursor (PNCl$_2$)$_3$ trimer to Cl$^-$ ions in PPBP was ascertained by XPS analysis. PPBP undergoes step-wise reversible one electron-transfer reactions and whilst simultaneously switches from colorless to purple to dark blue, finally yielding the reduced PPBP species containing the phosphonitrilic trimer ensconced by di-quaternized radical cations which is immobilized as a colored film on the electrode surface. Complementary PPBP-PB ECDs were fabricated with a PB film as the anode while the cathodically coloring PPBP hybrid was dissolved in a ionic liquid polymeric gel electrolyte. The gel was characterized by wide operational thermal (upto 160 °C) and electrochemical potential (~ 5 V) stability windows and high optical transparency in the visible region along with a temperature invariant large ionic conductivity, which illustrated its' suitability for reflective/transmissive electrochromic ECDs. A high coloration efficiency of 504 cm^2 C^{-1}, and a remarkably large transmission modulation of 70.5% at 590 nm, one of the highest reported transmittance changes in organic electrochromics, and short color-bleach times of about 1-2 s were registered for the PPBP-PB ECD. The ECD endured 1000 repetitive cycles between colorless and blue states without undergoing any appreciable degradation as ~96% of the original transmission modulation was retained. EIS studies revealed a low magnitude for charge transfer resistance and a high value of Warburg parameter for radical cation propagation during reduction, which were correlated to the observed faster coloration during redox switching. These studies not only bring out the significance of the inorganic (PNCl$_2$)$_3$ trimer in directing the synthesis of new organo-inorganic hybrid polymers, with unparalleled application potential but also pave ways to exploit this trimer for synthesizing a different class of novel high performance electroactive compounds.

References

[1] H.R. Allcock, R.L. Kugel, Inorg. Chem. 5 (1966) 1016.
[2] H.R. Allcock, R.L. Kugel, J. Am. Chem. Soc.87 (1965) 4216
[3] P. Dallas, A.B. Bourlinos, D. Petridis, N. Boukos, K. Papadokostaki, D. Niarchos, N. Guskos, Polymer 49 (2008) 1137.
[4] J. Li, M. Josowicz, Chem. Mater. 9 (1997) 1451.
[5] K. Ciepluch, N. Katir, A.E. Kadib, A. Felczak, K. Zawadzka, M. Weber, B. Klajnert, K. Lisowska, A. -M. Caminade, M. Bousmina, M. Bryszewska, J.P. Majoral, Mol. Pharmaceutics 9 (2012) 448.
[6] M. Pelavin, D. Hendrickson, J. Hollander, W. Jolly, J. Phys. Chem. 74 (1970) 1116.
[7] D.N. Hendrickson, J. M. Hollander, W. L. Jolly, Inorg. Chem. 8 (1969) 2642.
[8] I. Niedermaier, C. Kolbeck, N. Taccardi, P. S. Schulz, J. Li, T. Drewello, P. Wasserscheid, H.-P. Steinrück, F. Maier, ChemPhysChem 13 (2012) 1725.
[9] S. Wolfgang, J. Lucke, F. Krumeich, Chem. Mater. 8 (1996) 281.
[10] K. Karunesh, S. Nem, J. E. Anil, Inorg. Chem. 49 (2010) 5753.
[11] S. Rudhziah, N. S. Mohamed, A. Ahmad, Int. J. Electrochem. Sci. 8 (2013) 421.
[12] O.G. Reid, K. Munechika, D.S. Ginger, Nano Lett. 8 (2008) 1602.
[13] G. Wang, X. Fu, J. Huang, C. Wu, L. Wu, Q. Du, Org. Electron. 12 (2011) 1216.
[14] R.J. Mortimer, J.R. Reynolds, Displays 29 (2008) 424.

[15] R.J. Mortimer, T.S.Varley, Sol. Energy Mater. Sol. Cells 99 (2012) 213.
[16] C.-W. Hua, K.-M. Lee, K.-C. Chen, L.-C. Chang, K.-Y. Shen, S.-C. Lai, T.-H. Kuo, C.-Y. Hsu, L.-M. Huang, R.Vittal, K.-C. Ho, Sol. Energy Mater. Sol. Cells 99 (2012) 135.
[17] T. Niwa, O. Takai, Thin Solid Films 518 (2010) 5340.

Chapter 8

Summary and conclusions

8.1 Summary and conclusions

This thesis mainly focused on the synthesis and applications of cathodic organic electrochromes such as PEDOT and new viologen based materials and devices thereof. Suitable choice of nitrogen substituents in viologens to attain the appropriate molecular orbital energy levels, can in principle, impart a color of choice for the radical cation. The type of organic groups at the pyridyl nitrogen controls their spectral response which is also reflected in the plethora of synthetic efforts concerning new electrochromic viologens with different functional groups. The viologens have spurred considerable research interest, due to their significant commercial success. Gentex, NREL and Sage Electrochromics have successfully commercialized viologen based EC mirrors for vehicles. So the quest for high performance viologens stems from their huge potential in the commercial sector. Conducting polymers are widely used as electrodes in electrochemical devices such as electrochromic devices (smart windows, rear-view mirrors, elements of information displays etc.), chemical sensors, owing to ease of processability, ability to store and release charge by undergoing facile oxidation and reduction reactions, good electrochemical cycling stability and low cost. Further, large electro-optical contrasts and their ability to exhibit multiple colors under different applied potentials render them suitable especially for electrochromic applications.

In this thesis, electrodes of PEDOT and its' composites were synthesized and were evaluated in terms of both fundamental and practical viewpoints. PEDOT, is one of the most successful CPs, because of it's low band gap, excellent environmental stability, high electrical conductivity and good transparency, in the oxidized or doped state. PEDOT offers the possibility of cost-effective manufacturing, flexibility, and the exciting prospect of roll-to-roll large-scale production. Considering the gamut of advantages offered by PEDOT, the present thesis dealt with the synthesis, characterization and application of PEDOT and its' composites to electrochromic devices both on rigid support as well as on flexible substrates. The objective was to attempt and establish novel dopants for electropolymerizing PEDOT films and integrating it further with appropriate moieties to enhance the electrochemical and electro-optical performances. Electrochemistry tools such as cyclic voltammetry, impedance spectroscopy, *in-situ* spectroelectrochemistry etc. used to establish structure-property correlations in these films. ECDs were successfully constructed using PEDOT based electrodes and viologen based materials and their performance parameters were evaluated for practical applications. The efforts are summarized below.

- PEDOT films were synthesized by a facile electropolymerization route by using poly(diallyldimethylammonium) chloride (PDDA) as the counter-ion source. To enhance their efficacy, the fullerene derivative N–methyl fulleropyrrolidine (N-FP) was embedded in the PEDOT/PDDA films since the electron-conducting ability of the N-FP can enhance the conductivity, optical contrast, and ion-storage capacity in PEDOT/PDDA/N-FP film compared to that of PEDOT/PDDA film. Both the PEDOT/PDDA and PEDOT/PDDA/N-FP films showed an unprecedented dramatic digression from the expected optical response of conventional PEDOT, exhibiting distinct π–π* absorptions in the visible region in air, corresponding to a bandgap of 1.1–1.3 eV. The neutral state of these films showed split components, which was simultaneously accompanied by a reversible color change from bright blue (in oxidized form) to deep brown (in reduced form). Atomic force microscopy and Kelvin probe force microscopy provided evidence for the higher nanoscale current-carrying capacity and lower localized work function for PEDOT/PDDA/N-FP than for PEDOT/PDDA; both the energetics and conductivity well observed to be conducive for fast redox switching. The obtained results for PEDOT/PDDA and PEDOT/PDDA/N-FP pave the way for the utilization of this material for electronic, electrochemical, and optical functions.

- PEDOT and PB films were deposited via electrodeposition route and ECDs were fabricated by two approaches. In one approach, an *in-situ* polymerized ionic liquid based gel electrolyte using methylmethacrylate monomer (MMA) was used for PEDOT-PB (MMA) devices. In another approach, a gel with PMMA dispersed in IL was used. From the impedance, electrochemical and spectroelectrochemical studies it was found that the *in-situ* polymerized device showed superior performance compared to the PMMA based devices. Using the *in-situ* polymerization process, HV based large area ECDs (8 cm × 6 cm) with PB as counter electrode were prepared. Reflective (specular) modulation for the ECD was observed to be 64 % at 614 nm at a reduction potential of −3.0 V and an oxidation potential of +1.5 V. Switching times of the order of ~5 s were observed, to induce a 50% change of the total contrast. The device was also found to have a cycling life of at least a 1000 cycles of clear to dark and dark to clear and a shelf life time of one year without undergoing degradation.

- Conducting plastic electrodes were prepared by depositing PEDOT on PET substrates. Uniform coverage of PEDOT over PET dimensions of ~20 cm × 6 cm was achieved. The sheet resistance of PEDOT/PET films was found to be 600 Ω/□ for a film with an optimized thickness of ~400 nm. The visible light transmittance offered by the film is 93% for an 80 nm thick film and it reduced nominally to 61% for a 400 nm thick film. Conducting atomic force microscopy studies showed the

nanoscale conductivity of the PEDOT/PET film to be 0.103 S cm^{-1} and the film was found to be composed of high current carrying domains spread over micron length scales. The ability of the PEDOT/PET film to function as an optically transparent conducting electrode, was demonstrated by electrodeposition of Prussian blue (PB) on the same, followed by the construction of an electrochromic PEDOT-PB device. The device underwent a color change from pale blue to deep violet-blue, under applied bias, and exhibited coloration efficiencies of 92 cm^2 C^{-1} at λ$_{max}$ of 585 nm and 750 cm^2 C^{-1} at 1190 nm. Repetitive cyclic voltammetry and kinetic data for the device revealed the device to be stable for 1000 cycles as it retained ~83% of its' original optical change, thus demonstrating its' use as an economically viable solar modulating smart window. The high homogeneity of the PEDOT deposit over PET, the optimal balance between conductivity and optical transparency, and the demonstration of an electro-optical device open up opportunities to employ this electrode in a variety of low cost optoelectronic devices.

- Influence of a butyl imidazole and ethyl indole in a viologen and on its' electrochromic behavior was studied. A new electrochromic viologen, 1,1′-bis-[4-(5,6-dimethyl-1H-benzimidazole-1-yl)-butyl]-4,4′-bipyridinium dibromide (IBV) was synthesized by di-quaternization of 4,4′-bipyridyl using 1-(4-bromobutyl)-5,6-dimethyl-1H-benzimidazole. The IBV−PB device underwent reversible transitions between transparent and deep blue hues; the color change was accompanied by high optical contrast (30.5% at 605 nm), a remarkably high coloration efficiency of 725 cm^2 C^{-1} at 605 nm and switching times of 2–3 s. The device was subjected to repetitive switching between the colored and bleached states and was found to incur almost no loss in redox activity, up to 1000 cycles, thus ratifying its' suitability for electrochromic window/display applications.

- The effect of ethyl indole in a viologen on its' electrochromic behavior by synthesizing a new electrochromic viologen, 1,1'-bis(2-(1H-indol-3-yl)ethyl)-4,4'-bipyridinium diperchlorate (IEV), comprising of a 4,4′-bipyridyl core, sandwiched between two indole moieties, using 3-(2-bromoethyl)-indole. The indole moieties of the IEV^{2+} salt owing to their electron donating tendency can act like bleaching agents and bleach the viologen faster (IEV$^{+•}$→ IEV^{2+}) and this hypothesis was used for the improved write−erase efficiency of the device. The IEV−PB device underwent reversible transitions between transparent and deep violet-blue hues under applied potentials of ±1.5 V. The device color change was accompanied by a high optical contrast (52 % at 605 nm), a large coloration efficiency of 533 cm^2 C^{-1} at 605 nm and switching times of ~2 s and good stability of ~2000 cycles.

- The effect of inclusion of a hexacyclic phoshonitrillic core in a viologen on its' electrochromic response was studied. A new organo-inorganic hybrid electrochromic material poly(cyclotriphosphazene−4,4′-bipyridinium) chloride salt was synthesized wherein each

phosphorous in the triphosphazene core is linked by diquaternized 4,4′-bipyridyls (PPBP). ECDs were constructed with the PPBP hybrid dissolved in a highly conductive, thermally stable and electrochemically inert ionic liquid based gel electrolyte and a Prussian blue (PB) layer as the anode. The transparent PPBP material undergoes three reversible one electron-transfer reactions to yield a radical cation insoluble film which first acquires a purple hue and then turns deep blue. The PPBP-PB device showed superior EC properties wisely, an extremely large coloration efficiency of 504 $cm^2 \, C^{-1}$, an exceptionally high transmission modulation of 70.5 % at 590 nm, one among highest reported contrasts in organic electrochromics, a large reflectance contrast of 59.2 % at 545 nm and fast switching kinetics.

Overall, in this thesis, fundamental and applied aspects of cathodic organic electrochromes such as viologens and PEDOT based materials were studied, devices were constructed and the electrochemical studies showed that the materials are useful for practical applications like ECRA mirrors and smart windows. PEDOT coated PET films have the potential to replace conventional ITO or fluorine doped tin oxide (FTO) in optoelectronic and electrochemical devices. By using organo-inorganic hybrid polymeric materials like poly(cyclotriphosphazene−4,4′-bipyridinium) chloride based materials, high contrast and multichromic electrochromic materials can be designed. By using new bulky substituents on the bipyridyl core, it is possible to synthesize new viologens which undergo less dimerization during switching and therefore can offer high write-erasure efficiency for superior performance ECDs.

8.2 Future directions / developments

By continuing to develop new EC compounds and by further improving device design and by cost optimization, the applications and usage of these materials are bound to increase. The development of ECDs is a very interesting research area due to their possible application in building architecture, vehicles, trains, sunroofs, and dispalys and aircrafts glazings. Rearview mirrors are already used in vehicles and automobiles. Research on electrochromes and devices is driven by the possibility of numerous applications such as smart windows, small- and large-area displays, solar cells, frozen food monitoring and document authentication. Another important class of ECDs are flexible ECDs and these flexible devices can be even applied to commercial products where the seal of the packaging unit can be attached to a small strip of flexible ECD that can be switched with a low voltage battery, so that customers are assured that the product is 100% genuine. Thus plastic flexible devices can be used for distinguishing genuine products from fake ones. This kind of application has a very widespread usage and demand and our work in flexible ECDs can be applied to this field.

Another advantage related to the use of PEDOT as active material is found in its' easy patterning using photolithography, and it is possible to design pixels or logos based on electrochromic devices. In a typical

example, a thin layer of a photoresist is deposited by spin-coating and exposed to UV light in the presence of a given photomask. After exposure, the photoresist is developed and the uncovered PEDOT is passivated using a diluted bleach (NaOCl) solution. Then, the remaining photoresist is stripped. Finally, the patterned foil is used to construct an electrochromic device. A typical patterned ECD in the colored state shows the presence of a given logo, and this signage is even visible in broad daylight.

Here, flexible electrodes of PEDOT were developed on PET. We can further enhance the conducting properties of the CP by incorporating Ag nanostructures (nanowires or nanoparticles). These Ag regions will act like conducting fillers and carbonaceous nanostructures like fullerenes and graphene can also be used to enhance electronic transport properties of CPs. Further, by utilizing nanoparticles of PEDOT, one can increase EC characteristics in terms of switching speeds and contrast of ECDs. The development of full solid-state electrochromic (EC) devices on polymeric substrates like PET is attractive and conducting flexible electrodes can thus play a major role in the EC display/window industry.

Novel low cost EC materials utilizing inorganic molecules in the viologens can offer high performance ECDs. These materials can be utilized for facades / windows in buildings or sunroofs in cars. In the present thesis, as we applied the $(PNCl_2)_3$ trimer for the synthesis of an organo-inorgaic hybrid viologen and variants of this viologen can be synthesized using the tetramer of $(PNCl_2)_4$ and also $B_3N_3Cl_6$ which may result in electrochromes that may be even superior to the traditional organic viologens in terms of contrast, kinetics and operational life. These new materials with more number of elecrochromes per representative units or viologen salt can result in high contrast and high performance devices. As the polymers of phosphonitrillic compounds are thermally stable, EC applications can be possible at relatively higher temperatures.

We found the *in-situ* polymerization technique for fabrication of ECDs to be very useful for developing large area devices (> 20 cm × 6 cm dimensions). In the recent times, most of the building constructions rely on smart architectures involving the use of glazings which can be energy saving EC windows or smart windows. So the *in-situ* technique that we developed can be a good choice for architectures that use smart windows of very big sizes for office buildings.

Overall, some new viologens capable of offering exceptionally high optical modulation, moderately fast switching speeds and good durability were demonstrated and their electrochemistries were dicussed in detail. Fresh insights to PEDOT (as a film on rigid and plastic support) and PEDOT based devices were provided. These studies on organic electrochromes can be of great use for a variety of practical applications.

List of publications included in the thesis

[1] R. Sydam, M. Deepa, A.K. Srivastava, Electrochromic device response controlled by an *in-situ* polymerized ionic liquid based gel electrolyte, RSC Adv. 2 (2012) 9011-9021.

[2] R. Sydam, M. Deepa, Color in poly(3,4-ethylenedioxythiophene) with profound implications for electronic, electrochemical, and optical functions, ChemPlusChem 77 (2012) 1-12.

[3] R. Sydam, M. Deepa, A.G. Joshi, A novel 1,1′-bis[4-(5,6-dimethyl-1H-benzimidazole-1-yl)butyl]-4,4′-bipyridinium dibromide (viologen) for a high contrast electrochromic device, Org. Electron. 14 (2013) 1027-1036.

[4] R. Sydam, M. Deepa, A new organo-inorganic hybrid of poly-(cyclotriphosphazene-4,4′-bipyridinium)chloride with a large electrochromic contrast, J. Mater. Chem. C 1 (2013) 7930-7940.

[5] R. Sydam, A. Ghosh, M. Deepa, Enhanced electrochromic write–erase efficiency of a device with a novel viologen: 1,1'-bis(2-(1H-indol-3-yl)ethyl)-4,4'-bipyridinium diperchlorate, Org. Electron. 17 (2015) 33-43.

[6] R. Sydam, R.K. Kokal, M. Deepa, A fast, direct, low cost route to scalable, conductive and multipurpose poly(3,4-ethylenedixoythiophene) coated plastic electrodes, ChemPhysChem, DOI: 10.1002/cphc.201402862. (17 Feb 2015).